

**ISTANBUL TECHNICAL UNIVERSITY ★ EARTHQUAKE ENGINEERING AND DISASTER
MANAGEMENT INSTITUTE**

SEISMIC PERFORMANCE OF TUNNEL IN LIQUEFIABLE SOIL



M.Sc. THESIS

Mohsen Fathieh

Department of Earthquake Engineering and Disaster Management

Earthquake Engineering Programme

April 2018

SEISMIC PERFORMANCE OF TUNNEL IN LIQUEFIABLE SOIL



M.Sc. THESIS

**Mohsen Fathieh
(802141239)**

Earthquake Engineering and Disaster Management Institute

Earthquake Engineering Programme

Thesis Advisor: Prof. Dr. Ayfer Erken

April 2018

**İSTANBUL TEKNİK ÜNİVERSİTESİ ★ EARTHQUAKE ENGINEERING AND
DISASTER MANAGEMENT INSTITUTE**

SIVILAŞABİLEN ZEMİN TÜNELİ SİSMİK PERFORMANSI

YÜKSEK LİSANS TEZİ

**Mohsen Fathieh
(802141239)**

Deprem Mühendisliği ve Afet Yönetimi Enstitüsü

Deprem Mühendisliği Programı

Tez Danışmanı: Prof. Dr. Ayfer Erken

April 2018

Mohsen Fathieh, a M.Sc. student of ITU **Institute of Earthquake Engineering and Disaster Management** student ID **802141239** successfully defended the thesis/dissertation entitled “**SEISMIC PERFORMANCE OF TUNNEL IN LIQUEFIABLE SOIL**”, which he prepared after fulfilling the requirements specified in the associated legislations, the jury whose signatures are below.

Thesis Advisor: **Prof. Dr. Ayfer Erken**
Istanbul Technical University

Jury Members: **Prof. Dr. Abdul Hayır**
Istanbul Technical University

Prof. Dr. Ayşe Edinçliler
Bogazici University

Date of Submission: 30 March 2018

Date of Defense: 30 April 2018



To my family,



FOREWORD

First of all, I would like to express my sincere gratitude to my supervisor Prof.Dr.Ayfer Erken for her motivation, supports and patience during this thesis. I am also really grateful for my parents for supporting me.

March 2018

Mohsen Fathieh
(BSc.P.E)





TABLE OF CONTENTS

FOREWORD	v
TABLE OF CONTENTS	vii
ABBREVIATIONS	xi
SYMBOLS	xiii
LIST OF TABLES	xvii
LIST OF FIGURES	xix
SUMMARY	xxv
ÖZET	xxix
1. INTRODUCTION	1
1.1 Purpose of Thesis	3
2. UNDERGROUND STRUCTURES IN LIQUEFIABLE SOIL:	
LITERATURE REVIEW	5
2.1 Introduction	5
2.2 Forces Acting on Submerged Structures in Saturated Soil in Equilibrium Condition	9
2.2.1 Forces Acting On Submerged Structures In Saturated Soil During Liquefaction	10
2.2.2 Calculation of Forces Acting on Floated Structures During Liquefaction Condition.....	11
2.3 Factor of Safety Against Uplift	12
2.4 Mitigation of Tunnel Against Uplift	22
2.5 Effect of Buried Depth on Tunnel Uplift Behavior.....	25
2.6 Effect of Diameter and Width of Tunnel on Uplift Behavior	29
2.7 Effect of Soil Permeability on Tunnel Uplift Behavior	30
2.8 Effect of Input Ground Motion on Tunnel Uplift Behavior.....	34
2.8.1 Effect of Vertical Excitation on Tunnel Uplift Behavior.....	37
2.9 Effect of Dilation Angle of Soil on Tunnel-Soil System	46
2.10 Effect of relative density of soil on tunnel-soil system	47
2.11 Effect of Friction Angle of Soil on Tunnel-Soil System.....	49
3. LIQUEFACTION PHENOMENON	51
3.1 Introduction	51
3.2. Triggering Liquefaction	54
3.2.1 Effect of Input Ground Motion on Liquefiable Soil	54
3.2.2 Relative Density ($D_r\%$).....	56
3.2.3 Grain Distribution and Shapes	56
3.2.4 Strain History and Reconsolidation	57
3.3. Liquefaction-induced Potential and Susceptibility Evaluation	58
3.3.1 Numerical Evaluation of Liquefaction Potential	59
3.4 Post-liquefaction Settlement	61
3.4.1 Post-liquefaction Reconsolidation of Sand	62
4. MECHANICAL BEHAVIOR OF SAND	65
4.1 Response of Sand Under Monotonic and Cyclic Loadings.....	65
4.1.1 Response of Sand Under Monotonic Loading	65
4.1.1.1 Sand Response in Low-strain Condition.....	65
4.1.1.2 Response of Sand in Compression.....	66
4.1.1.3 Response Under Monotonic Loading in Drained Condition	66

4.1.1.4 Response to Monotonic Loading Under Undrained Condition.....	67
4.1.2 Response of Sand Under Cyclic Loading	68
4.1.2.1 Sand Response in Low-strain Condition.....	68
4.1.2.2 Sand Response Due to Cyclic Loading	69
5. FINITE ELEMENT MODELING.....	71
5.1 Introduction	71
5.2 Fully Coupled Fluid- Solid Multiphase Formulation in Opensees Platform....	73
5.2.1 Governing Equations for Fully Saturated Behavior with a Single Pore Fluid	75
5.2.2 Fully Coupled Equations Solution	76
5.2.3 Large Deformation Fully Coupled Formulation	78
5.3 Numerical Stability Fully Coupled Fluid-Solid Effective Stress Analysis	80
5.3.1 Mesh Geometry and Element Size (Δh).....	80
5.3.2 Time Step (Δt).....	83
5.4 Soil Constitutive Models	84
5.4.1 Cyclic Mobility Behavior.....	84
5.4.2 PressureDependentMultiyield (PDMY02 and PDMY) Constitutive Models	85
5.5 Input Ground Motion Selection and Processing.....	89
5.6 Boundary Condition	95
5.6.1 Absorbing Boundary Condition	95
5.6.2 Free Field Boundary Condition.....	97
5.7 Analysis Procedure	99
5.7.1 Transient Gravity Analysis and Corresponding Results	100
5.7.2 Transient Dynamic Analysis and Corresponding Results.....	101
6. SOIL CONSTITUTIVE MODEL CALIBRATION AND SITE RESPONSE VALIDATION	103
6.1 Calibration of Soil Constitutive Model	103
6.1.1 Yield Surface.....	103
6.1.2 Size of Yield Surface, Friction Angle	105
6.1.3 Difference Between Triaxial Compression Friction Angles (ϕ_{TXC}) and Direct Simple Shear Friction Angle (ϕ_{DSS}).....	107
6.1.4 Deviatoric Stress-Strain Relationships.....	109
6.1.5 G/Gmax Curves.....	111
6.1.6 Flow Rule	113
6.1.7 Constitutive Model Input Parameters.....	118
6.1.8 Constitutive Model Input Parameters Validation Against Laboratory Direct Simple Shear Test Data.....	132
6.2 Finite Element Model Procedure for Nonlinear 2D Site Response.....	135
6.3 Wildlife Array (WLA) Site Response Evaluation During 1987 Superstition Hills Earthquake	137
6.4 Port Island Station Site Response Evaluation During 1995 Kobe Hyogoken- Nanbu Earthquake.....	142
6.5 Summary and Conclusion.....	145
7. NUMERICAL EVALUATION OF TUNNEL BEHAVIOR IN LIQUEFIABLE SOIL.....	147
7.1 Effect of Frequency Content of Ground Motion on Uplift Behavior of Tunnel	147
7.2 Effect of Vertical Input Motion on Uplift Behavior of Tunnel	149

7.3 Post-liquefaction Consolidation Settlement Behavior of Tunnel-Soil System	154
7.3.1 Comparison of Tunnel-Soil Response in Vertical Direction	155
7.3.1.1 Excess Pore Water Pressure Generation and Vertical Displacement of Soil in Far-Field	155
7.3.1.2 Excess Pore Water Pressure Generation and Vertical Displacement of Soil in Near-Field.....	159
7.3.1.3 Excess Pore Water Pressure Generation and Vertical Displacement of Soil at Center of Tunnel.....	164
7.3.2 Comparison of Tunnel-Soil Response in Horizontal Direction	167
7.3.3 Ground Surface Vertical Displacement	170
7.4 Effect of Relative Density and Permeability.....	172
8. CONCLUSION AND FUTURE WORK RECOMMENDATION.....	175
REFERENCES	177
APPENDICES	183
CURRICULUM VITAE.....	205



ABBREVIATIONS

FD	: Finite difference method
FE	: Finite element method
PGA	: Peak ground acceleration
EPWP	: Excess pore water pressure
HS	: Hardening soil model
CSR	: Cyclic shear stresses ratio
CRR	: Cyclic resistance ratio
SPT	: Standard penetration resistance
CPT	: Cone penetration resistance
LCC	: Limiting Compression Curve
CSL	: Critical state line
FSSI	: Fluid-soil-structure interaction
PEER	: Pacific Earthquake Engineering Center
CFL	: Courant-Friedrichs-Lewy condition
PT	: Phase Transformation Surface
PDMY	: Pressure Depend Multi Yield
PIMY	: Pressure Independ Multi Yield
TXC	: Triaxial compression test
DSS	: Direct simple shear test
EPRI	: Electric Power Research Institute
USGS	: United States Geological Survey
WLA	: Wildlife Array



SYMBOLS

F_{Vtotal}	: Effective buoyant force
F_B	: Archimedes floatation force
F_T	: Structure's weight
F_{SP}	: Shear friction force
F_{WS}	: Weight of overlaying soil mass
F_{resist}	: Total resistance of overlaying soil mass
H	: Depth of soil
γ'	: Saturated unit weight of soil
K	: Coefficient of lateral earth pressure
ϕ	: Friction angle of soil
D	: Diameter of structure
f	: Frictional resistance factor of soil
K_0	: Lateral earth pressure coefficient
ϕ'	: Friction angle in drained condition
F_{Vtotal}	: Archimedes effective buoyant force
F_{EPP}	: Force of pore water pressure at the bottom of structure
L	: Gradient of shear planes above structure
F_s	: Factor of safety
Q	: Friction resistance force of side walls against soil
U_s	: Archimedes buoyant force due to hydrostatic pressure
U_d	: Uplift force due to excess pore water pressure
F_{seep}	: Seepage force of viscous flow
γ_f	: Specific weight of liquefied soil
γ_{sat}	: Saturated unit weight
γ_t	: Total specific weight of sand above water table
γ_p	: Gross unit weight of pipe
b	: Thickness of pipe lining
γ_0	: Unit weight of pipe's material
D	: Pipeline diameter
γ_m	: Unit weight of manhole
W_s	: Weight of overlaying soil mass

W_S	: Weight of structure
Q_S	: Shear frictional resistance
Q_B	: Shear frictional resistance
U_S	: Static pore water pressure
U_D	: Pore water pressure at invert of tunnel
σ'_{v1}	: Effectice stresses at top of the structure
σ'_{v2}	: Effectice stresses at bottom of the structure
$R_{\text{depth,computed}}$: Depth effect ratio
S	: Modification factor
Dr	: Relative density
K	: Permeability
ψ	: Dilatancy angle
γ	: Unit weight of soil
h	: Depth
σ	: Total stress
u	: Pore water pressure
ε_v	: Volume strain
γ_{\max}	: Maximum shear strain
G_{\max}	: Maximum shear modulus in elastic state
p'	: Mean effective stress
ε	: Axial strain
σ'	: Effective stress tensor
p	: Pore pressure
δ	: Second-order identity tensor
ρ	: Density
n	: Porosity
\mathbf{u}	: Displacement vector
\mathbf{g}	: Gravity acceleration vector
Q	: Undrained bulk modulus
\mathbf{K}	: Hydraulic gradient tensor
ρ_f	: Fluid density
\mathbf{g}	: Gravity acceleration
∇	: Gradient operator

$\dot{\nabla}$: Divergence operator
\mathbf{M}	: Mass matrix
\mathbf{U}	: Displacement matrix
\mathbf{B}	: Strain-displacement matrix
$\boldsymbol{\sigma}'$: Effective stress vector
\mathbf{Q}	: Discrete gradient operator
\mathbf{P}	: Pore pressure matrix
\mathbf{H}	: Permeability matrix
\mathbf{S}	: Compressibility matrix
\mathbf{f}_s	: Body force
\mathbf{f}_p	: Boundary conditions matrix
\mathbf{R}_i	: Viscous drag force
\mathbf{N}_u	: Shape function of the skeleton
\mathbf{N}_p	: Shape function of the fluid
\mathbf{N}_U	: Shape function of the pore pressure
\mathbf{P}_{ij}	: First Piola-Kirchhoff stress tensor
\mathbf{r}_0	: Mass density
\mathbf{m}	: Fluid mass content per initial volume
\mathbf{F}_{ij}	: Deformation Gradient
\mathbf{J}	: Jacobian of the transformation
\mathbf{a}_i	: Tortuosity vector
\mathbf{D}_{km}	: Lagrange strain rate
\mathbf{E}_{IJ}	: Lagrange strain tensor
\mathbf{K}_s	: Bulk modulus of the solid phase
\mathbf{K}_f	: Bulk modulus of the fluid phase
\mathbf{V}_s	: Shear wave velocity
\mathbf{V}_p	: Dilatation velocity
Δl	: Mesh size in vertical direction
λ	: Wavelength
\mathbf{f}	: Frequency
$\boldsymbol{\sigma}'$: Effective Cauchy stress tensor
$\boldsymbol{\delta}$: Second-order identity tensor
\mathbf{p}'	: Mean effective stress
$\boldsymbol{\alpha}$: Second-order deviatoric tensor

M	: Size of yield surface
M_f	: Size of largest yield surface
ϕ	: Friction angle of soil
φ_{TXC}	: Triaxial compression friction angle
φ_{DSS}	: Direct simple shear friction angle
P	: Flow direction of plasticity
P''	: Volumetric measure of plasticity flow
Ψ	: Contraction and dilation function
e	: Deviatoric strain tensor
τ	: Shear stress
J_2	: Second invariant
K_0	: Lateral earth pressure coefficient
K_σ	: Overburden pressure
γ_r	: Reference shear strain
P'	: Effective confining pressure
p_r'	: Reference pressure
$G_{\max,r,\text{oct}}$: Octahedral shear modulus
$\gamma_{\max,r}$: Maximum shear strain
\tilde{Q}	: Normal vector to the yield surface
\tilde{P}	: Normal vector to the plastic potential
ε_c	: Accumulative volumetric strain
γ_d	: Accumulative octahedral shear strain

LIST OF TABLES

	<u>Page</u>
Table 2.1 : Moment and internal force of tunnel lining due to increased buried depth. (Azadi & Hosseini.2010).	26
Table 2.2 : Shear force and moment of lining for to diameter of tunnel (Azadi & Hosseini.2010).	30
Table 2.3 : Centrifuge tests conditions (Ling et al.2003).	35
Table 2.4 : The overall caractristics of input motions conducted by researchers.	36
Table 2.5 : PGA of Input motions used in shaking table tests(Zhuang et al.2016)..	44
Table 2.6 : Dilation angle vs. vertical displacement (Sharafi & Parsafar,2016).....	47
Table 2.7 : Tunnel uplift at different relative densities (Sharafi & Parsafar,2016)...	48
Table 4.1 : Suggested empirical relations for F(e) function (Vytiniotis, 2011).	65
Table 5.1 : Detail of horizontal component of 1995 Kobe earthquake.	90





LIST OF FIGURES

	Page
Figure 1.1 : Daikai subway station. (a) Settlements of the overlaying roadway caused by the subway collapse. (b) Collapse of the central columns of the station.	2
Figure 2.1 : Vertical uplift of manhole and densified surrounded soil.	6
Figure 2.2 : Uplift of parking lot during Tohoku Pacific Earthquake 2011 (Tokimatsu et al, 2012).	6
Figure 2.3 : Uplift of manhole during Tohoku Pacific Earthquake 2011 (Tokimatsu et al, 2012).	7
Figure 2.4 : Heaving of soil under retaining wall during Tohoku Pacific Earthquake 2011 (Tokimatsu et al, 2012).	7
Figure 2.5 : Schematic of forces acting on an embedded structure statically (Chian & Madabhushi, 2012).	9
Figure 2.6 : Schematic of forces acting on pipeline (left) and manhole (right) (Chian & Tokimatsu.2012).	10
Figure 2.7 : Sequence of uplift of buried structure (Koseki et al.1997).	13
Figure 2.8 : Forces acting on buried structure (Koseki et al.1997).	14
Figure 2.9 : Vertical sliding surface of overlay soil mass (Koseki et al.1997).	14
Figure 2.10 : Schematic of buried pipe (Ling et al.2003).	15
Figure 2.11 : Schematic of buried manhole (Tobita et al.2011).	16
Figure 2.12 : Forces acting on embedded structure in liquefiable soil (Lee et al.2017).	18
Figure 2.13 : Excess pore water pressure contour at different Toyoura sand thickness (Xia et al, 2010).	21
Figure 2.14 : Cutoff wall installation Schematic (Liu et al,2006).	22
Figure 2.15 : Post liquefaction responses of tunnel: (a) settlement of tunnel, (b) excess pore water pressure dissipation (Liu et al,2006).	23
Figure 2.16 : Influence of walls on tunnel uplift.	23
Figure 2.17 : Uplift of the structure with different reinforcement thicknesses (Bao et al,2017).	24
Figure 2.18 : Vertical displacements of ground surface with different reinforcement thicknesses (Bao et al,2017).	25
Figure 2.19 : Uplift of pipe with different buried depths (normalized by pipe diameter)(Saeedzadeh & Hataf.2011).	26
Figure 2.20 : Vertical and horizontal displacements of the structure.	28
Figure 2.21 : Subway tunnel uplift displacement in different buried depth (Liu & Song.2005).	29
Figure 2.22 : Uplift of pipeline in term of different pipe diameter (Saeedzadeh & Hataf.2011).	29
Figure 2.23 : Uplift and settlement of tunnel due to permeability variation (Madabhushi & Madabhushi, 2015).	32
Figure 2.24 : Soil vertical displacement at the ground surface above center line of tunnel for different soil permeabilities (Madabhushi & Madabhushi, 2015).	32
Figure 2.25 : Variation of average axial strain with decreasing hydraulic conductivity (Madabhushi & Madabhushi, 2015).	33
Figure 2.26 : Liquefaction ratio near base of centrifuge model at 13 m depth during 1st earthquake (Chian et al 2012).	34

Figure 2.27 : Uplift of tunnel due to different vertical acceleration amplitudes (Liu & Song,2005).	37
Figure 2.28 : Acceleration response of soil at the bottom of tunnel (Liu & Song,2005).	38
Figure 2.29 : Excess pore pressure at the bottom of tunnel due to vertical excitations with different amplitudes (Liu & Song,2005).	38
Figure 2.30 : Uplift of tunnel due to sinusoidal wave in horizontal and vertical directions (Liu & Song,2005).	39
Figure 2.31 : Excess pore water pressure ratio contour at different vertical amplitudes (Bao et al,2017).	40
Figure 2.32 : (a) ground level vertical displacement and (b) uplift displacement with different vertical motion amplitudes (Bao et al,2017).	40
Figure 2.33 : Excess pore water pressure ratio vs. acceleration histories at different ground depth (Bao et al,2017).	41
Figure 2.34 : Pore pressure at bottom of tunnel for 1Hz frequency excitation (Azadi & Hosseini,2010).	42
Figure 2.35 : Pore pressure at bottom of tunnel for 3Hz frequency excitation (Azadi & Hosseini,2010).	43
Figure 2.36 : Uplift of tunnel due to different wave amplitudes (Azadi & Hosseini,2010).	43
Figure 2.37 : Uplift of medium dense sand in post-earthquake phase (Hu & Liu,2017).	44
Figure 2.38 : Tests results for pore pressure ratio at top of the soil domain (Zhuang et al,2016).	45
Figure 2.39 : Pore water pressure generation at different depths due to different dilation angles (Azadi & Hosseini,2010).	46
Figure 2.40 : Tunnel uplift at different dilation angles (Sharafi & Parsafar,2016).	47
Figure 2.41 : Tunnel uplift at different relative densities (Sharafi & Parsafar,2016).	48
Figure 2.42 : Effect of relative density on pipeline uplift at different buried depths (Saeedzadeh & Hataf,2011).	49
Figure 2.43 : Effect of variation of friction angle on pipeline uplift (Sharafi & Parsafar,2016).	49
Figure 2.44 : Effect of variation of friction angle on pipeline uplift (Azadi & Hosseini,2010).	50
Figure 3.1 : Liquefaction at Niigata earthquakes in 1964 (kramer,1996).	51
Figure 3.2 : Schematic of flow liquefaction and cyclic mobility.	53
Figure 3.3 : Cyclic mobility and flow liquefaction response of soil under cyclic and monotonic shear (Rauch, 1997).	53
Figure 3.4 : Effect of peak ground acceleration on liquefied sand thickness (Sharp et al,2003).	55
Figure 3.5 : Stress strain relation during repeated cyclic loading (Ye et al.2007).	57
Figure 3.6 : Liquefaction potential zone assessment by cyclic stress method (Su,2005).	59
Figure 3.7 : Post-liquefaction volumetric strain plotted against maximum shear strain (Ishihara,1996).	61
Figure 3.8 : Schematic of stresses and pore water pressure within the saturated soil.	63

Figure 4.1 : Limiting Compression Curve (LCC) and Critical State Line (CSL) (Limiting Compression Curve (LCC), Pestana & Whittle, 1993 as cited in Vytiniotis, 2011).	66
Figure 4.2 : Process of deformation in sand under shear stress (Vytiniotis, 2011). .	67
Figure 4.3 : Definition of secant shear modulus, G_{sec} , and damping ratio ξ (Vytiniotis, 2011).	68
Figure 4.4 : Experimental data for the: (a) degradation of G/G_{max} vs. y_{cyclic} (b) ξ vs. y_{cyclic} curves for dry Toyoura sand (Vytiniotis, 2011).	69
Figure 4.5 : Typical response of sand in constant volume for Undrained Direct Simple Shear test (gingery, 2014).	70
Figure 5.1 : Schematic of overall soil profile for finite element modeling.	72
Figure 5.2 : Maximum element size in vertical direction for meshing.	81
Figure 5.3 : Typical schematic of nine nodes fully coupled quadrilateral plain strain element (Yang & Elgamal.2002).	82
Figure 5.4 : Schematic of conical yield surfaces in principal stresses and deviatoric plane (Elgamal et al (2002); Elgamal et al, (2003); Yang et al, (2003)).	86
Figure 5.5 : Shear stress-shear strain and shear stress-effective confinement pressure responses of pressure dependent constitutive model.	86
Figure 5.6 : NS record of the 1979 Italian earthquake at Nocera Umbra station, baseline shifted at 5.6 and 8.3(s) (Boore & Bommer.2005).	89
Figure 5.7 : First 60s of horizontal component of 1995 Kobe earthquake.	90
Figure 5.8 : 1995 Kobe earthquake parameters.	91
Figure 5.9 : Fourier amplitude versus frequency contents of 1995 Kobe earthquake.	91
Figure 5.10 : Fourier amplitude versus period of 1995 Kobe earthquake.	92
Figure 5.11 : Elastic acceleration response spectra of 1995 Kobe earthquake for 2% and 5% damping ratio.	92
Figure 5.12 : Elastic acceleration response spectra versus frequency contents of 1995 Kobe earthquake for 2% and 5% damping ratio.	93
Figure 5.13 : Arias intensity of 1995 Kobe earthquake.	93
Figure 5.14 : Fourier amplitude versus frequency contents of 1995 Kobe earthquake for 0.1-10Hz and 0.1-25Hz Band-pass Filtering.	94
Figure 5.15 : Schematic of example free-field boundary condition (McGann & Arduino, 2011).	98
Figure 5.16 : Detail of soil profile, dimensions and boundary condition.	99
Figure 6.1 : Principle of Multi yield surface soil constitutive model.	103
Figure 6.2 : Schematic of triaxial compression test for obtaining the size of yield surface.	106
Figure 6.3 : Various definitions of shear strain.	107
Figure 6.4 : Schematic of stresses and friction angle description in direct simple shear test (ϕ_{DSS}).	108
Figure 6.5 : Deviatoric octahedral backbone curve at effective confining pressure P'	109
Figure 6.6 : Stress-strain relationship at reference pressure pr'	111
Figure 6.7 : Effect of γ_{max} , r variation on stress-strain backbone curve	111
Figure 6.8 : Backbone stress-strain relationship retrieved from the yield surfaces.	112
Figure 6.9 : G/G_{max} curve retrieved from the backbone stress-strain relationship curve.	112
Figure 6.10 : Yield surface and Phase transformation surface (PT).	114
Figure 6.11 : Contraction response due to variation of input parameter c_1	115

Figure 6.12 : Contraction state response due to variation of input parameter c_2	115
Figure 6.13 : Contraction behavior due to overburden stress ($K\sigma$ effect) and input parameter c_3 variation.	116
Figure 6.14 : Dilation response due to variation of input parameter d_1	117
Figure 6.15 : Dilation response due to variation of input parameter d_2	118
Figure 6.16 : Undrained monotonic direct simple shear test simulation response for blow count $(N_1)_{60}=5$ and vertical confining pressures $\sigma'_{vc} = 100$ and 400 KPa.	120
Figure 6.17 : Response of undrained monotonic direct simple shear test simulation for blow count $(N_1)_{60}=35$ and vertical confining pressures $\sigma'_{vc} = 100$ and 400 KPa.	121
Figure 6.18 : Response of undrained cyclic direct simple shear simulation for blow count $(N_1)_{60}=5$ and vertical confining pressure $\sigma'_{vc} = 100$ kPa and load bias $\alpha=0, 0.1, \text{ and } 0.2$	122
Figure 6.19 : Cyclic shear stress ratio versus number of cycles in direct simple shear test simulation for target single-amplitude shear strain of 3%, blow count $(N_1)_{60}=5$, vertical confining pressures $\sigma'_{vc} = 100$ and 800 KPa and load bias $\alpha=0.0$	123
Figure 6.20 : Response of undrained cyclic direct simple shear test simulation for blow count $(N_1)_{60}=35$, vertical confining pressure $\sigma'_{vc} = 100$ KPa and load bias $\alpha=0.0, 0.1, \text{ and } 0.2$	124
Figure 6.21 : Response of undrained cyclic direct simple shear test simulation for blow count $(N_1)_{60}=35$ due to different cyclic stress ratios $CSR = 0.09, 0.50, \text{ and } 1.00$	125
Figure 6.22 : Response of drained monotonic direct simple shear test simulation for blow count $(N_1)_{60}=5$ and vertical confining pressure $\sigma'_{vc} = 100$ KPa.	126
Figure 6.23 : Response of drained monotonic direct simple shear test simulation for blow count $(N_1)_{60}=5$ and vertical confining pressure $\sigma'_{vc} = 100$ and 400 KPa.	127
Figure 6.24 : Response of drained monotonic direct simple shear test simulation for blow count $(N_1)_{60}=35$ and vertical confining pressure $\sigma'_{vc} = 100$ KPa.	128
Figure 6.25 : Response of drained monotonic direct simple shear test simulation for blow count $(N_1)_{60}=35$ and vertical confining pressure $\sigma'_{vc} = 100$ and 400 KPa.	129
Figure 6.26 : Responses of drained strain-controlled cyclic direct simple shear test simulation for blow count $(N_1)_{60}=5$ and vertical confining pressure $\sigma'_{vc} = 100$ and 400 KPa.	130
Figure 6.27 : Responses of drained strain-controlled cyclic direct simple shear test simulation for blow count $(N_1)_{60}=15$ and vertical confining pressure $\sigma'_{vc} = 100$ and 400 KPa.	131
Figure 6.28 : Shear stress and vertical effective stress comparison of the numerically simulated (bottom) and experimentally measured soil response for undrained cyclic simple shear (CSS) test performed on Nevada sand by Arulmoli et al, 1992 (top left) as cited by Karimi et al, 2015 (top right). Test conditions: $Dr=63\%$, $\sigma_{v0}=80$ kPa, and $CSR=0.3$	132
Figure 6.29 : Pore water pressure generation comparison of the numerically simulated (bottom) and experimentally measured soil response for undrained cyclic simple shear (CSS) test performed on Nevada sand by Arulmoli et al, 1992 (top left) as cited by Karimi et al, 2015 (top right). Test conditions: $Dr=63\%$, $\sigma_{v0}=80$ kPa, and $CSR=0.3$	133

Figure 6.30 : Pore pressure versus shear strain comparison of the numerically simulated (bottom) and experimentally measured soil response for undrained cyclic simple shear (CSS) test performed on Nevada sand by Arulmoli et al, 1992 (top left) as cited by Karimi et al, 2015 (top right). Test conditions: $D_r=63\%$, $\sigma_{v0}=80$ kPa, and $CSR=0.3$	133
Figure 6.31 : Shear strain versus number of cycles comparison of the numerically simulated (bottom) and experimentally measured soil response for undrained cyclic simple shear (CSS) test performed on Nevada sand by Arulmoli et al, 1992 (top left) as cited by Karimi et al, 2015 (top right). Test conditions: $D_r=63\%$, $\sigma_{v0}=80$ kPa, and $CSR=0.3$	134
Figure 6.32 : Diagram of finite element model and boundary condition for (a) compliant base boundary condition ; (b) rigid base boundary condition.....	136
Figure 6.33 : WLA 360 component Superstition Hills earthquake recorded at 7.5m depth.....	138
Figure 6.34 : WLA 360 component Superstition Hills earthquake recorded at ground surface level.	139
Figure 6.35 : Wildlife Array geotechnical data for site response simulations (retrieved from NEES,2014).	140
Figure 6.36 : Acceleration, velocity, displacement and response spectra at ground surface recorded vs computed by opensees for wildlife array site.....	141
Figure 6.37 : Port Island component 1995 Kobe earthquake recorded at ground surface level.	142
Figure 6.38 : Kobe Port Island geotechnical data for site response simulations (Cubrinovski et al.1996).....	143
Figure 6.39 : Acceleration, velocity and displacement at ground surface recorded vs computed by opensees for wildlife array site.....	144
Figure 7.1 : Excess pore water pressure generation due to different frequency contents of horizontal component of 1995 Kobe earthquake.....	148
Figure 7.2 : Excess pore water pressure generation due to different frequency contents of horizontal component of Kobe earthquake.....	148
Figure 7.3 : Horizontal components of 1995 Kobe earthquake scaled to 0.3g amplitude.....	149
Figure 7.4 : Vertical components of 1995 Kobe earthquake 0.3g (not scaled).....	150
Figure 7.5 : Vertical components of 1995 Kobe earthquake 0.25g.	150
Figure 7.6 : Combined vertical and horizontal components of 1995 Kobe earthquake for vertical motion with 0.25g, 0.35g and 0.4g and horizontal motion 0.3g amplitudes.	151
Figure 7.7 : Distribution of uplift displacement of ground surface.	152
Figure 7.8 : Distribution of uplift displacement of ground surface due to horizontal component combined with various amplitude of vertical excitation.	152
Figure 7.9 : Uplift displacement at lower middle node of tunnel due to horizontal and vertical components of 1995 Kobe earthquake.	153
Figure 7.10 : Excess pore water pressure at lower middle node of tunnel due to horizontal and vertical components of 1995 Kobe earthquake.....	153
Figure 7.11 : Schematic of extracted results for Far-field, near-field and center nodes of domain.	154
Figure 7.12 : Excess pore water pressure ratio variation in different depth at far-field.	155
Figure 7.13 : Excess pore water pressure ratio and vertical displacement of saturated sand at depth 2m in far-field.	156

Figure 7.14 : Excess pore water pressure ratio and vertical displacement of saturated sand at depth 6m in far-field.	157
Figure 7.15 : Excess pore water pressure ratio and vertical displacement of saturated sand at 14.4m depth (bottom of liquefiable) sand in far-field.....	157
Figure 7.16 : Vertical displacement at different depth at far-field.....	158
Figure 7.17 : Vertical displacement at different depth at far-field.....	158
Figure 7.18 : Excess pore water pressure ratio vs. vertical displacement of saturated sand at depth 2m in near-field 3m away from tunnel.....	159
Figure 7.19 : Excess pore water pressure ratio vs. horizontal displacement of saturated sand at depth 2m in near-field 3m away from tunnel.	160
Figure 7.20 : Excess pore water pressure ratio and vertical displacement of saturated sand at depth 6m in near-field 3m away from tunnel.....	161
Figure 7.21 : Excess pore water pressure ratio and vertical displacement of saturated sand at bottom of liquefiable sand beneath the tunnel.	162
Figure 7.22 : Excess pore water pressure ratio of saturated sand at 2m, 6m and 14.4m depth within the liquefiable sand in near-field 3m away from tunnel. .	162
Figure 7.23 : Vertical displacement at different depth within the liquefiable sand in near-field 3m away from tunnel.	163
Figure 7.24 : Schematic of extracted results for Far-field, near-field and center nodes of domain.....	164
Figure 7.25 : Schematic of extracted results for Far-field, near-field and center nodes of domain.....	165
Figure 7.26 : Schematic of extracted results for Far-field, near-field and center nodes of domain.....	165
Figure 7.27 : Excess pore water pressure ratios at top and bottom middle point of tunnel and beneath the tunnel.....	166
Figure 7.28 : Vertical displacement at different depth within the liquefiable sand in at vertical center line of tunnel.	166
Figure 7.29 : Distribution of vertical displacement at different depth.	167
Figure 7.30 : Excess pore water pressure ratio comparison for far-field, near-field and at center of domain at 2m depth.	168
Figure 7.31 : Excess pore water pressure ratio comparison for far-field, near-field and at center of domain at 6m depth.	168
Figure 7.32 : Excess pore water pressure ratio comparison for far-field, near-field and at center of domain at 14.4m depth.	169
Figure 7.33 : Acceleration vs. vertical displacement at ground surface level in far-field.....	170
Figure 7.34 : Acceleration versus vertical displacement at ground surface level in near-field 3m away from tunnel.	171
Figure 7.35 : Acceleration versus vertical displacement at ground surface level above the tunnel.	171
Figure 7.36 : Excess pore water pressure ratio generation and dissipation history at middle point under the tunnel.....	173
Figure 7.37 : Uplift of Tunnel due to different relative densities at middle point beneath the tunnel.....	174
Figure 7.38 : Distribution of ground surface displacement for different relative densities.	174

SEISMIC PERFORMANCE OF TUNNEL IN LIQUEFIABLE SOIL

SUMMARY

Seismic performance evaluation of structures below the ground surface such as tunnels, manholes, pipelines, subway stations, deep foundation and lifeline systems is an important issue in growing modern urban areas. Therefore, needs for developing reliable tools and methods to decrease damage risk is a priority especially in high seismic risk regions. Evaluation of risk for designing an underground structure can be accomplished by gaining insight into the ground response during strong ground motion. During past two decades, uplift of underground structures buried in liquefiable site has been come to attention between scholars. In this thesis, the emphasize was to evaluate the uplift of tunnel due to geotechnical aspects rather than structural.

In second chapter, some background information available in literature related to underground structures in liquefiable soils were given. Effect of different parameters such as buried depth, wide to buried depth ratio of tunnel, direction of ground motion propagation, permeability, friction angle and dilation angle of soil on tunnel behavior in liquefiable sand were explored. It should be noted that, current understanding on the influences of these parameters on the seismic behavior of tunnels is restricted due to lack of experiments or real case data. Present numerical methods are based on assumptions. Therefore, for the rationality and validation of numerical analyses can be established by carrying out experimental studies and numerical simulations cautiously.

In fifth chapter, the procedure of finite element modeling for implementation in Opensees platform related to tunnel buried in saturated sand explained in detail. The most important issues that may occur during modeling such as chosen time step and adequate element mesh size clarified. Different available and practical boundary conditions procedure in geotechnical computation are described. However, in this research only absorbent boundary condition used and the effect of different boundary conditions on soil-tunnel system behavior was neglected. The numerical outline for free-field analyses consists more attention to the boundary condition to reduce the reflection of energy from far-field lateral sides of the domain and to represent structural and hydraulic interactions at the soil-tunnel interface.

In the analyses procedure gravity analyses performed following by dynamic analysis to evaluate tunnel uplift behavior. The model analyzed with different ground motion amplitudes to investigate the effect of peak ground acceleration on tunnel uplift behavior. Additional evaluation performed for post-liquefaction behavior of tunnel in cohesionless saturated loose sand.

Chapter 6 describes characteristics of the site response model used to perform the parametric analyses as described in Chapter 5. Single element level calibrations procedure was enlightened which were conducted for both cyclic and

monotonic under drained and undrained conditions. The soil constitutive parameters calibrated against a commonly used semi empirical liquefaction triggering routine. As procedure of this constitutive model calibration, a new way was used for assuring that shear modulus reduction curve is compatible with soil shear stiffness.

An extensive soil constitutive model calibration was carried out for PressureDependentMultiYield model (PDMY02) in Opensees. The aim was to capture more accurate response of the soil to be implemented in nonlinear 2D site response analyses for real liquefiable profile case studies. Calibration was only conducted for loose to dense sand with different blow counts of SPT test reported by researchers. Numerical evaluation was conducted with Single element simulation for monotonic and cyclic simple shear test. Different initial confining vertical pressures was considered to simulate soil behavior at different depths. The simulation results was compared with EPRI1993 recommended modulus reduction for sand. The result of calibrated parameters were in agreement with EPRI1993 recommended modulus reduction. Furthermore, the calibrated constitutive model parameters were used to validate the 2D site response of Wildlife Array site and Kobe port island site as real case studies. For Wildlife Array site, downhole array record of Superstition Hills earthquake was used as an input motion at the base of the model. For Kobe Port Island station site, the downhole array record at depth 32m of 1995 Kobe earthquake was used as an input motion. The acceleration, velocity and displacement time histories at ground surface level from simulations were in good agreement with recorded data at each site.

In the second part of chapter 6, the calibrated model parameters are then verified against real case solutions for the linear behavior, and validated against down-hole array recording for Superstition Hills earthquake at the Wildlife Liquefaction Array (WLA) site and Hyogoken-Nanbu, Kobe earthquake at Kobe Port Island site. a series of parametric 2D site response analyses were performed to validate the soil parameters and to study geotechnical parameter that are typically unavailable in the empirical data.

The resulting surface acceleration spectra are compared in a way that is comparable to the empirical method. The differences might be attributable to the inability of the 1D site response analyses to capture 2D and 3D effect such as surface wave and basin effect, or possibly shortcomings the in the 1D model's ability to faithfully represent all salient aspects of 1D wave propagation under liquefaction. Effect of different soil constitutive model parameters on uplift and settlement of soil structure system, effect of geometric of tunnel and soil domain on uplift and settlement of tunnel-soil system such as buried depth of tunnel and effect of height to wide ratio of tunnel and effect of ground motion characteristic's parameters such as frequency contents of motion, amplitude of ground motion and duration are the main parameters effecting behavior of tunnel.

On the other hand, investigation the effect of geometry and ground motion characteristics, only frequency content and acceleration amplitude, on tunnel-soil system in liquefiable soil have been widely evaluated in literature due to simpler procedure for implementation.

In this research, emphasize was on evaluating effect of combined horizontal and vertical excitation, post-liquefaction phase on uplift and settlement of tunnel-soil system and effect of different relative density on tunnel uplift.

In terms of evaluating the effect of horizontal and vertical excitation combination, for vertical to horizontal maximum amplitude ratio higher than unity ($V/H > 1$) an increase in uplift displacement of tunnel was observed. On the other hand, combination of horizontal and vertical excitation with V/H less than 1 will reduces the uplift displacement as it damps out the effect of horizontal excitation. Sand with higher relative density did not liquefied due to generation of less pore water pressure. Therefore, dissipation begins earlier compare to sand with smaller relative density. The rate of uplift and settlement displacement of tunnel increases as relative density decreases.

For evaluation of post-liquefaction consolidation settlement of tunnel numerical simulations using solid-fluid fully coupled effective stress were conducted in OpenSees open source code platform. horizontal components of 1995 Kobe earthquake records was selected and first 40s of records only considered in analyses without any change in frequency contents of motion. The soil assumed as medium dense Nevada sand with relative density $Dr=57\%$ overlaying dense sand with relative density $Dr=74\%$. Extracted results for Far-field, near-field and center nodes of domain. To evaluate the tunnel behavior with the liquefiable soil, critical points within the soil domain are considered horizontally and vertically. Both uplift of tunnel near-field and settlement in far-field in sand with higher relative density are smaller as relative density increases.



SIVILAŞABİLEN ZEMİN TÜNELİ SİSMİK PERFORMANSI

ÖZET

Tüneller, menholler, boru hatları, metro istasyonları, derin temeller ve cankurtaran sistemleri gibi zemin yüzeyinin altındaki yapıların sismik performans değerlendirilmesi, modern kentsel alanların büyümesinde önemli bir konudur. Bu nedenle, özellikle yüksek sismik risk bölgelerinde hasar riskini azaltmak için güvenilir araç ve yöntemler geliştirilmesine duyulan ihtiyaç bir önceliktir. Zemin yüzeyinde bulunan yapıların sismik performansları genellikle yapının atalet kuvvetlerine, zemin büyütmesine ve yapının temel sistemi ile temel zeminine bağlıdır. Doğal periyot ve titreşim modları yeraltı yapıları için anlamsızdır, dolayısıyla yeraltı yapıları deformasyonu göreceli deplasmanlar tarafından yönetilir. Deprem sırasında yapıyı çevreleyen zeminin davranış biçimi yapı üzerinde etkilidir. Bir yeraltı yapısının tasarlanması için riskin değerlendirilmesi, güçlü yer hareketi sırasında oluşabilecek davranış biçimlerine karşı önlem almaktır. Geçtiğimiz yirmi yıl içinde, depremler sırasında sivilaşmış zemine gömülü yeraltı yapılarının zemin yüzeyine çıkması araştırmacıların ilgi alanı olmuştur. Bu tez çalışması kapsamında geoteknik açıdan deprem kuvvetleri altında sivilaşan zeminde oluşan boşluk suyu basıncı nedeni ile tünelin zemin yüzeyine doğru hareket etmesi incelenmiştir.

İkinci bölümde, sivilaşmış zeminlerde yeraltı yapıları ile ilgili literatürde mevcut bazı arka plan bilgileri verilmiştir. Gömülü derinlikte tünel davranışı üzerine derinliğin, tünelin gömülü derinlik oranının, yer hareketi yayılım yönünün, geçirgenlik, sürtünme açısı ve zeminin dilatasyon açısı gibi farklı parametrelerin etkisi incelenmiştir. Bu parametrelerin, tünellerin sismik davranışları üzerindeki etkilerine ilişkin mevcut anlayışın, deney eksikliği veya gerçek durum verileri nedeniyle kısıtlandığı belirtilmelidir. Mevcut sayısal yöntemler varsayımlara dayanmaktadır. Bu nedenle, sayısal analizlerin validasyonu, deneysel çalışmalar ve nümerik simülasyonlar dikkatli bir şekilde gerçekleştirilerek oluşturulabilir.

Beşinci bölümde, suya doymuş kumda gömülü tünel ile ilgili Opensees platformunda uygulama için sonlu eleman modellemesi yöntemi ayrıntılı olarak açıklanmıştır. Seçilen zaman adımı ve yeterli eleman ağ gözü büyüklüğü gibi modelleme sırasında ortaya çıkabilecek en önemli konular netleştirilmiştir. Geoteknik hesaplamalarda kullanılan pratik sınır koşulları açıklanmıştır. Bununla birlikte, bu çalışmada kullanılan absorb (etki azaltan) sınır koşulu ve farklı sınır koşullarının zemin-tünel sistemi davranışı üzerindeki etkisi ihmal edilmiştir. Serbest alan analizleri için sayısal ana hat, alanın uzak alan kenarlarından gelen enerjinin yansımalarını azaltmak ve zemin-tünel arayüzünde yapısal ve hidrolik etkileşimleri temsil etmek amacıyla sınır koşuluna daha fazla dikkat edilmektedir.

Analiz prosedüründe öncelikle tünel-zemin sisteminin zemin yüzeyine doğru hareket etme davranışını değerlendirmek için dinamik analiz ile yerçekimi analizleri gerçekleştirilmiştir. Daha sonra, sonlu elemanlar modelinde, tünelin yükselme davranışındaki maksimum zemin ivmesinin etkisini araştırmak için farklı yer hareketi genlikleri ile analiz edilmiştir. Kohezyonsuz doygun gevşek kum içinde sıvılaşma sonrası zemin davranışı için ilave analizler yapılmıştır.

Bölüm 6'da kullanılan zemin tepkisi modelinin özellikleri Bölüm 5'te olduğu gibi açıklanmış, parametrik analizleri gerçekleştirilmiştir. Tek eleman seviyesinin kalibrasyonu, drenajlı ve drenajsız koşullar için hem dinamik hem de monotonik olarak çözümlenmiştir. Zemin tabakalarını oluşturan parametreler, yaygın olarak kullanılan yarı deneysel sıvılaşmayı tetikleyen yöntemlere karşı kalibre edilmiştir. Oluşturulan model kalibrasyonunun bir prosedürü olarak, kayma modülü azalım eğrisinin zemin kesmedayanımı ile uyumlu olmasını sağlamak için yeni bir yol kullanılmıştır.

Openses programında PressureDependentMultiYield (PDMY02) modeli için kapsamlı bir bünyesel zemin model kalibrasyonu uygulanmıştır. Gerçek sıvılaşabilir profil çalışmaları için doğrusal olmayan 2D zemin tepkisi analizlerinde kullanılacak zeminin daha doğru yanıtını yakalamak amacıyla kalibrasyon araştırmacılar tarafından bildirilen SPT testinin farklı darbe sayılarına sahip olan yoğun kumlara göre yapılmıştır. Monotonik ve dinamik basit kesme kuvveti deneyi için tek elemanlı simülasyon ile nümerik değerlendirme yapılmıştır. Farklı başlangıç sınırlarında düşey basınçların farklı derinliklerde zemin davranışını simüle ettiği düşünülmüştür. Simülasyon sonuçları, kum için EPRI1993 önerilen modül azaltımı ile karşılaştırılmış, kalibre edilmiş parametrelerin sonucu, EPRI1993 önerilen modül azaltımı ile uyumlu olduğu gözlenmiştir.

Altıncı kısmın ikinci bölümünde, kalibre edilmiş yapısal model parametreleri, Wildlife Array bölgesi ve Kobe liman adası alanının 2D saha sonuçlarını gerçek vaka çalışmaları ile doğrulamak için kullanılmıştır. Wildlife Liquefaction Array (WLA) alanı için, Superstition Hills depreminin down-hole array, modelin tabanında bir girdi hareketi olarak kullanılmıştır. Kobe Port Island istasyon sahası için, deprem kaydı olarak 1995 Kobe depreminin 32m derinliğindeki kayıt kullanılmıştır. Simülasyonlardan zemin seviyesindeki hız, hız ve yer değiştirme zamanlarının, her bir sahadaki kayıtlı verilerle iyi bir uyum içinde olduğu gözlenmiştir. Kalibre edilmiş model parametreleri daha sonra doğrusal davranış için gerçek vaka çözümlerine göre doğrulanmış ve Superstition Hills depremi Wildlife Liquefaction Array (WLA) bölgesinde ve Hyogoken-Nanbu'daki için down-hole array kaydına karşı doğrulanmıştır. Kobe liman adasındaki Kobe depremine ait zemin parametrelerini doğrulamak ve tipik olarak ampirik verilerde bulunmayan geoteknik parametrelerin incelenmesi için bir dizi parametrik 2D saha analizi yapılmıştır.

Sonuçta elde edilen yüzey ivme spektrumları deneysel yöntemle benzer bir şekilde karşılaştırılmaktadır. Yüzey dalgası ve basen etkisi gibi 2D ve 3D efektlerini veya 1D modelinin sıvılaşma altındaki 1D dalga yayılımının tüm göze çarpan yönlerini gösterme kabiliyetindeki olası eksiklikleri yakalamak için 1B saha yanıt analizi dikkate alınmıştır. Zemin yapı sisteminin yukarı hareket etmesi veya oturması üzerinde zemini parametrelerinin etkisi, tünel ve zemin alanının geometrik etkisinin tünel-toprak sisteminin tünel ve derinlikteki tünel-zemin sistemi üzerindeki etkisi ve yüksekliğinin tünel ve etki oranına etkisi bu hareketin frekans içeriği olarak yer hareketi karakteristik parametrelerinin, yer hareketinin ve süresinin genliği tünelin davranışına etkileyen ana parametrelerdir.

Öte yandan, sıvılaşabilir zeminde yer alan tünel-zemin sistemi üzerinde etkisi nedeniyle sadece frekans içeriğine ve ivme genlik olarak incelenen geometrinin ve yer hareketi özellikleri etkisi, literatürde yaygın olarak kullanılan basit bir yöntem olarak gerçekleştirilmektedir.

Bu araştırmada, aynı anda yatay ve düşey olarak uygulanan deprem ivmesinin, sıvılaşan zeminde tünel-zemin sisteminin düşey yönde yukarı doğru hareket miktarı ve oturma üzerindeki etkisi ve farklı relatif sıklığın tünel-zemin sisteminin düşey yönde yükselmesi üzerindeki etkisinin incelenmiştir.

Yatay ve düşey ivme kombinasyonunun etkisini değerlendirmek açısından, düşeyden yatay maksimum genlik oranıyla birlikte ($V / H > 1$), tünelin yükselme eğiliminde bir artış olduğu gözlemlenmiştir. Öte yandan, V / H ile 1'den küçük yatay ve düşey uyarım kombinasyonu, yatay ivmenin etkisini azaltarak yukarı doğru hareket miktarını azaltacaktır. Yüksek Relatif sıklıkta olan kumda ilave boşluk suyu basıncının oluşmaması nedeniyle sıvılaşma olmamıştır. Relatif sıklık azaldıkça tünelin yer değiştirmesi ve yer değiştirme hızının arttığı gözlenmiştir.

OpenSees açık kaynak kod platformunda katı akışkan tam efektif stres kullanılarak tünel sayısal simülasyonlarının sıvılaşma sonrası oturmasının değerlendirilmesi için yapıldı. 1995 Kobe deprem kayıtlarının yatay bileşenleri seçilmiş ve frekans aralığında değişiklik olmaması nedeni ile kayıtların ilk 40 saniyesi analizinde dikkate alınmıştır. Orta sıklıkta $D_r = 57\%$ olan Nevada kumu $D_r = 74\%$ olan kumun üstünde yer almaktadır. Tünel davranışını sıvılaşırılabilir zemin ile inceleyebilmek için, zemin içindeki yatay ve düşey kritik noktalar olarak alınmıştır. Relatif sıklık arttıkça, uzak alan, yakın alan ve alanın merkezindeki oluşan tünelin yukarı doğru hareketi ve oturmalar azalmaktadır.

1. INTRODUCTION

Seismic performance evaluation of structures below the ground surface such as tunnels, manholes, pipelines, subway stations, deep foundation and lifeline systems is an important issue in growing modern urban areas. Needs for developing reliable tools and methods to decrease damage risk is a priority especially in high seismic risk regions. Underground structures embedded in saturated soils are vulnerable to uplift or settlement during earthquake events.

One of main features of underground structures is that they are not vibrate independently like structures above the ground surface and they generally displaced with the soil simultaneously despite the soil type and conditions. Such displacements can be formed by seismic waves within the soil and exert excessive loads caused by interaction between soil and underground structures.

Seismic behavior of structures beneath the ground surface, more precisely tunnels, have been investigated by many researchers (Madabhushi, et al.2015; Zhang, et al.2011; Chian, et al.2012,2015; Lee, et al.2017; Chen et al.2014; Zhou et al.2014; Azadiab,2011) for the past decades due to several significant damages observed in past earthquake events such as severe damages reported in Daikai subway station during the Hyogoken-Nambu 1995 Kobe earthquake and tunnel damages during 1999 earthquake in Taiwan at central region of Taiwan (Liu & Song.2005), severe damages and permanent displacements occurred in incomplete section of Bolu tunnels during Kocaeli earthquake in 1999. (Maugeri & Soccodato.2014).Damage to the Sendai Airport transport underground railway caused by uplift during Tohoku Earthquake on Pacific Coast with magnitude $M_w=9.0$ in 2011. After Tohoku earthquake severe damages observed due to really strong ground shaking followed by tsunami half an hour after main shock (Unjoh et al.2012).

Failure in road tunnel in Turkey during Duzce earthquake in 1999 and collapse of structures during china Tangshan earthquake in 1976 and 1989 Loma Perieta earthquake in United States were also another cases of damages in underground structures during earthquake (Liu & Song.2005).

Seismic performance of structures which exist above ground surface generally, depend on inertia force and structural amplification due to ground amplification or specifically foundation of structure, while natural period and vibration modes are meaningless for underground structures alone therefore the underground structures deformation is governed by relative displacements of the soil surrounding the structure during earthquakes.



(a)



(b)

Figure 1.1 : Daikai subway station. (a) Settlements of the overlaying roadway caused by the subway collapse. (b) Collapse of the central columns of the station.

1.1 Purpose of Thesis

Many attempt has been done by scholars to evaluate the behavior of underground structures when the soil has liquefaction potential. However, less attention paid to the post liquefaction phenomena after an earthquake event. The purpose of this thesis is to overcome some of the most important shortcomings of previous works using more advanced soil constitutive model such as capturing post liquefaction, creep behavior and anisotropic stiffness of sand in dynamic analysis.

The present research aim is to investigate the behavior of tunnel in liquefiable sand due to horizontal and vertical seismic wave with emphasize on post liquefaction. In this research, the uplift and settlement of the rectangular tunnel will be evaluated by using finite element modeling.



2. UNDERGROUND STRUCTURES IN LIQUEFIABLE SOIL: LITERATURE REVIEW

2.1 Introduction

By growing society in modern cities, design and constructing lifelines and transportation facilities such as subway stations under the ground surface is an essential. Seismic design routines available for structures above the ground surface is not applicable to underground structures, therefore, adequate procedures need to be developed to design more reliable and safe structures under the ground. Seismic performance of underground structures has been studied by several scholars for various scenarios.

However, in areas where soil is partially or fully saturated the risk of damages to the underground infrastructures and lifelines is very high. Liquefiable loose sand has high potential to generate enormous amount of excess pore water pressure under strong ground motion loading.

Excess pore water pressure can cause severe damages to underground structures such as Subway stations, tunnels, pipelines, gas and oil lifelines, manholes and deposit tank embedded in liquefiable soil due to lateral spreading and uplift during strong ground motion. (Hu & Liu .2017). Researchers discovered that damages to underground structures are mostly due to active fault, slope failure, liquefaction uplift, post-liquefaction settlement and lateral spreading of soil.

Several cases of severe damages to underground structures due to uplift have been reported globally in literature (as cited in Lee et al, 2017). In this case, the uplift behavior of tunnels and subway stations have been investigated by many researches(Chian et al.2014, Kang et al.2014, Zhou et al.2014, Madabhushi & Madabhushi.2015, Lee et al.2017, Chian & Madabhushi.2012, Zhuang et al.2015, Zhuang et al.2016, Li et al.2015, Sharp et al.2003, Liu & Song.2006, Orense et al.2003, Chen et al.2014, Chian & Madabhushi.2012, Chen et al.2015, Hu & Liu.2017).



Figure 2.1 : Vertical uplift of manhole and densified surrounded soil.

Observations and field investigation after strong earthquakes revealed that liquefaction is one of the main cause of damages to large underground structures due to floatation and uplift displacement (see Figures 2.1, 2.2, 2.3 and 2.4). The 1989 Loma Prieta earthquake in Northern California, Northridge earthquake and 1995 Kobe earthquake in Japan are the renowned cases of underground structures failures (Saeedzadeh & Hataf.2011).



Figure 2.2 : Uplift of parking lot during Tohoku Pacific Earthquake 2011 (Tokimatsu et al, 2012).



Figure 2.3 : Uplift of manhole during Tohoku Pacific Earthquake 2011 (Tokimatsu et al, 2012).



Figure 2.4 : Heaving of soil under retaining wall during Tohoku Pacific Earthquake 2011 (Tokimatsu et al, 2012).

The investigation consists of numerous centrifuge tests and finite element analyses of underground structures in saturated and dry soil during cyclic loading under drained and undrained conditions.

Many procedures proposed for evaluating seismic performance of underground structures against uplift. Moreover, different mitigation methods examined by researchers for remediation of tunnels and pipelines against uplift during liquefaction.

Due to complexity of fluid-soil-structure interaction involving and affected by many factors, still there is no unified method to capture effects of all the factors on seismic performance of underground structures adequately. Therefore, more investigation needed to get better insight into behavior of embedded structures in liquefiable and non-liquefiable soil. In the following chapter, a brief review of behavior of underground structures embedded in liquefiable soil will be explored.



2.2 Forces Acting on Submerged Structures in Saturated Soil in Equilibrium Condition

According to Archimedes law of submerged objects in fluid, underground structures can be lifted by upward force due to floating forces exerted on structure in equilibrium condition. The net force exerted on underground structure can be written as:

$$F_{V_{total}} = F_B - F_T \quad (2.1)$$

Where, $F_{V_{total}}$ is the effective buoyant force, F_B is floating force and F_T is structure's weight.

The other forces acting on structure are shear friction force (F_{SP}) and weight (F_{WS}) of overlaying soil mass as illustrated in Figure 2.5. Therefore, the equilibrium condition for acting forces can be expressed as:

$$F_B - F_T \leq F_{WS} + F_{SP} \quad (2.2)$$

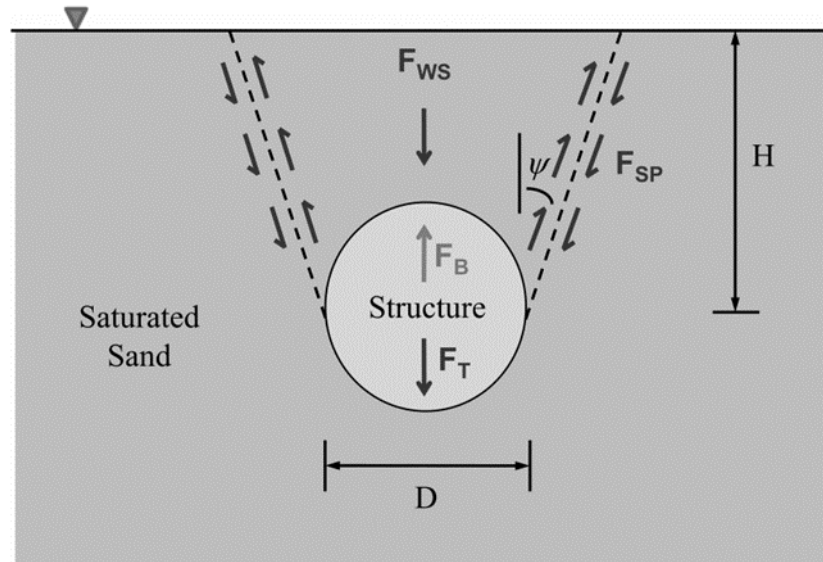


Figure 2.5 : Schematic of forces acting on an embedded structure statically (Chian & Madabhushi, 2012).

According to Veritas.2007, total resistance of overlaying soil mass can be written as:

$$F_{resist} = F_{WS} + F_{SP} = \gamma' \cdot H \cdot D + \gamma' \cdot D^2 \left(\frac{1}{2} - \frac{\pi}{8} \right) + K \cdot \tan(\phi) \cdot \gamma' \cdot \left(H + \frac{D}{2} \right)^2 \quad (2.3)$$

Where, H is depth of soil, γ' is saturated unit weight of soil, K is coefficient of lateral earth pressure which is also evaluating increased stress in vertical direction, ϕ is friction angle of soil and D is diameter of structure.

The equation 2.2 also can be described as:

$$F_{resist} = F_{WS} + F_{SP} = \gamma' \cdot H \cdot D + \gamma' \cdot D^2 \left(\frac{1}{2} - \frac{\pi}{8} \right) + f \cdot \gamma' \cdot \left(H + \frac{D}{2} \right)^2 \quad (2.4)$$

Where, $f = K_0 \cdot \tan(\phi') = (1 - \sin\phi') \tan(\phi')$ is defined as frictional resistance factor of soil, K_0 is the lateral earth pressure coefficient and ϕ' is friction angle in drained condition.

Eq.2.3, only consider the weight of soil exactly above pipeline as illustrated in Figure 2.6 and not like Figure 2.5. This assumption will cause shear friction resistance force to be underestimated.



Figure 2.6 : Schematic of forces acting on pipeline (left) and manhole (right) (Chian & Tokimatsu.2012).

2.2.1 Forces Acting On Submerged Structures In Saturated Soil During Liquefaction

When liquefaction happens loose dense soil will softened and can not resist any shear strength. Therefore, the shear frictional resistance stresses on the inclined shear surfaces will be decreased and underground structure may suffer floatation if resistance forces F_{WS} and F_{SP} are less that Archimedes effective buoyant force (F_{Vtotal}), Thus:

$$F_B - F_T > F_{WS} + F_{SP} \quad (2.5)$$

When liquefaction happened, the pore water pressure is also imposed forces at the bottom of structure therefore eq 2.4 can be rewritten as:

$$F_B - F_T + F_{EPP} > F_{WS} + F_{SP} \quad (2.6)$$

2.2.2 Calculation of Forces Acting on Floated Structures During Liquefaction Condition

According to Chian & Madabhushi.2012, the Archimedes floatation force (F_B) can be computed by specific weight of water multiply by volumetric displacement which means larger structures have larger volume, therefore, they have larger volumetric displacement and imposed by larger floatation force. During constant volumetric displacement, floatation force will remain constant.

When soil is liquefied it behave like a high viscosity liquid, however, in computation of floatation force specific weight of water will be used.

The force imposed by submerged structure's weight (F_T) can be calculated by unit mass of structural material. The weight of soil mass on top of the structure (F_{WS}) can be calculated by:

$$F_{WS} = \left[\left(H.D - \frac{\pi.D^2}{8} + H^2 \cdot \tan\phi' \right) \cdot \gamma' \right] \quad (2.7)$$

Frictional Shear resistance force against uplift (F_{SP}) of structure can be increased as buried depth increases. Shear resistance force against uplift can be calculated as shear stress of soil multiplied by gradient length of shear surface.

During liquefaction effective stress reaches zero and interaction between soil particles will be reduced to zero which led the soil lose shear strength and effect the inclined frictional shear resistance force of overlaying soil mass. Therefore, during liquefaction shear stress changes linearly proportional to degree of liquefaction and can be computed by following relationship:

$$F_{SP} = (\tau_{ave} \cdot 2 \cdot L \cdot \cos\phi') \cdot (1 - r_u) \quad (2.8)$$

Where, L is gradient of shear planes above structure

In circular shape structures, the force imposed by pore water pressure generation can be exerted on lower semi-circular of the structure and it can be computed by integration of pore water pressure on the lower semi-circular of the structure as follow:

$$F_{EPP} = F_{EPP-invert} = \int_{-\frac{D}{2}}^{\frac{D}{2}} P_{EPP-invert} dD \quad (2.9)$$

Chian & Madabhushi.2012 examined and confirmed the formulation by comparing calculated values with centrifuge tests results in different loading and material conditions.

2.3 Factor of Safety Against Uplift

One of the early attempts to investigate uplift behavior of tunnel was conducted by Koseki et al.1997. They carried out a series of shaking table tests with different input motions and Toyoura sand parameters. The tested boxes buried partially and fully within the soil. The soil models prepared with different pore fluid viscosity during experiments. Based on the result of uplifted box three different phase observed during tests.

First phase, Figure 2.7(a), started by lateral deformation of soil mass moving to bottom of box due to losing shear resistance caused by liquefaction. At the second stage pore fluid movement to bottom of box (Figure 2.7(b)). They stated that the difference of vertical stress at bottom of box compare to surround soil at the same level due to existence of structure causes creation of hydraulic conductivity in horizontal direction which is the reason pore fluid flowing toward bottom of buried box. At stage three, Figure 2.7(c), the soil start to densify and box settles due to dissipation of pore pressure.

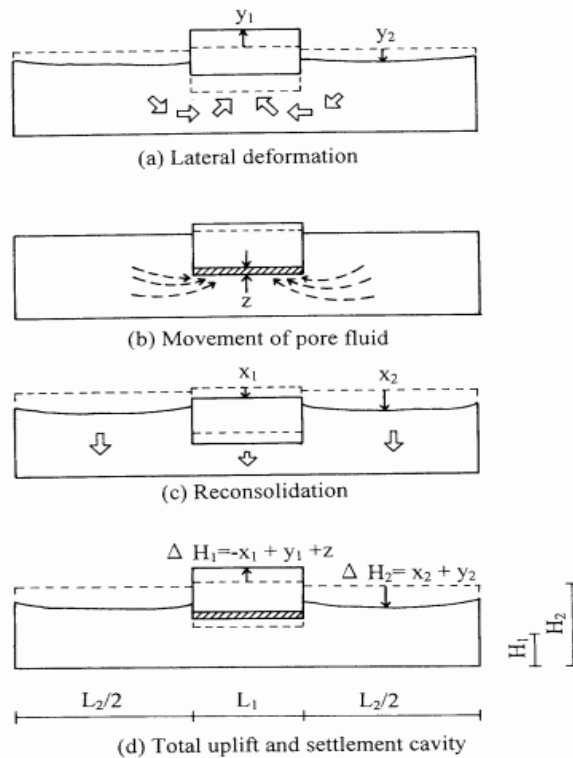


Figure 2.7: Sequence of uplift of buried structure (Koseki et al.1997).

Finally, they came up with following equation and defined so-called factor of safety against uplift:

$$F_s = \frac{W+Q}{U_s+U_d+F_{seep}} \quad (2.10)$$

Where,

W is the structure weight

Q is friction resistance force of side walls against soil

U_s is Archimedes buoyant force due to hydrostatic pressure

U_d is uplift force due to excess pore water pressure

F_{seep} is the seepage force of viscous flow of water within the soil.(Figure 2.8)

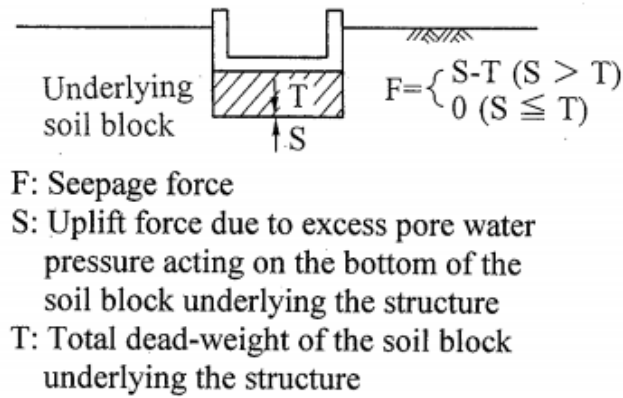


Figure 2.8 : Forces acting on buried structure (Koseki et al.1997).

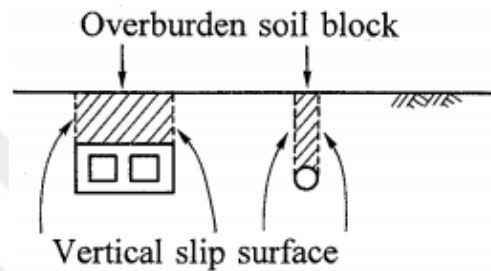


Figure 2.9 : Vertical sliding surface of overlay soil mass (Koseki et al.1997).

Parameter F depends on magnitude of excess pore water pressure and it can be neglected if the pore pressure is not relatively large enough to cause seepage flow. In the case of completely buried box, it was indicated that soil mass above the structure can be considered as part of buried structure (see Figure 2.9). Therefore, the vertical slip friction force (Q) should be increased. They stated that value of factor of safety (F_s) should be approach to 1 if the structure start to uplift due to equilibrium of vertical forces. Therefore, F_s can be used to evaluate uplift triggering of buried structure caused by liquefaction.

Later on, Ling et al.2003 and Tobita et al.2011 verified the factor of safety concept proposed by Koseki et al.1997.

Ling et al.2003 investigated the uplift behavior of buried pipeline in different depths by conducting eight centrifuge tests under 30g gravitational field. They used laminar box, filled with Nevada sand with relative density of 38% under sinusoidal wave at an amplitude of 0.5g. It was indicated that laminar box can replicate the free-field response which can simulate boundary condition properly. Mitigation of buried pipe with gravel deposite was also evaluated during tests.

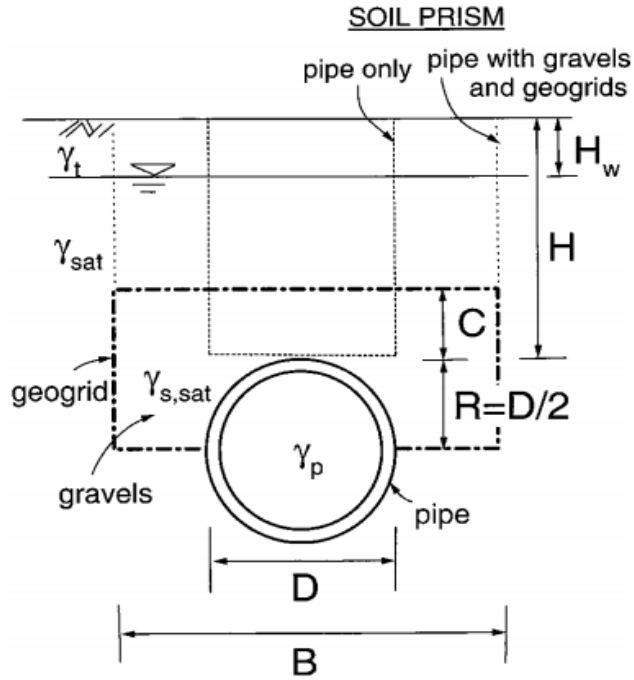


Figure 2.10 : Schematic of buried pipe (Ling et al.2003).

They proposed a technique according to limit equilibrium approach (Figure 2.10) while neglect the shear resistance of the soil mass overlaying on top of the buried pipe during liquefaction. Self weight of pipe and effective weight of overlaying soil were considered as resistance forces to uplift. In terms of mitigation of pipe with gravel, the weight of gravel mass added to overlaying soil mass.

The liquefied soil considered as liquid with specific weight of γ_f same as saturated unit weight γ_{sat} . Moreover, if the water table is not at ground surface level, the total specific weight of sand above water table is denoted as γ_t (Ling et al.2003).

The gross unit weight of pipe can be calculated as:

$$\gamma_p = \frac{(2D-b)b}{D^2} \gamma_0 \quad (2.11)$$

Where, b is thickness of lining, γ_0 is unit weight of pipe's material and D is pipeline diameter. Ling et al.2003 concluded the design procedure by defining factor of safety for pipeline as:

$$F_S = \frac{D(H-H_w)\gamma' + DH_w\gamma_t + w_p}{\pi D^2 \gamma_f / 4} \quad (2.12)$$

By a series of centrifuge tests for buried manhole, Tobita et al.2011 proposed factor of safety against uplift by considering vertical displacement of manhole and consolidation settlement of surrounded soil based on factor of safety suggested by Koseki et al.1997.

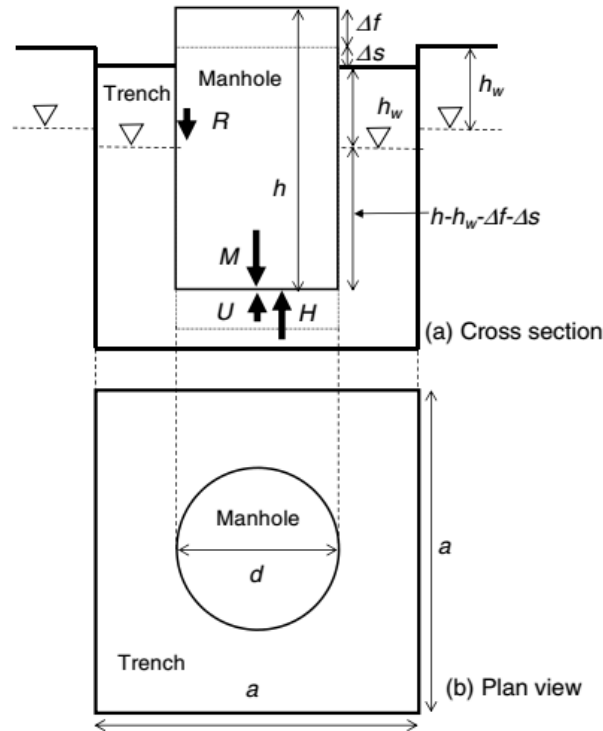


Figure 2.11 : Schematic of buried manhole (Tobita et al.2011).

They assumed water table at ground surface and liquefaction happened in backfill soil. the cross section of trench considered to be large enough.

According to floatation and gravity forces acting on manhole the uplift of manhole defined as:

$$\Delta f = \left(1 - \frac{\gamma_m(h, d)}{\gamma_{sat}}\right)h \quad (2.13)$$

Where, h and d are length and diameter of manhole respectively, γ_m is unit weight of manhole and γ_{sat} is saturated unit weight of backfill.

As it is clear from Eq. 2.12 uplift of manhole can be expressed as ratio of manholes unit weight to saturated unit weight of soil buried in.

A schematic of buried manhole shown in Figure 2.11. They considered manhole buried within a trench with square cross section with side a and water table denoted as h_w .

Although the consolidation settlement might occur in surrounding soil due dissipation of excess pore water pressure but they neglected volumetric strain change due to consolidation and assumed that volume of backfill does not change during floatation and volume of manhole's uplift is equal to settlement of backfill.

Because of short duration of floatation, the water table in surrounding soil deposit considered as constant.

Kang et al. (2014) conducted a comparison between a centrifuge test followed by an effective stress numerical analysis with 2.05 m/s², 4.64 m/s² and 7.15 m/s² input accelerations using multiple shear mechanism and proposed a simplified method that overcome the limitation of previous proposed method by Tobita et al. (2012) which overestimates the maximum uplift displacement of shallow circular pipe exposed to small ground acceleration based on resultant net forces act upon the pipe (Kang et al.,2014).

Based on the Koseki et al.1997 proposed factor of safety against uplift by defining equilibrium of forces contributing in vertical direction , Lee et al.2017 suggested a factor of safety (FS) against uplift for rectangular shape tunnel during liquefaction.

As it is shown in Figure 2.12, the forces acting on structure in equilibrium condition can be written as:

$$W_s + W_B + Q_s + Q_B = U_s + U_D \quad (2.14)$$

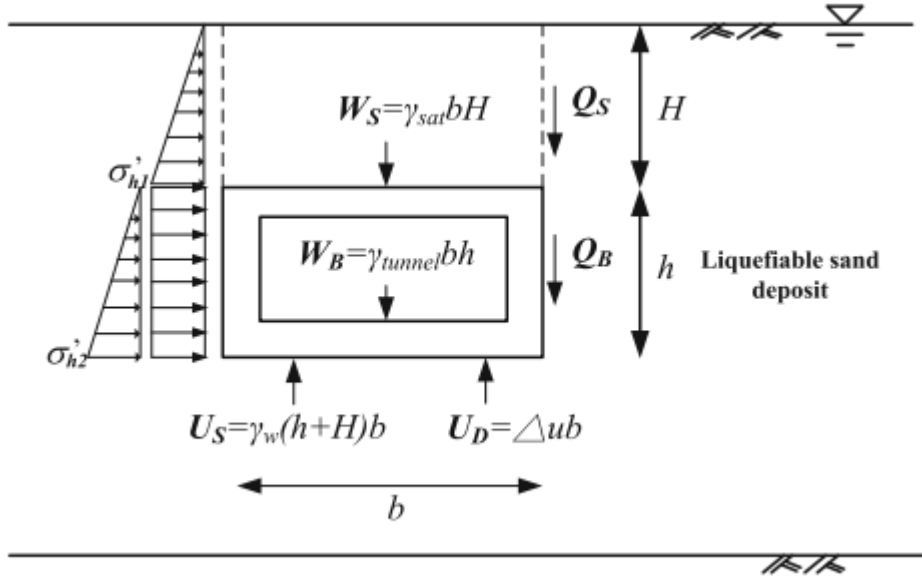


Figure 2.12 : Forces acting on embedded structure in liquefiable soil (Lee et al.2017).

Where,

$W_S = \gamma_{sat} b h$ is the weight of overlaying soil mass,

$W_B = \gamma_{tunnel} b h$ is weight of structure,

$Q_S = H \sigma'_{v1} K_0 \tan \phi$ is shear frictional resistance of soil,

$Q_B = h(\sigma'_{v1} + \sigma'_{v2}) \cdot K_0 \tan \delta$ is shear frictional resistance of soil on left and right side of structure,

$U_S = \gamma_{water} (h + H) b$ is static pore water pressure at invert of tunnel,

$U_D = \Delta u b$ is pore water pressure at invert of tunnel, σ'_{v1} and σ'_{v2} are effective stresses at top and bottom of the structure.

Lee et al.2017 suggested the safety factor against uplift as:

$$FS = \frac{W_s + W_B + Q_s + Q_B}{U_s + U_D} \quad (2.15)$$

Lee et. al,2017 validate the proposed factor of safety (FS) by conducting a series of centrifuge tests on rectangular tunnel.

They concluded that, as long as the factor of safety (FS) computed by Eq.2.14 is less than unity tunnel may suffer floatation during cyclic loading and when the factor of safety approaches to more than unity the uplift displacement will be stopped.

It was observed that tunnel uplift is mainly influenced by embedded depth of tunnel, the input acceleration amplitude at the base and the loading number of cycles.

When saturated sand liquefied, it started to squeeze toward invert of tunnel due to seepage.

A series of fluid-solid fully coupled effective stress finite element-finite difference analyses conducted by Bao et al. 2017 to evaluate the seismic performance of a large rectangular cut and cover subway station tunnel buried in shallow depth of liquefiable sand overlaying clay layer.

Hu & Liu (2017) conducted coupled finite element-finite difference analyses on rectangular tunnel at different depth and relative densities under moderate ground motion. They stated that since the buried structure during earthquake can suffer from both densification (settlement) and floatation therefore the liquefaction itself is not the main cause yet it is a prerequisite to the underground structure uplift.

Furthermore, they indicated that liquefaction degree, liquefied zone of saturated soil and force-induced flow of liquefied soil toward invert of structure have significant influence.

Chian et al. (2014) investigated the effects of ground motion acceleration and buried depth of the shallow circular manhole in liquefiable soil with a series of numerical analyses and dynamic centrifuge experiments. The results showed that both numerical analysis and experimental tests are in agreement that uplift displacement of the structure increase with increasing the excess pore water pressure caused by larger ground acceleration. They also indicated that shallower the buried depth is, the shear resistance and weight of overlying soil are lessened which cause larger uplift. The interaction between soil and structure causes limitation to degradation of shear modulus in the soil around structure which was observed by constant rate of uplift after liquefaction triggered.

The uplift displacement of tunnel mostly influenced by type of the input ground motion, in which sinusoidal acceleration will cause considerably larger uplift compared to real ground motion (Madabhushi, 2014).

The tunnel overlying soil reaches full liquefaction while in the soil at the invert of the tunnel begins to generate excess pore water pressures which is rapidly affected with relative suctions when the tunnel starts to displace upward.

Zhang et al.2011, used coupled finite element and the finite difference method (FE-FD) to investigate the seismic behavior of rectangular subway station embedded in loose sand. They considered the tunnel lining as a rigid body (neglect the soil-structure interaction) and neglect the lining internal forced. They concluded that excess pore water pressure maintained within the soil even after earthquake event finished for some time which caused uplift displacement due to liquefied soil around the tunnel. They also mentioned that vertical displacement of tunnel could be decreased by decreasing the overlaying liquefiable soil thickness.

The result also showed that liquefaction happened at certain depth, not more than 28m, in which at higher depth, the excess pore water pressure is generated slower.

Chen et al.2014 compared 2D and 3D finite element models of rectangular tunnel in heterogeneous saturated soil, in which large deformation could occur when soil liquefied.

In terms of permeability, the 3D model result showed that water can dissipates from both left and right sides of structure. Also it was observed the water could dissipate from infront and back side, therefore, growth of excess pore pressure due to soil water dissipation behavior in 3D model is more rapid compare to 2D model.

Zhuang et al,(2016) implemented a series of shake table tests of rectangular subway station model embedded in liquefiable sand with different peak ground acceleration ground motions.

Dynamic properies of fine sand sample were founded by resonant column technique.

The results showed that when staurated sand in partially liquefied phase, it can not recover the accumulated strain and as a result the cumulative residual strain is muh higher than non-liquefied and post liquefaction phaeses.

The results also revealed that uplift displacement of tunnel station is largest when the soil is completely liquefied. Zhuang et al,(2016) indicated that when the sand part above the tunnel in completely liquefied the dynamic pressure on left and right sides of tunnel is larger.

Usually the uplift behavior of tunnel and pipelines assessed by factor of safety due to equilibrium of applied forces on underground structures perpendicular to the ground

surface. However in practice the design methods may not be properly able to capture the uplift deformation of structure by taking the factor of safety into the account.

chen et al.2011 evaluated the effect of peak ground acceleration(PGA), excess pore water pressure (EPWP) and maximum strain response on a rectangular two story subway tunnels using centrifuge tests under near and far filed seismic loads.

Xia et al.2010 analyzed a rectangular two story tunnel model by using solid-fluid fully coupled finite element method with emphasize on liquefiable Toyoura sand thickness. They used soil constitutive model adapted according to cyclic mobility concept which is an extensive version of modified Cam Clay constitutive mode with anisotropy and overconsolidation assumptions. The analyses focus was on effect of liquefiable soil thickness on seismic performance of saturated Toyoura sand. The result of analyses for different saturated Toyoura sand thickness illustrated in Figure 2.13.

According to Figure 2.13, uplift displacement observed under the tunnel structure due to sand liquefaction and liquefied sand flow toward invert of tunnel from both sides of tunnel. It is also declared that increasing of liquefiable sand thickness led to larger uplift displacement.

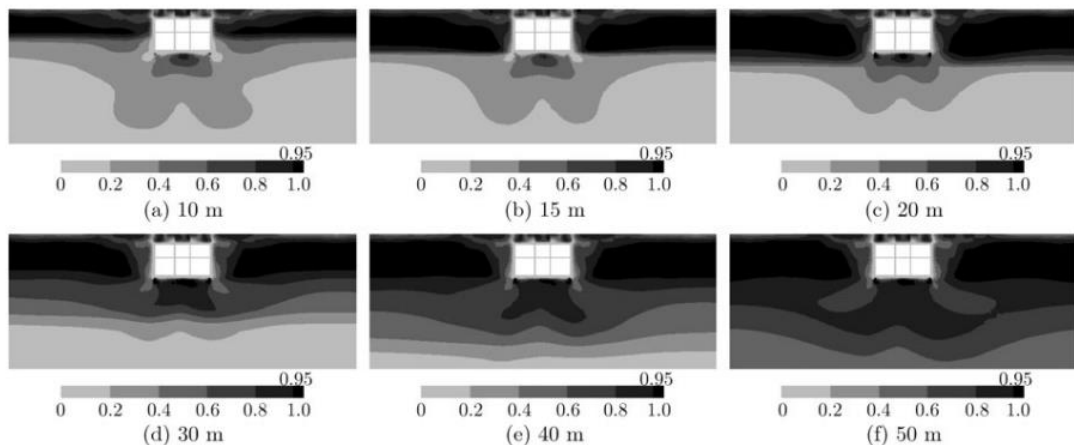


Figure 2.13 : Excess pore water pressure contour at different Toyoura sand thickness (Xia et al, 2010).

2.4 Mitigation of Tunnel Against Uplift

Light weight of tunnel compare to surrounding saturated soil, excess pore water pressure generation and flow of liquefied soil toward invert of tunnel are the most important factors in uplift behavior of tunnel during earthquake which can be reduced by preventing liquefied soil flow toward bottom of tunnel.

Liu et al,2006 performed fully coupled finite element analyses for shallow rectangular subway station tunnel and proposed cutoff wall installation (Figure 2.14) to mitigate the uplift of tunnel in liquefiable soil. They compared results with and without cutoff wall existance.

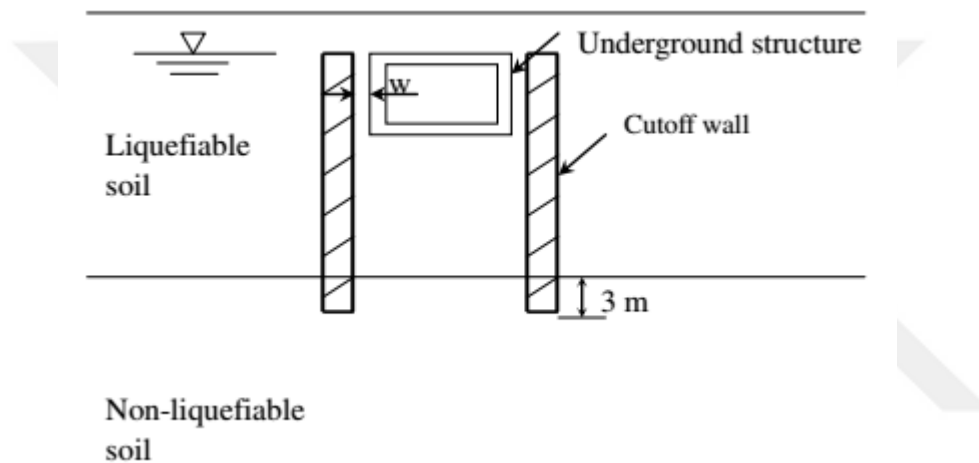


Figure 2.14 : Cutoff wall installation Schematic (Liu et al,2006).

To mitigate uplift, two permeable walls installed along the depth of liquefiable soil at both sides of tunnel with 0.6 m thickness.

The result from analyses showed that installed walls are capable of restricting liquefied soil to flow toward invert of tunnel. However, walls are not able to inhibit excess pore water generation.

In post liquefaction phase, tunnel can suffer settlement due to dissipation of excess pore water pressure. Liu et al,2006 concluded that installed settlement can be decreased by existance of walls (Figure 2.15).

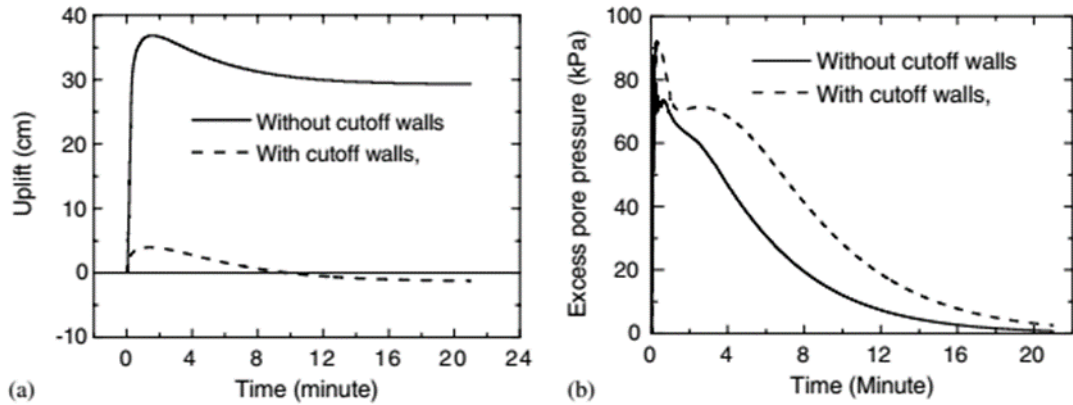


Figure 2.15 : Post liquefaction responses of tunnel: (a) settlement of tunnel, (b) excess pore water pressure dissipation (Liu et al,2006).

The results also indicated that walls effective performance is at colsest distance to tunnel structure. Geometry or material stiffnesses should be large sufficiently.

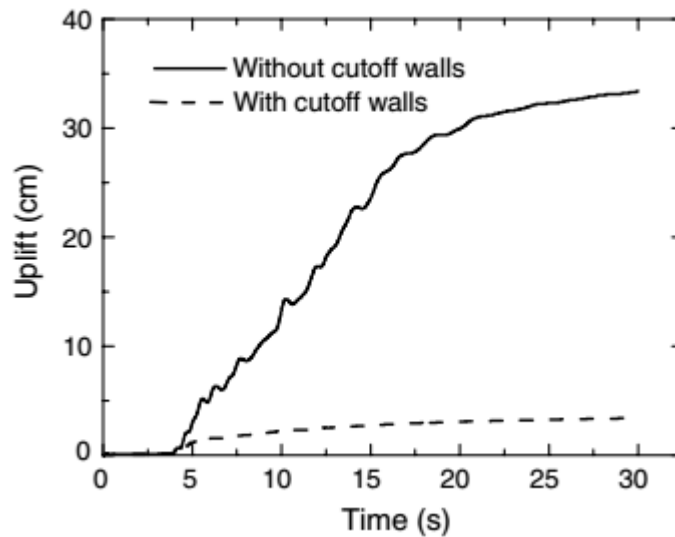


Figure 2.16 : Influence of walls on tunnel uplift.

During past earthquakes, It was observed that the underground structure uplift due to earthquake liquefaction is a usual risk to the underground structure, which may cause much more serious damages to the structures. Therefore, appropriate actions are necessary to decrease the structure uplift caused by soil liquefaction. Bao et al,2017 used mitigation technique for seismic liquefaction which is established recently. Based on the current researches, it is know that soil conditions are important factors for the seismic response of underground structures. Thus, adjusting reinforcement within the liquefiable sand underneath the structure by injection grouting method was used by Bao et al,2017. The reinforcement area takes its length of 22 m (the same with the

structure length), while the thickness increases gradually ranging from 2.5 m to 14 m. Several patterns with the same length L of 22 m but different reinforcement thicknesses H, which are 2.5m, 5m, 7.5m, 12m and 14m, were investigated respectively. The reinforced sand soil was simulated as a linear elastic material with the Young's modulus of 100 MPa, Poisson's ratio of 0.2 and the unit weight of 19.9 kN/m³ used in the analysis.

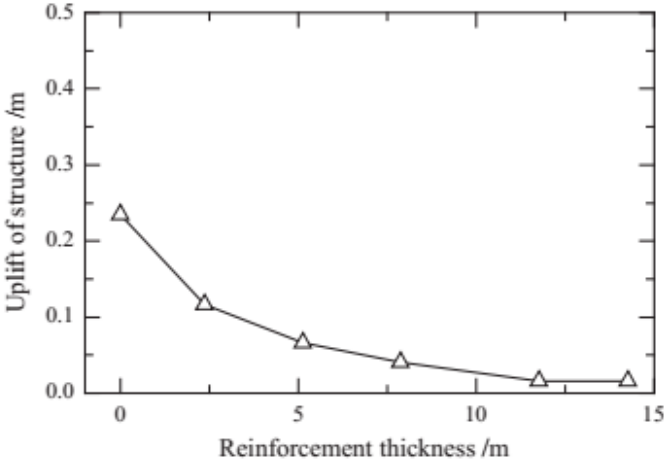


Figure 2.17 : Uplift of the structure with different reinforcement thicknesses (Bao et al,2017).

Figure 2.17 shows the curve of structure uplift with different reinforcement thicknesses beneath structure at the end of earthquake motion. It was confirmed again that structure uplift could be gradually decreased when the reinforcement thickness increased to a certain value, above which the reduction of structure uplift was not obvious with the increase of the reinforcement thickness.

Figure 2.18 shows the vertical displacements on the ground surface at the end of earthquake motion with different reinforcement thicknesses. Obviously, the case with reinforcement could significantly reduce the uplift of tunnel structure.

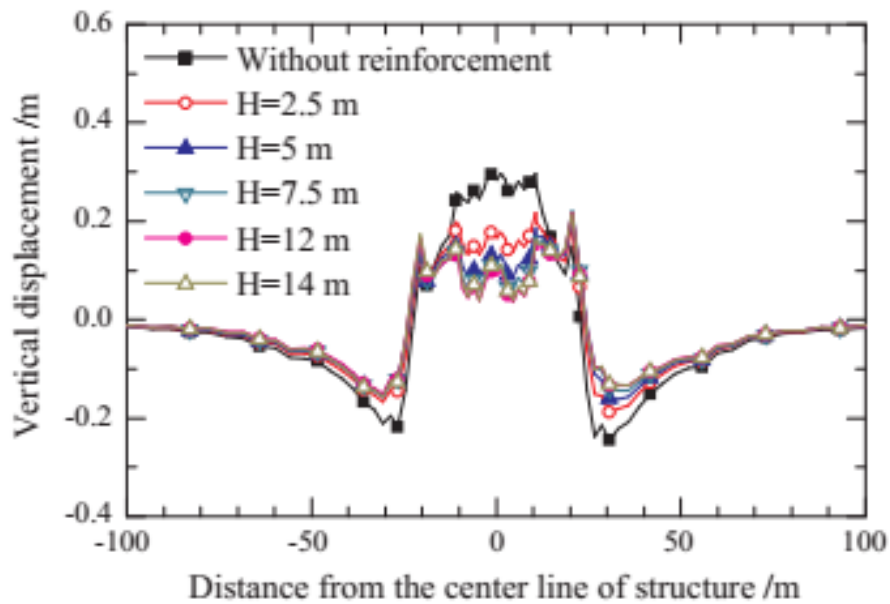


Figure 2.18 : Vertical displacements of ground surface with different reinforcement thicknesses (Bao et al,2017).

2.5 Effect of Buried Depth on Tunnel Uplift Behavior

The buried depth underground structures is an important factor especially in soil that has liquefaction potential. Increasing buried depth will increase the safety against uplift of underground structure (Liu et al., 2005 as cited in Azadi & Hosseini.2010).

However, results from centrifuge tests and numerical analyses showed that increasing buried depth will also increase internal forces and moment in structural elements. Therefore, more examination is essential to find out the optimum buried depth of underground structures.

Increasing internal forces and reduction in uplift force on tunnel due to increase of burial depth confirmed by Azadi & Hosseini.2010. The analyses on circular tunnel with 10 to 20 m buried depths in liquefiable soil showed a significant increase in moment and axial forces in lining.

The more detail of analyses results shown in table 2.1.

Increasing the buried depth will cause increasing the weight of overlaying soil mass and lateral earth pressure acting on the lining.

Table 2.1 : Moment and internal force of tunnel lining due to increased buried depth. (Azadi & Hosseini.2010).

Depth of the tunnel axis (m)	Maximum bending moment (ton-m)	Maximum axial force
8	11	54.3
10	11.1	73.5
13	15.2	98.9
15	16.9	105.1
18	21.9	124.2
20	25.5	126.0

To evaluate the effect of buried depth of underground structure in liquefiable soil a series of numerical simulations of buried pipe in saturated Nevada sand with density ratio 40% were carried out by Saeedzadeh & Hataf.2011. The analyses conducted by 3 circular pipes with 3m diameters and buried in 1.5m, 3m and 4.5m depths respectively. As the results shown in Figure 2.19, the analyses revealed that increasing the burial depth, reduces the uplift displacement of pipe.

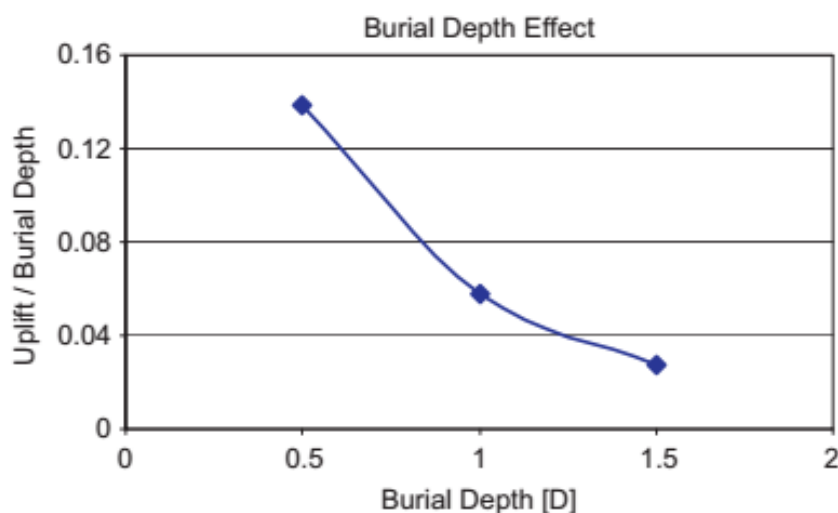


Figure 2.19 : Uplift of pipe with different buried depths (normalized by pipe diameter)(Saeedzadeh & Hataf.2011).

According to aforementioned theoretical aspect of acting forces on underground structures in, friction shear force, weight of overlaying soil mass acting on structure and weight of structure itself against pore water pressure generation at the bottom of

structure, which tries to lift the structure, are involve in uplift displacement of embedded structure. The forces acting on structure mostly dependent on buried depth of structure.

As mentioned in section 2.2, according to Archimedes law for submerged objects in fluid, the total forces exerted on underground structure during both static and dynamic conditions can be written as:

$$F_{V_{total}} = FB - FT \quad (2.16)$$

Where, $F_{V_{total}}$ is the effective buoyant force, FB is floating force and FT is structure's weight.

To evaluate effects of buried depth on uplift behavior of structure, a depth effect ratios based on effective buoyant force proposed by Chian & Madabhushi.2012 by conducting a series of centrifuge tests.

For convenience in study of similar embedded structures at distinct burial depths, they carried out evaluation by means of static equilibrium condition and suggested so called "depth effect ratio" which is the ratio of forces acting on the structure buried at shallow depth to same structure at deeper depth.

Chian & Madabhushi.2012 proposed depth effect ratio as follow:

$$R_{depth,computed} = \frac{F_{shallow}}{F_{deep}} = \frac{[F_{net,b}/(F_{WS}+F_{SP})]_{shallow}}{[F_{net,b}/(F_{WS}+F_{SP})]_{deep}} \times S = \frac{(F_{WS}+F_{SP})_{deep}}{(F_{WS}+F_{SP})_{shallow}} \times S \quad (2.17)$$

Where, S is modification factor for input motion.

They compared the depth effect ratio computed from centrifuge tests's results with Eq 2.17.

They described the depth effective ratio of centrifuge test in the form of:

$$R_{depth,exp} = \frac{\text{uplift of shallow buried depth}}{\text{uplift of structure buried in deep}} \quad (2.18)$$

They indicated that, both weight of top soil mass (F_{WS}) and frictional shear force above the structure (F_{SP}) are governed by planted depth of underground structure.

Structure implanted at shallower depth will have less overburden pressure and less shear force resistance surfaces which led to larger deformation.

Geometry condition, shape of tunnel lining and buried depth of tunnel have high influence on uplift displacement of tunnel embedded in liquefiable soil.

By knowing the correlation between buried depth and diameter of tunnel, height of side wall in rectangular section tunnel, the uplift displacement of tunnel can be evaluated by comparing it against performance results from previous tests with same soil parameters and seismic load conditions (Chian et al.2012).

Chian et al.2012 also conducted centrifuge tests on circular structure buried in shallow depth with different soil and shaking situations. They concluded that

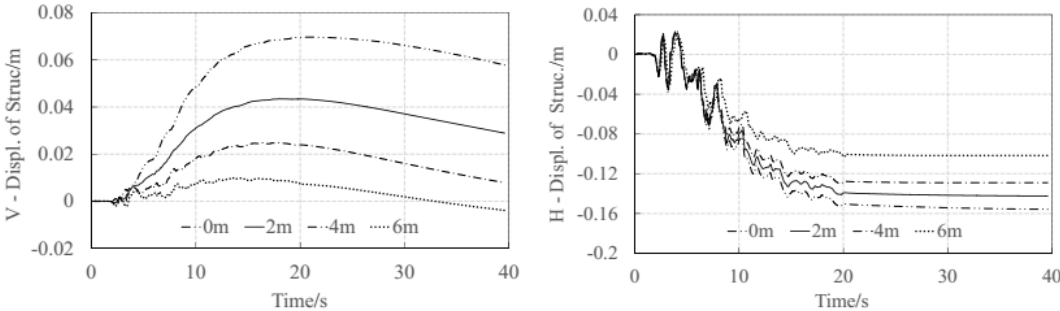


Figure 2.20 : Vertical and horizontal displacements of the structure.

Liu & Song.2005, also investigated the effect of five different buried depths, 4, 7, 10, 13 and 16 m, on uplift of two story subway station with two different loading scenarios, horizontal excitation and horizontal plus vertical excitation. The numerical results demonstrated that uplift displacement decreased as buried depth increased in linear manner during both excitation scenarios (Figure 2.21).

The results also showed that, reduction of excess pore water pressure through depth and weight of overlaying soil mass are two factors against uplift displacement of buried structure.

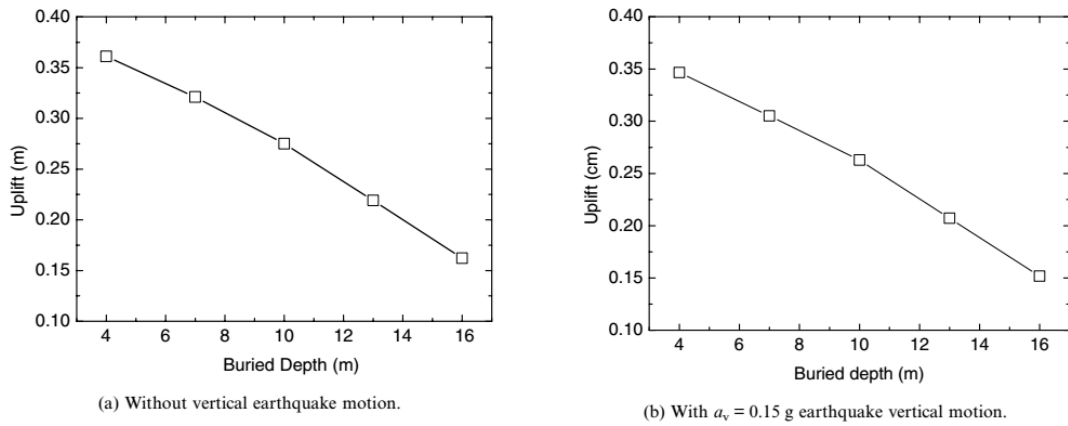


Figure 2.21 : Subway tunnel uplift displacement in different buried depth (Liu & Song,2005).

It was also observed that tunnel internal forces due to combined hydrostatic pressure and dynamic load increased by increasing buried depth. However, they believed that internal forces and moments were detected to be only because of earthquake load. It is interesting that they found out similar moment and shear forces on center wall of subway.

2.6 Effect of Diameter and Width of Tunnel on Uplift Behavior

Saeedzadeh & Hataf,2011 analyses for different buried pipeline diameters revealed that, increasing pipe diameter will cause pipe to uplift more. They examined 1m, 2m and 3m diameters for pipe buried at 3m depth within saturated Nevada sand with 40% relative density. They showed that the ratio of uplift to diameter will decrease by increasing diameter (Figure 2.22).

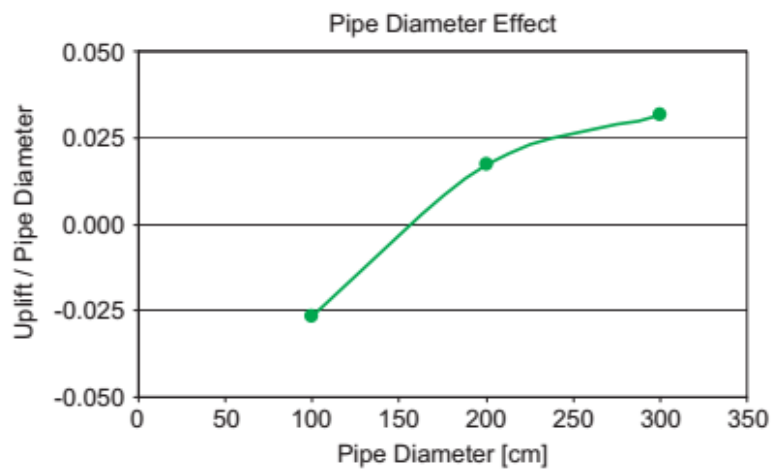


Figure 2.22 : Uplift of pipeline in term of different pipe diameter (Saeedzadeh & Hataf,2011).

Saeedzadeh & Hataf.2011 were also indicated that although by increasing diameter of pipe the resistance weight of overlaying soil mass increases but the influence of pore water pressure generation at the bottom of the pipe is more due to growing rate of pore water generation compare to growing rate of overlaying soil pressure.

The effect of diameter of pipe on uplift behavior also examined by Azadi & Hosseini.2010 where they investigated the behavior of circular tunnel with 0.58, 1 and 1.16 ratio's (ratio of diameter of tunnel to initial model with 6.3m diameter). As demonstrated in Table 2.2, they found out that increasing tunnel diameter will cause internal forces and moment of tunnel lining increases.

Table 2.2: Shear force and moment of lining for to diameter of tunnel (Azadi & Hosseini.2010).

Ratio of tunnel diameter	Maximum bending moment (tom-m)	Maximum axial force (ton)	Maximum shear force (ton)	Tunnel uplift (cm)	Surface ground heave (cm)
0.58	3.95	43.2	9.4	14.3	9.5
1	11.1	73.5	9.7	42.7	24.5
1.16	22.3	79.4	11.4	48.9	32.0

The results revealed that by increasing the tunnel diameter the internal forces and moment increase as well.

It is worth noting that most of efforts that have been done in litreature by scholars on behavior of underground structures, are conducted on pipelines and circular shape tunnels.

Geometry and shape of structure may effect uplift behavior of underground stucture and may led to different results. However, there are very few researches have been done on buried depth effect on rectangular shape of tunnel against uplift.

2.7 Effect of Soil Permeability on Tunnel Uplift Behavior

The tunnel uplift due to liquefaction is dependent to excess pore water pressure generated and maintained within the soil. As pointed out before during and after earthquake, soil properties such as relative density (Dr) and permeability (k) with

different values cause different excess pore water pressure generation and dissipation behavior.

Low permeability could cause Tunnels undergo floatation in fine grain soils, while coarse grain soil with higher permeability can make tunnel compressed downward due to settlement of soil around tunnel walls and invert due to the quick consolidation of the liquefiable soils. Also, decreasing permeability in overlaying soil will cause decrease in average axial strains in the tunnel overlaying soil. (Madabhushi & Madabhushi, 2015).

(Madabhushi & Madabhushi, 2015) conducted a series of numerical analyses for tunnel to evaluate the effect of permeability variation on tunnel uplift or settlement. They carried out analyses with permeability within the range 1×10^{-7} m/s to 0.5 m/s. Figure 2.23 illustrates the uplift and settlement of tunnel in terms of different permeabilities.

As it is shown in Figure 2.23, they found out that for fine grain soil with values of permeability (also called hydraulic conductivity) smaller than 1×10^{-2} m/s, the tunnel will be uplifted due to upward floatation, while, for higher permeabilities the tunnel will suffer settlement due to quick dissipation of pore water pressure.

In addition to the tunnel uplift or settlement, it is also important to evaluate the vertical displacement of soil at ground surface. Figure 2.24. shows the result of analyses carried out by (Madabhushi & Madabhushi, 2015) for vertical displacement at ground surface exactly at center line of tunnel with different permeabilities. As it is shown Figure 2.24, the tunnel suffer uplift in fine grain soil with lower permeability while it settles as permeability increases for soil with larger grain sizes.

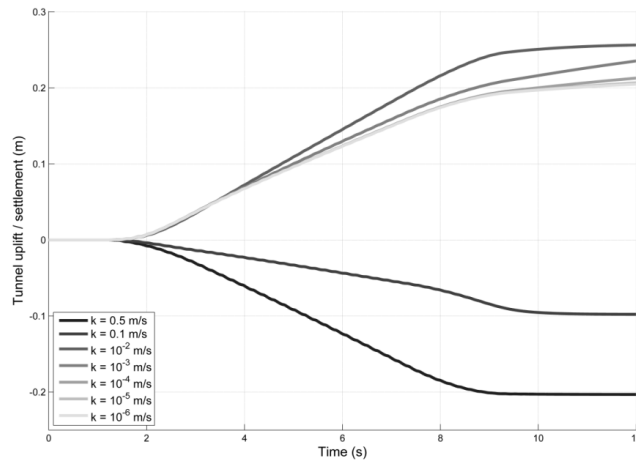


Figure 2.23 : Uplift and settlement of tunnel due to permeability variation (Madabhushi & Madabhushi, 2015).

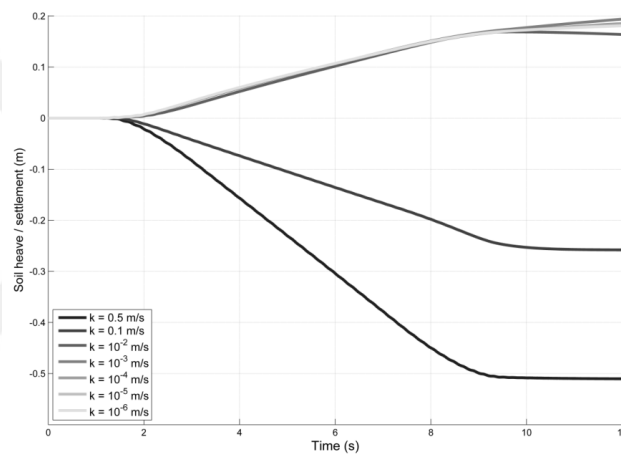


Figure 2.24 : Soil vertical displacement at the ground surface above center line of tunnel for different soil permeabilities (Madabhushi & Madabhushi, 2015).

However, According to (Madabhushi & Madabhushi, 2015), in the soil with high hydraulic conductivity, the settlement is larger at ground surface compare to tunnel level. Therefore, they stated that it is suitable to compute the average axial strain within the domain between surface level and tunnel lining. Figure 2.25. shows the variation of hydraulic conductivity and average axial strain between ground surface level and tunnel lining. According to Figure 2.25, they concluded that the soil can suffer from compression axial strain due to settlement of ground level soil during consolidation after earthquake and tunnel uplift from buoyancy force. This correlation is nonlinear and the rate of axial strain variation reduced by decreasing hydraulic conductivity.

The axial strains are not affected by the hydraulic conductivity further than a specific value.

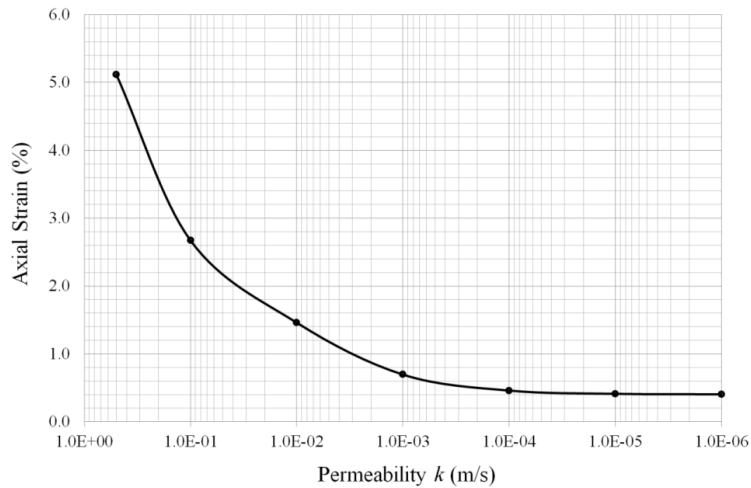


Figure 2.25 : Variation of average axial strain with decreasing hydraulic conductivity (Madabhushi & Madabhushi, 2015).

It is worthwhile to mention that different viscosity and density of pore fluid can also effect permeability and as a result effect the different uplift and settlement in the saturated soil.

Higher fluid viscosity causes lower permeability and vice versa. Lee et al 2017 investigated the effect of permeability on uplift behavior of tunnel by carrying out a series of centrifuge tests. The tests showed that the shallow tunnel in low permeability saturated soil experience larger uplift. They also emphasized that uplift behavior of tunnel significantly affected by pore fluid viscosity and buried depth of tunnel. The result showed that with lower viscosity of pore fluid which also indicate higher permeability, tunnel will experience smaller uplift displacement.

Chian et al 2012 carried out series of centrifuge tests and investigated the behavior of saturated soil with different fluid viscosity.

The tests showed similarity at the initial stage of excess pore pressure generation between fluid with viscosity 7.4 cSt (DC-04-EQ1)) and water (DC-02-EQ1) as shown in Figure 2.26:

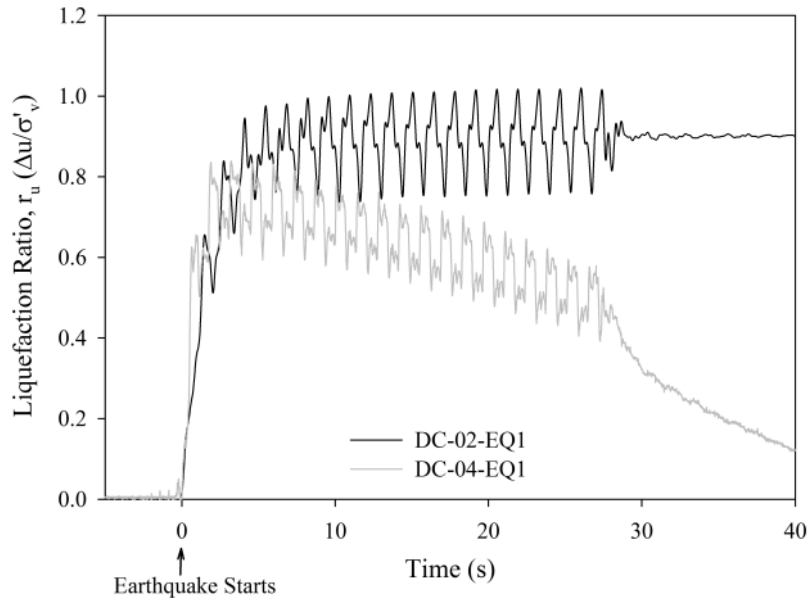


Figure 2.26 : Liquefaction ratio near base of centrifuge model at 13 m depth during 1st earthquake (Chian et al 2012).

The effect of the permeability on generation of excess pore pressure has been examined by many scholars (Chian et al 2012, Madabhushi et.al.2015, Lee et al 2017). Madabhushi et.al.2015 showed that in fine grain soils with low permeability causes tunnel to be uplifted, while in more coarse grain soils with higher permeability the tunnel can be settled due to the rapid pore pressure dissipation.

2.8 Effect of Input Ground Motion on Tunnel Uplift Behavior

Tunnel behaviour during earthquake shaking is influenced by many features such as geometry, buried depth and stiffness of the tunnel lining and the characteristics of the ground motion. However, current understanding on the influences of these parameters on the seismic behaviour of tunnels is restricted due to lack of experiments or real case data. Present numerical methods are based on assumptions, the rationality and validation that required to be established by carrying out experimental studies and numerical simulations cautiously. This section emphasizes on the influence of ground motion characteristics on seismic behaviour of tunnels.

Ling et al.2003 used sinusoidal wave in horizontal direction as an input motion in centrifuge tests for buried pipeline. The sinus wave applied with duration 20 and 60 seconds and frequencies of 3 and 5 Hz. The centrifuge tests conditions demonstrated in table 2.3.

Table 2.3 : Centrifuge tests conditions (Ling et al.2003).

Test No.	Box	Saturating fluid	Frequency (Hz)	Duration (s)	Dry density (g/cm^3)		Burial depth (m)	Test conditions
					Sand	Gravel		
1	Laminar	Metolose	3	60	1.55	—	—	Sand only
2	Laminar	Water	3	60	1.49	—	—	Sand only
3	Rigid	Metolose	3	60	1.53	—	—	Sand only
4	Rigid	Water	3	60	1.55	—	—	Sand only
5	Laminar	Metolose	5	20	1.54	—	1.5	Pipe
6	Laminar	Metolose	5	20	1.54	1.65	1.5	Pipe mitigated
7	Laminar	Metolose	3	60	1.54	—	3.0	Pipe
8	Laminar	Metolose	3	60	1.52	2.3	3.0	Pipe mitigated

The results showed that, test (No.5) conducted by input motion with 20s and 5Hz caused 17.3 cm uplift and input motion in test 7 and 8 with 60s duration and frequency 3 Hz caused 40cm uplift. It was not cleared that more uplift in tests 7 and 8 is due to duration, in other word number of cycles in sinusoidal motion, or the frequency contents of waves.

Table 2.4 shows the characteristics of input motion for evaluating the behavior of tunnel in liquefiable soil during experimental and numerical analyses that conducted by researches.

Table 2.4 : The overall characteristics of input motions conducted by researchers.

Reference	Event	PGA	Duration	frequency (Hz)
Hu & Liu.2017	kobe 1995	0.2g	24	
Kang et al.2014	sinusoidal			1.25
Chian et al.2014	sinusoidal	0.22&0.1	27	
Liu & Song.2005	1995 Kobe earthquake	hor0.3g-ver0.05,0.1,0.15,0.2g	30	
	sinusoidal	hor0.2g--ver0.1g	10	
Azadi & Hosseini.2010	sinusoidal	0.1g	10	1
Cilingir & Madabhushi.2011	sinusoidal	0.165g	15	1
	sinusoidal	0.135g	20	1
	sinusoidal	0.24g	20	1
	sinusoidal	0.126g	20	1
	sinusoidal	0.216g	20	1
	sinusoidal	0.143g	20	1
	sinusoidal	0.22g	20	1
	sinusoidal	0.133g	20	1
	sinusoidal	0.218g	20	1
	sinusoidal	0.088g	20	0.8
	sinusoidal	0.079g	20	0.8
	sinusoidal	0.291g	20	1.2
	sinusoidal	0.315g	20	1.2
	sinusoidal	0.22g	30	1
	sinusoidal	0.218g	30	1
	1995 Kobe earthquake	0.22g	20	1hz-3hz
	1995 Kobe earthquake	0.218g	20	1hz-3hz
Zhuang et al.2015	1995 Kobe earthquake	0.1-0.2-0.3g	40	0.5 to 4 Hz
	El-Centro earthquake	0.1-0.2-0.3g	40	
	Nanjing artificial motion	0.15 g	22	
Sharafi et al.2015	Naghan earthquake			
	Tabas earthquake			
Chian et al.2015	sinusoidal	0.6g	10	3hz
	sinusoidal	0.2g	35	
Madabhushi & Madabhushi.2015	sinusoidal	0.5g	8	
	1995 Kobe earthquake	0.6g	8	
	1996 Kobe earthquake	0.8g	8	
Watanabe et al.2016	sinusoidal		13	3hz
Zhuang et al.2016	1996 Kobe earthquake	0.8g	40	
	El-Centro earthquake	.03-0.11-0.166-0.266-0.328-0.511	40	
Ling et al.2003	sinusoidal	0.5g	60	3hz
	sinusoidal	0.5g	20	5hz
Lee et al.2017	sinusoidal	0.13g	16	1hz
	sinusoidal	0.23g	16	1hz
	sinusoidal	0.25g	16	1hz
Tobita et al.2011	sinusoidal	0.2g-0.7g	30	1.27hz
	sinusoidal	0.6g	10	3hz
Saeedzadeh & Hataf.2011	Tabas earthquake		25	
	Naghan earthquake		5	
	Northridge earthquake		16	
	Landers earthquake		20	
Azadiab.2011	sinusoidal	0.1g	10	1hz
Yang & Wang.2013	sinusoidal	0.1g	10	1hz
Zhang et al.2011	artificial(not clear)	0.1-0.2-0.3-0.4g	30	
Chian & Madabhushi.2012	sinusoidal	0.21-0.22-0.23-0.25g	25-40-50	

2.8.1 Effect of Vertical Excitation on Tunnel Uplift Behavior

As it is known earthquake motion propagates in multidirectional within the soil media and ground motion records has three components, two horizontally and one vertically. The correlation between vertical and horizontal components of motion has been investigated extensively. However, in practice it is common to neglect the effect of vertical components of motion and just consider horizontal excitation as it is common in 1D ground response analysis between scholars.

To investigate the effect of excitation on behavior of subway station tunnel in liquefiable soil Liu & Song.2005 performed finite element analyses with both horizontal and vertical excitation. They conducted the analyses with only horizontal direction and horizontal plus vertical combination. They also investigated the tunnel behavior with sinusoidal wave excitation.

The well known 1995 Kobe earthquake components were selected as an input motion. The horizontal component scaled to 0.3g and vertical components scaled to 0.5g, 0.1g, 0.15g and 0.2g to find out the effect of vertical motion on the net displacement of tunnel. They only considered first 30s of records due to difficulty to perform analysis. The results was interesting as they observed not too much differences in overall uplift of tunnel when horizontal and vertical motion applied simultaneously as it is demonstrated in Figure 2.27.

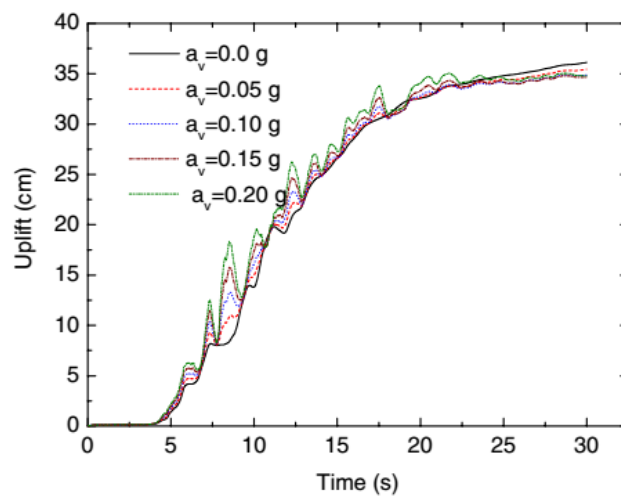


Figure 2.27 : Uplift of tunnel due to different vertical acceleration amplitudes (Liu & Song.2005).

They also observed that vertical excitation has no effect on horizontal motion as illustrated in Figure 2.28. However, acceleration response of soil right at the bottom of tunnel showed significant EPWP fluctuation at certain interval in vertical motion and after that there is no notable difference in EPWP (Figure 2.29).

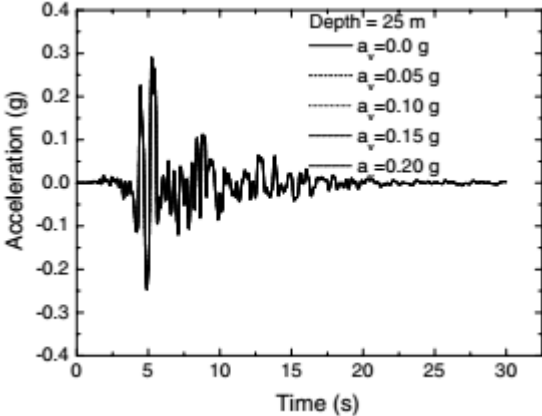


Figure 2.28 : Acceleration response of soil at the bottom of tunnel (Liu & Song,2005).

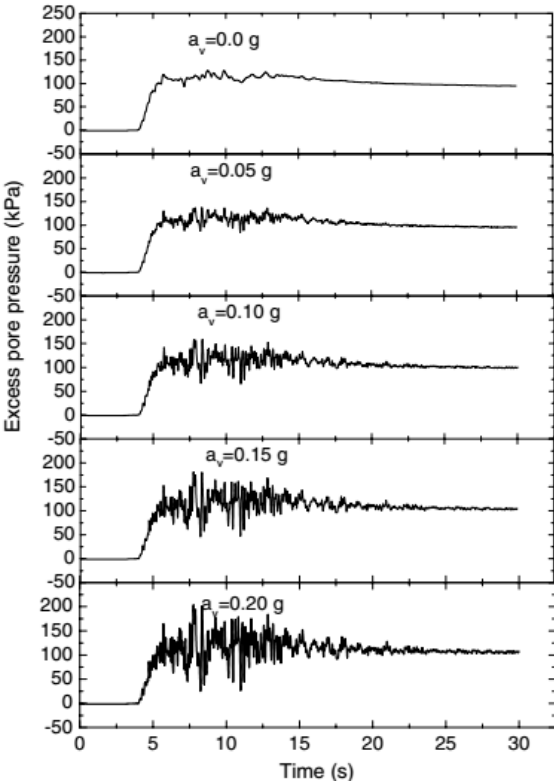


Figure 2.29 : Excess pore pressure at the bottom of tunnel due to vertical excitations with different amplitudes (Liu & Song,2005).

It was stated that this behavior of liquefiable soil due to vertical acceleration is because vertical motion which propagate as p-wave can just generate compression stress, in

which case pore pressure try to permeate this compression stress and start fluctuated more.

As they mentioned, result of combined horizontal and vertical motion from the analyses were not consistent with previous work done by Mohri et al (as cited in Liu & Song,2005) on uplift behavior of pipeline where they used sinusoidal wave as an input. Therefore, to investigate this conflict Liu & Song,2005 also conducted analyses with sinusoidal shaking with 0.2g amplitude in horizontal direction and 0.1g in vertical direction and frequency 2Hz. The results with sinusoidal shaking was in agreement with Mohri et al (as cited in Liu & Song,2005) work as shown in Figure 2.30.

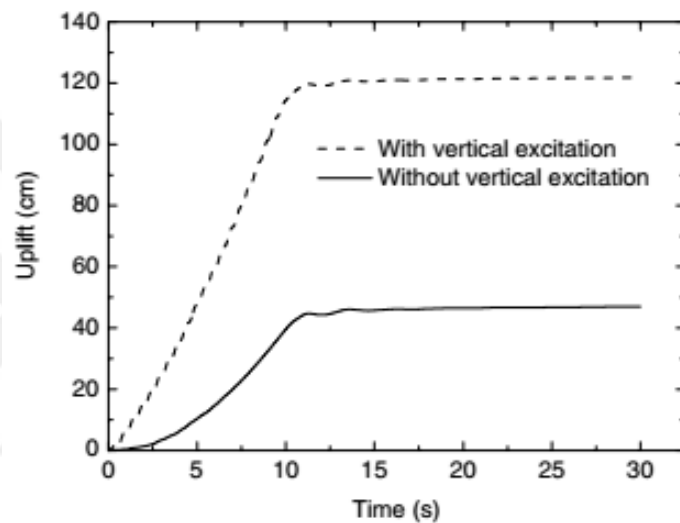


Figure 2.30 : Upift of tunnel due to sinusoidal wave in horizontal and vertical directions (Liu & Song,2005).

They concluded that the different results from real earthquake records and sinusoidal wave shaking may depend on broad characteristics of ground motion and not just peak amplitude (Liu & Song,2005). The results of analyses with real vertical ground motion conducted by Liu & Song,2005 are in contrast with Bao et al,2017 results.

Bao et al,2017 investigated the effect of vertical motion on subway tunnel in liquefiable sand using soild-fluid fully coupled effective stress finite element analysis. They selected vertical components of 1995 Kobe earthquake and scaled to 0.05, 0.1, 0.15 and 0.2g acceleration amplitudes for numerical analyses to evaluate effect of vertical excitation by keeping other numerical analysis conditions identical. They applied vertical and horizontal components concurrently and compared the results with analyses with horizontal excitation only.

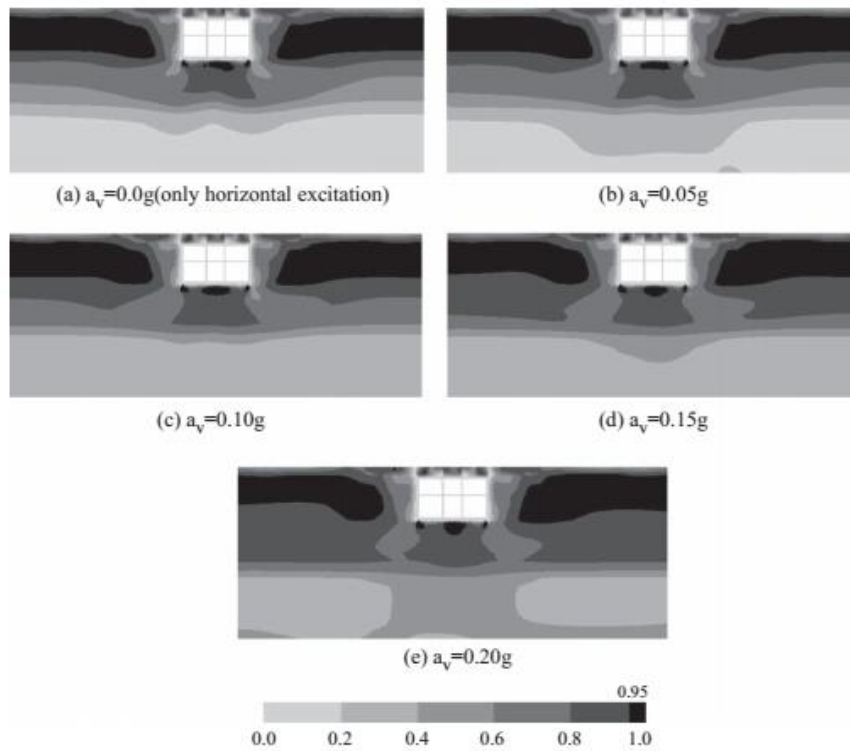


Figure 2.31 : Excess pore water pressure ratio contour at different vertical amplitudes (Bao et al,2017).

Figure 2.31 shows excess pore water generation at different vertical motion amplitudes. It was concluded that when the excitation in vertical direction is being amplified, it causes the liquefied zone to increase. However, vertical amplification has almost no effect on shear force and moment in structural elements (Bao et al,2017).

As shown in Figure 2.32, they also stated that when vertical components of real ground motion is being amplified it can increase the uplift displacement of tunnel which is in conflict with Liu & Song,2005 results.

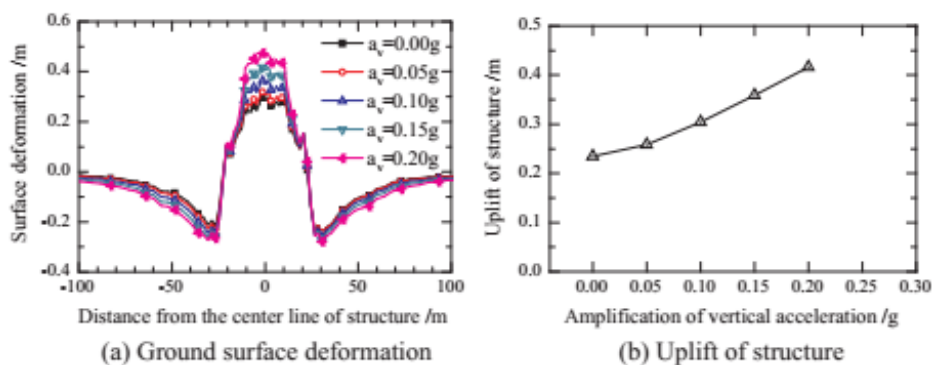


Figure 2.32 : (a) ground level vertical displacement and (b) uplift displacement with different vertical motion amplitudes (Bao et al,2017).

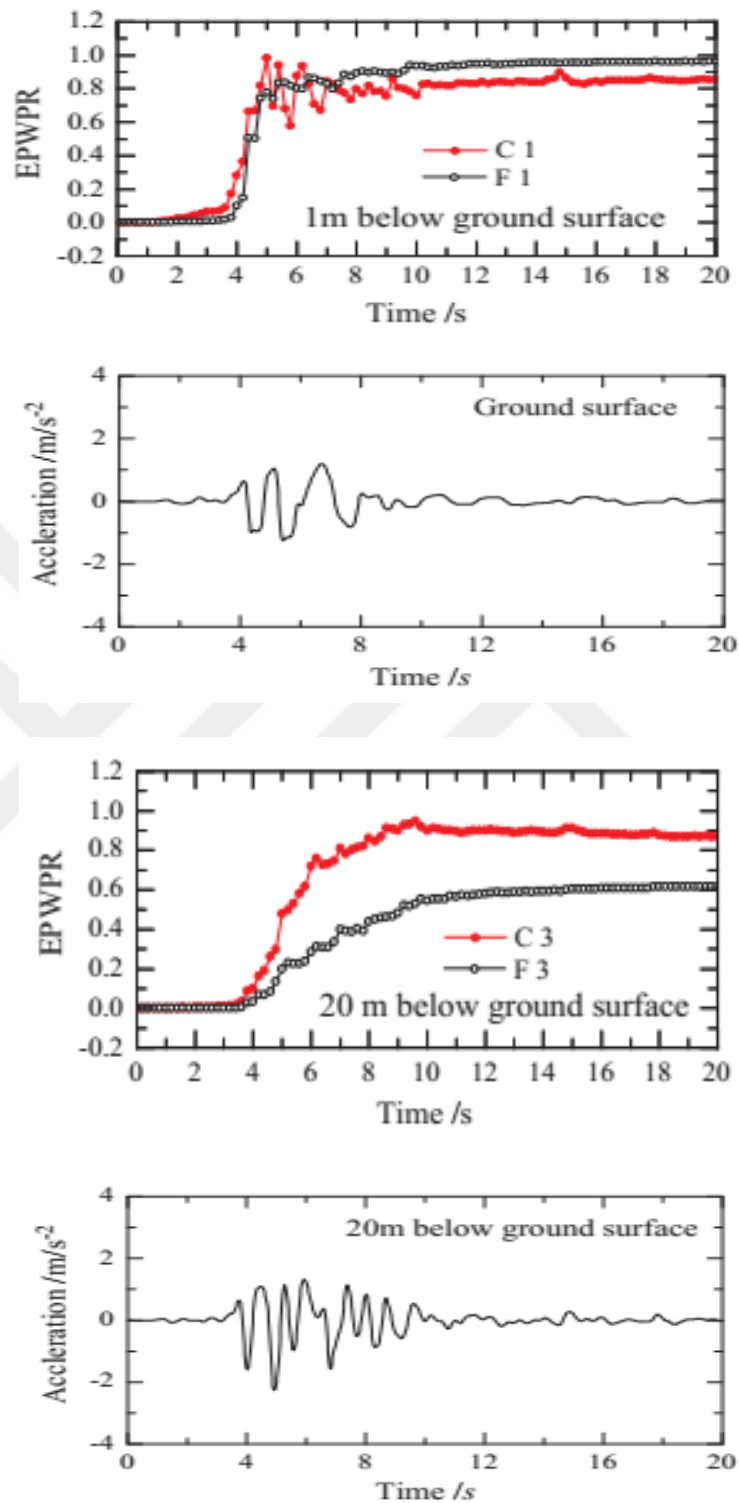


Figure 2.33 : Excess pore water pressure ratio vs. acceleration histories at different ground depth (Bao et al,2017).

Although it was proved that vertical excitation has minimum effect on above the ground structures, but in term of existance of structure within the soil it needs to be investigated more.

Body acceleration and lateral displacement of the ground influenced by frequency contents of motion significantly. Short to medium height structures above the ground has small period (high frequency) which means they are more vulnerable to high frequency contents of motion due to resonance may be occur between their vibrations. On the other hand low frequency wave can effect mid-rise to very tall structure which have higher period but low frequencies.

However, earthquake waves with higher frequency contents has less effect on structural elements of underground structure. Azadi & Hosseini.2010 conducted a series of finite element analyses for circular tunnel embedded in liquefiable soil. They applied sinusiodal wave with 0.1g amplitude and 1 Hz frequency. They concluded that reducing frequency contents of motion from 3 Hz to 1 Hz can increase shear and moment distribution on tunnel lining more that 100% but can cause higher pore water pressure around tunnel Figure 2.34 and Figure 2.35.

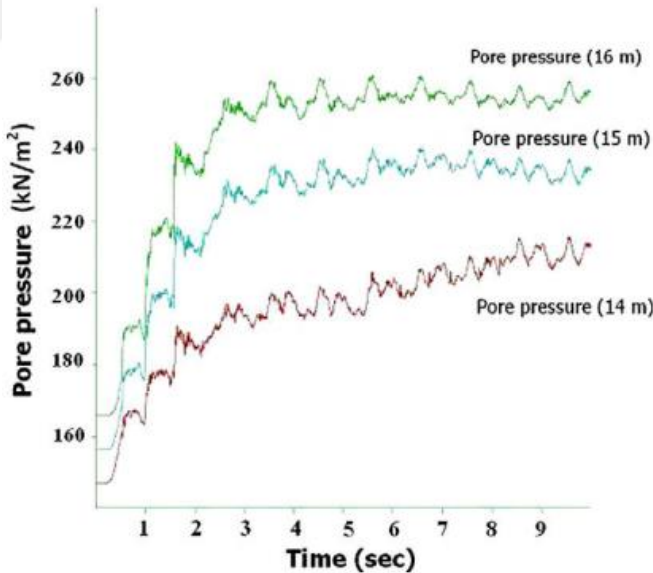


Figure 2.34 : Pore pressure at bottom of tunnel for 1Hz frequency excitation (Azadi & Hosseini.2010).

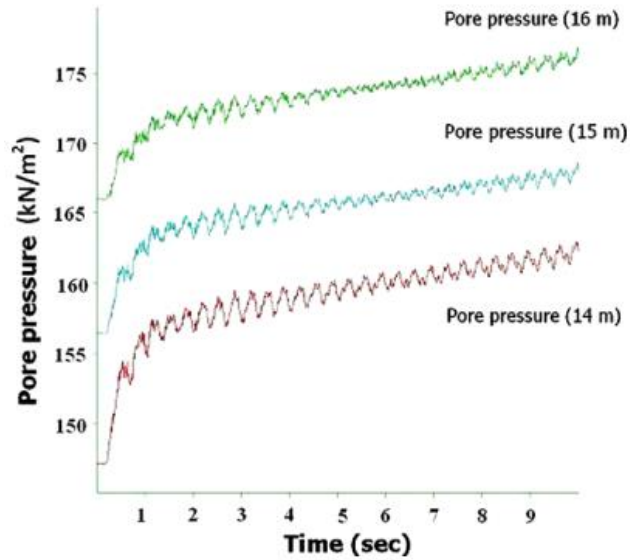


Figure 2.35 : Pore pressure at bottom of tunnel for 3Hz frequency excitation (Azadi & Hosseini.2010).

To investigate effect of amplification of motion on tunnel behavior, Azadi & Hosseini.2010 also carried out analyses by different input motions with 0.05,0.1,0.15,0.2 and 0.25g amplifications in both horizontal and vertical directions. As illustrated in Figure 2.36, the result of analyses showed that by increasing amplitude of motion in horizontal direction the uplift displacement of tunnel increases due to increase in pore water pressure. However, vertical direction motion has no significant effect on uplift behavior. Furthermore, they added that the increase in amplitude of horizontal and vertical motions, increase shear forces and moments in tunnel structure.

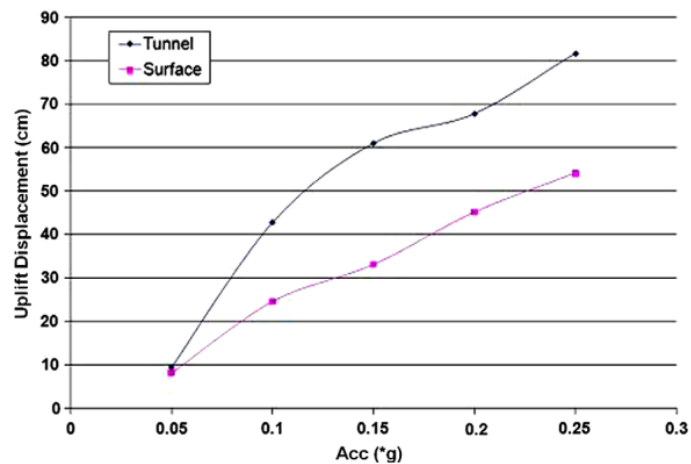


Figure 2.36 : Uplift of tunnel due to different wave amplitudes (Azadi & Hosseini.2010).

A recent evaluation of tunnel in liquefiable soil conducted by Hu & Liu.2017 to find out uplift of two story tunnel using numerical analysis. They selected 1995 Kobe earthquake in Japan for analyses. The original record has PGA around 0.835g which was scaled to 0.2g. They performed analyses for liquefaction and post-liquefaction by continuing analysis after the Kobe earthquake stopped and gave the domain enough time to dissipate pore water pressure gradually in long run.

Hu & Liu.2017 stated that Kobe earthquake with 0.2g PGA generated enough excess pore water pressure that uplift continued even after earthquake stopped completely (Figure 2.37).

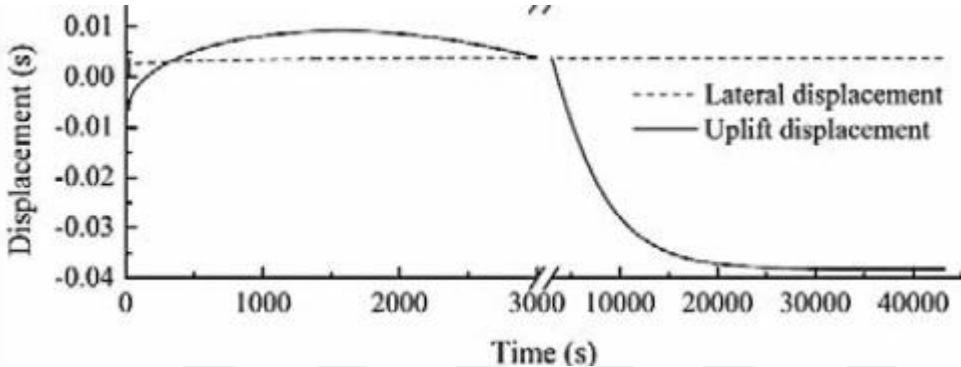


Figure 2.37 : Uplift of medium dense sand in post-earthquake phase (Hu & Liu.2017).

To evaluate the behavior of large tunnel structure, a series of shaking table tests carried out by Zhuang et al.2016 using scaled Elcentro ground motion. Different peak ground acceleration applied in tests shown in table 2.5.

Table 2.5 : PGA of Input motions used in shaking table tests(Zhuang et al.2016).

Test number	Earthquake wave	Loading condition	Horizontal PGA (g)
1	White noise	B1	0.030
2	El Centro wave	E1	0.110
3	El Centro wave	E2	0.166
4	El Centro wave	E3	0.266
5	El Centro wave	E4	0.328
6	El Centro wave	E5	0.511

The tests results showed that thickness of liquefied soil increases by increasing motion amplitudes. Liquefaction not happened untill ground motion amplified to 0.266g and soil domain liquefied entirely during motion with 0.511g.

As it is shown in Figure 2.38, results of pore water pressure ratio at point W1 showed that pore water pressure at amplitude 0.266g reaches 100% while it did not occur during 0.328g and 0.511g.

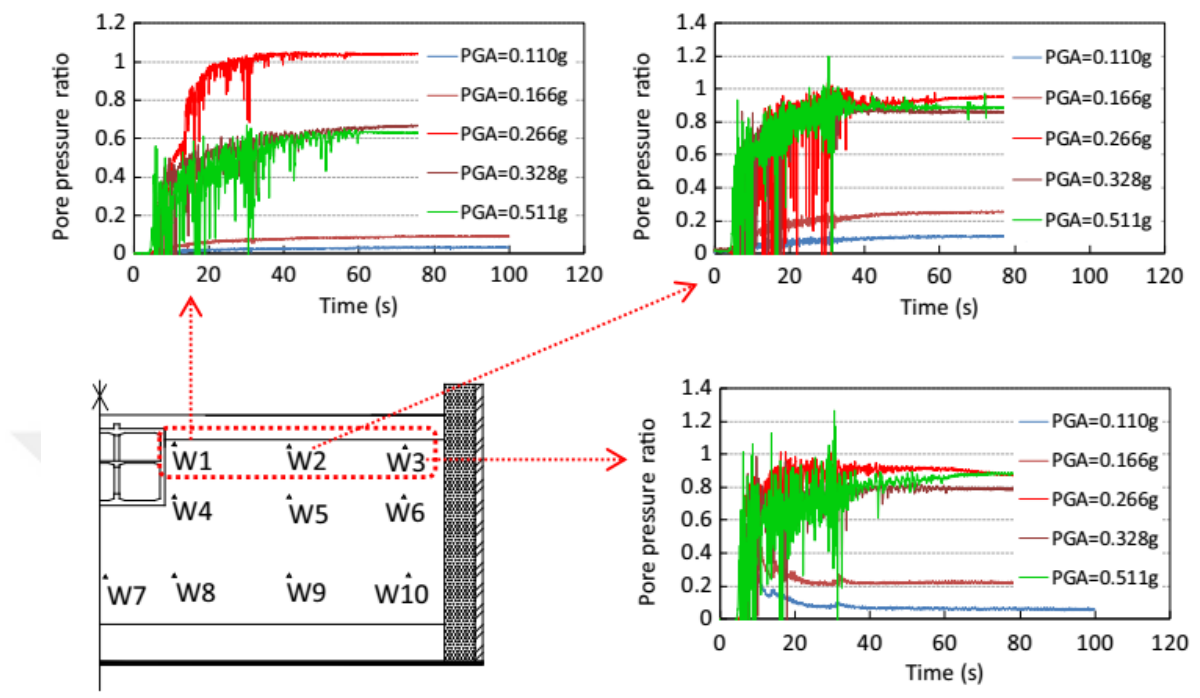


Figure 2.38 : Tests results for pore pressure ratio at top of the soil domain (Zhuang et al.2016).

They explained that difference in pore water pressure ratio at point W1 is because of after certain amplitude, more uplift of tunnel due to increased amplitude, the soil part around tunnel have smaller effective stress which show pore water pressure ratio less than real values and it is not reach unity.

Madabhushi & Madabhushi,2015 did examined the seismic performance of rectangular shape tunnel in liquefiabe soil.1995 Kobe earthquake ground motion was selected and scaled with maximum amplitudes 0.6g and 0.8g to be implemented in the numerical analyses. They also used fade-out and fade-in sinusoidal shaking with amplitude 0.5g to evaluate acceleration ground response during liquefaction.

Sinusoidal and more realistic earthquake input motions are considered The generation of excess pore pressures in the soil around the tunnel and the consequent floatation of the tunnel are observed for both types of input motions. It will be shown that the amount of tunnel uplift depends on the type of input motion with the sinusoidal motion leading to a significantly larger uplift compared with the more realistic Kobe motion.

2.9 Effect of Dilation Angle of Soil on Tunnel-Soil System

Generally by reduction of soil dilation angle causes volume reduction of the soil during monotonic and cyclic shaking. Therefore, pore pressure generation can increase or decrease if soil dilation angle decrease or increase respectively (Azadi & Hosseini,2010).

To evaluate the effect of dilatancy angle on soil-structure system (Azadi & Hosseini,2010) conducted finite element simulation with different dilatancy angles, $\psi=0, 5$ and 10 , and compare pore water pressure generation at different depth within the liquefiable soil. Figure 2.39 shows the result of simulations.

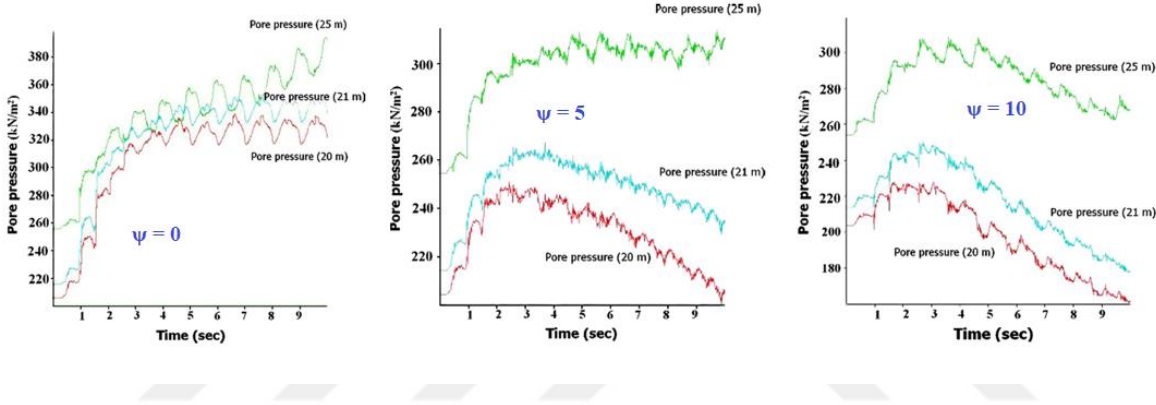


Figure 2.39 : Pore water pressure generation at different depths due to different dilation angles (Azadi & Hosseini,2010).

(Azadi & Hosseini,2010) stated that by increasing dilation angle the pore water pressure increases significantly even less than initial pore water pressure. By reducing of pore water pressure the uplift displacement of tunnel will also decreases.

They also indicated that dilation angle variation will effect the shear forces and bending moments in structural elements. By increasing dilation angle from 0 to 10 the bending moment and shear force reduced about 17% and 39% respectively.

(Sharafi & Parsafar,2016) also investigated the effect of dilation angle on uplift of underground structure in liquefiable soil. They conducted 3d finite element simulation on 3m diameter pipeline buried at 1.5 m depth. The simulation carried out by applying sinusoidal wave with 0.6g and frequency 3Hz for 10s while keep relative density constant as 40%.

Table 2.6 : Dilation angle vs. vertical displacement (Sharafi & Parsafar,2016).

Ψ (Deg)	Uplift (cm)
1	6
2.3	10.05
3.7	9.1

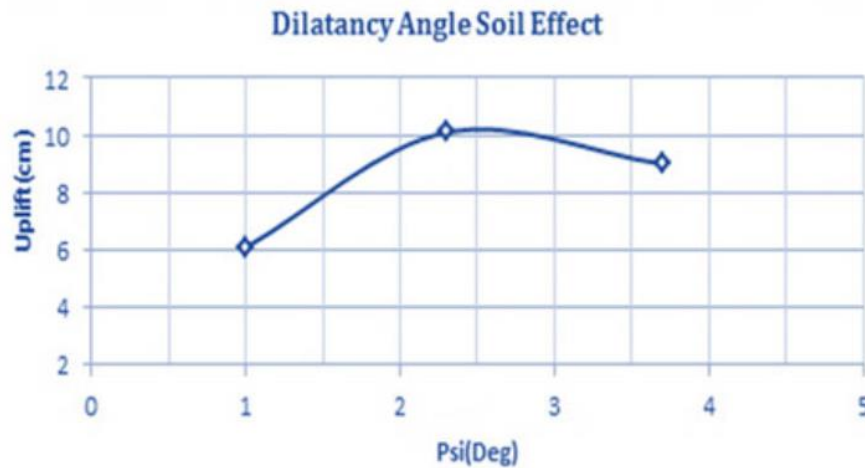


Figure 2.40 : Tunnel uplift at different dilation angles (Sharafi & Parsafar,2016).

As illustrated in Table 2.6 and Figure 2.40, buried pipeline vertical displacement increases by increasing the dilation angle. However, uplift decreased by increasing dilation angle at certain value interval.

2.10 Effect of relative density of soil on tunnel-soil system

Evaluating the effect of soil material on tunnel uplift is not an easy task specially for elasto-plastic multiyield soil constitutive models which consists many parameters. However, effect of different parameter can be evaluated by conducting proper model parameters calibration.

Sharafi & Parsafar,2016 investigated the effect of different relative densities on uplift behavior of circular tunnel with 3m in diameter and identical burial depth, 1.5m below ground surface. They conducted the analyses using well-known Finn model capable of capturing volumetric strain and excess pore water generation. Further detail on Finn model can be found on Sharafi & Parsafar,2016.

By increasing the relative density the uplift displacement of tunnel reduced (Figure 2.41), however, the rate of uplift reduction after relative density 55% decreased noticeably.

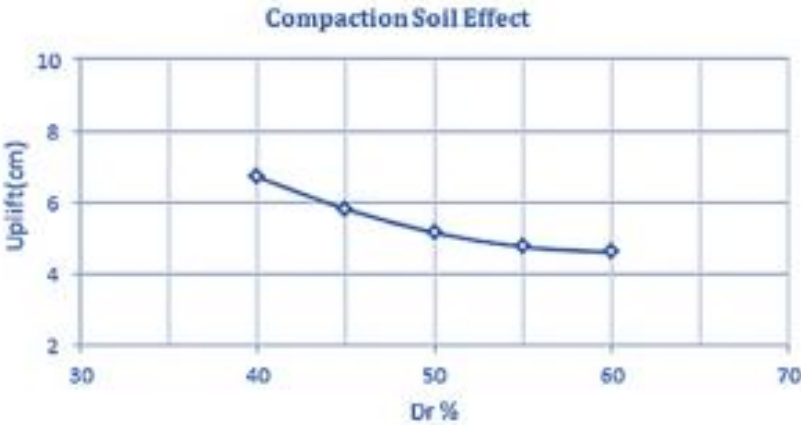


Figure 2.41 : Tunnel uplift at different relative densities (Sharafi & Parsafar,2016).

Table 2.7 : Tunnel uplift at different relative densities (Sharafi & Parsafar,2016).

Dr (%)	Uplift (cm)
40	6.85
45	5.95
50	5.20
55	4.90
60	4.30

Saeedzadeh & Hataf,2011 also conducted numerical analyses to investigate the effect of relative density on uplift of pipeline with 3m diameter and buried at 1.5m below ground surface. They used hardening soil model (HS) available in Plaxis for simulating soil behavior. Hardening soil model (HS) is a plasticity model with yield cap consisting dilation parameter. Due to evaluating pipe behavior at shallow depth, they retrieved the soil parameters data from consolidation undrained compression test at small confining pressure.

Saeedzadeh & Hataf,2011 considered Nevada sand with 40, 50, 60 and 70% relative densities. The result of the analyses demonstrated in Figure 2.42.

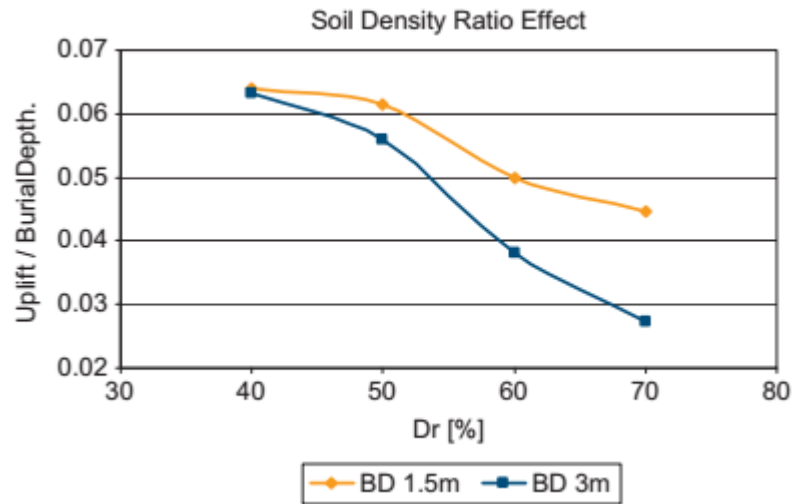


Figure 2.42 : Effect of relative density on pipeline uplift at different buried depths (Saeedzadeh & Hataf,2011).

2.11 Effect of Friction Angle of Soil on Tunnel-Soil System

(Sharafi & Parsafar,2016) performed numerical simulation to evaluate the effect of friction angle on pipeline uplift in liquefiable soil. They carried out simulations with different friction angles as demonstrated in Figure 2.43.

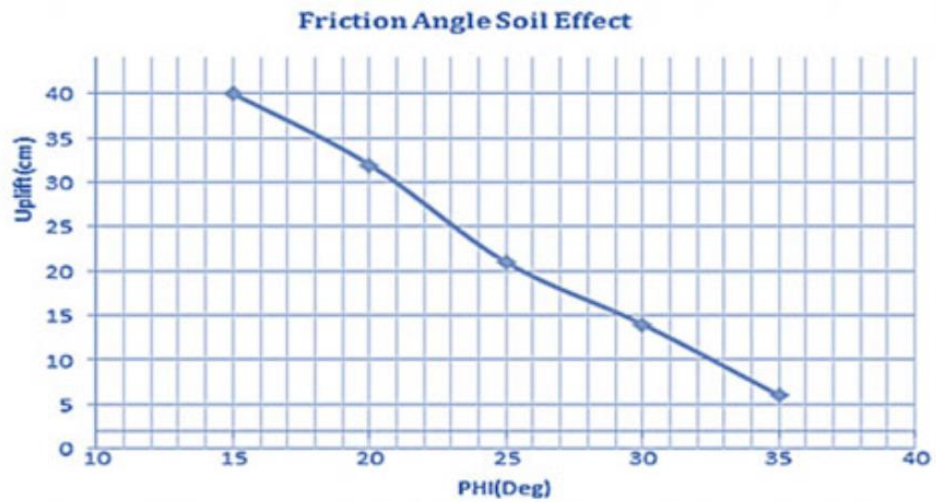


Figure 2.43 : Effect of variation of friction angle on pipeline uplift (Sharafi & Parsafar,2016).

The result showed that by increasing friction angle the uplift of buried pipeline will reduced. The more frictional force between soil particles will cause less pore water

pressure generation. It is indicated that increasing friction angle can reduce uplift considerably.

As illustrated in Figure 2.44, the result of simulations by (Azadi & Hosseini,2010) are also in agreement with the result of (Sharafi & Parsafar,2016). They showed that higher friction angle values reduces the uplift displacement of tunnel in liquefiable sand.

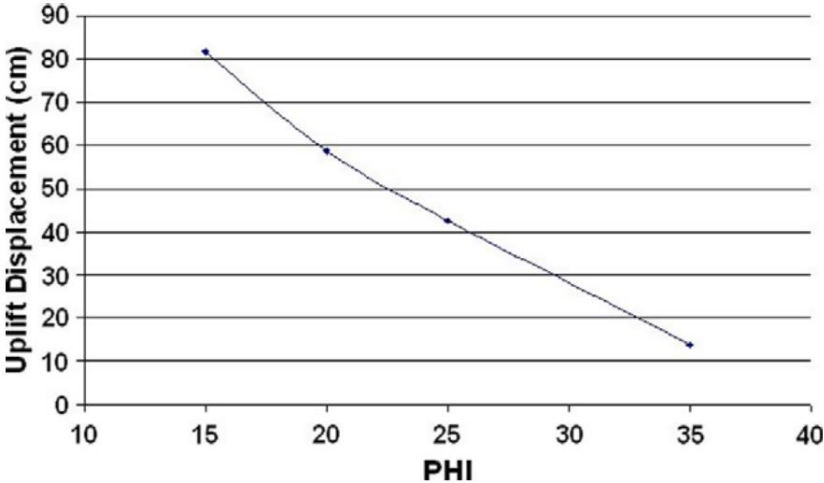


Figure 2.44 : Effect of variation of friction angle on pipeline uplift (Azadi & Hosseini,2010).

The most important shortcoming of previous work is soil constitutive models like Finn soil constitutive model implemented by Sharafi & Parsafar,2016 and Azadi & Hosseini,2010 which is not capable of capturing post liquefaction behavior of sand.

According to Ti et al,2009 the Hardeing soil model used by Saeedzadeh & Hataf,2011 is not able to capture creep behavior and anisotropic stiffness of sand in dynamic analysis.

Although the simulations have been given satisfactory results but the method used as changing only one soil model parameter is not logical specially for more advanced soil constitutive models. More advanced soil models consisting various parameters correlated tightly in which changing one parameter will effect the other parameters and consequently causes the soil to behave significantly different. To capture the effect of soil material parameters on behavior of buried structures within the liquefiable soil more advance centrifuge testing and parameters calibration needed.

3. LIQUEFACTION PHENOMENON

3.1 Introduction

After Alaska and Niigata earthquakes in 1964 significant damaged observed in buried pipelines, foundations and bridges and drew attention of many researchers and engineers to investigate this phenamena which was called “liquefaction”. The “liquefaction” expression firstly coined by Magimo and Kubo in 1953 (kramer,1996). Since then the term liquefaction has been used for variety situations involve cohesionless saturated soil deformation under undrained condition due to monotonic or cyclic loadings.



Figure 3.1 : Liquefaction at Niigata earthquakes in 1964 (kramer,1996).

The most recent definition of liquefaction proposed by (Idriss & Boulanger, 2008) in which the normal stress within the saturated soil mass could transfer to pore water pressure due to contraction tendency of loose cohesionless soil during cyclic load under undrained condition.

Cohesionless loose saturated sand deposit tends to densify under intensive earthquake loads and the volume decreases as water flows out. Dependent on drainage conditions, the densification of saturated soil mass is delayed as water could not dissipate rapidly and excess pore water pressure will be generated. By increasing cyclic load's number of cycles the excess pore water pressure will be equal to total overburden stress at

certain depth. At this phase the tension between soil grains reduces and effective stress will be zero. Total vertical stress at specific depth within the soil can be evaluated as:

$$\sigma_v = \gamma \cdot h \quad (3.1)$$

Where, γ is unit weight of soil and h is depth.

According to the principle of effective stress, the total stress is equal to the combination of effective stress and the pore water pressure or in other word effective stress can be calculated by subtracting hydrostatic pressure from pore water pressure at the moment and can be expressed as:

$$\sigma' = \sigma - u \quad (3.2)$$

where σ' is effective stress,

σ is total stress

and u is represent pore water pressure.

When the effective stress magnitude approaches to zero, the cohesionless saturated sand loses its shear strength and the soil behave like liquid which cannot resist any shear stress. Several soil constitutive models show that the shear stiffness of the saturated soil is mostly depend on the effective stress magnitude of the saturated soil.

As mentioned before this phenomena is called “liquefaction” and since liquefaction refer to express wide range of saturated soil behavior such as static liquefaction and liquefaction due to seismic activities. therefore, it is vital to categorize this term in two main group:

Flow liquefaction refer to static condition and cyclic mobility (or cyclic softening) refer to liquefaction during earthquake. (kramer.1996, Jefferies & Been.2015)

In static state of equilibrium if the shear stress is greater than shear strength of soil deposit then the soil enter failure state which is called “Flow liquefaction” and can cause rapid ground deformation.

On the other hand, cyclic mobility happens due to larger shear strength compare to shear stress which can be increasing incrementally during earthquake. Cyclic mobility can cause large permanent deformation due to either cyclic shear stress or static shear stress. Lateral spreading is the consequence of cyclic mobility deformation which can cause significant damage to the existence structures. (see Figures 3.2 and 3.3)

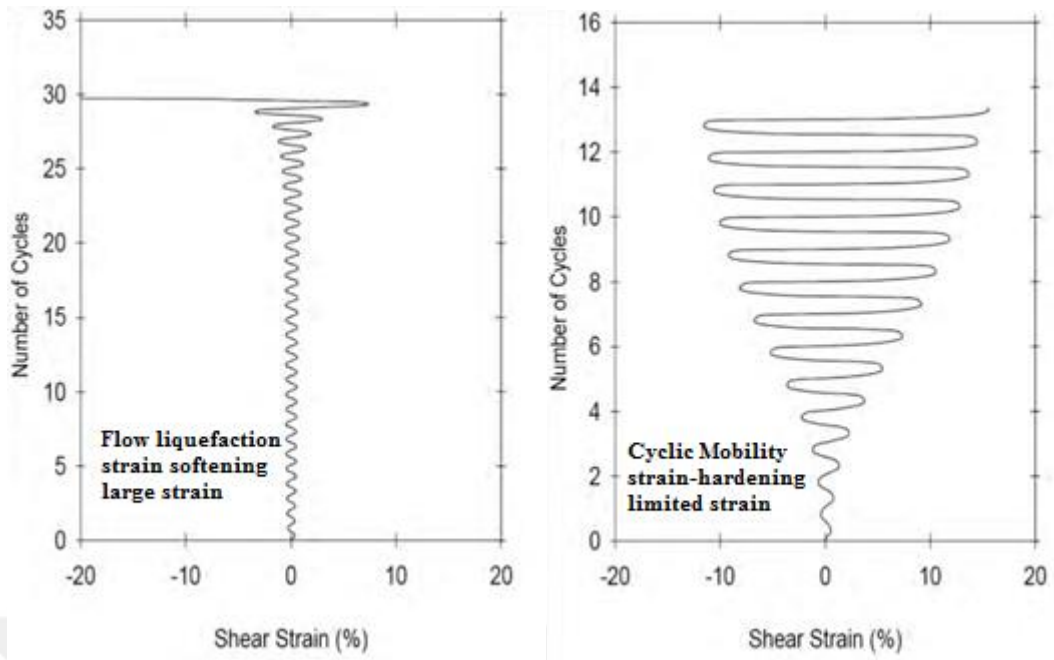


Figure 3.2 : Schematic of flow liquefaction and cyclic mobility.

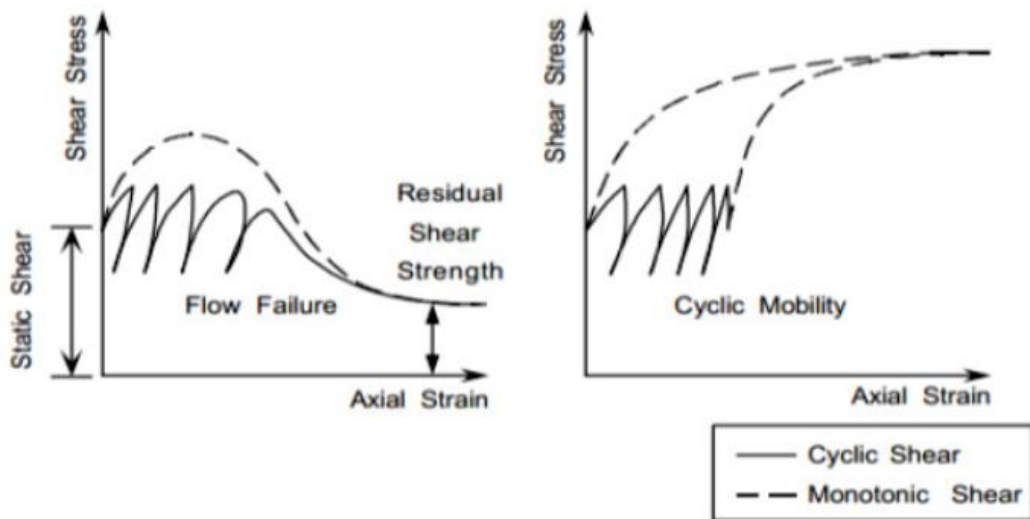


Figure 3.3 : Cyclic mobility and flow liquefaction response of soil under cyclic and monotonic shear (Rauch, 1997).

3.2. Triggering Liquefaction

Liquefaction generally initiated at very small shear strain, while soil body maintains primary shear strength. before liquefaction initiated displacement and as a result strain magnitudes are noticeably small. however, when liquefaction started the rate of strain increases quickly.

When liquefaction triggered, large deformation within the cohesionless saturated soil observed during earthquake. Therefore estimation of initiation time of liquefaction and factors effecting the soil to be liquefied is a vital (Greenfield.2017).

Most common factors which cause the cohesionless saturated sand to be liquefied are:

- 1- Input motion characteristics
- 2- Grain size distribution and grain shapes
- 3- Relative density
- 4- Drainage condition
- 5- Characteristics and magnitude of initial applied load.
- 6- Number of load cycles
- 7- Strain and consolidation history

3.2.1 Effect of Input Ground Motion on Liquefiable Soil

Number of cycle influenced by duration of strong ground motion applied to the cohesionless saturated soil which has an effect on generation of pore water pressure within the soil. The other ground motion parameter that has effect on pore water pressure generation is peak ground motion(PGA). Long duration ground motion can cause higher pore water pressure.

Stiffness reduction tendency, tend to softened, within the soil when it is liquefied has significant impact on frequency content of seismic wave. The soil can transfer strong ground motion with high frequency contents due to higher stiffness compare to when it is liquefied. However, when the soil liquefied it could just pass on low frequency contents.

The soil mass responses to low frequency contents of ground motion due to stiffness reduction after liquefaction triggered. Measuring ground motion intensity by using low frequency contents of ground motion can gives better understanding of the liquefaction consequences (Greenfield,2017).

To study effects of input ground motion, relative density and permeability on liquefaction potential of sand, Sharp et al,2003 conducted a series of centrifuge tests on Nevada 120 sand. The centrifuge tests carried out with relative densities 45,65 and 75% and peak ground accelerations close to 0.2g and 0.4g.

The results of centrifuge tests showed that the thickness of liquefied zone increases as the magnitude of peak ground acceleration increases.

It was also indicated that, regardless of the magnitude of peak ground motion acceleration, the whole sand model with relative density 45% ($D_r=45\%$) liquefied completely. As illustrated in Figure 3.4, the tests result showed that peak ground acceleration has less effect on liquified soil thickness.

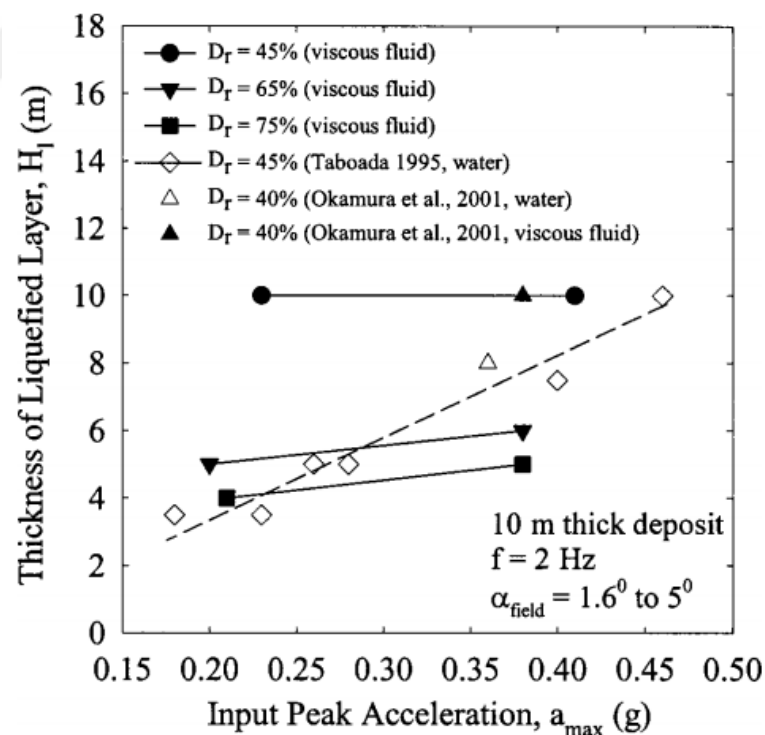


Figure 3.4 : Effect of peak ground acceleration on liquefied sand thickness (Sharp et al,2003).

3.2.2 Relative Density ($D_r\%$)

Relative density influences cohesionless soil response significantly during cyclic shear loading. Dense sand has less tendency to shrink and densify due to cyclic shear stress while loose sand will be densified with proper drainage condition. In undrained condition, excess pore water pressure generated in loose sand will cause liquefaction. However, in denser sand has less liquefaction potential due to lower excess pore water pressure.

Poorly graded saturated sands with smaller relative densities have low cyclic resistance strength compare to well graded saturated sand with identical relative density.

Gradation possibly will effects the rate of contraction response in saturated sand and therefore, liquefaction failure can take place at lower relative density. (Vaid et al.1990)

Pore water pressure generation increase considerably during cyclic loading which led to increase in uplift or consolidation settlement. According to typical stress-strain relationship of soil, the slope of the stress-strain curve expresses the stiffness of soil mass against shearing which is steeper for denser sand. Consequently, the liquefaction triggering likelihood in loose sand is much higher (Su,2005).

Measured parameter	Testing parameters		
	Relative density D_r	Input acceleration a_{max}	Prototype permeability k
Thickness of liquefied soil H_l	H_l decreases when D_r increases	H_l increases with a_{max}	H_l decreases when k increases, especially when a_{max} is small
Lateral displacement D_H	D_H decreases when D_r increases	D_H increases with a_{max} , especially when k is high	D_H decreases when k increases
Settlement S	S decreases when D_r increases	S increases with a_{max} , especially when k is high	S remains constant or slightly decreases when k increases for $a_{max}=0.2$ g, S increases when k increases for $a_{max}=0.4$ g

3.2.3 Grain Distribution and Shapes

Porosity, tortuosity, soil grain size and distribution and degree of saturation influence diffusion and flow through a porous medium (Matyka et al.2008).

Therefore grain size and distribution effect permeability which has an important role in generation and dissipation of excess pore water pressure.

Gradation and soil type has impact on behavior of soil under cyclic load and therefore liquefaction potential. For instance, soil such as clay can response exactly like

liquefied saturated sand due to strain softening but actually liquefaction is not happened within the clay.

Well-graded soil consists of uniform particles sizes has higher potential to liquefy compare to irregular particle sizes soil due to tendency of small particles to fill the gaps within the soil. Therefore, during seismic loading, the soil mass has less tendency to densify and generating excess pore water pressure (Su.2005).

3.2.4 Strain History and Reconsolidation

Consolidated Liquefiable sand can densify again during second and subsequent cyclic loading. Sand desify more and more during re-liquefaction and reconsolidation and acceleration of ground motion increase progressively. However, the time needed for pore water pressure to dissipate decreases.

Study that conducted by Ye et al.2007 showed that there is no change in cyclic mobility behavior of liquefied loose sand under cyclic load for the first time after it was consolidated, however, more cyclic mobility observed in the subsequent loading.

It was also observed that when the loose sand densify more, the resistace to shear stress increases, cyclic mobility loop gets larger and due to larger stiffness the slope of stress-strain curve increases (Figure 3.5).

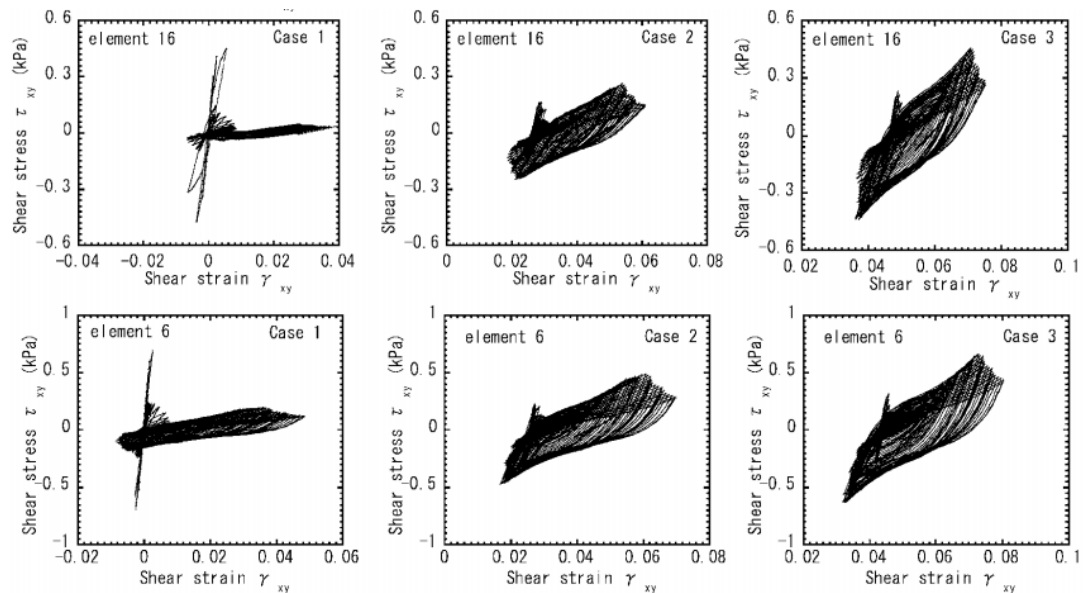


Figure 3.5 : Stress strain relation during repeated cyclic loading (Ye et al.2007).

In this context, for more convenient of the reader “re-liquefaction” will be used to represent repeated liquefied soil which was liquefied before.

Saturated sand preshearing can effect resistance of liquefiable sand against liquefaction (as cited in Su.2005).

Despite the fact that liquefied sand gets more denser during re-liquefaction, but resistance of soil to re-liquefaction decreases significantly compare to first time liquefied-reconsolidated to initial effective stress.

3.3. Liquefaction-induced Potential and Susceptibility Evaluation

Quantitative evaluation of liquefaction potential is the first step in projects involving liquefaction under seismic load. During past decades, many methods and procedures proposed to evaluate the soil liquefaction potential such as:

- 1- Cyclic stress methods proposed by Seed and Idriss in 1971.
- 2- Cyclic strain methods proposed in 1982 by Dobry and colleagues.
- 3- Energy based methods such as Arias intensity approach proposed by Kayen and Mitchell in 1997. (Choobbasti et al.2012).
- 4- Probability based methods
- 5- Numerical methods (nonlinear total stress and effective stress approaches)

Cyclic stress approach is the most common used method for evaluating liquefaction potential.

In 1960's, Seed and his colleagues did extensive experiments on liquefaction initiation under cyclic shear stress loading. They described Liquefaction potential based on frequency domain and number of cycles which is called "cyclic stress method". The concept of cyclic stress method is rather simple in which seismic load of strong ground motion characterized by cyclic shear stresses ratio(CSR) against shear stresses of liquefiable soil which describe liquefaction resistance of soil expressed by cyclic resistance ratio(CRR). A simplified approach proposed (Seed and Idriss 1971 as cited in Choobbasti et al.2012) to evaluate cyclic stress ratio (CSR). If the seismic load is larger than liquefiable soil resistant strength then the liquefaction initiated within the soil. As illustrated in Figure 3.6, in stress cyclic stress method by evaluating shear stress due to seismic load against shear stress demand of liquefiable soil the liquefaction potential depth within the soil can be estimated.

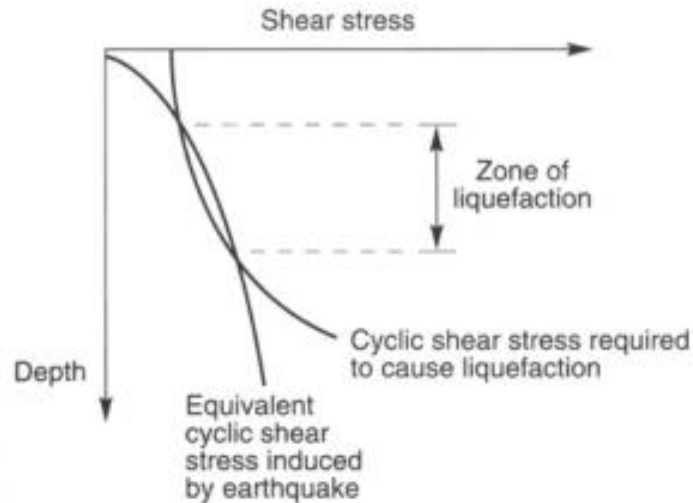


Figure 3.6 : Liquefaction potential zone assessment by cyclic stress method (Su.2005).

There are two procedures for evaluating the soil resistance against liquefaction:

- 1- Laboratory tests on undisturbed soil samples.
- 2- Semi-empirical methods based on correlations between the free field soil behavior and in situ tests.

Almost all the mentioned techniques for evaluating liquefaction potential have restrictions and lack of prediction of pore water pressure in a common limitation. Therefore, numerical evaluation of ground response for estimation of build-up pore water pressure and shear resistance of soil due to strong ground motion is an advantage.

3.3.1 Numerical Evaluation of Liquefaction Potential

In geotechnical area, the liquefaction evaluation and soil response due to earthquake load gets more complex if soil interact with structures above or below the ground surface and the conventional methods are less effective to evaluate the soil behavior. To overcome this deficiency it is essential to use powerful tool that can predict soil liquefaction reliably.

Finite element method is a promising tool as it developed and improved so fast during past decades. Total stress analysis and effective stress analysis are the Most common approaches for evaluating ground response due to seismic loads using finite element formulation. However, total stress analysis is not proper for evaluation

- **Total stress analysis:**

In total stress approach, fluid and solid phases are considered as as unified phase and the pore pressure generation or dissipation are not evaluated during the seismic analysis.

- **Effective stress analysis:**

Effective stress method is based on evaluation of effect of pore water pressure in dynamic analysis. Effective stress can be expressed by fluid solid fully coupled formulation which is dependent on the soil constitutive model used during analysis.



3.4 Post-liquefaction Settlement

Generally, soil deformation in vertical direction can happen by either repeated consolidation of saturated sand after liquefaction which cause soil to settle or lateral shear deformation due to lateral spreading.

As described before, liquefiable sand under cyclic loading will lose shear strength due to excess pore water pressure. The excess pore water pressure tends to dissipate through drainage paths within the soil which cause the soil to densify and shrink. Densification of liquefied soil will cause settlement on the ground surface.

Study on behavior of clean saturated sand under cyclic load in undrained condition (Tokimatsu & Seed.1987, Ishihara & Yoshimine.1992 as cited in Ishihara.1996) revealed that mass density and notably maximum shear strain of saturated sand can affect volumetric strain¹ in post-liquefaction phase.

They proposed that relationship of volume strain ($\epsilon_v\%$) and maximum shear strain (γ_{max}). (Figure 3.7)

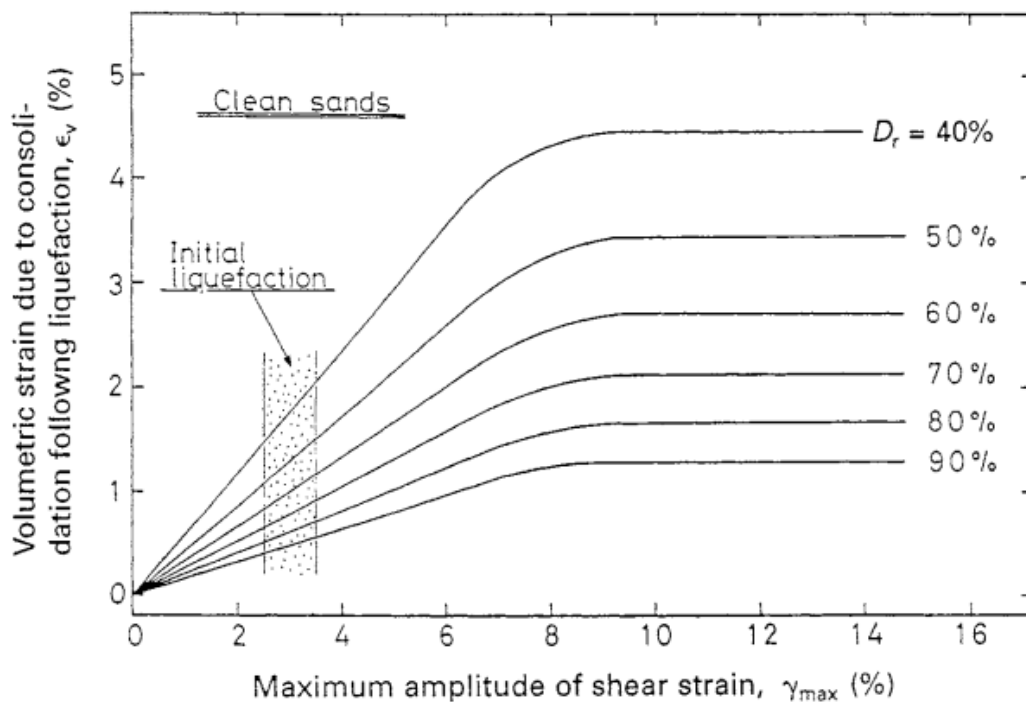


Figure 3.7 : Post-liquefaction volumetric strain plotted against maximum shear strain (Ishihara.1996).

¹ The volumetric strain is the change in current volume divided by the initial volume.

As demonstrated in Figure 3.7, at shear strain about 3% , pore water pressure gets equal to vertical stress at certain amplitude of cyclic load. Liquefaction onset will be at maximum shear strain of 2% ~3%.

It is obvious that volume strain continues to increase after liquefaction onset up to about 8%.

The proposed relationships can be estimated by (Yoshimine et al. 2006 as cited in Idriss & Boulanger.2008):

$$\varepsilon_v = 1.5 \cdot \exp(-2.5D_R) \cdot \min(0.08, \gamma_{\max}) \quad (3.3)$$

Where, D_R and shear strain can be fraction number. The relationship can also be written in terms of standard penetration resistance (SPT) and cone penetration resistance (CPT) as:

$$\varepsilon_v = 1.5 \cdot \exp\left(-0.369\sqrt{(N_1)_{60cs}}\right) \cdot \min(0.08, \gamma_{\max}) \quad (3.4)$$

$$\varepsilon_v = 1.5 \cdot \exp\left(2.551 - 1.147(q_{c1Ncs})^{0.264}\right) \cdot \min(0.08, \gamma_{\max}) \quad (3.5)$$

3.4.1 Post-liquefaction Reconsolidation of Sand

Reconsolidation is an action in which excess pore water pressure tends to dissipate and effective stress between the soil particles start to back to the initial state. In the reconsolidation process, total vertical stress is not changing because it is combination of effective stress and pore water pressure at every moment and the change in one of the pore water pressure and effective stress just transmitted to other one. In homogeneous soil mass reconsolidation can be considered as unidirectional phenomena and therefore just vertical stress is considered. Figure 3.8 shows the diagram of stresses and pore fluid in saturated porous material such as soil.

Reconsolidation is flow through porous media phenomena. Terzaghi suggested a consolidation relationship between soil particles and pore fluid by principle of mass balance, Darcy's permeability relationship and principle of effective stress. Terzaghi consolidation relationship is based on partial differential equation that variable density is substituted by excess pore water pressure. In terms of evaluation of reconsolidation after liquefaction, Terzaghi's consolidation equation is not proper to be used.

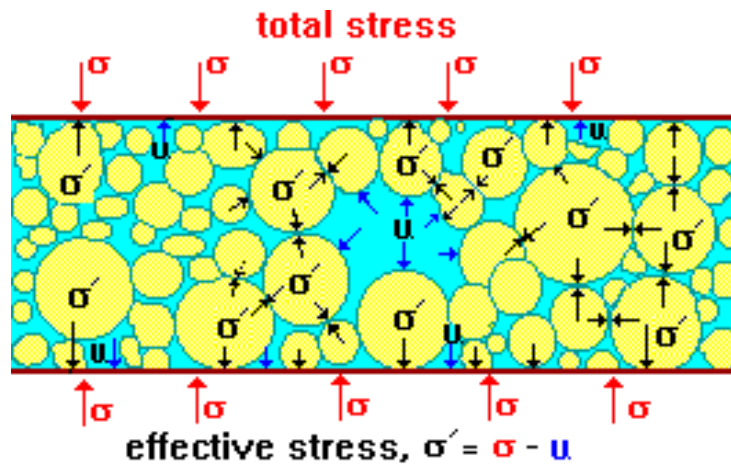


Figure 3.8 : Schematic of stresses and pore water pressure within the saturated soil.

During reconsolidation the soil mass considered as fully saturated in which soil particles and pore water are not compressible. Changing the porosity can correlate with change of effective stress, while, permeability coefficient and shear strength of soil can be constant although it not proper to evaluate reconsolidation during liquefaction (Adamidis & Madabhushi,2016).



4. MECHANICAL BEHAVIOR OF SAND

This Chapter reviews key aspects of the mechanical behavior of sands, with particular focus on the response under cyclic loading.

4.1 Response of Sand Under Monotonic and Cyclic Loadings

Relative density ($D_r\%$), effective confining pressure and consolidation history of sand has a significant impact on the typically complicated stress-strain relationship of sand due to cyclic or monotonic loading conditions (Vytiniotis, 2011; Idriss & Boulanger, 2008).

4.1.1 Response of Sand Under Monotonic Loading

4.1.1.1 Sand Response in Low-strain Condition

Behavior of sand can be considered as an elastic only in really low strains, not more than 0.001%, while more than 0.001% it will behave completely nonlinear plastic (Vytiniotis, 2011).

Maximum shear modulus of sand in elastic state, at point near origin in stress-strain graph, can be written as:

$$G_{max} = F(e)p'^n \quad (4.1)$$

Where, p' is mean effective stress, n exponential power which is between 0.4 and 0.5, and $F(e)$ is function of the void ratio (e). In table 4.1 some of the proposed function for $F(e)$ is given.

Table 4.1 : Suggested empirical relations for $F(e)$ function (Vytiniotis, 2011).

Soil type	$F(e)$	n	Void ratio range	Test method
Round-grain Ottawa sand	$(2.174-e)^2/1+e$	0.5	0.3-0.8	RC
Angular-grain crushed	$(2.973-e)^2/1+e$	0.5	0.6-1.3	RC
Several sands	$(2.17-e)^2/1+e$	0.5	0.6-0.9	RC
Toyourea sand	$(2.17-e)^2/1+e$	0.5	0.6-0.8	Cyclic TX
Several cohesionless soil	$1/0.3+0.7e^2$	0.5	NA	RC
Ticino sand	$(2.27-e)^2/1+e$	0.43	0.6-0.9	RC and TS
General equation form	$G_{max}=F(e) p'^n$	$G_{max}=F(e) p'^n$	$G_{max}=F(e) p'^n$	$G_{max}=F(e) p'^n$

4.1.1.2 Response of Sand in Compression

Response of sand due to large monotonic shear stress is similar despite the different initial densities used in experiments. (Limiting Compression Curve (LCC), Pestana & Whittle, 1993 as cited in Vytiniotis, 2011)

Sand response can be considered as elastic in large compression stress as demonstrated in $\log e - \log(p'/p_{at})$ diagram in the Figure 4.1.

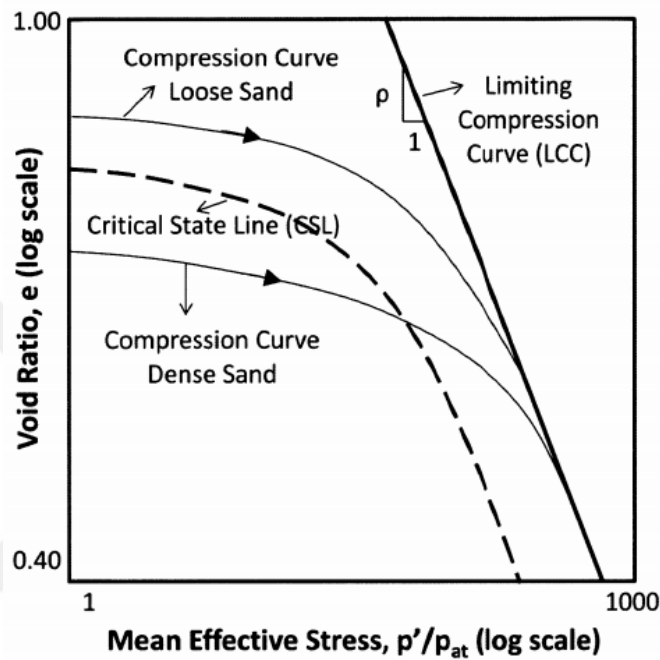


Figure 4.1 : Limiting Compression Curve (LCC) and Critical State Line (CSL)
(Limiting Compression Curve (LCC), Pestana & Whittle, 1993 as cited in Vytiniotis, 2011).

For mean effective stress less than 200 kPa displacement can be considered as elastic. However, when the mean effective stress is too high, compression will be inelastic.

4.1.1.3 Response Under Monotonic Loading in Drained Condition

When soil is not saturated it could undergo volumetric deformation due to shear stress. As it is shown in Figure 4.2, slippage can occur due to low shear stress at the beginning of shearing and reduce the void between the particles which result in volume decrease.

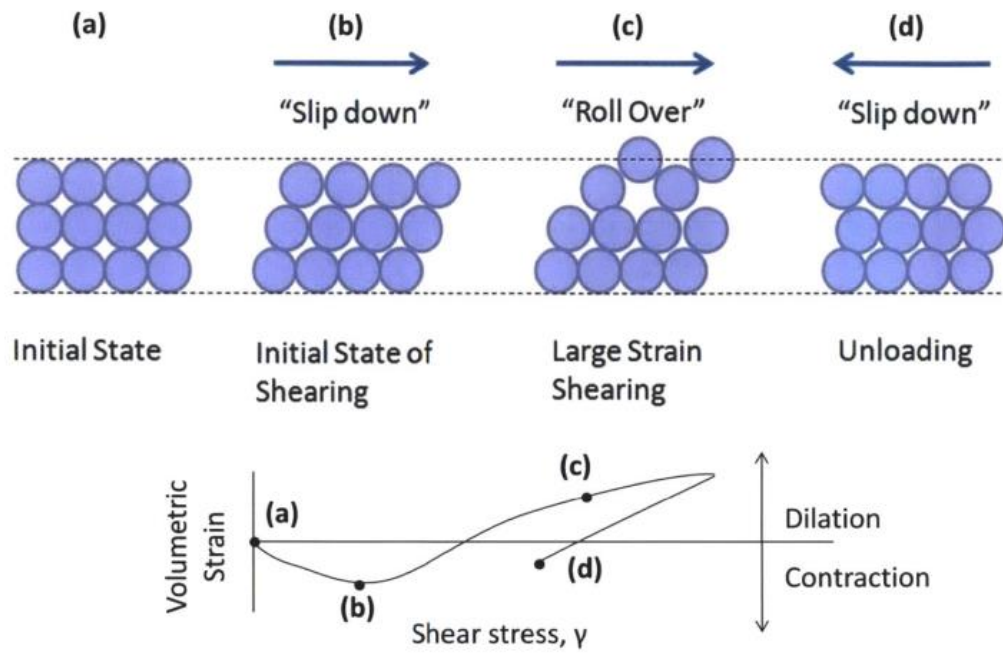


Figure 4.2 : Process of deformation in sand under shear stress (Vytiniotis, 2011).

By increasing loading the sand particles start rolling over each other which causes sand to dilate with more displacement and different void ratio (Vytiniotis, 2011).

At this stage, when loading continue, there is no more volumetric or stress change within the sand which is called “critical state”. The critical state can be represented by critical state line (CSL) as illustrated in Figure 4.1 which denotes relationship of different void ratios and confining stresses (Idriss & Boulanger,2008).

4.1.1.4 Response to Monotonic Loading Under Undrained Condition

When there is no diffusion of pore water pressure within the liquefiable soil it can be assumed as undrained condition.

If the loading imposed in very short time compare the time needed for water to dissipate, the pore water pressure increases rapidly due to incompressibility of pore fluid (water). Generation of pore water pressure causes an excessive pore water pressure within the soil mass and total pressure can be handle more and more with pore water pressure. As a result vertical effective stress and also shear stiffness of soil decrease.

Two common laboratory procedures for evaluating saturated sand behavior under cyclic shearing and undrained condition are:

- 1- Stress or strain controlled cyclic direct simple shear test
- 2- Undrained triaxial cyclic test

The test results from triaxial tests conducted by (Ishihara,1996) for loose and dense Toyoura sand samples with relative densities 16% and 64% and effective confining pressure of 0.1 MPa to 3 MPa showed that for axial strain (ϵ) higher than 25% the sand samples shows

4.1.2 Response of Sand Under Cyclic Loading

4.1.2.1 Sand Response in Low-strain Condition

Under cyclic loading, the behavior of sand in small-strain (for $\gamma_{cyclic} < 0.001$) range is nonlinear however shows very small permanent strains. In saturated sands it has been shown that there exists a limit shear strain in which no excess pore water pressure change occurs during cyclic loading below that limit. This elastic behavior of a sand is well expressed by the secant shear modulus used to evaluate the reduction of the strength with the number of cycles shown in Figure 4.3. The secant shear modulus is the equivalent linear modulus required to reach the same level of shear stress and strain. Energy dissipation in the non-linear system is described by the damping ratio, ξ , that can be evaluated by the following expression:

$$\xi = \frac{1}{4\pi} \frac{\Delta W}{W} \tag{4.2}$$

where ΔW is the area enclosed by the hysteretic loop and $W = 1/2 \tau_c \gamma_c$ (Figure 4.3)

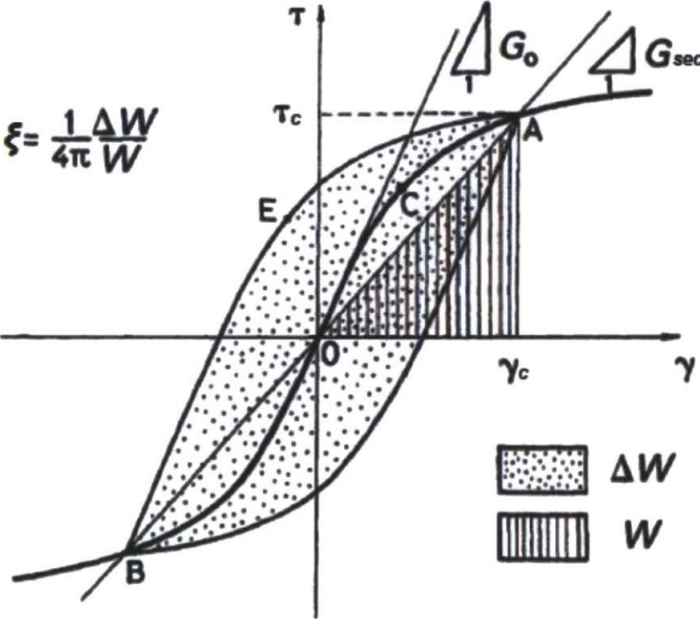


Figure 4.3 : Definition of secant shear modulus, G_{sec} , and damping ratio ξ (Vytiniotis, 2011).

Due to the nonlinearity of the stress-strain curve, both G_{sec} and ξ are dependent strongly on the maximum amount of the cyclic shear strain. In current practice, it is customary to present the variations of G_{sec} and ξ vs. y_{cyclic} in terms of normalized shear modulus (G_{sec}/G_{max} vs. y_{cyclic}) and damping ratio curves (ξ vs. y_{cyclic}). Figure 4.4 shows the degradation of modulus and damping for Toyoura sand after 10 cycles of shearing at an effective stress, $\sigma'_{v0}=100\text{kPa}$. The secant modulus degrades very quickly and damping increases significantly for events exceeding $y_{cyclic}=10^{-2}\%$.

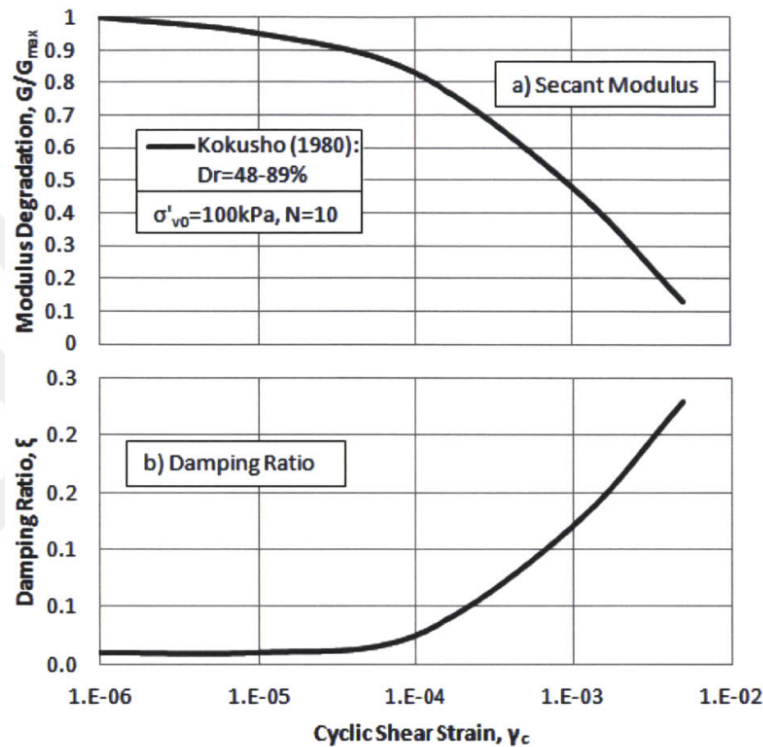


Figure 4.4 : Experimental data for the: (a) degradation of G/G_{max} vs. y_{cyclic} (b) ξ vs. y_{cyclic} curves for dry Toyoura sand (Vytiniotis, 2011).

4.1.2.2 Sand Response Due to Cyclic Loading

Continuous reduction of strength during undrained shearing, shows the tendency of a sand to behave more contractive during loading. Liquefaction state refers to the condition in which large deformations occur and almost zero shear strength are observed (during both monotonic or cyclic shearing), when excess pore pressures changes and approach the limiting condition where $\Delta u/\sigma'_{v0}$ approaching 1.0. Liquefaction resistance of sand depends on several features, including the number of cycles, amount of cyclic shear stress, relative density of soil, confining pressure, initial hydrostatic pressure and consolidation history.

Figure 4.5 shows typical results for the response of a dense sand in constant volume simple shear experiments. Figure 4.5(a) shows the effective stress path of the specimen. The test is performed with constant Cyclic Shear Stress Ratio, $CSR = \tau_c/\sigma'_{v0}=0.4$. As the number of load cycles increases, the vertical effective stress is reduced in order to maintain constant volume (i.e., $\Delta\sigma'_v/\sigma'_{v0} = -\Delta u/\sigma'_{v0}$). For number of cycles more than 10-15, the shearing cycles reach a lowest effective stress level because phase transformation causes effective stresses to increase.

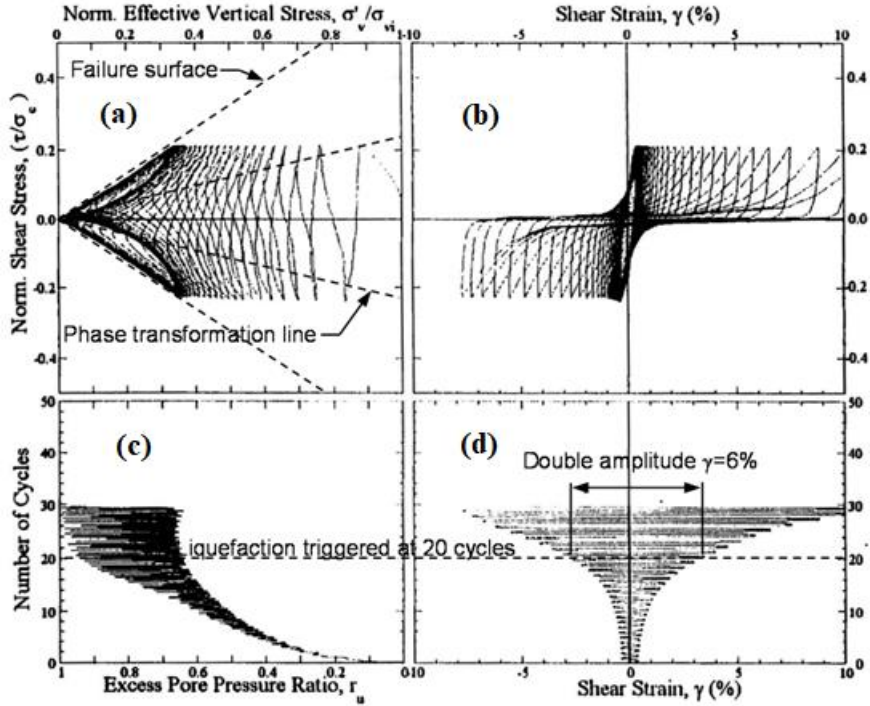


Figure 4.5 : Typical response of sand in constant volume for Undrained Direct Simple Shear test (gingery, 2014).

5. FINITE ELEMENT MODELING

5.1 Introduction

In geotechnical earthquake engineering, nonlinear finite element analysis generally is carried out for complex geometries and sophisticated soil constitutive models. Existence of too many number of degree of freedoms due to large soil domain and interaction between fluid, soil and embedded structure under drained or undrained condition need more precise formulation and computation effort to evaluate complex behavior of multiphase porous media.

Many efforts have been made to provide efficient numerical formulation that can be used as unified approach to solve soil as porous media. The efforts was based on developing formulation for elements that can overcome volumetric locking in incompressible multiphase media, have better flexural resistance and less effected by distortion during analysis.

In 1941 Biot proposed governing equations of multiphase porous media under quasi-static condition and later on he proposed an improved formulation for dynamic condition (Zienkiewicz & Shiomi.1984, McGann.2013).

Due to complexity of fluid-soil-structure interaction (FSSI), the analysis would be so sophisticated to be handle by conventional and experimental methods. Therefore, by implementation of nonlinear fully coupled effective stress finite element analysis it is possible to achieve this goal.

Effective stress analysis of ground response due to liquefaction consists of three key aspects:

- Proper soil model that can capture cyclic loading effectively.
- Explicit fluid-solid fully coupled formulation to capture interaction between solid phase, pore fluid and embedded structure.
- Reliable and more accurate numerical approach such as finite element-finite difference method, finite element-discrete element method and material point method even there is low effective stress magnitudes.

The accuracy and reliable results of numerical analysis are mostly governed by characteristics of ground, the method for finding soil parameters from in-situ or

laboratory experiments, proper soil constitutive model and characteristics of input motion. Therefore, difficulty in accurate estimation and evaluation of any of these factors will led to an inaccurate results.

During fully coupled effective stress finite element analysis mechanical parameters of cohesionless saturated soil and underground structure during gavity and seismic analyses can be evaluated more precisely in which it emphesizes that fully coupled effective stress analysis is an effective approach to predict soil liquefaction phenamena and underground structure response during earthquake. Previous implementations of numerical analysis and comparison to shaking table tests have been proved that numerical analysis is capable of simulating all saturated soil characterictics, Bao et al.2017.

In this study finite element model implemented in open-source code software OpenSees developed by Pacific Earthquake Engineering Center (PEER). OpenSees platform is capable of simulation and analysis of 2D and 3D soil structure interaction under static and dynamic loadings. Opensees also has capability to simulate soil linearity and nonlinearity under drain and undrained conditions.

To investigate the seismic performance of tunnel, the tunnel assumed to be buried in two layer soil profile consisting of loose sand overlaying a medium dense sand as demonstrated in Figure 5.1. the detail of soil constitutive models and calibration will be provided in the next chapter.

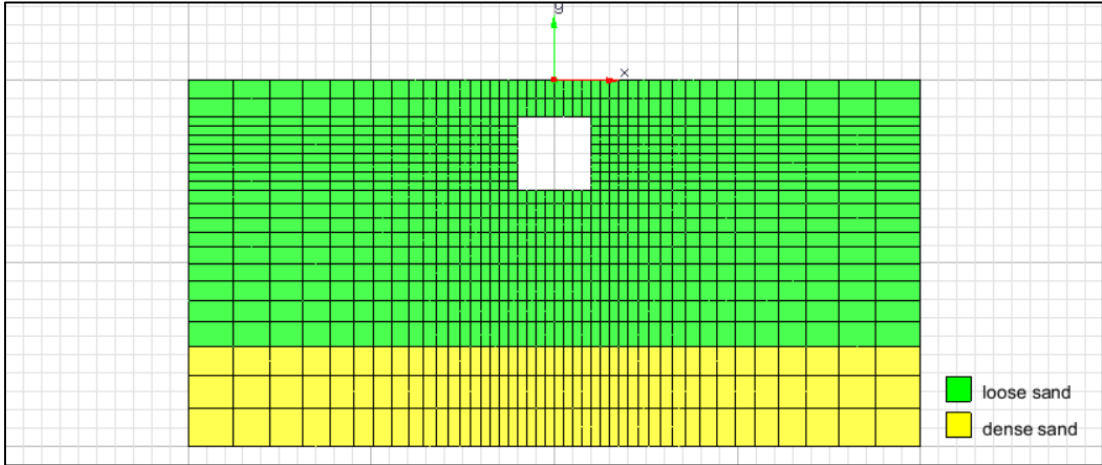


Figure 5.1 : Schematic of overall soil profile for finite element modeling.

Furthermore, in this chapter fluid-solid fully coupled plain strain finite element formulation in Opensees following by implementation and modeling of rectangular tunnel in liquefiable soil will be explored in detail.

5.2 Fully Coupled Fluid- Solid Multiphase Formulation in Opensees Platform

Behavior of saturated soil as a multiphase continuum can be describe by interaction between soil particles and pore fluid. Fully coupled effective stress principle is based on coupling pore fluid and soild phase interactions in saturated soil. After Biot proposed formulation for flow through porous media, different numerical formulation and approaches proposed to include pore pressure degree of freedom into formulation.

Zienkiewicz and Shiomi,(1984) categorized fully coupled fluid-soild formulation for saturated or partially saturated soil in 3 different approaches:

u-U element formulation, u-p-U element formulation and u-p formulation (McGann.2013).

U degree of freedom in u-p-U which represent the full coupled system of equations is the relative acceleration of fluid and solid. u-U is the simplified u-p-U system of equations which consider fluid as an incompressible material. u-p formulation is simplified u-p-U formulation by neglecting U degree of freedom.

The formulation is established based on the following assumptions:

- Small deformation with neglecting rotational degree of freedoms.
- Constant density for both fluid and solid
- Constant porosity
- Solid phase considered as incompressible material.
- Both pore fluid and solid particles have the same acceleration.

The u-p formulation is consist of two principles:

- 1- General equation of motion adapted for coupled soild and fluid.
- 2- Conservation of mass principle for fluid phase following darcy's law.

$$\nabla \cdot (\boldsymbol{\sigma}' + p\boldsymbol{\delta}) - \rho(\ddot{\mathbf{u}} - \mathbf{g}) = \mathbf{0} \quad (5.1)$$

$$\nabla \cdot \dot{\mathbf{u}} + \frac{\dot{p}}{Q} + \nabla \cdot \left[\frac{\mathbf{k}}{\rho_f g} (\nabla p - \rho_f \ddot{\mathbf{u}} + \rho_f \mathbf{g}) \right] = 0 \quad (5.2)$$

Where,

$\boldsymbol{\sigma}'$ is effective stress tensor, p is pore pressure, $\boldsymbol{\delta}$ is second-order identity tensor, ρ is density, \mathbf{u} is displacement vector of the solid phase, \mathbf{g} is gravity acceleration vector, Q is undrained bulk modulus, \mathbf{K} is hydraulic gradient tensor, ρ_f is fluid density, g is gravity acceleration, ∇ is gradient operator, $\nabla \cdot$ is divergence operator and dot is derivative in terms of time.

The governing formulation can be written as

$$\mathbf{M}\ddot{\mathbf{U}} + \int_{\Omega} \mathbf{B}^T \boldsymbol{\sigma}' d\Omega + \mathbf{Q}\mathbf{p} - \mathbf{f}^s = \mathbf{0} \quad (5.3)$$

$$\mathbf{Q}^T \dot{\mathbf{U}} + \mathbf{S}\dot{\mathbf{p}} + \mathbf{H}\mathbf{p} - \mathbf{f}^p = \mathbf{0} \quad (5.4)$$

Where, \mathbf{M} is mass matrix, \mathbf{U} is displacement matrix, \mathbf{B} is strain-displacement matrix, $\boldsymbol{\sigma}'$ is effective stress vector, \mathbf{Q} is discrete gradient operator coupling the solid and fluid phases, \mathbf{p} is pore pressure matrix, \mathbf{H} is permeability matrix, \mathbf{S} is compressibility matrix, \mathbf{f}_s is body force and \mathbf{f}_p is boundary conditions matrix (Yang & Elgamal.2002).

In the following section a brief expression of the u-p fully coupled fluid-solid formulation and their governing equations and solutions will be explored in more detail.

5.2.1 Governing Equations for Fully Saturated Behavior with a Single Pore Fluid

The effective stress principle, Jeremic.2001, can be described by

$$\sigma'_{ij} = \sigma_{ij} + \delta_{ij}p \quad (5.5)$$

And incremental constitutive function is

$$d\sigma'_{ij} = E_{ijkl} (d\varepsilon_{kl} - d\varepsilon_{kl}^0) \quad (5.6)$$

Due to small strain hypothesis, the increments in strain, $d\varepsilon_i$, for the soil can be evaluated in terms of displacement increments, du_i , as follow

$$d\varepsilon_{ij} = \frac{1}{2}(du_{i,j} + du_{j,i}) \quad (5.7)$$

The overall equilibrium or momentum balance relation for the soil-fluid mixture can be then written as

$$\sigma_{ij,j} - \rho\ddot{u}_i - \rho_f[\ddot{w}_i + \dot{w}_j\dot{w}_{i,j}] + \rho b_i = 0 \quad (5.8)$$

where b_i is the body force acceleration. The underlined term refers to the acceleration of the fluid, written in Eulerian terms and including the relative convective term.

The second equilibrium equation ensures the momentum balance of the fluid, written as

$$-p_{,i} - \frac{R_i}{n} - \rho_f\ddot{u}_i - \rho_f[\ddot{w}_i + \dot{w}_j\dot{w}_{i,j}]/n + \rho_f b_i = 0 \quad (5.9)$$

in which R_i represents the viscous drag force² which, assuming the Darcy seepage law, can be written as

$$\frac{R_i}{n} = k_{ij}^{-1}w_j \quad or = k^{-1}w_i \quad (5.10)$$

where k_{ij} represents anisotropic hydraulic gradient coefficients of darcy's law.

² When laminar fluid flow streams around a block, it exerts a viscous drag on the obstacle. Frictional forces accelerate the fluid backward (against the direction of flow) and the obstacle forward (in the direction of flow). The viscous drag force increases linearly with the speed of the fluid.

The equation for conservation of flow can be defined as

$$w_{i,i} + \alpha \varepsilon'_{ii} + \frac{\dot{p}}{Q} + n \frac{\dot{\rho}_f}{\rho_f} + \dot{s}_0 = 0 \quad (5.11)$$

Where,

$$\frac{1}{Q} \equiv \frac{n}{K_f} + \frac{\alpha - n}{K_s} \cong \frac{n}{K_f} + \frac{1 - n}{K_s} \quad (5.12)$$

5.2.2 Fully Coupled Equations Solution

A Modification of variables is introduced. In place of the relative displacements of the fluid w_i the total displacement of the fluid U_i is

$$U_i = u_i + \frac{w_i}{n} \quad (5.13)$$

Then the equation of the solid skeleton equilibrium becomes

$$\sigma'_{ij,j} - (\alpha - n)p_{,i} + (1 - n)\rho_s b_i - (1 - n)\rho_s \ddot{u}_i + R_i = 0 \quad (5.14)$$

The second equation will simply be [n £ (3:5)], i.e.,

$$-np_{,i} - R_i - n\rho_f(\ddot{u}_i + \frac{\ddot{w}_i}{n}) + \rho_f \dot{w}_j \dot{w}_{i,j} + n\rho_f b_i = 0 \quad (5.15)$$

It is known that $\ddot{U}_i = \ddot{u}_i + \ddot{w}_i/n$ and by removing the term $\dot{w}_j \dot{w}_{i,j}$,

$$-np_{,i} + n\rho_f b_i - n\rho_f \ddot{U}_i - R_i = 0 \quad (5.16)$$

The main unknowns u_i , U_i , and p can be approximated by using shape functions as

$$\begin{aligned} u_i &= N_K^u \bar{u}_{Ki} \\ U_i &= N_K^U \bar{U}_{Ki} \\ p &= N_K^p \bar{p}_K \end{aligned} \quad (5.17)$$

After some algebraic computations the system of discretized equations reads

$$\begin{bmatrix} \mathbf{M}_s & 0 & 0 \\ 0 & 0 & 0 \\ 0 & 0 & \mathbf{M}_f \end{bmatrix} \begin{bmatrix} \ddot{\bar{u}} \\ \ddot{\bar{p}} \\ \ddot{\bar{U}} \end{bmatrix} + \begin{bmatrix} \mathbf{C}_1 & 0 & -\mathbf{C}_2 \\ 0 & 0 & 0 \\ -\mathbf{C}_2^T & 0 & \mathbf{C}_3 \end{bmatrix} \begin{bmatrix} \dot{\bar{u}} \\ \dot{\bar{p}} \\ \dot{\bar{U}} \end{bmatrix} + \begin{bmatrix} \mathbf{K}^{EP} & -\mathbf{G}_1 & 0 \\ \mathbf{G}_1^T & \mathbf{P} & \mathbf{G}_2^T \\ 0 & -\mathbf{G}_2 & 0 \end{bmatrix} \begin{bmatrix} \bar{u} \\ \bar{p} \\ \bar{U} \end{bmatrix} = \begin{bmatrix} \bar{f}_s \\ \bar{f}_p \\ \bar{f}_f \end{bmatrix} \quad (5.18)$$

or

$$\begin{bmatrix} (M_s)_{KijL} & 0 & 0 \\ 0 & 0 & 0 \\ 0 & 0 & (M_f)_{KijL} \end{bmatrix} \begin{bmatrix} \ddot{u}_{Lj} \\ \ddot{p}_L \\ \ddot{U}_{Lj} \end{bmatrix} + \begin{bmatrix} (C_1)_{KijL} & 0 & -(C_2)_{KijL} \\ 0 & 0 & 0 \\ -(C_2)_{LjiK} & 0 & (C_3)_{KijL} \end{bmatrix} \begin{bmatrix} \dot{u}_{Lj} \\ \dot{p}_L \\ \dot{U}_{Lj} \end{bmatrix} + \begin{bmatrix} (K^{EP})_{KijL} & -(G_1)_{KiL} & 0 \\ (G_1)_{LjK} & (P)_{KL} & (G_2)_{LjK} \\ 0 & -(G_2)_{KiL} & 0 \end{bmatrix} \begin{bmatrix} \bar{u}_{Lj} \\ \bar{p}_L \\ \bar{U}_{Lj} \end{bmatrix} = \begin{bmatrix} (\bar{f}_s)_{Ki} \\ (\bar{f}_p)_K \\ (\bar{f}_f)_{Ki} \end{bmatrix} \quad (5.19)$$

Or can be described as the general equation of motion

$$\mathbf{M}\ddot{\mathbf{x}} + \mathbf{C}\dot{\mathbf{x}} + \mathbf{K}\mathbf{u} = \mathbf{f}(t) \quad (5.20)$$

Where,

$$\begin{aligned}
\mathbf{M}_s &= (M_s)_{KijL} = \int_{\Omega} N_K^u (1-n) \rho_s \delta_{ij} N_L^u d\Omega \\
\mathbf{M}_f &= (M_f)_{KL} = \int_{\Omega} N_K^U n \rho_f \delta_{ij} N_L^U d\Omega \\
\mathbf{C}_1 &= (C_1)_{KijL} = \int_{\Omega} N_K^u n^2 k_{ij}^{-1} N_L^u d\Omega \\
\mathbf{C}_2 &= (C_2)_{KijL} = \int_{\Omega} N_K^u n^2 k_{ij}^{-1} N_L^U d\Omega \\
\mathbf{C}_3 &= (C_3)_{KijL} = \int_{\Omega} N_K^U n^2 k_{ij}^{-1} N_L^U d\Omega \\
\mathbf{K}^{EP} &= (K^{EP})_{KimP} = \int_{\Omega} N_{K,j}^u D_{ijml} N_{P,l}^u d\Omega \\
\mathbf{G}_1 &= (G_1)_{KiL} = \int_{\Omega} N_{K,i}^u (\alpha - n) N_L^p d\Omega \\
\mathbf{G}_2 &= (G_2)_{KiL} = \int_{\Omega} n N_{K,i}^U N_L^p d\Omega \\
\mathbf{P} &= P_{KL} = \left[\int_{\Omega} N_K^p \frac{1}{Q} N_L^p d\Omega \right] p_L \\
(\bar{f}_s)_{Ki} &= (f_1^u)_{Ki} - (f_4^u)_{Ki} + (f_5^u)_{Ki} \\
(f_f)_{Ki} &= (f_1)_{Ki} - (f_2)_{Ki} \\
(f_1^u)_{Ki} &= \int_{\Gamma_t} N_K^u n_j \sigma_{ij}'' d\Gamma \\
(f_4^u)_{Ki} &= \int_{\Gamma_p} N_K^u (\alpha - n) n_i p d\Gamma \\
(f_5^u)_{Ki} &= \int_{\Omega} N_K^u (1-n) \rho_s b_i d\Omega \\
(f_1)_{Ki} &= \int_{\Gamma_p} n N_K^U n_i p d\Gamma \\
(f_2)_{Ki} &= \int_{\Omega} N_K^U \rho_f b_i d\Omega
\end{aligned} \tag{5.21}$$

Nu; Np; NU are shape functions of the skeleton fluid and pore pressure. The expressions ; %os; %of are the density of the total, and the solid and fluid phases, respectively. The porosity n, is used in the definition %o = (1 - n)%os + n%of.

5.2.3 Large Deformation Fully Coupled Formulation

The formulation of fully coupled fluid-solid effective stress within the openses platform is able to capture large deformation characteristics. Also the compressibility and incompressibility of fluid phase can be captured as well during computation procedure. Coupled eulerian-lagrangian method is used to develop governing equations.

The soil mass assumed as lagrangian and pore water formulated as eulerian domain.

It is shown that the multiplicative breakdown of the deformation gradient, utilized in the large deformation elastic-plastic formulation for solid phase, can be used to precisely control the volumetric response of the fluid phase. The fluid content is decomposed additively. The basic unknown variables are the absolute displacement of solid phase (u_i), pore pressure (p), and relative displacement of fluid phase (U_i). The strong form is based on the Equation of Motion (3.18), Fluid Mass Conduction (3.19), and Fluid Mass Conservation (3.20)

$$P_{ij,j} + (r_o + m)b_i - \rho_o^s(1 - n)\ddot{u}_i - (m + \rho_o^{fl} n)\ddot{U}_i = 0 \quad (5.22)$$

$$JnF_{ij}^{-1}\dot{U}_i + k_{ij} \left[p_{,j} + \rho^{fl} F_{ij} b_i - \rho^{fl} F_{ij} \ddot{U}_i - \rho^{fl} F_{ij} a_i \right] = 0 \quad (5.23)$$

$$(1 - n)\dot{E}_{ii}\rho^{fl} + \left(\frac{n}{K_{fl}} + \frac{(1 - n)}{K_s} \right) (\dot{p} + p_{,i}u_i) + J\rho^{fl}n \left(F_{ij}^{-1}\dot{U}_{i,j} + F_{ij}^{-1}\dot{U}_i \right) = 0 \quad (5.24)$$

where the following notation is used: P_{ij} = First Piola-Kirchhoff stress tensor; r_o = Mass density; m = Fluid mass content per initial volume; b_i = Body force; ρ_o^s = Initial mass density for solid phase; ρ_o^{fl} = Initial mass density for fluid phase; n = Porosity; F_{ij} = deformation Gradient; J = Jacobian of the transformation $J = \det F_{ij}$; k_{ij} = Permeability tensor (anisotropic); ρ^{fl} = Current mass density for fluid phase; a_i = Tortuosity vector; D_{km} = Lagrange strain rate; E_{IJ} = Lagrange strain tensor; K_s = Bulk modulus of the solid phase; and K_{fl} = Bulk modulus of the fluid phase.

5.3 Numerical Stability Fully Coupled Fluid-Solid Effective Stress Analysis

Stability of nonlinear dynamic analysis computation depends on two important factors:

- 1- The distance between nodes in the mesh (element size, Δh)
- 2- Analysis step time (Δt)

Δh and Δt by approaching to zero, the numerical analysis results get more accurate and precise, therefore, by estimating proper values of Δh and Δt demanded accuracy can be achieved.

5.3.1 Mesh Geometry and Element Size (Δh)

Computation cost is dependent on density and element size of elements. Although larger number of elements increase, the computation time but on the other hand it increase the more accuracy in results and avoid element distortion, which might happen during analysis.

There are many methods available in literature such as adaptive mesh method, which is finding the optimum element size based on the existing computation capability. However, mesh geometry is dependent on frequency contents of ground motion's shear waves and the mesh size of soil domain should be adequately fine to certain element numbers adjusted in wavelength of shear wave and be able to capture the high frequency content of ground motion.

According to (Zhuang et al. 2015), the maximum size of mesh element h_{max} for the shear wave motion propagating through the soil media can be define as follow:

$$h_{max} = \left(\frac{1}{75} - \frac{1}{160} \right) V_s / f_{max} \quad (5.25)$$

Where V_s is the shear wave velocity, which can be represented by

$G_0 = qV_s^2$, and q is the mass density of the soil. f_{max} is the maximum frequency of the ground motion.

Kuhlemeyer and Lysmer (1973) suggested that to avoid distortion of transmitting wave the size of elements of mesh for numerical simulating of seismic wave propagation should satisfy (as cited in Lu.2016):

$$\Delta l \leq \frac{\lambda}{10} \sim \frac{\lambda}{8} \quad (5.26)$$

Where, Δl is the dimension of mesh element in vertical direction and λ is the wavelength of the maximum frequency content of ground motion, which is defined as:

$$\lambda = \frac{v}{f} \quad (5.27)$$

Where, v is shear wave velocity and f is frequency.

From equation of (x.x) it is obvious that before meshing the soil domain the role of frequency content should be considered for limited element size range.

For ground motions, which have larger frequency contents, smaller size of mesh should be provided and in that case increase computation time.

The meshing in model established by considering desired frequency cut-off range between 0.1 Hz and 100 Hz. According to equations (x.x) and (x.x), it can be written:

$$\lambda = \frac{v}{f} = \frac{250}{100} = 2.5 \text{ m}$$

$$\text{Maximum mesh size} \quad \frac{\lambda}{8} = \frac{2.5}{8} = 0.3125 \text{ m}$$

Figure 5.2 shows the maximum element size considered for simulation.

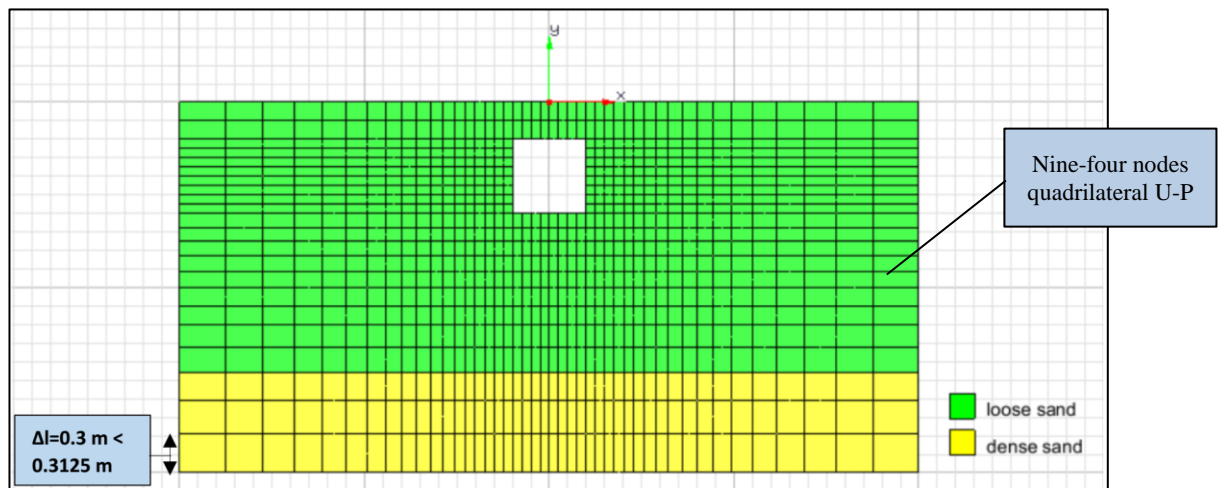


Figure 5.2 : Maximum element size in vertical direction for meshing.

A nine-four nodes quadrilateral U-P plane strain element was used for soil domain.

A nine-node quad U-P element layout is demonstrated in Figure 5.3. The corner nodes have 3 degrees of freedom (two translational degree of freedom and one for pore pressure) and the interior nodes have two translational degrees of freedom. The nodes numbering is according to the Cuthill-McKee pattern (Cuthill et al.1969).

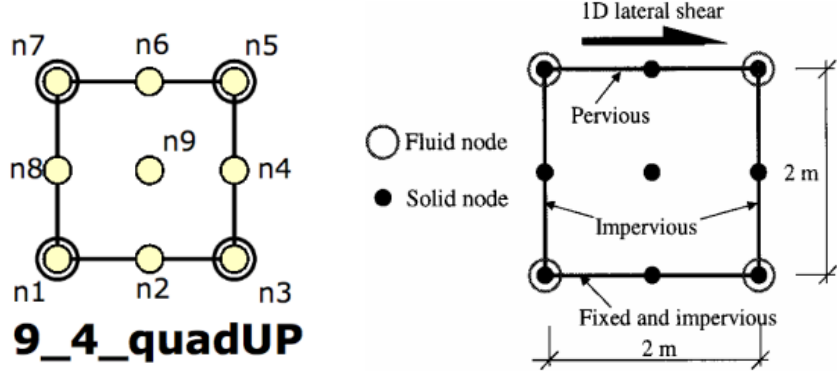


Figure 5.3 : Typical schematic of nine nodes fully coupled quadrilateral plain strain element (Yang & Elgamal.2002).

5.3.2 Time Step (Δt)

For stable time step during analysis, Courant-Friedrichs-Lewy (CFL) condition was used to ensure that formulation is stabilized for converging in terms of shear wave velocity and element size of the mesh. The algorithm for CFL condition implemented in tcl code as follow:

Computation in explicit scheme is much faster than implicit scheme. However, it may not converge during computation. To overcome this issue in finite element-finite difference analysis the following Courant-Friedrichs-Lewy (CFL) condition can be used to stabilize the step time during analysis:

$$f \leq (0.1 \sqrt{\mu/\rho})/L \quad (5.28)$$

$$\Delta t \leq L/(\sqrt{E/\rho}) \quad (5.29)$$

Where, L is the element size, E and μ are elastic modulus. Note that, $\sqrt{\frac{\mu}{\rho}}$ is shear wave velocity, which represent one wavelength, should be at least 10 times bigger than element size, as mentioned in pervious section ($\Delta l \leq \frac{\lambda}{10}$).

Depend on frequency content of ground motion and soil properties proper element size and time step can be estimated.

```
#!/usr/bin/tcl
#---DETERMINE STABLE ANALYSIS TIME STEP USING CFL CONDITION
# maximum shear wave velocity (m/s)
set vsMax $Vs(1)
# duration of ground motion (s)
set duration [expr $motionDT*$motionSteps]
# trial analysis time step
set kTrial [expr $sizeEleX/(pow($vsMax,0.5))]
# define time step and number of steps for analysis
if { $motionDT <= $kTrial } {
    set nSteps $motionSteps
    set dT $motionDT
} else {
    set nSteps [expr floor($duration/$kTrial)+1]
    set dT [expr $duration/$nSteps]
}
puts "number of steps in analysis: $nSteps"
puts "analysis time step: $dT"
```

In this algorithm, time step and number of steps generated automatically. For time step generated by algorithm larger than time step of input motion, the time step of ground motion is selected. Δt_{max} value should be updated if bedrock has smaller shear wave velocity due to any change in soil profile.

5.4 Soil Constitutive Models

Sand mechanical behavior is dependent on many factors such as grain size distribution and shapes, relative density, consolidation history and degree of saturation, which make it so complex to be described in unified way. Many efforts have been done by scholars to express the sand behavior under monotonic and cyclic loads. Sand mechanical behavior can be totally change due to change in any factors mentioned above. Failing response of saturated cohesionless loose sand under cyclic load and in undrained condition may emerge as cyclic mobility or flow liquefaction due to the relative density (D_r %) of the loose sand (Zhang et al,2011)

In geotechnical engineering, most of the monotonic and cyclic constitutive soil models are based on three important aspects:

- Yield surface generation of model
- Plastic associate or non-associate flow direction
- Developing proper softening and hardening rule with function that can define yield surface evolution and plastic flow direction in terms of inelastic strains (Jeremić & Yang,2002).

5.4.1 Cyclic Mobility Behavior

In saturated sand when volumetric strain gets larger, the sand tend dilate and expands in volume. This expansion will cause the pore water pressure to decrease and effective stress come back to intial state which led to increase stiffness of soil deposite.

During cyclic loading with large amplitude, changing saturated sand volume from expansion to contraction and vice versa can be described by changing phase which is

called Phase Transformation Surface (PT) as demonstrated in Figure 5.5. Shear strain increases gradually during each cycle of loading through phase transformation which is defined as Cyclic mobility or cyclic liquefaction behavior (Gingery, 2014; Elgamal et al., 2003).

5.4.2 Pressure Dependent Multiyield (PDMY02 and PDMY) Constitutive Models

The Pressure Dependent MultiYield (PDMY) and Pressure Dependent MultiYield02 (PDMY02) soil constitutive models are multiyield surface elasto-plastic models, which proposed by Yang et al. 2003, Elgamal et al. 2002 and Elgamal et al. 2003, have been used for modeling frictional saturated sand behavior under both monotonic and cyclic loading during drained and undrained conditions. The PDMY and PDMY02 are capable to evaluate contraction and dilation behavior of saturated sand simultaneously with generation excess pore water pressure during cyclic mobility. These models implemented and available in Opensees platform. More detail insight into PDMY and PDMY02 constitutive models given in following sections.

5.4.2.1 Yield Function

Material has elastic behavior following by plastic behavior. The elastic behavior is considered linear and isotropic while it is assumed that the nonlinear and anisotropic behavior is due to plasticity.

The yield function as illustrated in Figure 5.4 is defined as:

$$f = \frac{3}{2} [s - (p' + p_0')\alpha] : [s - (p' + p_0')\alpha] - M^2 (p' + p_0')^2 = 0 \quad (5.30)$$

Where,

In the space where $p' > 0$, $s = \sigma' - p'\delta$ is deviatoric stress tensor;

σ' is effective Cauchy stress tensor

δ is second-order identity tensor; p' is mean effective stress

α is a second-order deviatoric tensor representing the midpoint of yield surface in the domain inside deviatoric stress, p_0' is a small positive constant (generally, 0.1 kPa)

M is size of yield surface and ":" indicates product of tensors.

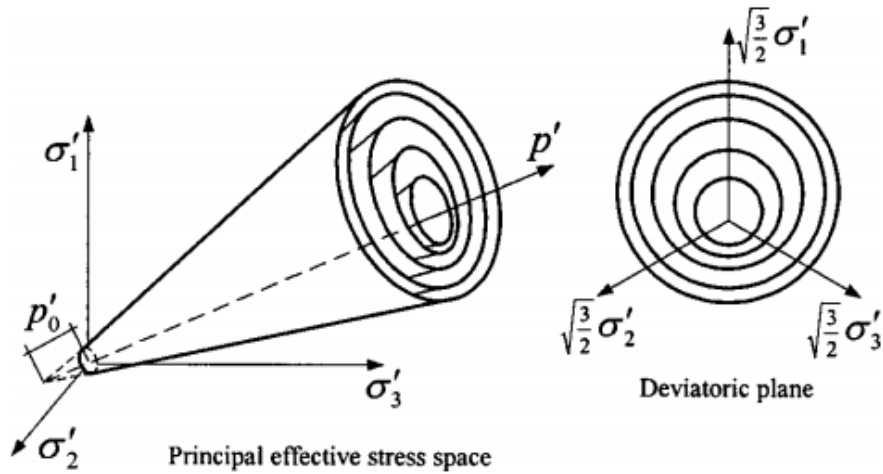


Figure 5.4 : Schematic of conical yield surfaces in principal stresses and deviatoric plane (Elgamal et al (2002); Elgamal et al, (2003); Yang et al, (2003)).

Generally hardening within the multiyield surface plasticity framework is expressed by identical yield surfaces with an equivalent peak at $-p'_0$ on hydrostatic line.

Friction angle of soil (ϕ), governs the size of largest surface, denoted by M_f , which is considered as failure surface.

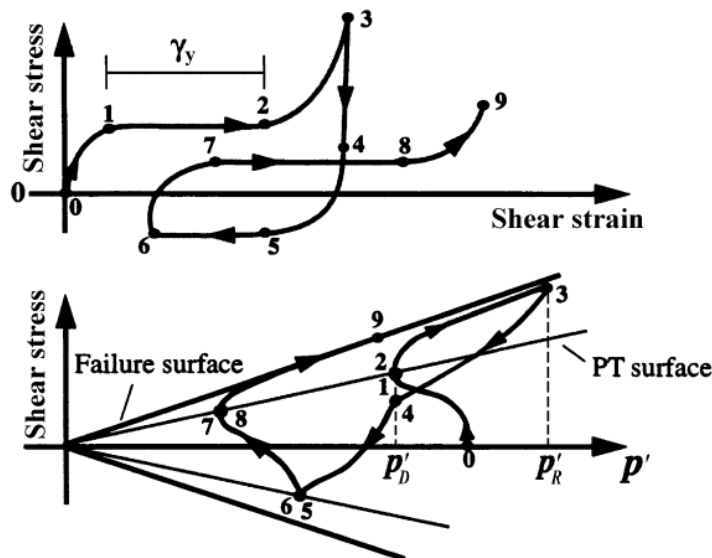


Figure 5.5 : Shear stress-shear strain and shear stress-effective confinement pressure responses of pressure dependent constitutive model.

5.4.2.2 Flow Rule

By considering a proper definition of non-associate flow rule according to plasticity theory (Elgamal et al,2003), the phase transformation between contraction, or dilation, with shearing stress can be captured accurately.

\mathbf{P} is flow direction of plasticity and \mathbf{P}'' is the volumetric measure of plasticity flow which is nonassociative and govern the adaptivity of flow rule to phase transformation according to experiment results. According to Elgamal et al,2003, \mathbf{P}'' can be defined as:

$$3\mathbf{P}'' = \frac{1 - (\eta/\bar{\eta})^2}{1 + (\eta/\bar{\eta})^2} \Psi \quad (5.31)$$

Where, $\eta = \sqrt{(3/2)\mathbf{s}:\mathbf{s}}/(p' + p_0')$ is defined as effective stress ratio, $\bar{\eta}$ is component of material which representing stress ratio of phase transformation surface, Ψ is a function which governs amount of contraction and dilation. If $\bar{\eta} > \eta$ the stress remain inside phase transformation surface and if $\bar{\eta} < \eta$ the stress exceed phase transformation surface. η is increases and decreases during loading and unloading respectively (Elgamal et al,2003).

At very small confining pressure the behavior of saturated sand during cyclic loading under undrained condition can be describe in three main stages based on general stress-strain relationship as illustrated in Figure 5.5 (Elgamal et al,2003):

- 1- When the shear strain is small saturated sand tends to densify volume which led to excess pore water pressure generation and causes the effestive stress to reduce.

The space inside phase transformation surface from point 0 to 1 in Figure 5.5 is where contraction occur regardless of applied stress condition. The function which govern the amount of contraction (Ψ) is assumed to be in the form of:

$$\Psi = c_1 e^{(c_2 \frac{p'}{p_a})} \quad (5.32)$$

Where,

- 2- As described before, during transformation phase from contraction to dilation and vice versa, at certain point during cyclic shear stress there is significant

change in strain while shear stress increased or decreased small. (1-2, 5-6, 7-8 in Figure 5.5).

In the soil constitutive model this changing phase can be described separately by an assumed function fitting the general shape of curvature. In PDMY and PDMY02 models proposed by Elgamal et al,2003; Elgamal et al,2002;Yang et al,2003, they defined this phase as:

$$\gamma_y = y_1 + y_2 \gamma_T \quad (5.33)$$

Where, $\gamma = \sqrt{\frac{2}{3} \mathbf{e} : \mathbf{e}}$ is octahedral shear strain, \mathbf{e} is deviatoric strain tensor and ":" indicates product of tensors.

5.5 Input Ground Motion Selection and Processing

Ground motion characteristics and seismic demands can be established from database obtained from accelerographs recordings. However, these acceleration time histories data are raw, which may need to be processed to be able to use in numerical analysis. When analogue record from analogue accelerograph converted to digital, for processing in computer, there is a shift in the baseline. Figure 5.6 demonstrates a shifted baseline in record during Italy earthquake in 1979 as an example. In similar manner, baseline can be shifted in the records from digital accelerographs due to frequency instrumental sensitivity (Boore & Bommer.2005).

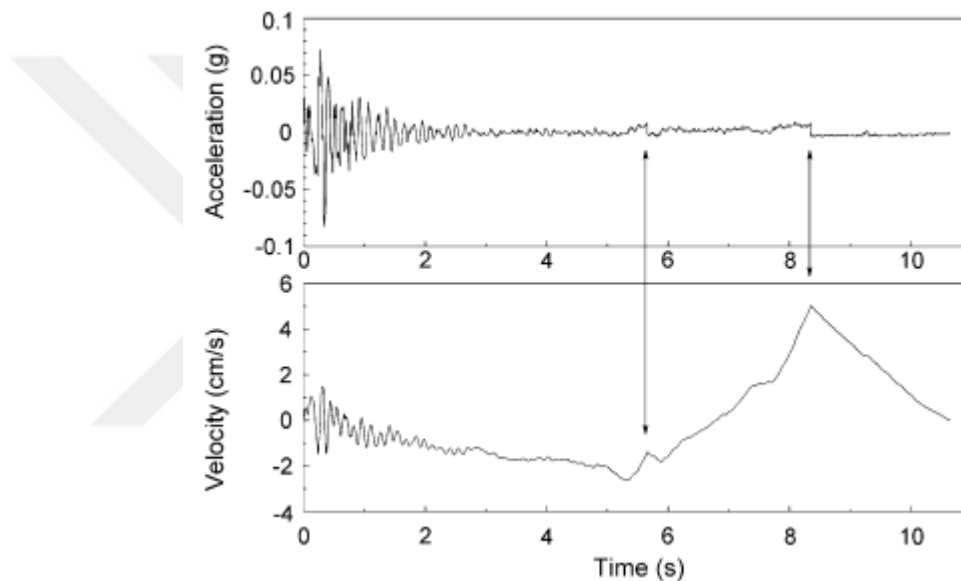


Figure 5.6 : NS record of the 1979 Italian earthquake at Nocera Umbra station, baseline shifted at 5.6 and 8.3(s) (Boore & Bommer.2005).

This shift in baseline is due to signal noises and they should be removed from the record through some proper procedures.

Most common methods to overcome this issue are Baseline correction, High-pass filtering, Low-pass filtering, Band-pass filtering. Raw ground motion data, no matter acceleration or velocity time history, can cause inaccurate results during dynamic analysis.

Integration of uncorrected acceleration record may lead to non-zero value for velocity and displacement histories at the end of ground motion duration, when earthquake stopped. Baseline correction can reduce this error by approaching in velocity and

displacement histories to zero after excitation. More detail about baseline correction and signal processing of ground motion can be found in Boore & Bommer (2005).

For this study, 1995 Kobe earthquake was selected as an input ground motion. The detail of horizontal component of Kobe earthquake illustrated in table 5.2, Figure 5.7, Figure 5.8, Figure 5.9, Figure 5.10, Figure 5.11, Figure 5.12 and Figure 5.13.

Table 5.1 : Detail of horizontal component of 1995 Kobe earthquake.

Earthquake name	Kobe-Japan
Year	1995
Station name	HIK
Magnitude	Row C
Mechanism	Strike slip
Rjb (km)	95.72
Rrup (km)	95.72
Vs30 (m/sec)	256
Lowest usable frequency (Hz)	0.0625
5-75% duration (sec)	6.1
5-95% duration (sec)	17.4
Arias intensity	0.4

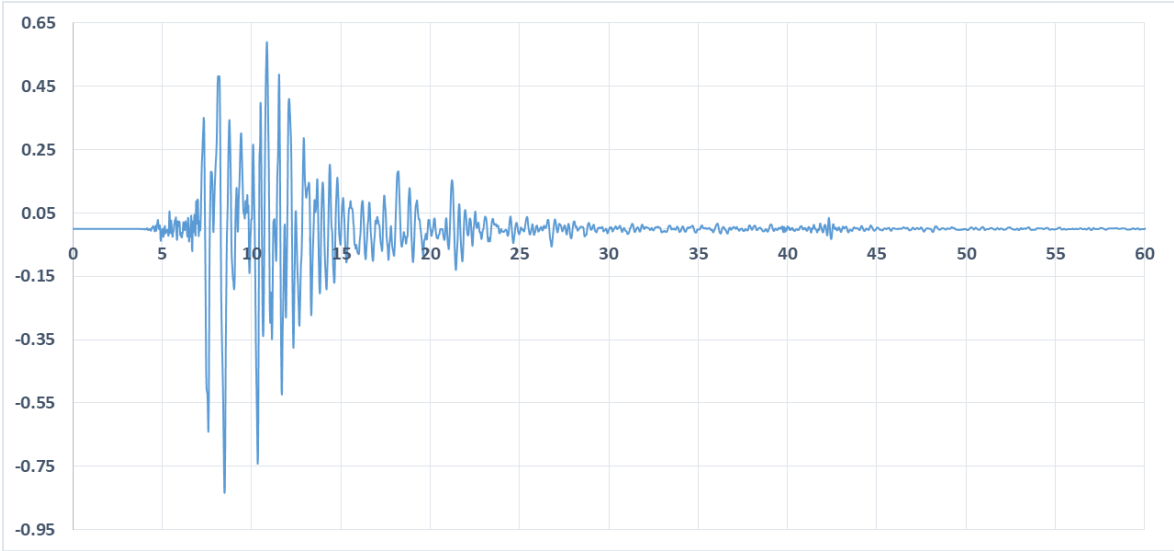


Figure 5.7 : First 60s of horizontal component of 1995 Kobe earthquake.

Maximum Acceleration: 0.834g
 at time t=8.480sec

 Maximum Velocity: 0.911m/sec
 at time t=8.280sec

 Maximum Displacement: 0.212m
 at time t=8.480sec

 Vmax / Amax: 0.111sec

 Acceleration RMS: 0.060g
 Velocity RMS: 0.071m/sec
 Displacement RMS: 0.020m

 Arias Intensity: 8.393m/sec
 Characteristic Intensity (Ic): 0.181
 Specific Energy Density: 0.760m²/sec
 Cumulative Absolute Velocity (CAV): 21.727m/sec

 Acceleration Spectrum Intensity (ASI): 0.723g*sec
 Velocity Spectrum Intensity (VSI): 4.113m
 Housner Intensity: 3.631m

 Sustained Maximum Acceleration (SMA): 0.641g
 Sustained Maximum Velocity (SMV): 0.537m/sec

 Effective Design Acceleration (EDA): 0.817g

 A95 parameter: 0.824g

 Predominant Period (Tp): 0.360sec
 Mean Period (Tm): 0.644sec

Figure 5.8 : 1995 Kobe earthquake parameters.

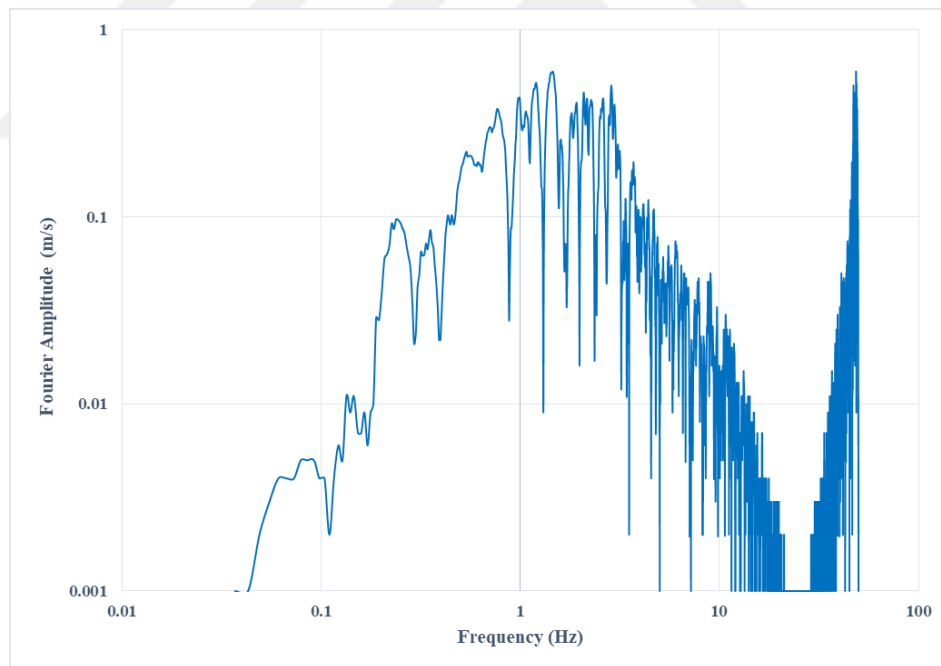


Figure 5.9 : Fourier amplitude versus frequency contents of 1995 Kobe earthquake.

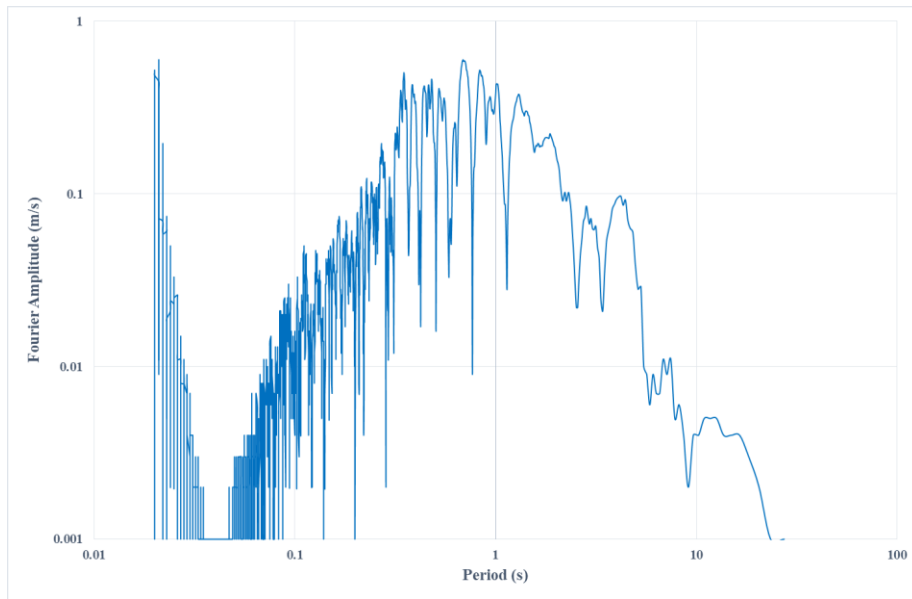


Figure 5.10 : Fourier amplitude versus period of 1995 Kobe earthquake.

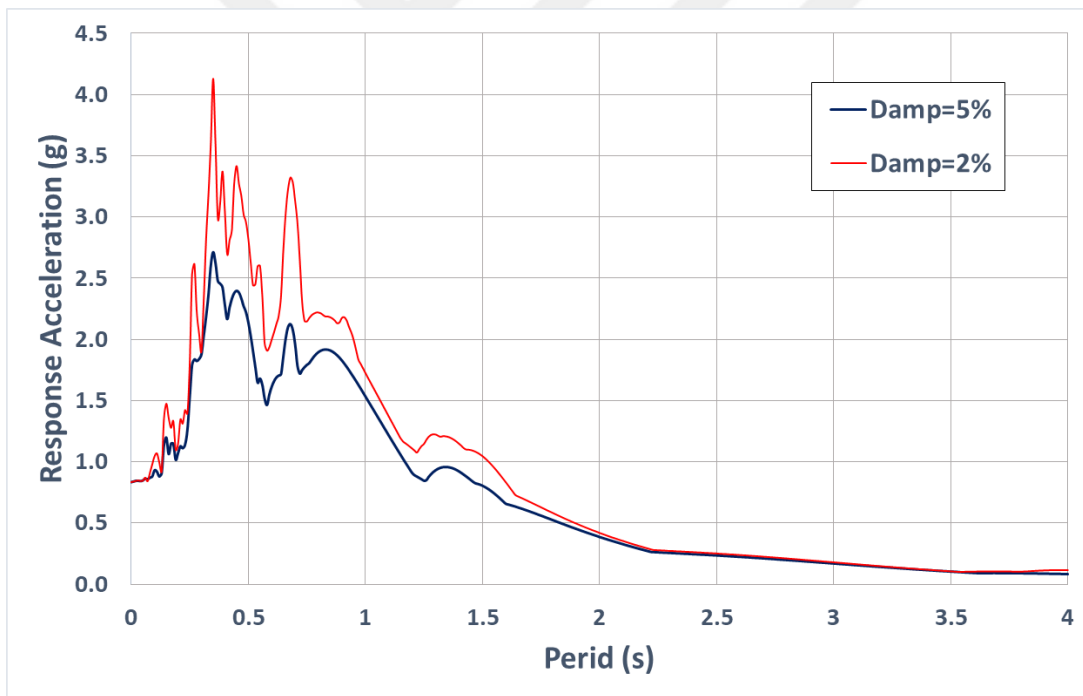


Figure 5.11 : Elastic acceleration response spectra of 1995 Kobe earthquake for 2% and 5% damping ratio.

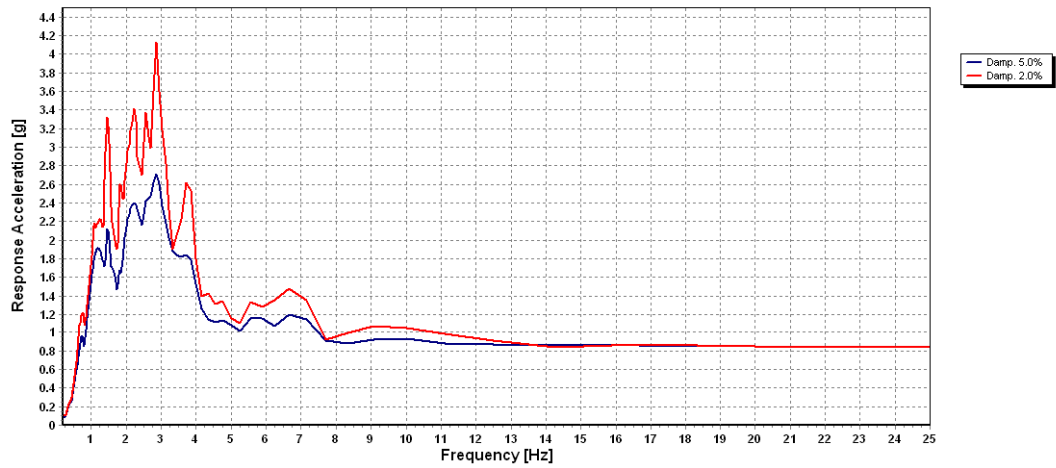


Figure 5.12 : Elastic acceleration response spectra versus frequency contents of 1995 Kobe earthquake for 2% and 5% damping ratio.

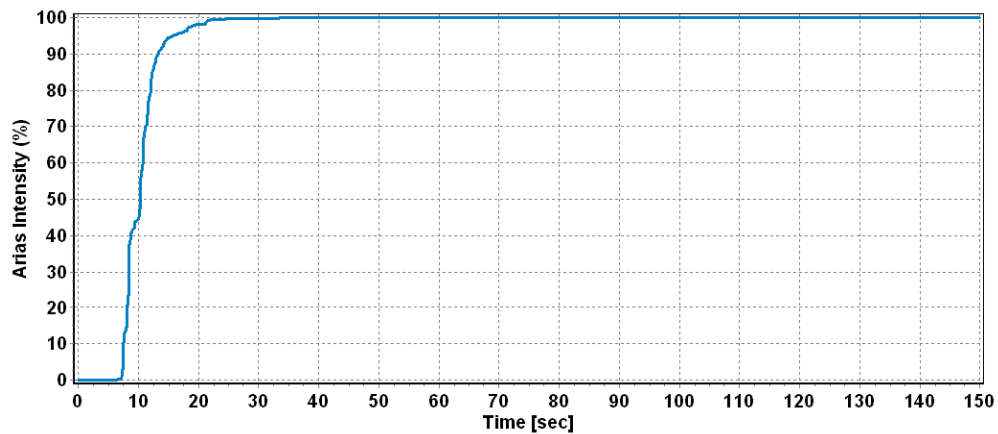


Figure 5.13 : Arias intensity of 1995 Kobe earthquake.

High-pass and band-pass filtering are the main efforts in processing the ground motion signal for liquefaction. Liquefied soil can increase amplification of long duration records due to softening behavior. In order to processing the raw acceleration record for removing the noise and baseline correction, if there is, the correction implemented in SeismoSignal. Since the Kobe earthquake record retrieved from Pacific Earthquake Engineering Research Center (PEER) database and it has been already baseline corrected there was no need to correct the record. However to consider the effect of frequency contents of ground motion on the tunnel in liquefiable soil, band-pass filtering implemented in SeismoSignal for frequency contents between 0.1Hz-10Hz and 0.1Hz-25Hz. The difference of Fourier amplitude spectrum between two different band-pass intervals are demonstrated in Figure 5.14.

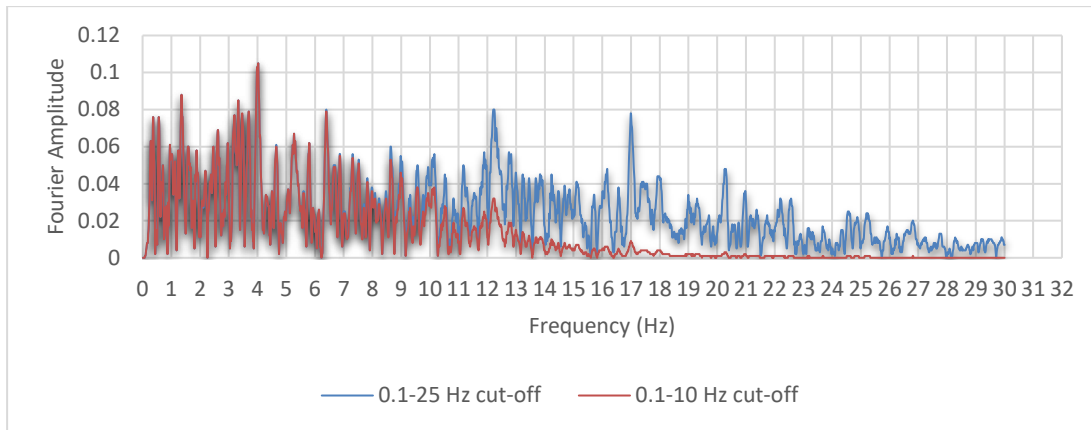


Figure 5.14 : Fourier amplitude versus frequency contents of 1995 Kobe earthquake for 0.1-10Hz and 0.1-25Hz Band-pass Filtering.



5.6 Boundary Condition

Efficient boundary condition can led to more accurate and precise results in finite element analysis especially for soil domain.

In practice, due to limited capability of computers and time of computation it is common that in finite element modeling only small segment of ground soil under ground motion considered in analysis, and the effect of eliminated soil domain should be taken into account by simulated boundary condition. In gravity analysis, boundary condition can be fixed without effecting the accuracy of results. However, in dynamic analysis, results can suffer from reflection of ground motion wave within the domain.

The easiest way to reduce this effect is to extend soil domain horizontally and vertically that it takes some time for seismic wave to reflect from boundary.

By extending the soil domain the effect of wave reflection within the soil can be reduce. However, it should be noted that extension should be enough that not affect the computation cost.

Generally, there are three common methods for providing simulated boundary condition in practice:

- Absorbing boundary condition
- Free-field boundary condition
- domain reduction condition

5.6.1 Absorbing Boundary Condition

As mentioned in previous section, accuracy of analysis depend on element size, less than 12.5% of wavelength of input motion. It is also needed to reduce the soil domain due to computation cost may arise during large analysis domain. However, by decreasing the soil domain the effect of boundary condition and treatment of wave propagation within the soil becomes more important as ground motion wave tends to reflect toward the soil domain.

The equation of 1-D shear wave propagating within the soil can be described as:

$$\frac{\partial^2 u(x,t)}{\partial t^2} = v_s^2 \frac{\partial^2 u(x,t)}{\partial x^2} \quad (5.34)$$

Where, u represent displacement of soil and $v_s = G/\rho$ is shear wave velocity.

Eq.5.34 can be solved as:

$$u(x,t) = u_r \left(t - \frac{x}{v_s} \right) + u_i \left(t + \frac{x}{v_s} \right) \quad (5.35)$$

Where, u_r and u_i could be any assumed functions. The first part on the right hand side of Eq.5.35 is wave propagation with velocity v_s and second part defines wave propagation with similar velocity v_s in positive and negative x directions respectively.

By taking partial derivative of Eq.5.35 respect to t and multiply by ρv_s , it can be represent as:

$$\rho v_s \frac{\partial u(x,t)}{\partial t} = \rho v_s u_r' \left(t - x/v_s \right) + \rho v_s u_i' \left(t + x/v_s \right) \quad (5.36)$$

Then, shear stress-strain relationship of linear elastic can be expressed as:

$$\tau(x,t) = G \frac{\partial u(x,t)}{\partial x} = -\frac{G}{v_s} u_r' \left(t - x/v_s \right) + \frac{G}{v_s} u_i' \left(t + x/v_s \right) \quad (5.37)$$

Where, τ represents shear stress. By adding equations (5.37) and (5.36), it can be written as:

$$\tau(x,t) = -\rho v_s \frac{\partial u(x,t)}{\partial t} + 2\rho v_s u_i' \left(t + x/v_s \right) \quad (5.38)$$

The term $-\rho v_s \frac{\partial u(x,t)}{\partial t}$ is the force per unit area of a dashpot with coefficient ρv_s and $2\rho v_s u_i' \left(t + x/v_s \right)$ is force per unit area related to shear wave velocity. Therefore, the nodes at the boundary can be replaced by dashpots representing the above conditions (Zhang et. al, 2003).

To simulate the effect of underlying elastic half-space on soil domain, different methods proposed such as absorbing boundary condition which is also called periodic boundary condition or transmitting boundary condition.

Absorbing boundary condition firstly proposed by (Lysmer & Kuhlemeyer, 1969 as cited in Lu, 2016) based on above explanation for deriving eq.5.38.

They used dashpots with viscous material to absorb the ground motion wave in the normal and shear directions. These dashpots provide viscous normal and shear forces, denoted respectively by σ and τ , given by:

$$\sigma = -\rho V_p v_n \quad (5.39)$$

$$\tau = -\rho V_s v_s \quad (5.40)$$

Where,

V_p is dilatation velocity; V_s is shear wave velocity; v_n is normal vector of velocity and v_s is tangent components of the velocity.

This method works very well when the angle of incidence of shear wave velocity against dashpot direction is larger than 30° (Lu.2016).

This method is simple and practical for implementation in nonlinear dynamic analysis to damp out energy of reflected seismic wave but it should be paid attention that before dynamic analysis, gravity analysis has to be carried out.

In absorbing boundary condition using Lysmer and Kuhlemeyer (1969) approach instead of applying acceleration as an input ground motion, a force, related to shear wave velocity of input ground motion and material parameters outside of soil domain, is applied to relate the compliance between soil domain and the unbounded area. For instance, Elgamal et al. (2008) used this technique to provide dashpots in three directions at all the base nodes of soil domain for simulation of underlying elastic half-space behavior (as cited in McGann.2013).

5.6.2 Free Field Boundary Condition

Absorbing boundary condition, which can dissipate reflected wave, should be modified when the seismic wave propagating from external media toward the soil domain. Zienkiewicz et al. (1989) and Wolf (1988) suggested free-field boundary condition where additional two separate soil columns can be provided at both sides of soil domain as demonstrated in Figure 5.15.

The free-filled columns and soil domain are computed simultaneously. Despite the fact that in 2D plain strain finite element the thickness of soil domain elements are considered small to represent plain strain conditions, the thickness of free-field columns should be large enough to simulate the behavior of unbounded media. In this

approach, free-field column can transfer seismic wave effects toward soil domain and not vice versa. Therefore, fluid-soil-structure interaction has little effect on behavior of free-field soil columns provided that be far enough from embedded structure.

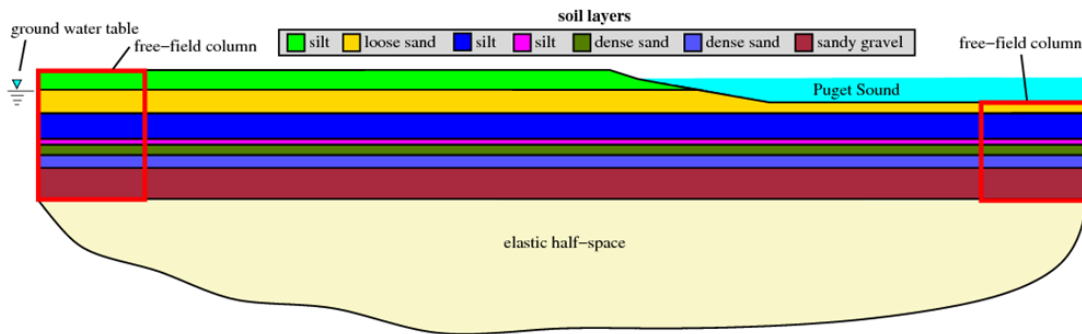


Figure 5.15 : Schematic of example free-field boundary condition (McGann & Arduino, 2011).

In other words, dimension of soil domain is better to be large enough that displacement of nodes at left and right side boundaries can be assumed as free field displacement. Despite the absence of absorbing boundary condition, Free-field boundary condition approach alone can properly simulate the effect of soil material nonlinearity and lower relative density of soil domain against bedrock.

In this study absorbing boundary condition proposed by Lysmer & Kuhlemeyer. (1969) is used to simulate the behavior of underlying bedrock by providing dashpot at base.

A “zeroLength” dashpot element provided with viscous material to absorb the reflected seismic wave. One end of the dashpot fixed in horizontal and vertical directions, while, the other node can move simultaneously with node at bottom left corner of soil domain. Uniaxial viscous material defined for the dashpot coefficient

```
# define dashpot material
set colArea      [expr $sElemX*$thick(1)]
set rockVS       760.0
set rockDen      2.5
set dashpotCoeff [expr $rockVS*$rockDen]
uniaxialMaterial Viscous [expr $numLayers+1] [expr $dashpotCoeff*$colArea] 1
```

Nodes at the bottom of model fixed in vertical direction and constrained together to move simultaneously in horizontal direction (equalDOF) to behave similar to elastic

half space layer under soil domain. Node at left lower corner of soil domain is considered as master node and the rest of base nodes are slave nodes. For simulating the drainage condition and dissipation of pore water pressure, at ground surface, third degree of freedom of corner nodes of soil elements (Nine_Four_Node_QuadUP) were fixed at element's corner nodes in surface level, which let the water to dissipate freely through the ground surface. The detail of model demonstrated in Figure 5.16.

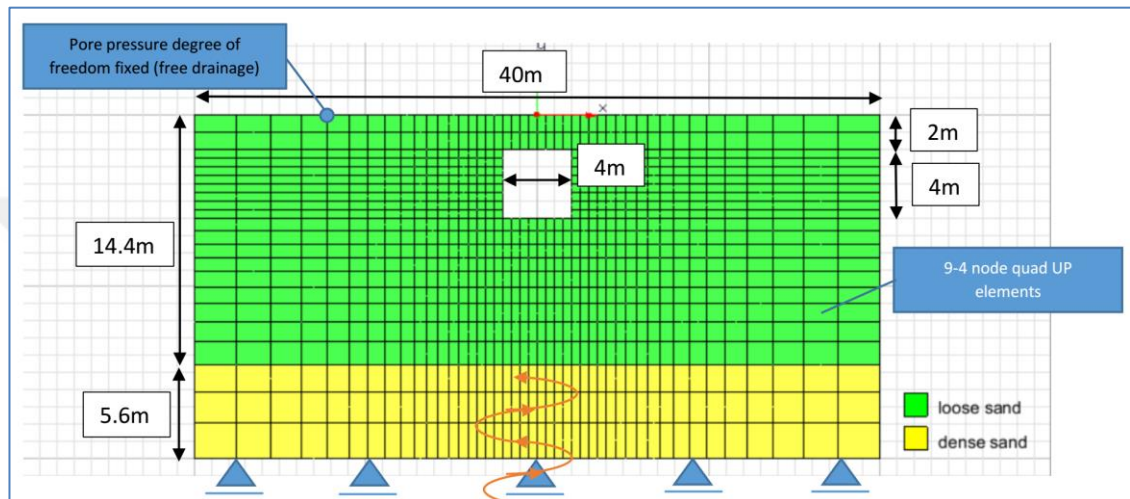


Figure 5.16 : Detail of soil profile, dimensions and boundary condition.

5.7 Analysis Procedure

In fully coupled fluid-solid effective stress analysis, before dynamic analysis it is essential that hydrostatic pore water pressure and effective stress distribution within the soil be initiated and evaluated. For this reason, transient gravity analysis performed to ensure that initial state condition established.

The pore water pressures obtained from gravity analysis were used as initial values for dynamic analysis.

To avoid conflict between result of gravity analysis and dynamic analysis and reduce the difference between end and initial steps for gravity and dynamic analyses respectively, dynamic analysis conducted with zero excitation values for a very short period.

The soil structure interaction (SSI) and excavation procedure is not considered in this study therefore, the initial stress within the soil and structural elements may not be captured precisely.

5.7.1 Transient Gravity Analysis and Corresponding Results

As mentioned before, prior to effective stress seismic analysis, in the first stage transient gravity analysis established to ensure initial effective stress and hydrostatic pore water pressure distribution captured properly in equilibrium state within the soil. Within the code, different recorders provided to separate gravity analysis results from seismic analysis. Results of stress, strain, displacement, acceleration, and pore water pressure recorded for each node.

The transient gravity analysis consists of two stage. In first stage, 9_4_nodes_quadUP element of soil domain assumed to behave linear elastic. This assumption established by adjusting `updateMaterialStage` command for `PressureDependMultiYield02` material model to behave linear elastic and set up the stage as zero to adapt confining pressure.

updateMaterialStage -material \$stag -stage \$sNum

In the second stage, plasticity of constitutive model included for plastic gravity analysis and stage number updated to one.

In first stage for linear elastic considered to perform as transient instead of static to reduce the errors that might appear in the situations where static analysis followed by transient dynamic analysis. At linear elastic stage, time steps considered large enough, typically $5.0e1$ to $5.0e3$, to capture hydrostatic pressure properly and during analysis it was found out increasing steps will improve the interface results between gravity analysis and dynamic analysis.

It is a manual evaluation procedure to find out the optimum values for steps to not effect duration of whole analyses.

Due to difficulty in convergence during second stage, which is plastic gravity analysis, the time steps for the analysis assumed small enough to achieve convergence and avoid additional displacements, which may occur due to oscillation of the ground.

The analysis steps in plastic analysis also manually increased to 150 steps to optimize and reduce difference of interface results between gravity and dynamic analyses.

5.7.2 Transient Dynamic Analysis and Corresponding Results

As explained in 3.6.1 section, to avoid convergence issue during dynamic analysis an algorithm added to the tcl/tk code for reducing time step and continuing analysis without effecting duration of analysis. If there is a convergence problem occur during analysis, the time step will decrease by half and analysis will continue.

If this procedure is not enough to continue for analysis, a proper initial time step should be provided at the beginning of analysis. As mentioned before in section x.x the earthquake ground motion applied as force time history.





6. SOIL CONSTITUTIVE MODEL CALIBRATION AND SITE RESPONSE VALIDATION

6.1 Calibration of Soil Constitutive Model

The pressure dependent multi yield (PDMY02) constitutive model which is available in Opensees platform was used to model loose sand overlaying a medium dense sand at bottom of the soil realm.

The PDMY02 constitutive model parameters needed to be calibrated for the specific site under investigation. In the calibration process the features of stress-strain relationship path and their correlation which express the yield surfaces should be considered cautiously.

6.1.1 Yield Surface

Both PDMY02 and PIMY constitutive models are multi surfaces yield surfaces which are capable of capturing the post-liquefaction behavior of soil. The form of yield surfaces are conical with shared cap positioned at the origin of main space. The failure gauge is expressed by outmost conical yield surface while the inner surfaces represent hardening zone (see Figure 6.1).

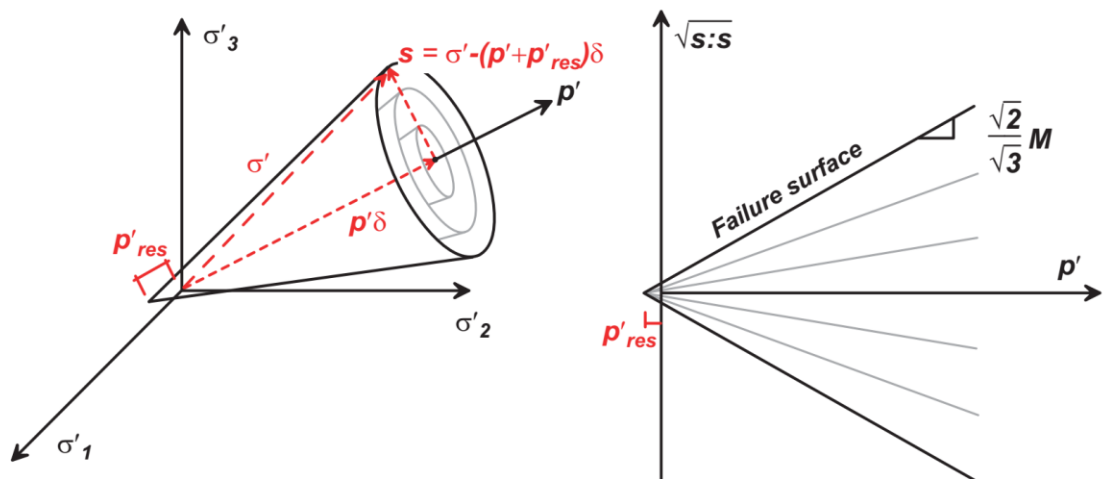


Figure 6.1 : Principle of Multi yield surface soil constitutive model.

Yield surface is expressed by second invariant (J_2) yield formulation which can be obtained by:

$$\tilde{\sigma}' = \begin{bmatrix} \sigma'_{11} & \sigma_{12} & \sigma_{13} \\ \sigma_{21} & \sigma'_{22} & \sigma_{23} \\ \sigma_{31} & \sigma_{32} & \sigma'_{33} \end{bmatrix} = \begin{bmatrix} \sigma'_1 & 0 & 0 \\ 0 & \sigma'_2 & 0 \\ 0 & 0 & \sigma'_3 \end{bmatrix} \quad (6.1)$$

Stress invariants can be expressed as:

$$I_1 = \text{tr}(\tilde{\sigma}'), \quad I_2 = \frac{1}{2} [\tilde{\sigma}' : \tilde{\sigma}' - \text{tr}(\tilde{\sigma}')^2], \quad I_3 = \det(\tilde{\sigma}') \quad (6.2)$$

And volumetric stress and deviatoric stress can be written as:

$$p' = \frac{\sigma'_{11} + \sigma'_{22} + \sigma'_{33}}{3}, \quad \tilde{s} = \tilde{\sigma}' - p' \tilde{I} = \begin{bmatrix} \sigma'_{11} - p' & \sigma_{12} & \sigma_{13} \\ \sigma_{21} & \sigma'_{22} - p' & \sigma_{23} \\ \sigma_{31} & \sigma_{32} & \sigma'_{33} - p' \end{bmatrix} \quad (6.3)$$

Deviatoric stress invariants are expressed by:

$$J_1 = \text{tr}(\tilde{s}) = 0 \quad (6.4)$$

$$J_2 = \frac{1}{2} [\tilde{s} : \tilde{s} - \text{tr}(\tilde{s})^2] = \frac{1}{2} [\tilde{s} : \tilde{s}] \quad (6.5)$$

$$J_3 = \det(\tilde{s}) \quad (6.6)$$

Matching the second invariant to a constant can be represents yield surface. Herein the constant is $M^2 P'^2 / 3$.

$$J_2 = M^2 P'^2 / 3 \quad (6.7)$$

Therefore it can be obtained:

$$\frac{3}{2} [\tilde{s} : \tilde{s}] - M^2 P'^2 = 0 \quad (6.8)$$

By introducing second-order deviatoric tensor (α), which represents the center of the yield surface in deviatoric stress subspace, the conical shape yield surface formulation can be expressed as:

$$f = \frac{3}{2} [\tilde{s} - p' \tilde{\alpha}] : [\tilde{s} - p' \tilde{\alpha}] - M^2 P'^2 = 0 \quad (6.9)$$

By considering small cohesion, when the effective confining pressure is near zero, the yield surface apex shifts through negative confining pressure by P'_{res} .

For cohesionless soil, when there is no cohesion and for satisfaction in numerical implementation and to avoid vagueness in expressing of normal vector to the yield surface when confining pressure is zero, the apex is shifted towards negative confining pressure by a very small positive constant (i.e. 0.01 KPa).

$$\mathbf{f} = \frac{3}{2} [\tilde{\mathbf{s}} - (\mathbf{p}' + \mathbf{p}'_{\text{res}})\tilde{\boldsymbol{\alpha}}] : [\tilde{\mathbf{s}} - (\mathbf{p}' + \mathbf{p}'_{\text{res}})\tilde{\boldsymbol{\alpha}}] - \mathbf{M}^2 (\mathbf{P}' + \mathbf{p}'_{\text{res}})^2 = 0 \quad (6.10)$$

Where, \mathbf{M} represents the size of yield surface. It is essential to distinguish the following descriptions of shear stress:

- The shear stress on the failure plane is represented by τ , which is obtained from triaxial compression test (TXC).
- The shear stress on horizontal plane is represented by $\sigma_{12} = \tau_h$, which is obtained from cyclic direct simple shear test (DSS).
- The deviatoric stress in three dimensional coordinate in models can be represented by octahedral shear stress which can be defined as:

$$\begin{aligned} \tau_{\text{oct}} &= \frac{1}{\sqrt{3}} \sqrt{\tilde{\mathbf{s}} : \tilde{\mathbf{s}}} \\ &= \frac{1}{3} \sqrt{(\sigma'_{11} - \sigma'_{22})^2 + (\sigma'_{22} - \sigma'_{33})^2 + (\sigma'_{11} - \sigma'_{33})^2 + 6\sigma_{12}^2 + 6\sigma_{13}^2 + 6\sigma_{23}^2} \end{aligned} \quad (6.11)$$

- “ q ” is an alternative way to represent the deviatoric stress, which is expressed as $(\sigma'_1 - \sigma'_3)$ in triaxial compression test. “ q ” in common form is defined by:

$$q = \frac{\sqrt{3}}{\sqrt{2}} \sqrt{\tilde{\mathbf{s}} : \tilde{\mathbf{s}}} = \frac{3}{\sqrt{2}} \tau_{\text{oct}} \quad (6.12)$$

6.1.2 Size of Yield Surface, Friction Angle

The size of furthest yield surface (failure yield surface) dependent on friction angle which can be evaluated by triaxial compression test (TXC) or direct simple shear test (DSS). The friction angle of direct simple shear test (DSS) is different from triaxial compression test (TXC). As it is illustrated in Figure 6.2, triaxial compression test can be used to find a relationship between size of yield surface and friction angle.

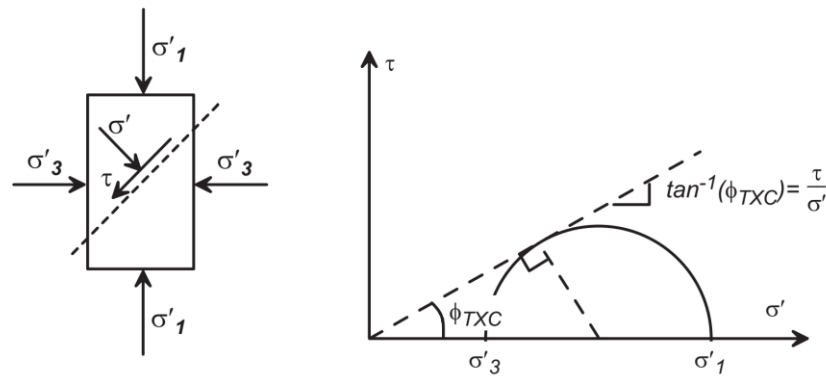


Figure 6.2 : Schematic of triaxial compression test for obtaining the size of yield surface.

By definition, the friction angle (φ_{TXC}) is expressed by:

$$\varphi_{TXC} = \tan^{-1} \left(\frac{\tau}{\sigma'} \right) \quad (6.13)$$

According to Figure 6.2 it can be written:

$$\sin(\varphi_{TXC}) = \frac{(\sigma'_1 - \sigma'_3)/2}{(\sigma'_1 + \sigma'_3)/2} \quad (6.14)$$

And,

$$\sigma'_1 = \sigma'_3 \frac{1 + \sin(\varphi_{TXC})}{1 - \sin(\varphi_{TXC})} \quad (6.15)$$

The advantage of a triaxial test is that the axial stress and radial stress are the principal stresses. Thus, the deviatoric stress (\tilde{s}) can be written as:

$$\begin{aligned} \tilde{s} = \tilde{\sigma}' - p' \tilde{I} &= \begin{bmatrix} \sigma'_1 & 0 & 0 \\ 0 & \sigma'_3 & 0 \\ 0 & 0 & \sigma'_3 \end{bmatrix} - \begin{bmatrix} p' & 0 & 0 \\ 0 & p' & 0 \\ 0 & 0 & p' \end{bmatrix} = \\ &= \frac{1}{3} \begin{bmatrix} 2(\sigma'_1 - \sigma'_3) & 0 & 0 \\ 0 & -(\sigma'_1 - \sigma'_3) & 0 \\ 0 & 0 & -(\sigma'_1 - \sigma'_3) \end{bmatrix} \end{aligned} \quad (6.16)$$

Therefore,

$$\tilde{s} : \tilde{s} = \frac{2}{3} (\sigma''_1 - \sigma'_3)^2 \quad (6.17)$$

According to Figure 6.3, depending on whether the vertical axis is τ_{oct} or q , the slope of the failure surface can be expressed by:

$$\begin{aligned} m_1 = \frac{\tau_{oct}}{p'} &= \frac{\frac{1}{\sqrt{3}} \sqrt{\tilde{s} : \tilde{s}}}{p'} = \frac{\frac{1}{\sqrt{3}} \frac{\sqrt{2}}{\sqrt{3}} (\sigma''_1 - \sigma'_3)}{\frac{(\sigma''_1 + 2\sigma'_3)}{3}} = \frac{\frac{\sqrt{2}}{3} \left(\frac{1 + \sin(\varphi_{TXC})}{1 + \sin(\varphi_{TXC})} - 1 \right) \sigma'_3}{\frac{(1 + \sin(\varphi_{TXC})) + 2}{3} \sigma'_3} \\ &= \frac{2\sqrt{2} \sin(\varphi_{TXC})}{3 - \sin(\varphi_{TXC})} \end{aligned} \quad (6.18)$$

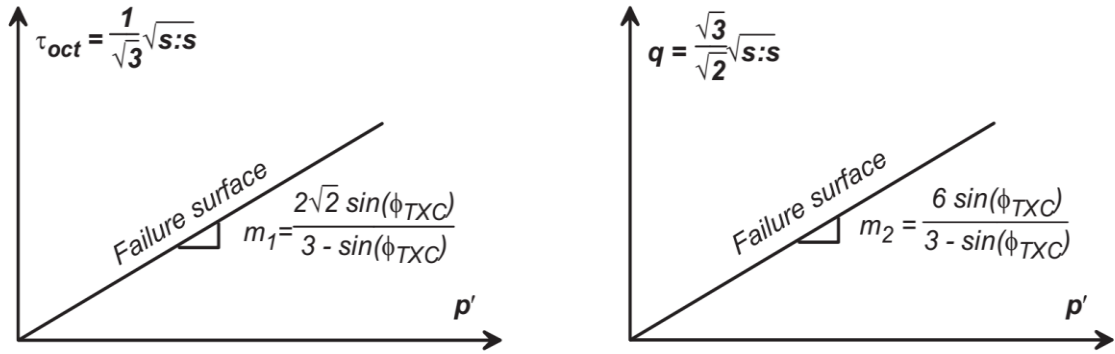


Figure 6.3 : Various definitions of shear strain.

Or,

$$m_2 = \frac{q}{p'} = \frac{\frac{3}{\sqrt{2}}\tau_{oct}}{p'} = \frac{6 \sin(\varphi_{TXC})}{3 - \sin(\varphi_{TXC})} \quad (6.19)$$

Solving (xw.xw) for φ_{TXC} results in:

$$\varphi_{TXC} = \frac{3m_1}{2\sqrt{2} + m_1} = \frac{3 \frac{\tau_{oct}}{p'}}{2\sqrt{2} + \frac{\tau_{oct}}{p'}} \quad (6.20)$$

6.1.3 Difference Between Triaxial Compression Friction Angles (φ_{TXC}) and Direct Simple Shear Friction Angle (φ_{DSS})

The friction angle obtained from triaxial compression test is different from direct simple shear test.

The friction angle which is derived from direct simple shear test (φ_{DSS}) is computed on horizontal plane which is not the maximum shear plane. Therefore, the direct simple shear test friction angle (φ_{DSS}) is less than actual friction angle which can be represented by φ_{TXC} in triaxial compression test. The relationship between direct simple shear test friction angle (φ_{DSS}) and triaxial compression test friction angle φ_{TXC} can be retrieved from eq xw.xw as:

$$\frac{\tau_{oct}}{p'} = \frac{2\sqrt{2}\sin(\varphi_{TXC})}{3 - \sin(\varphi_{TXC})} \quad (6.21)$$

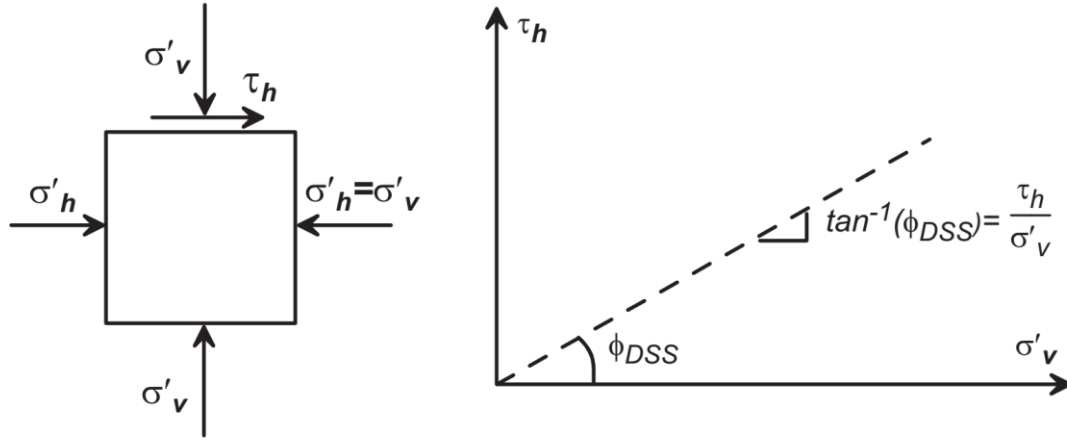


Figure 6.4 : Schematic of stresses and friction angle description in direct simple shear test (ϕ_{DSS}).

As it is illustrated in Figure 6.4, in direct simple shear test, where $K_0 = 1$ and $\sigma'_v = \sigma'_h$ it can be written:

$$\begin{aligned} \tau_{oct} &= \frac{1}{\sqrt{3}} \sqrt{\tilde{s} : \tilde{s}} \\ &= \frac{1}{3} \sqrt{(\sigma'_{11} - \sigma'_{22})^2 + (\sigma'_{22} - \sigma'_{33})^2 + (\sigma'_{11} - \sigma'_{33})^2 + 6\sigma_{12}^2 + 6\sigma_{13}^2 + 6\sigma_{23}^2} \\ &= \frac{\sqrt{6}}{3} \tau_h \end{aligned} \quad (6.22)$$

And,

$$p' = \frac{\sigma'_v + \sigma'_h + \sigma'_h}{3} = \sigma'_v \quad (6.23)$$

Therefore we get the followings:

$$\frac{\tau_{oct}}{p'} = \frac{\frac{\sqrt{6}}{3} \tau_h}{\sigma'_v} = \frac{\sqrt{6}}{3} \tan(\phi_{DSS}) = \frac{2\sqrt{2} \sin(\phi_{TXC})}{3 - \sin(\phi_{TXC})} \quad (6.24)$$

$$\phi_{DSS} = \tan^{-1} \left[\frac{2\sqrt{3} \sin(\phi_{TXC})}{3 - \sin(\phi_{TXC})} \right] \quad (6.25)$$

$$\phi_{TXC} = \sin^{-1} \left[\frac{3 \tan(\phi_{DSS})}{2\sqrt{3} + \tan(\phi_{DSS})} \right] \quad (6.26)$$

6.1.4 Deviatoric Stress-Strain Relationships

Deviatoric stress can be written as:

$$\tau_{oct} = \frac{1}{3} \sqrt{(\sigma'_{11} - \sigma'_{22})^2 + (\sigma'_{22} - \sigma'_{33})^2 + (\sigma'_{11} - \sigma'_{33})^2 + 6\sigma_{12}^2 + 6\sigma_{13}^2 + 6\sigma_{23}^2} \quad (6.27)$$

And the deviatoric strain can be expressed as:

$$\gamma_{oct} = \frac{2}{3} \sqrt{(\varepsilon_{11} - \varepsilon_{22})^2 + (\varepsilon_{22} - \varepsilon_{33})^2 + (\varepsilon_{11} - \varepsilon_{33})^2 + 6\varepsilon_{12}^2 + 6\varepsilon_{13}^2 + 6\varepsilon_{23}^2} \quad (6.28)$$

Where,

$$\varepsilon_{12} = \frac{1}{2} \gamma_{12} \quad (6.29)$$

As it is demonstrated in Figure 6.5, τ_{oct} and γ_{oct} backbone relationship for discretionary effective confining pressure p' can be described as follow:

- $G_{max,oct}$ represents the octahedral shear modulus at low strain and it is dependent on pressure:

$G_{max,oct} = G_{max,r,oct} \left(\frac{p'}{p'_r}\right)^d$, where $G_{max,r,oct}$ represents the octahedral shear modulus at low strain for the reference effective confining pressure (p') and can be calculated by:

$$G_{max,r,oct} = \left(\frac{3}{\sqrt{6}}\right) G_{max,\sigma'=1atm} = \left(\frac{3}{\sqrt{6}}\right) (\rho V_s^2) \quad (6.30)$$

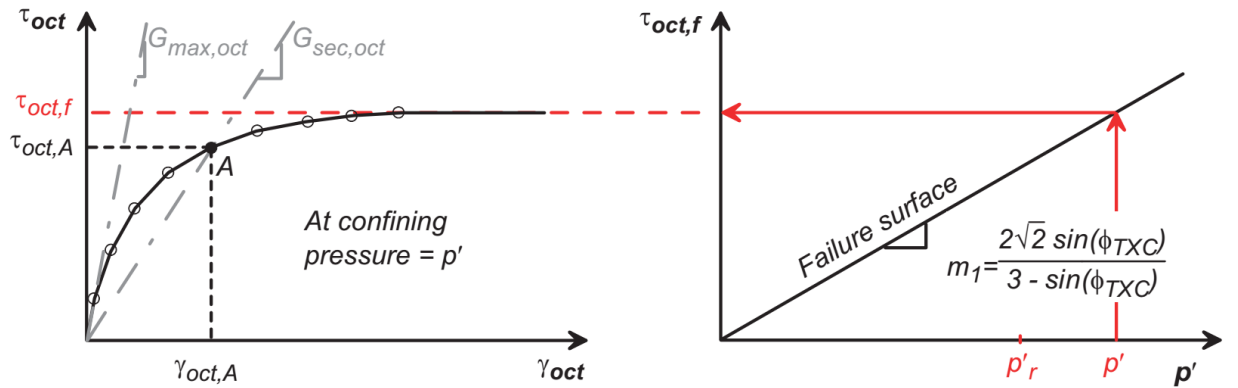


Figure 6.5 : Deviatoric octahedral backbone curve at effective confining pressure P' .

In this research, the constant d parameter assumed to be 0.5.

$$G_{max,r,oct} = f(K_o)G_{max,r} \quad (6.31)$$

Where,

$$G_{\max,r,\text{oct}} = \frac{\tau_{\text{oct}}}{\gamma_{\text{oct}}} \text{ and } G_{\max,r} = \frac{\tau_{12}}{\gamma_{12}} \quad (6.32)$$

When $K_0 \neq 1$, during anisotropic cyclic loading the K_0 approaching to 1, calibration can be done either to adjust the shear modulus at low-strain (when $K_0 \neq 1$), therefore, acquire more curvy backbone stress-strain relationship (i.e. G/G_{\max} curve shifted to the right; Figure 6.26 and Figure 6.27), or to do the calibration to obtained enhanced backbone curve stress-strain relationship.

$$\text{For } K_0 = 1 \text{ condition } G_{\max,r,\text{oct}} = \frac{\tau_{\text{oct}}}{\gamma_{\text{oct}}} = G_{\max,r} = \frac{\tau_{12}}{\gamma_{12}} \quad (6.33)$$

- The outmost (failure) yield surface which is related to the friction angle, can describe the maximum shear stress ($\tau_{\text{oct},f}$).
- The stress-strain relationship is also pressure dependent. For instance for point A in Figure 6.5, this relationship can be expressed as:

$$\tau_{\text{oct},A} = (G_{\text{sec.oct}})(\gamma_{\text{oct},A}) = \frac{G_{\max,r,\text{oct}}}{1 + \frac{\gamma_{\text{oct},A}}{\gamma_r} \left(\frac{p_r'}{p_r'}\right)^d} (\gamma_{\text{oct},A}) \quad (6.34)$$

Reference shear strain (γ_r) can be introduced within the constitutive model. It can be obtained by considering the stress-strain relationship at p_r' as demonstrated in Figure 6.6 γ_r is related to the highest shear stress and it can be written:

$$\tau_{\text{oct},r,f} = (G_{\text{sec},r,\text{oct}})(\gamma_{\max,r}) = \frac{G_{\max,r,\text{oct}}}{1 + \frac{\gamma_{\max,r}}{\gamma_r} \left(\frac{p_r'}{p_r'}\right)^d} (\gamma_{\max,r}) = \frac{2\sqrt{2}\sin(\varphi_{TXC})}{3 - \sin(\varphi_{TXC})} (p_r') \quad (6.35)$$

$\gamma_{\max,r}$ represents maximum shear strain. As it is illustrated in Figure 6.6, $\gamma_{\max,r}$ expresses the octahedral shear strain (at reference pressure p_r') at highest point in the backbone stress-strain curve.

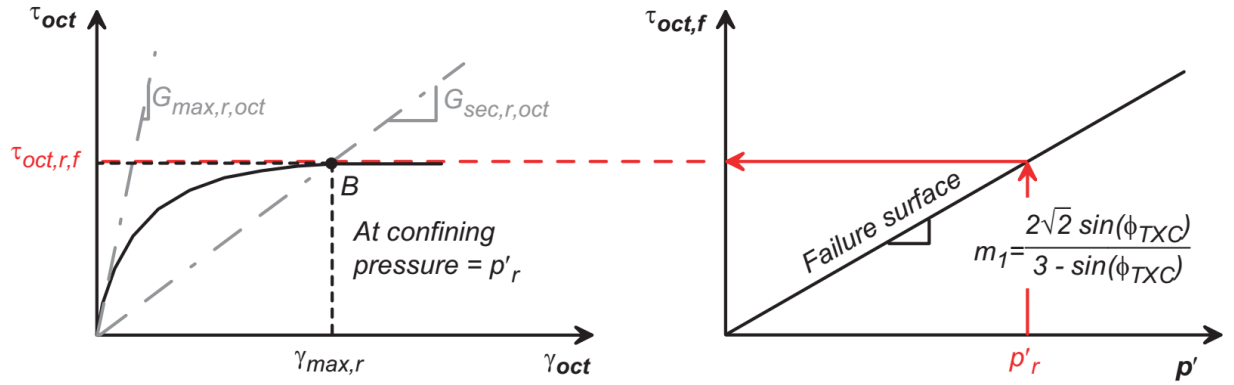


Figure 6.6 : Stress-strain relationship at reference pressure p'_r .

The effect of variation of $\gamma_{max,r}$ in monotonic direct simple shear loading is demonstrated in Figure 6.7. And γ_r obtained as follow:

$$\gamma_r = \frac{\tau_{oct,r,f} \gamma_{max,r}}{G_{max,r,oct} \gamma_{max,r} - \tau_{oct,r,f}} = \frac{\left[\frac{2\sqrt{2}\sin(\phi_{TXC})}{3 - \sin(\phi_{TXC})} p'_r \right] \gamma_{max,r}}{G_{max,r,oct} \gamma_{max,r} - \left[\frac{2\sqrt{2}\sin(\phi_{TXC})}{3 - \sin(\phi_{TXC})} p'_r \right]} \quad (6.36)$$

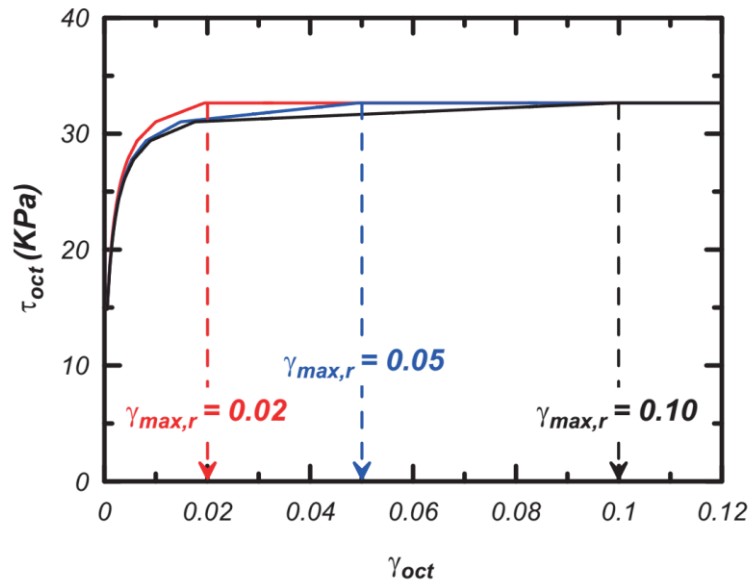


Figure 6.7 : Effect of $\gamma_{max,r}$ variation on stress-strain backbone curve

6.1.5 G/G_{max} Curves

The backbone stress-strain relationship can be acquired from the yield surfaces as it is demonstrated in Figure 6.8. Subsequently the G/G_{max} curve can be obtained from the

backbone stress-strain curve (Figure 6.9). It is important to know the difference between $G_{oct}/G_{max,oct}$ curve which is obtained from octahedral space and G/G_{max} curve which is commonly indicated in engineering practice (i.e. G/G_{max} curves from EPRI, 1993).

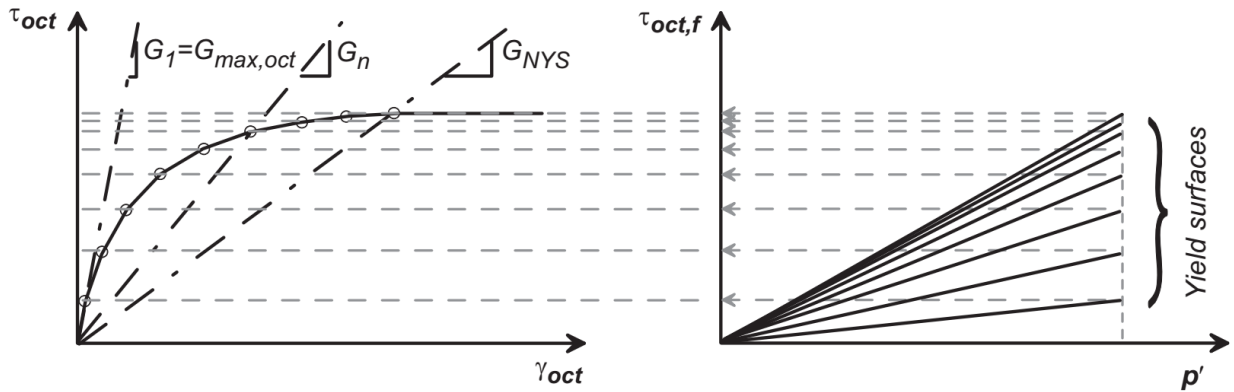


Figure 6.8 : Backbone stress-strain relationship retrieved from the yield surfaces.

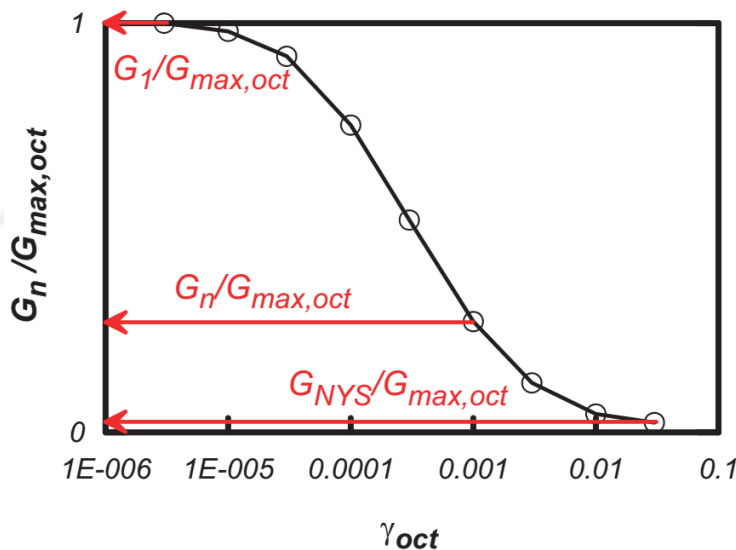


Figure 6.9 : G/G_{max} curve retrieved from the backbone stress-strain relationship curve.

The angles of yield surfaces are divided by constitutive model into identically scattered stresses. The G/G_{max} curve can also be described manually by constitutive model. The G/G_{max} curve is introduced as sets of G_{ratio} and γ_{12} . For each $G_{max,1,oct}G_{ratio}$ multiply by γ_{12} there should be corresponding τ_{12} at the referenced confining pressure (p_r'). Therefore, it is vital to pay attention that reasonable friction angle obtained from the given G/G_{max} curve and that the softening behavior does not occur due to backbone relationship of stress-strain. This can be achieved by conducting the reversed process

described previously in Figure 6.8 and Figure 6.9. The friction angle obtained from the last set of (G/G_{\max}) and (γ_{12}) can be written as:

$$\sin(\varphi) = \frac{3(\sqrt{3}\tau_{12,\max})/p'}{6 + (\sqrt{3}\tau_{12,\max})/p'} \quad (6.37)$$

And the last (G/G_{\max}) multiply by last (γ_{12}) is given $\tau_{12,\max}$.

If there is cohesion, the friction angle obtained can be written by:

$$\sin(\varphi) = \frac{3(\sqrt{3}\tau_{12,\max} - 2\text{cohesion})/p'}{6 + (\sqrt{3}\tau_{12,\max} - 2\text{cohesion})/p'} \quad (6.38)$$

In this research, the yield surfaces created by the constitutive model itself due to smoother response in various single element undrained cyclic test.

6.1.6 Flow Rule

The increments of plastic strain are consists of deviatoric and volumetric parts.

The deviatoric component of plastic strain act in accordance with associative flow rule, however the volumetric components of plastic strain following nonassociative rule. A vector normal to the yield surface (\tilde{Q}) and normal vector to the plastic potential (\tilde{P}) are described as deviatoric and volumetric constituents as follow:

- $\tilde{Q} = \tilde{Q}' + Q''\tilde{I}$ where \tilde{Q}' represents the deviatoric part, and $Q''\tilde{I}$ represents the volumetric part of the normal vector to the yield surface, and
- $\tilde{P} = \tilde{P}' + P''\tilde{I}$ Where \tilde{P}' denotes the deviatoric, and $P''\tilde{I}$ denotes the volumetric portion of the normal vector to the plastic potential.

Associative and non-associative flow rules are expressed as following:

- Associative flow rule is related to deviatoric phase by: $\tilde{P}' = \tilde{Q}'$
- Non-associative flow rule is related to volumetric phase by: $P'' \neq Q''$

Thus, normal vector to the plastic potential (\tilde{P}') can be described by vector normal to the yield surface (\tilde{Q}) which is related to the yield surface (associative flow rule). P'' , however, is not expressed by the yield surface (nonassociative flow rule). However, it can be expressed through phase transformation (PT) concept by equations cvn.cvn and cwn.cwn. The non-associative flow rule enables the constitutive model to capture “contractive” and “dilative” response of soil appropriately. Figure 6.10 illustrated the

difference between dilation phase and contraction phase in accordance with the existing stress state (whether within or outside of the phase transformation surface).

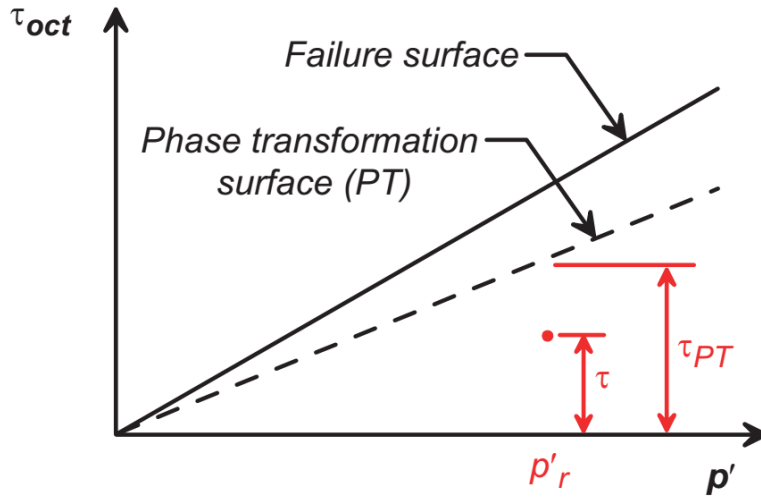


Figure 6.10 : Yield surface and Phase transformation surface (PT).

Equations for dilation and contraction induced volumetric components of plastic strain (expressed by P''):

- Contraction $[(\tau < \tau_{PT}) \text{ or } (\tau > \tau_{PT} \text{ and } \dot{\tau} < 0)]$

$$P'' = - \left(1 - \frac{\tau}{\tau_{PT}}\right)^2 (c_1 + \varepsilon_c c_2) \left(\frac{p' + p'_0}{p_{atm}}\right)^{c_3} \quad (6.39)$$

Where, c_1 , c_2 , and c_3 are model input parameters. Accumulative volumetric strain (denoted by ε_c) is a positive scalar that increases in dilation state and decreases in contraction state. The expression $\varepsilon_c c_2$ is a factor to capture fabric damage, i.e. large dilation causes larger contraction rate in the upcoming unloading.

- Dilation $[\tau > \tau_{PT} \text{ and } \dot{\tau} > 0]$

$$P'' = \left(\frac{\tau}{\tau_{PT}} - 1\right)^2 (d_1 + \gamma_d d_2) \left(\frac{p' + p'_0}{p_{atm}}\right)^{-d_3} \quad (6.40)$$

Where, d_1 , d_2 , and d_3 are the model input parameters. γ_d represents the accumulative octahedral shear strain increments from the onset of that specific dilation cycle.

Therefore, dilation increment increases as shear strain increases in that specific cycle.

Parameter d_3 and parameter c_3 govern the effect of overburden pressure (effect of K_σ).

Figure 6.11 shows the effect of different parameter c_1 on the contraction variation.

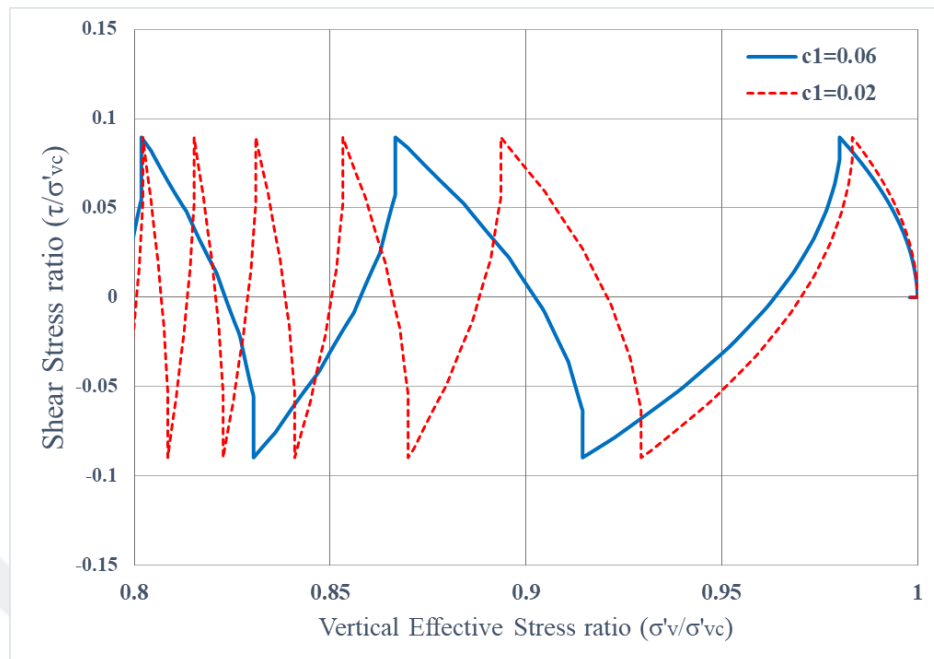


Figure 6.11 : Contraction response due to variation of input parameter c_1 .

Larger contraction means increase in the pore water pressure generation while vertical effective stress decreases more. The influence of second contraction coefficient (c_2) on the contraction variation is illustrated in Figure 6.12.

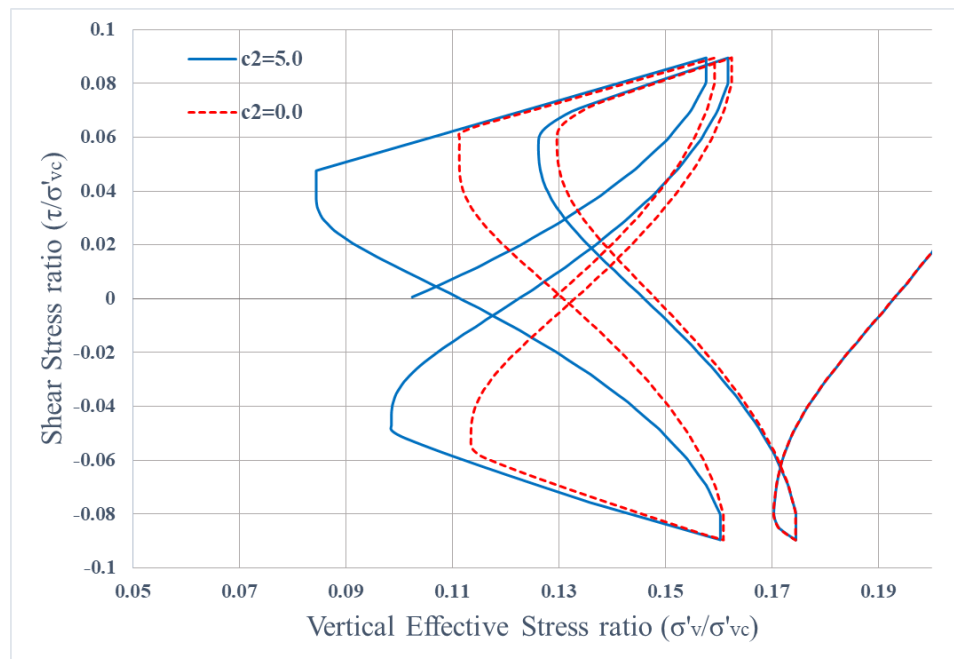


Figure 6.12 : Contraction state response due to variation of input parameter c_2 .

As it is shown in Figure 6.12, after the first dilation and if the fabric damage expression ($\epsilon_c c_2$) is triggered, the accumulative volumetric strain (ϵ_c) start to increase and soil for the next reloading shows more contraction response.

A value 5.0 is recommended for parameter c_2 . It also expresses how zero vertical effective stress is approachable after first butterfly relationship loop establishment. Larger value for parameter c_2 causes butterfly nature of the loop approaches to zero vertical effective ratio after the first loop.

Figure 6.13 shows the variation of overburden pressure (K_σ effect) and parameter c_3 for contraction behavior. The undrained cyclic direct simple shear loading responses for 100 kPa and 400 kPa initial vertical stresses are demonstrated in Figure 6.13 for when effect of overburden pressure is activated (i.e. $c_3 \neq 0.0$).

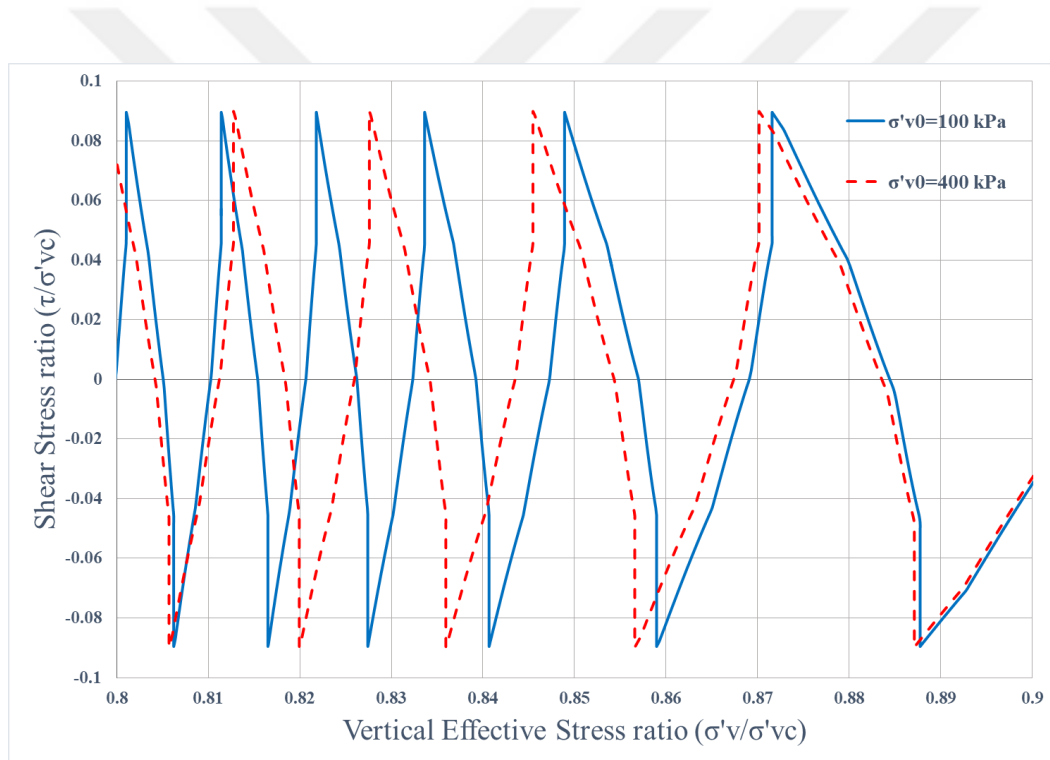


Figure 6.13 : Contraction behavior due to overburden stress (K_σ effect) and input parameter c_3 variation.

If the parameter c_3 is not zero, the expression $\left(\frac{p'+p_0'}{p_{atm}}\right)^{c_3}$ causes more contraction behavior for $\left(\frac{p'+p_0'}{p_{atm}}\right) > 1$ (where demonstrated in Figure 6.13), however for $\left(\frac{p'+p_0'}{p_{atm}}\right) < 1$ contraction behavior is reduced.

The impact of parameter d_1 variation can be evaluated in stress-strain relationship after the dilation state starts (as it is shown in Figure 6.14).

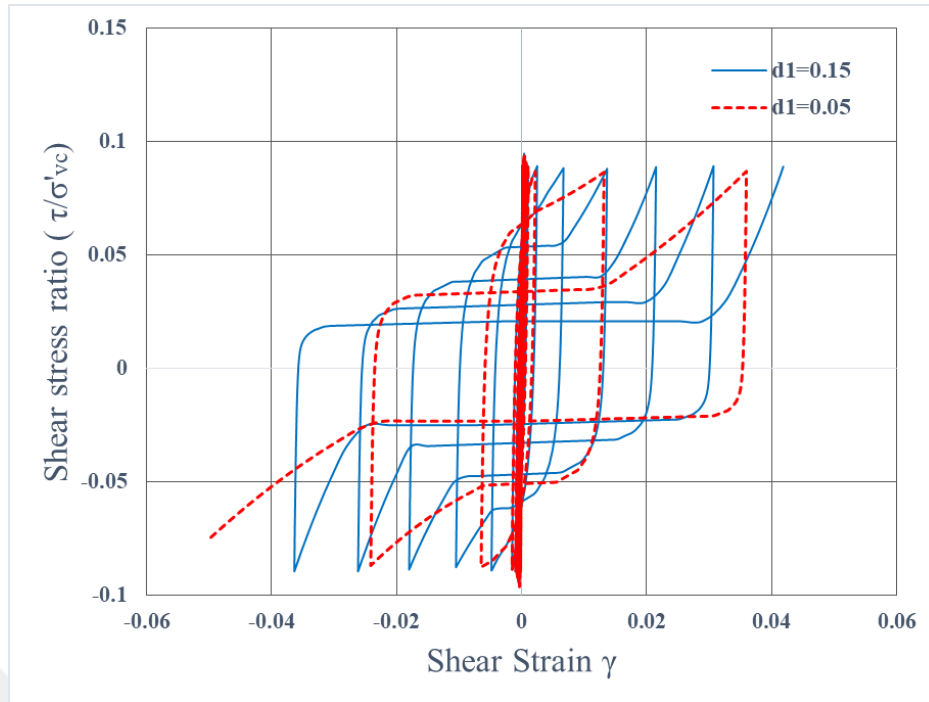


Figure 6.14 : Dilation response due to variation of input parameter d_1 .

When the dilation phase starts, it is followed by the decreasing in effective stress and the shear stress-vertical effective stress curve has a form like eight shape. Decreasing parameter d_1 causes reduction in the dilation behavior and therefore escalates the shear strain accumulation in each cycle. When the dilation started by modifying the parameter d_1 , the shear strain accumulation can be modified to be around 1% to 2%. The effects of parameter d_2 variation is demonstrated on Figure 6.15. The expression $\gamma_d^{d_2}$ in equation cwn.cwn is to capture fabric damage. To study the effects of this parameter, as it was described before γ_d represents the accumulative octahedral shear strain increments from the onset of that specific dilation cycle. Thus, accumulative octahedral shear strain increment (γ_d) is typically a small number, less than unity, in practice. Therefore, variation of d_2 parameter from 3.0 to 0.3, in the range of γ_d less than 1, causes expression $\gamma_d^{d_2}$ to increase and as a result a larger dilation response.

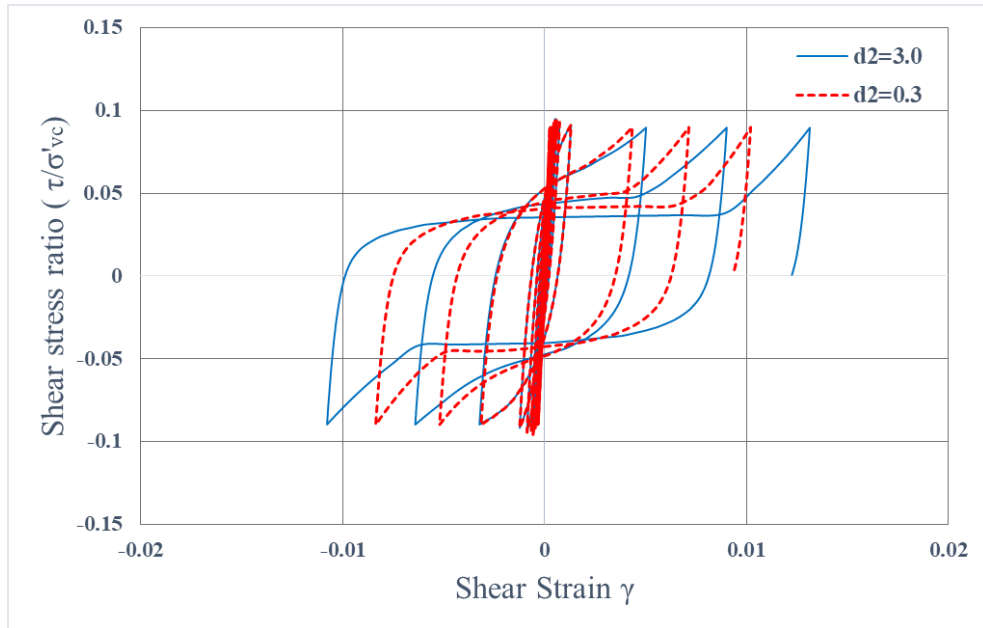


Figure 6.15 : Dilation response due to variation of input parameter d_2 .

As it is illustrated in Figure 6.15, larger dilation causes less accumulative octahedral shear strain increments in each cycle. It should further be noted that setting $d_2=0$ working vice versa as it causes $\gamma_d^{d_2}$ to be equal to unity, which is larger than common value of $\gamma_d^{d_2}$ when $d_2 \neq 0$. Parameter d_2 is suggested to be 3.0.

The effect of overburden pressure (K_σ) by d_3 parameter in the dilation phase of response is too complex depends on expression $\left(\frac{P'+P_0'}{P_{atm}}\right)$ which can be less than or above unity. Therefore, d_3 parameter is considered to be zero.

6.1.7 Constitutive Model Input Parameters

The calibration of constitutive model was carried out for different sands with different blow count of SPT test, $(N1)_{60}=5, 15, 25$ and 35. The calibrated values for parameters of PressureDependMultiYield02 model are presented in Table 6.1.

Different initial confining vertical pressures was considered to simulate soil behavior at different depths. The response of calibration data illustrated in Figures 6.16 to 6.25. The simulation results was compared with EPRI1993 recommended modulus reduction for sand. The result of calibrated parameters were in agreement with EPRI1993 recommended modulus reduction as shown in Figures 6.26 and 6.27.

Table 6.1 : Asymmetric Constitutive Model Input Parameters.

Parameter	Value				
(N1) 60	5	15	20	25	35
Dr%	0.33	0.57	0.63	0.74	0.87
Gs	2.65	2.65	2.65	2.65	2.65
emin	0.5	0.5	0.5	0.5	0.5
emax	0.89	0.89	0.89	0.89	0.89
e	0.76	0.67	0.63	0.6	0.55
ρ	1.94 ton/m ³	1.99 ton/m ³	2.00 ton/m ³	2.03 ton/m ³	2.06 ton/m ³
P'r	100 KPa	100 KPa	80 KPa	100 KPa	100 KPa
Vs1	141 m/s	174 m/s	185 m/s	195 m/s	210 m/s
Gmax,1	38.3 MPa	60.2 MPa	70.2 MPa	77.2 MPa	91.3 MPa
Gmax,1,oct	46.9 MPa	73.7 MPa	72.5 MPa	94.6 MPa	111.9 MPa
$\gamma_{max,r}$	0.1	0.1	0.1	0.1	0.1
K0	0.5	0.5	0.5	0.5	0.5
ν	0.33	0.33	0.33	0.33	0.33
B/G	2.67	2.67	2.67	2.67	2.67
Br	125.1 MPa	196.8 MPa	193.6 MPa	252.6 MPa	298.3 MPa
d	0.5	0.5	0.5	0.5	0.5
ϕ_{DSS}	30°	35°	38°	40°	45°
ϕ_{PDMY}	25.4°	30.3°	34.5°	35.8°	42.2°
ϕ_{PT}	20°	25.3°	26.5°	30.8°	32.2°
CRR1atm,3%	0.09	0.16	0.22	0.29	N.A.
c1	0.06	0.019	0.04	0.005	0.001
c2	5	3	2.5	1	0.5
c3	0.2	0.2	0.2	0.2	0
d1	0.15	0.15	0.07	0.15	0.4
d2	3	3	3	3	3
d3	0	0	0	0	0
liq1	1	1	1	1	1
liq2	0	0	0	0	0
NYS	20	20	20	20	20
cs1	0.9	0.9	0.9	0.9	0.9
cs2	0.02	0.02	0.02	0.02	0.02
cs3	0	0	0	0	0
cohesion	0.1	0.1	0.1	0.1	0.1

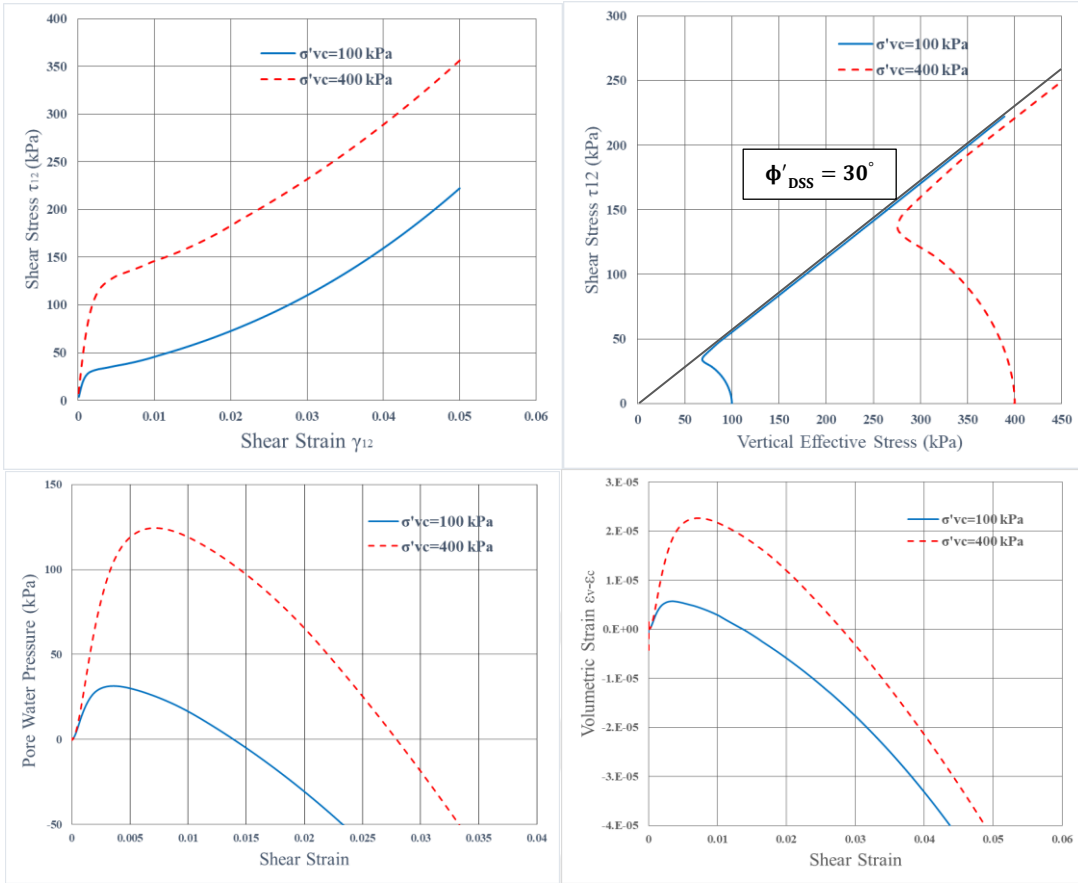


Figure 6.16 : Undrained monotonic direct simple shear test simulation response for blow count $(N_1)_{60}=5$ and vertical confining pressures $\sigma'_{vc} = 100$ and 400 KPa.

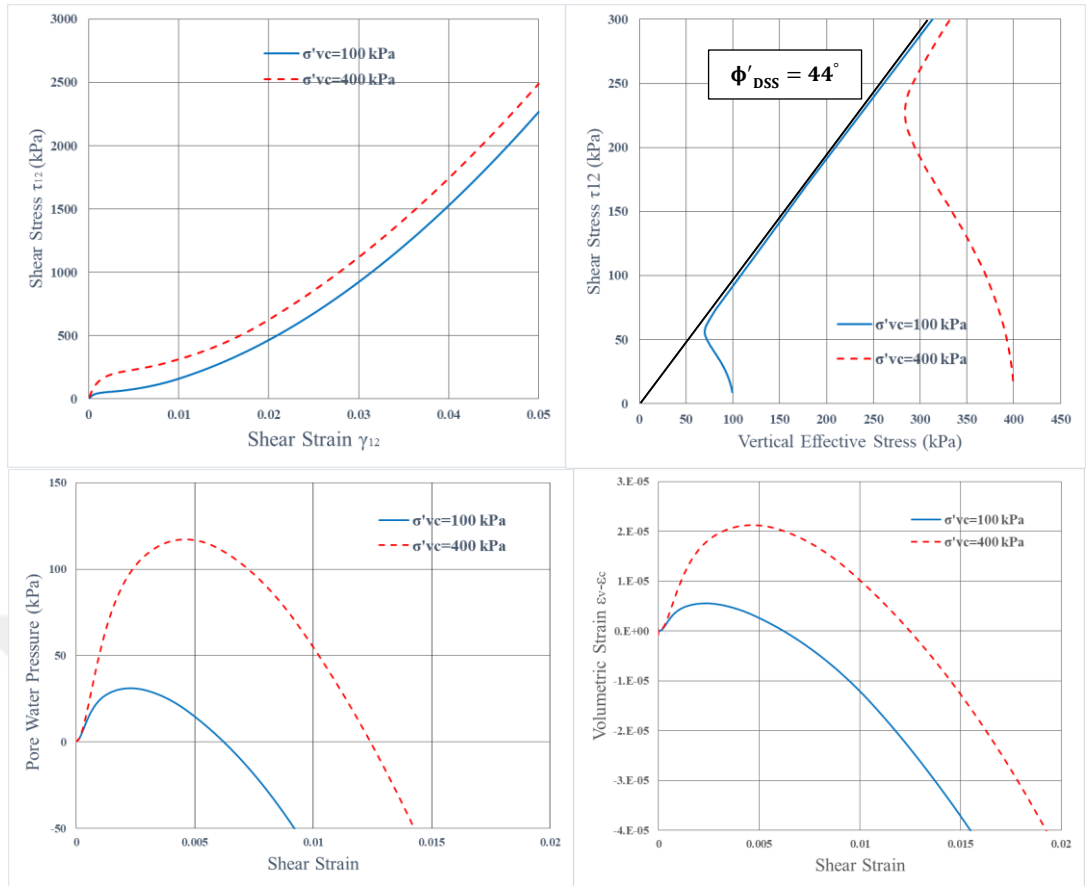


Figure 6.17 : Response of undrained monotonic direct simple shear test simulation for blow count $(N_1)_{60}=35$ and vertical confining pressures $\sigma'_{vc} = 100$ and 400 kPa.

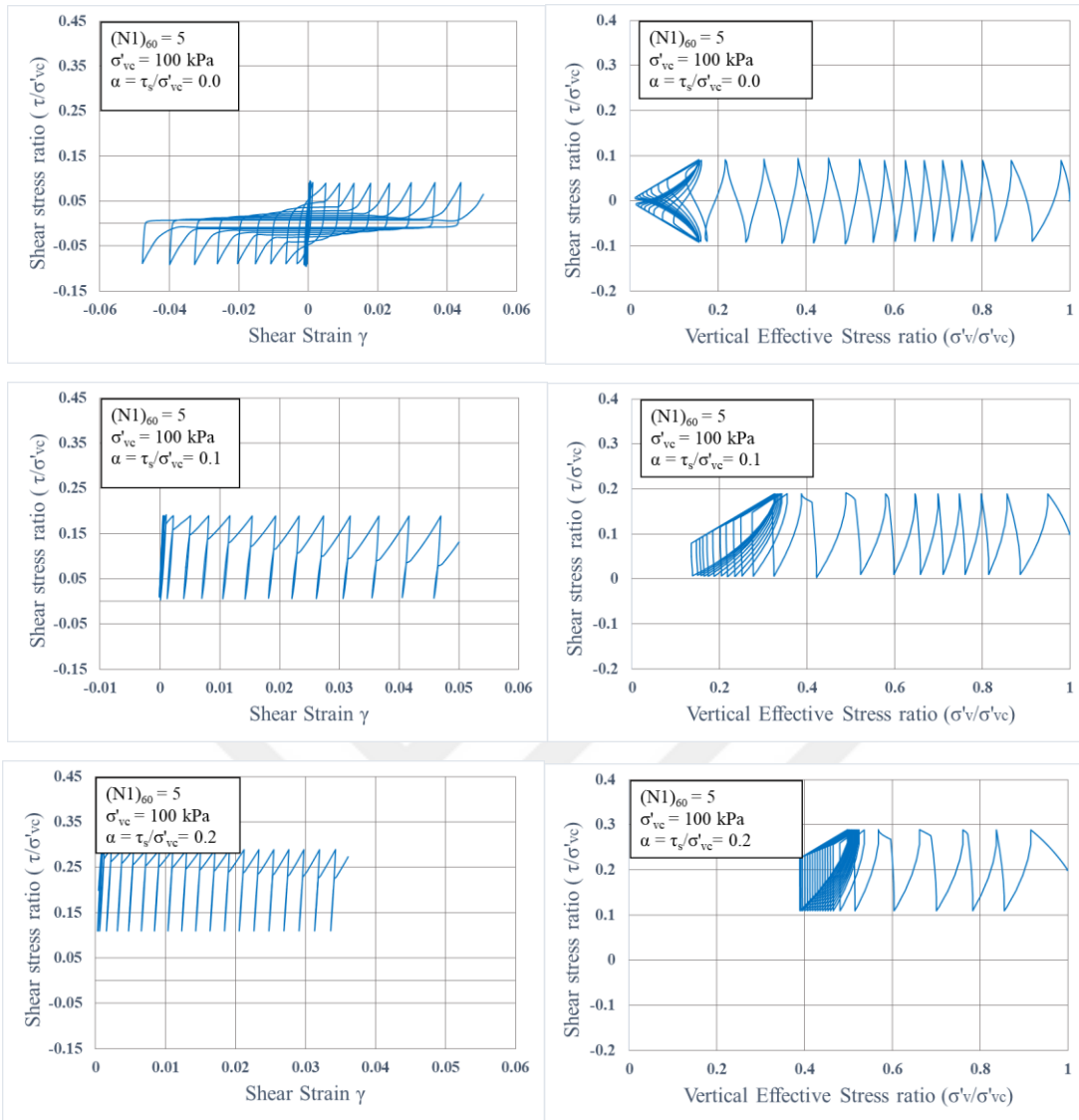


Figure 6.18 : Response of undrained cyclic direct simple shear simulation for blow count $(N1)_{60}=5$ and vertical confining pressure $\sigma'_{vc} = 100$ kPa and load bias $\alpha=0, 0.1, \text{ and } 0.2$.

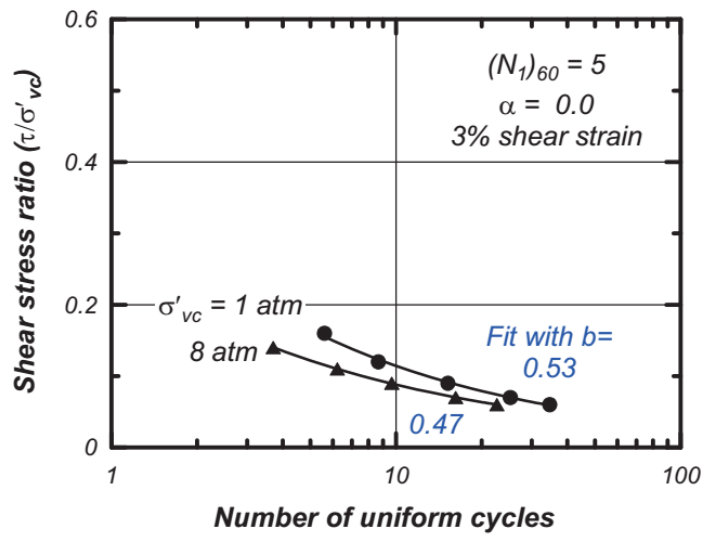


Figure 6.19 : Cyclic shear stress ratio versus number of cycles in direct simple shear test simulation for target single-amplitude shear strain of 3%, blow count $(N_1)_{60}=5$, vertical confining pressures $\sigma'_{vc} = 100$ and 800 KPa and load bias $\alpha=0.0$.

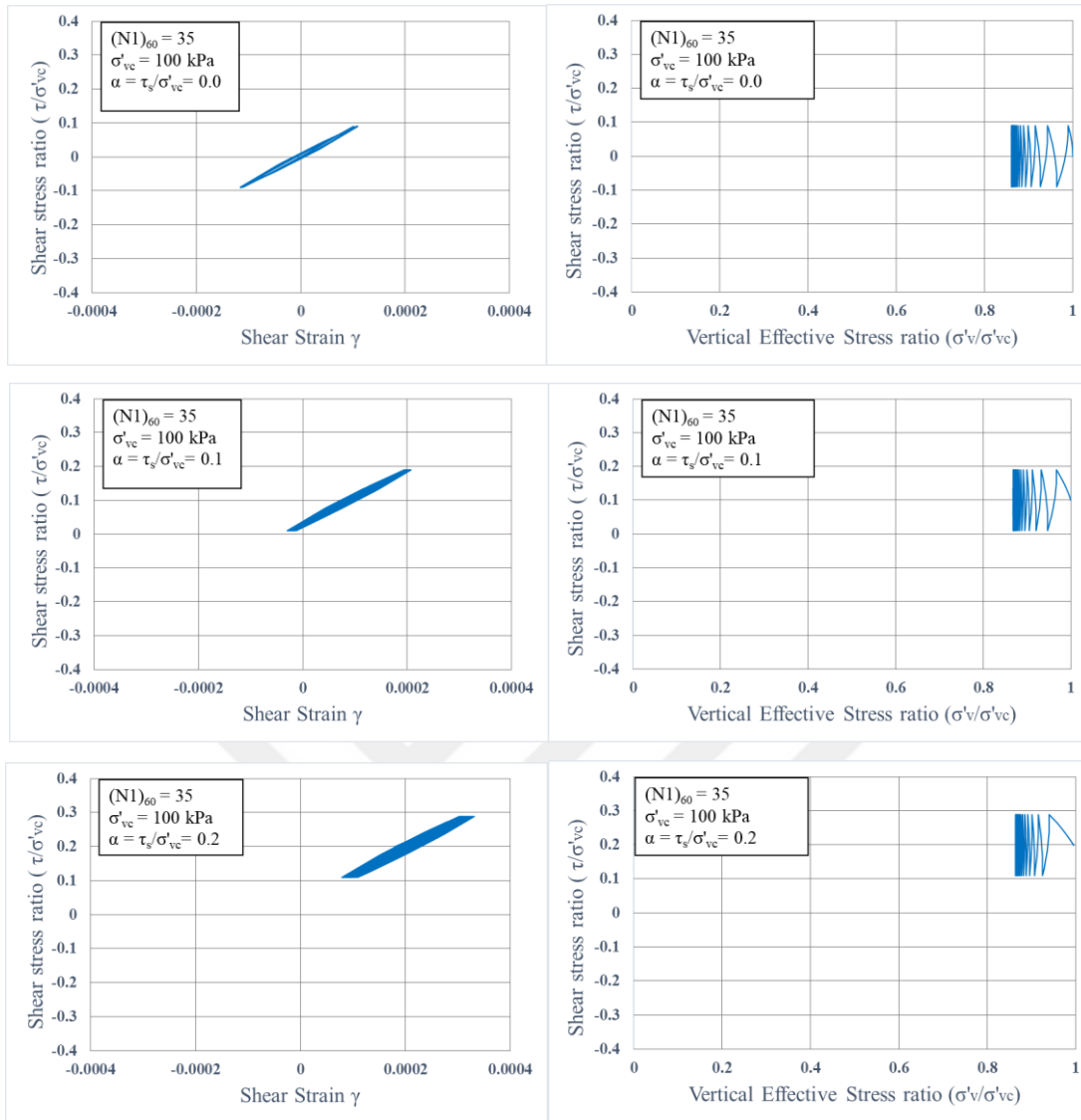


Figure 6.20 : Response of undrained cyclic direct simple shear test simulation for low count $(N1)_{60}=35$, vertical confining pressure $\sigma'_{vc} = 100$ KPa and load bias $\alpha=0.0, 0.1, \text{ and } 0.2$.

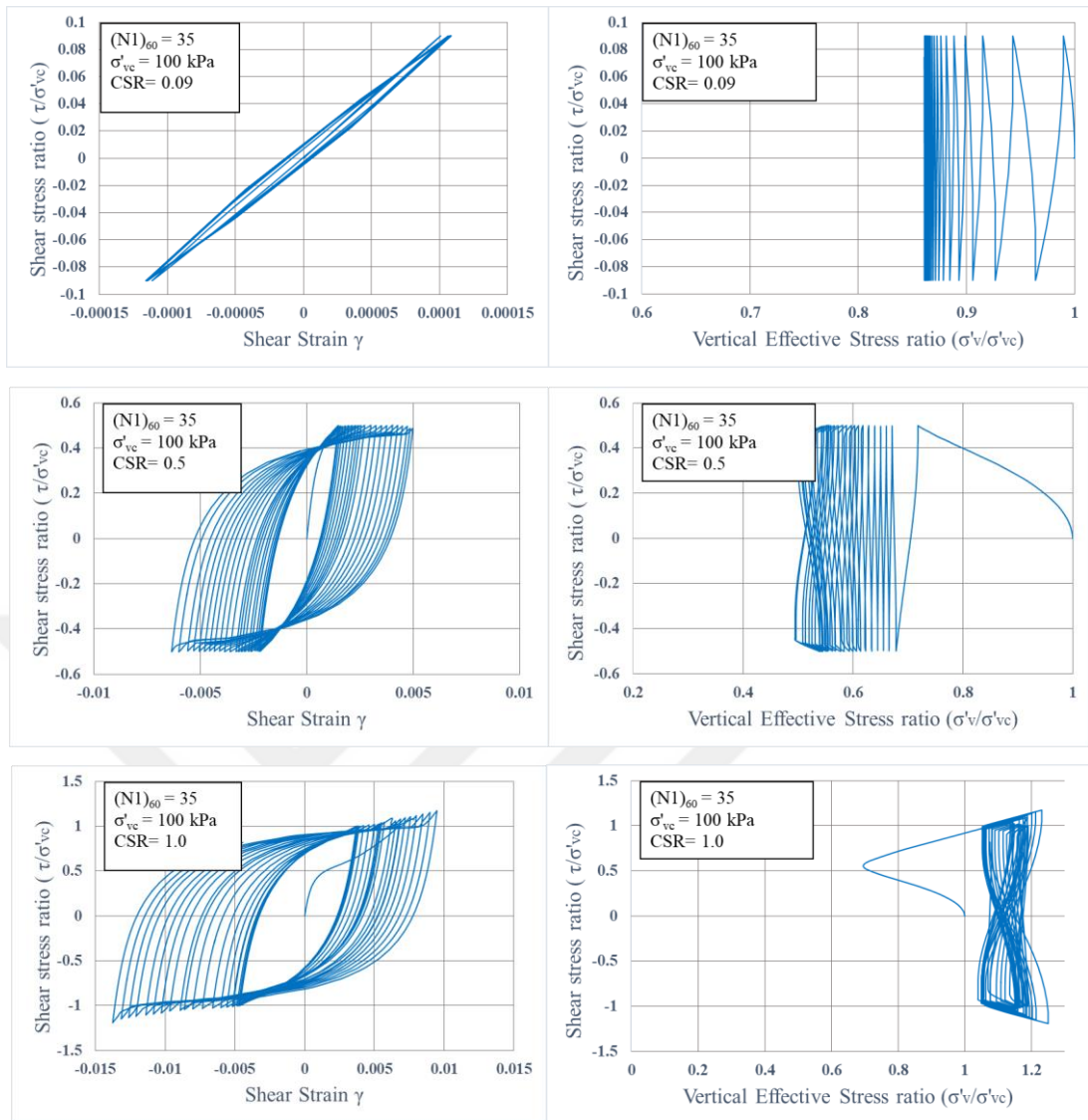


Figure 6.21 : Response of undrained cyclic direct simple shear test simulation for blow count $(N1)_{60}=35$ due to different cyclic stress ratios CSR = 0.09, 0.50, and 1.00.

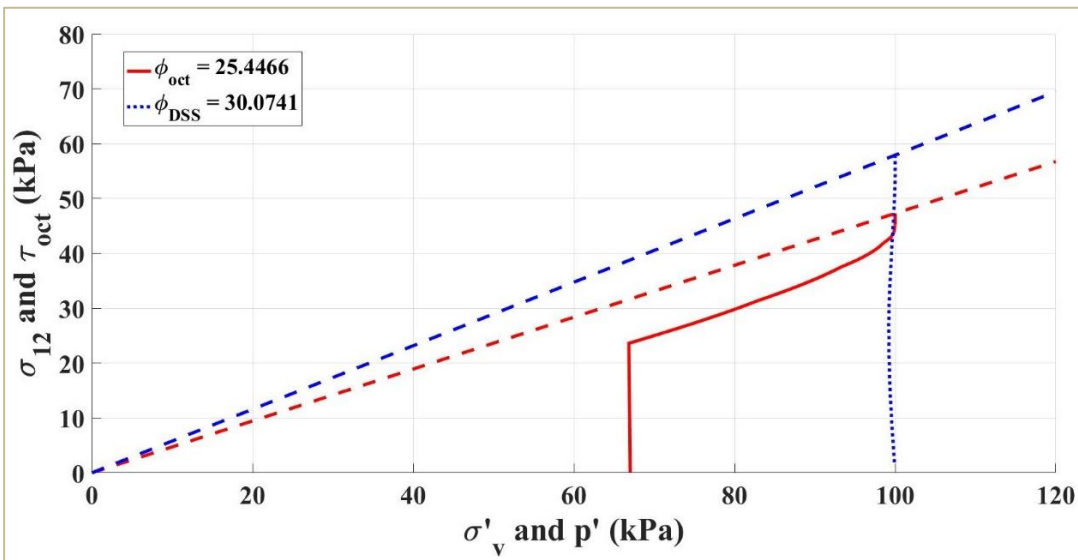
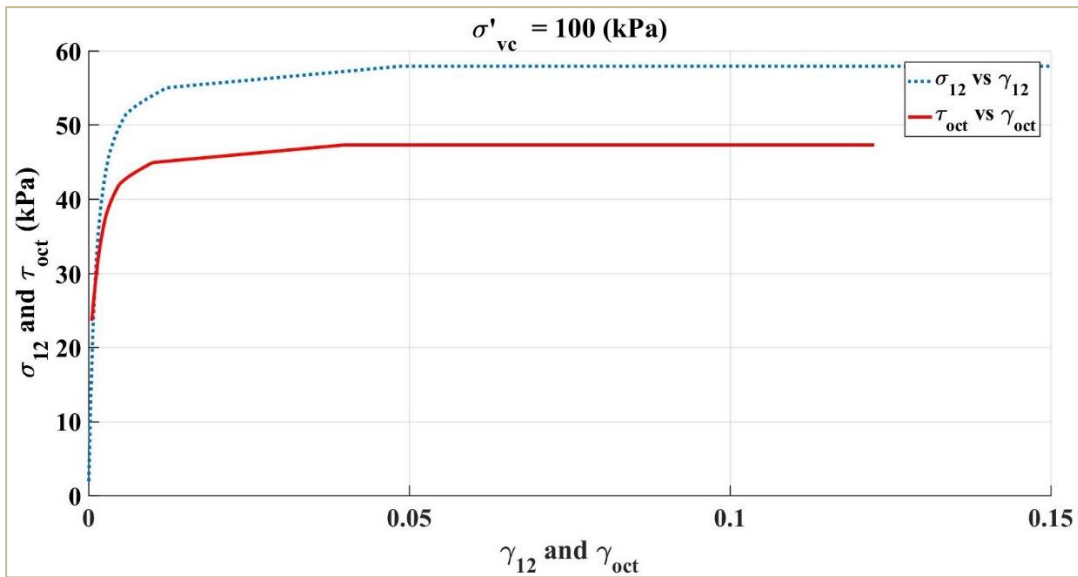


Figure 6.22 : Response of drained monotonic direct simple shear test simulation for blow count $(N_1)_{60}=5$ and vertical confining pressure $\sigma'_{vc} = 100$ KPa.

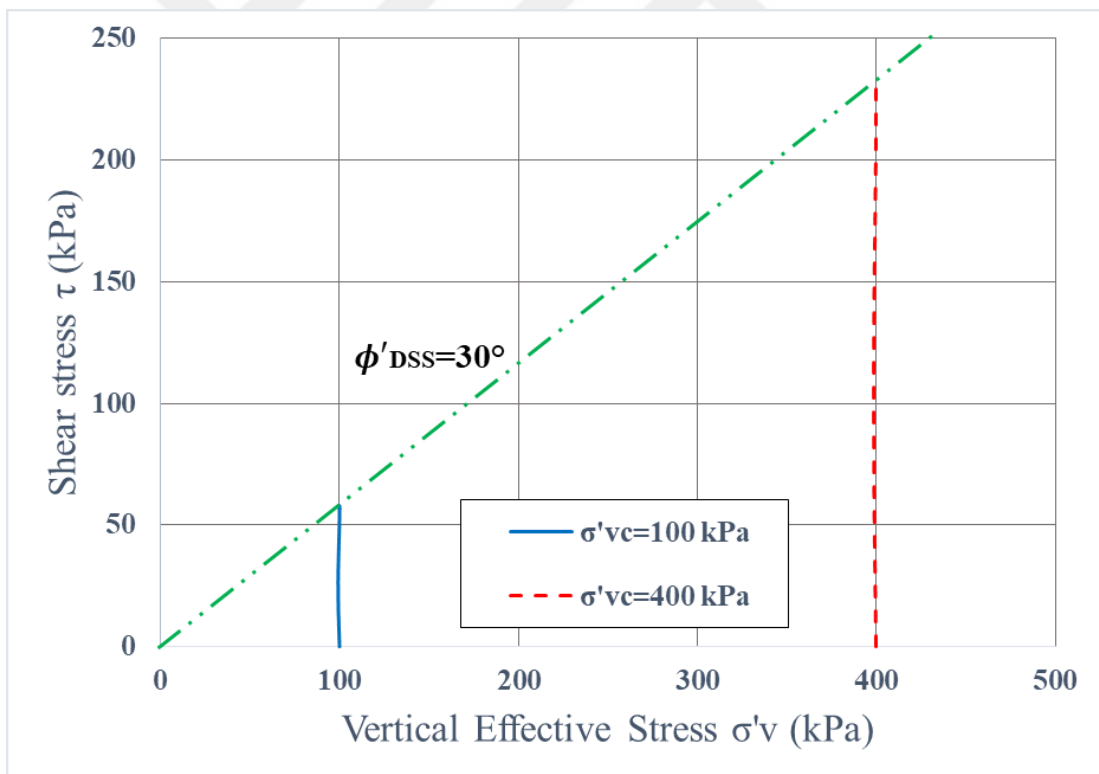
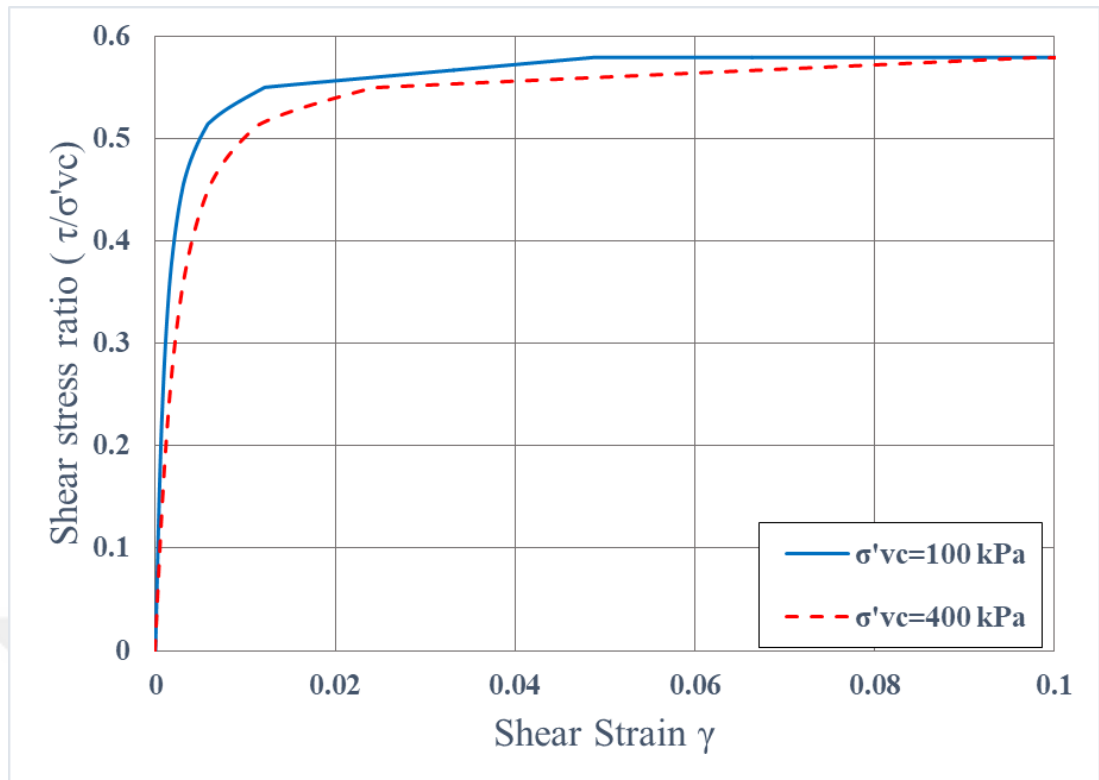


Figure 6.23 : Response of drained monotonic direct simple shear test simulation for blow count $(N_1)_{60}=5$ and vertical confining pressure $\sigma'_{vc} = 100$ and 400 KPa.

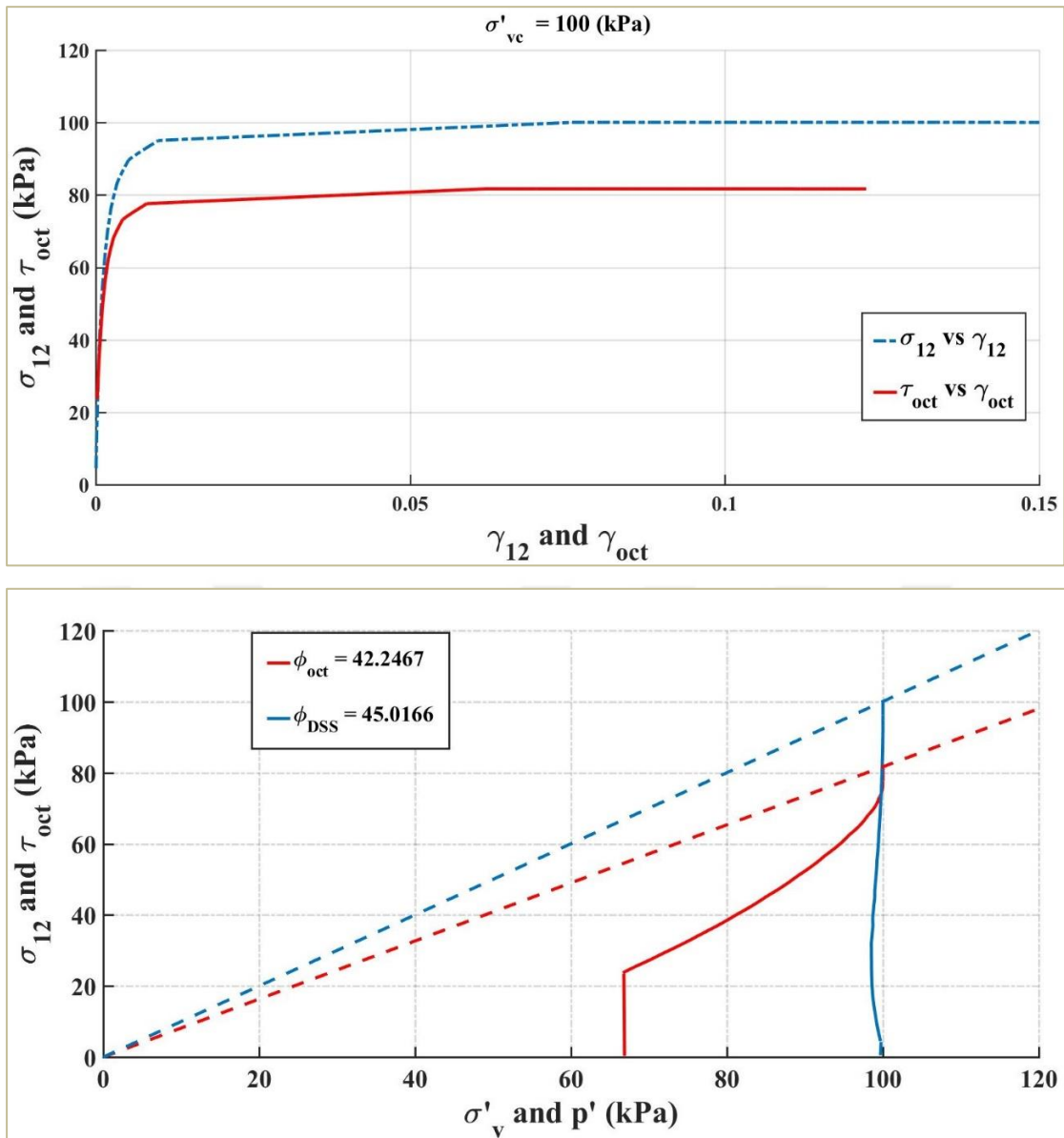


Figure 6.24 : Response of drained monotonic direct simple shear test simulation for blow count $(N_1)_{60}=35$ and vertical confining pressure $\sigma'_{vc} = 100$ KPa.

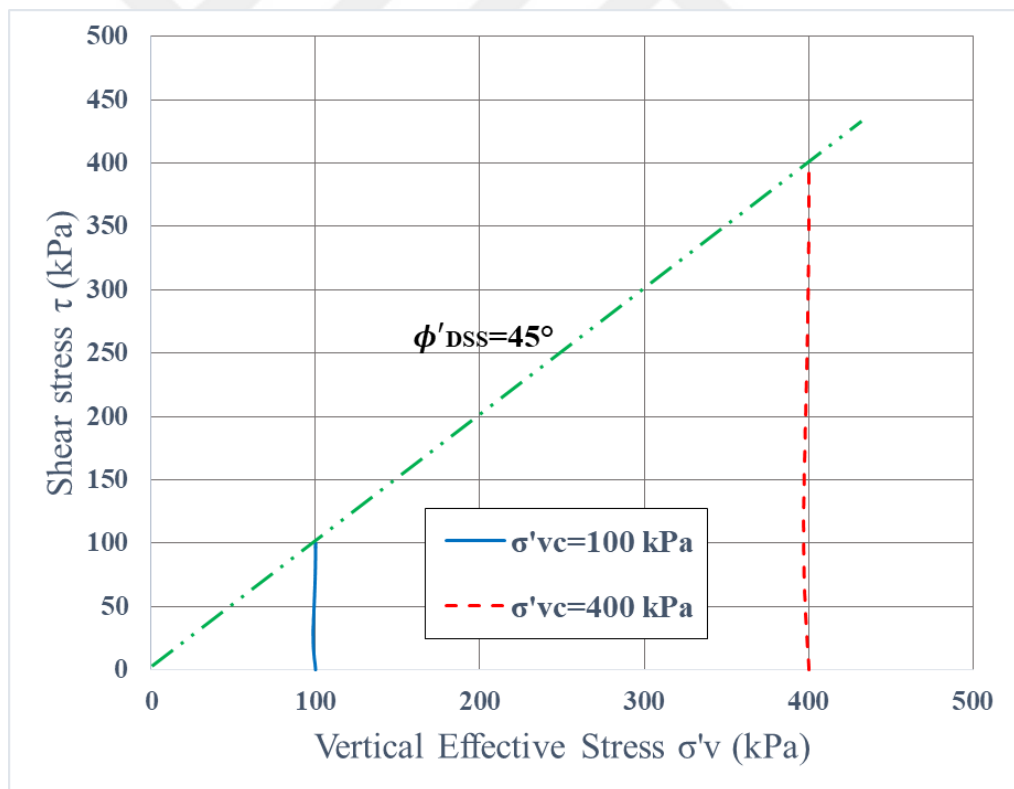
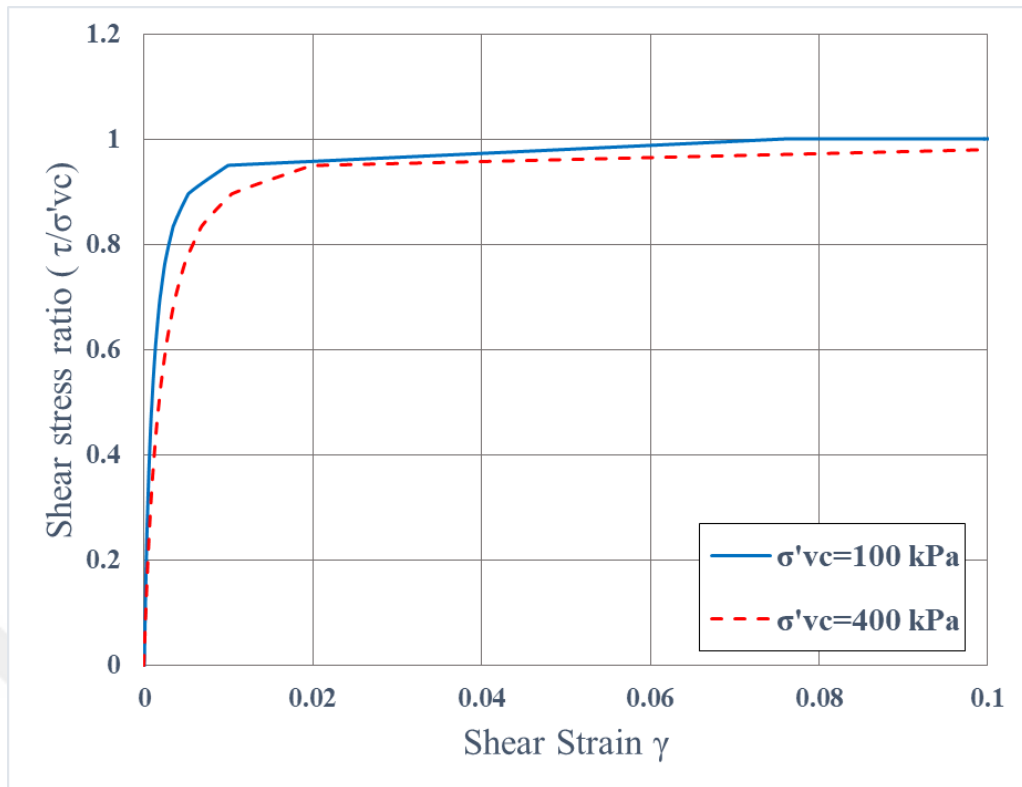


Figure 6.25 : Response of drained monotonic direct simple shear test simulation for blow count $(N_1)_{60}=35$ and vertical confining pressure $\sigma'_{vc} = 100$ and 400 KPa.

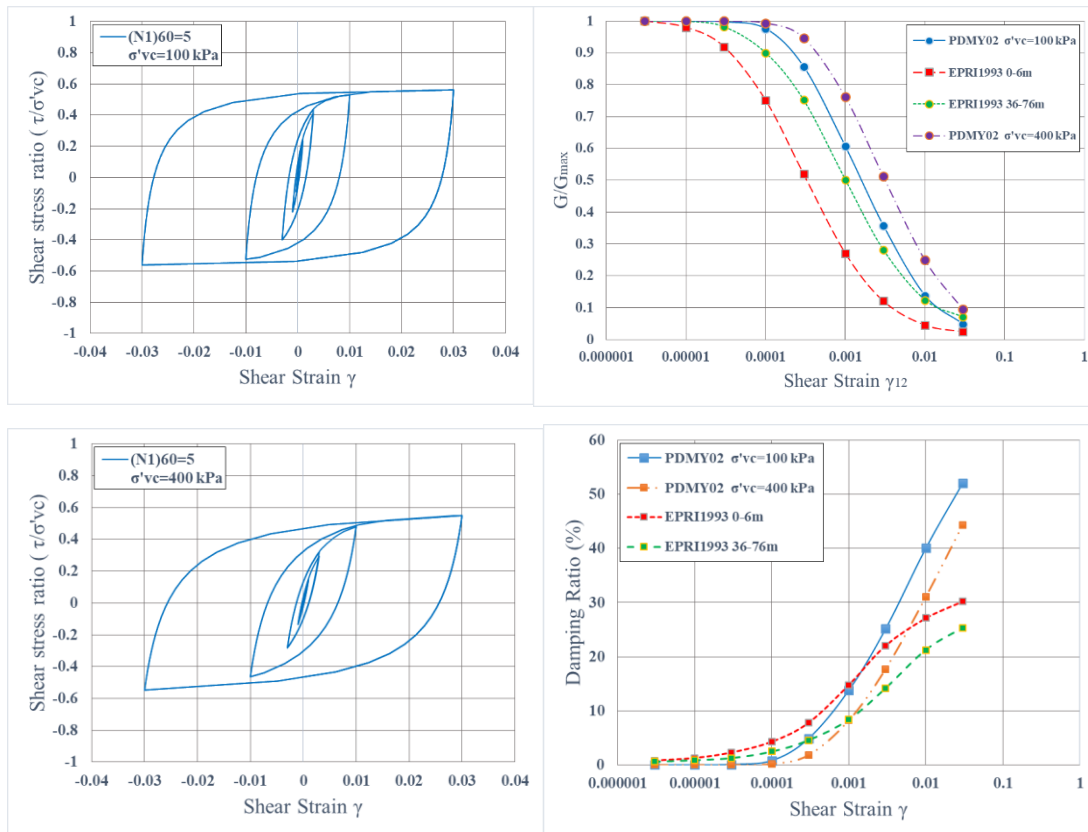


Figure 6.26 : Responses of drained strain-controlled cyclic direct simple shear test simulation for blow count $(N_1)_{60}=5$ and vertical confining pressure $\sigma'_{vc} = 100$ and 400 KPa.

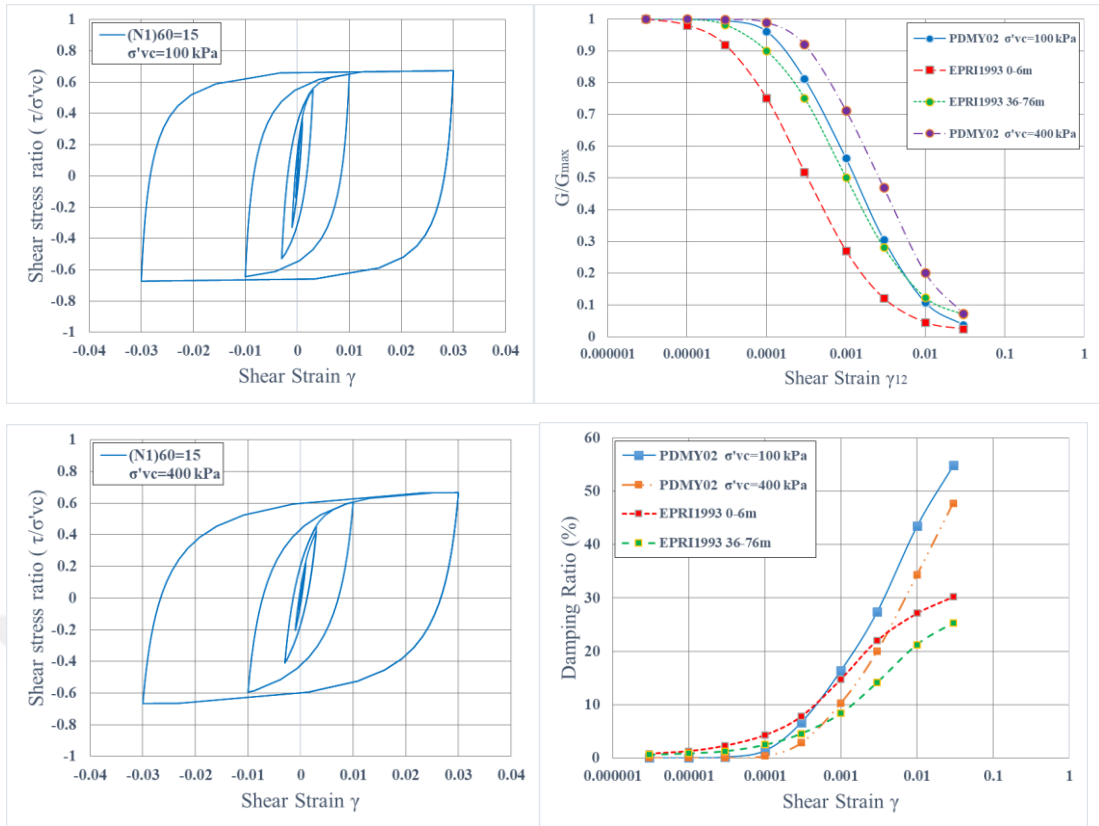


Figure 6.27 : Responses of drained strain-controlled cyclic direct simple shear test simulation for blow count $(N_1)_{60}=15$ and vertical confining pressure $\sigma'_{vc} = 100$ and 400 KPa.

6.1.8 Constitutive Model Input Parameters Validation Against Laboratory Direct Simple Shear Test Data

To evaluate the calibrated parameters and also validate the Opensees and Matlab codes for simulating direct simple shear test, the calibrated parameters for sand with relative density 63% were implemented as an input data for single element simulation of direct simple shear test in Opensees. The results of simulation compared with simple shear test data provided by Arulmoli et al, 1992 as cited by Karimi et al, 2015. The results of simulations are in good agreement with test data as illustrated in Figures 6.28, 6.29, 6.30 and 6.31.

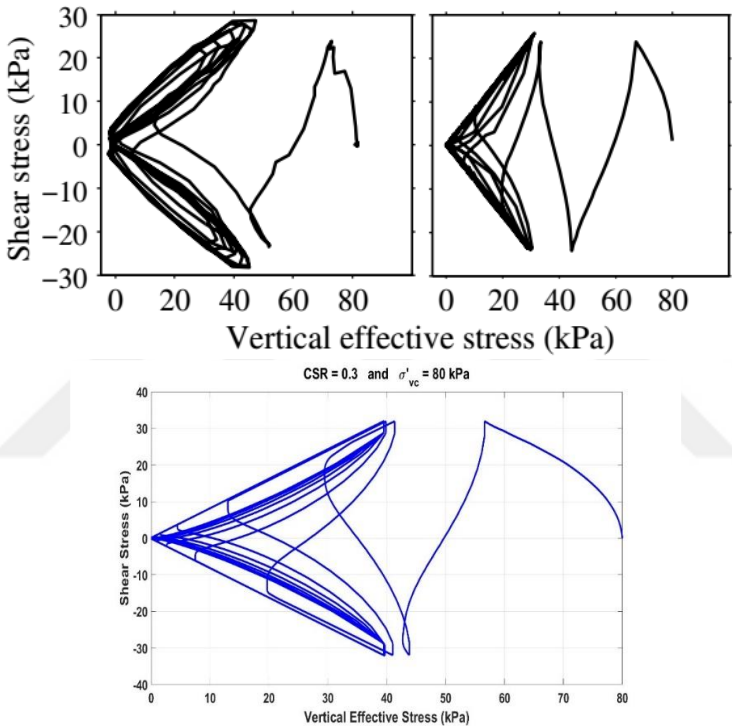


Figure 6.28 : Shear stress and vertical effective stress comparison of the numerically simulated (bottom) and experimentally measured soil response for undrained cyclic simple shear (CSS) test performed on Nevada sand by Arulmoli et al, 1992 (top left) as cited by Karimi et al, 2015 (top right). Test conditions: $D_r = 63\%$, $\sigma_{v0} = 80$ kPa, and $CSR = 0.3$

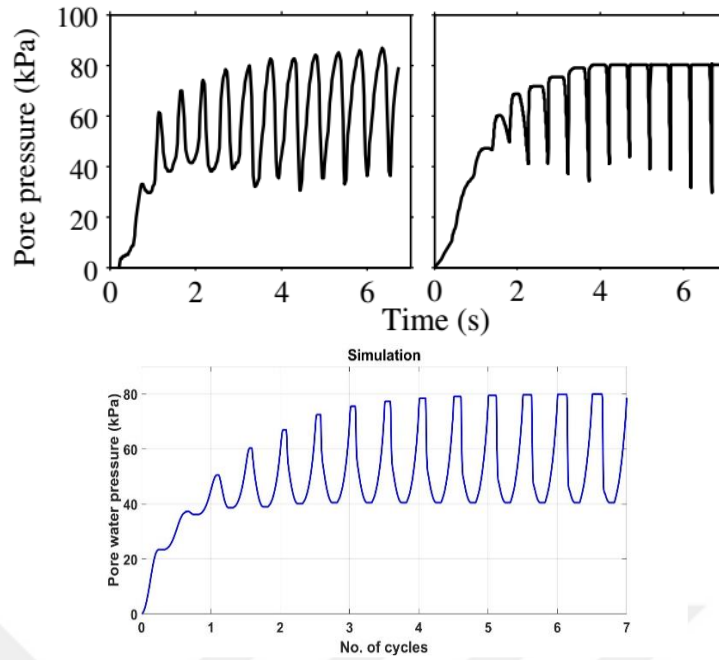


Figure 6.29 : Pore water pressure generation comparison of the numerically simulated (bottom) and experimentally measured soil response for undrained cyclic simple shear (CSS) test performed on Nevada sand by Arulmoli et al, 1992 (top left) as cited by Karimi et al, 2015 (top right). Test conditions: $D_r = 63\%$, $\sigma_v' = 80$ kPa, and $CSR = 0.3$

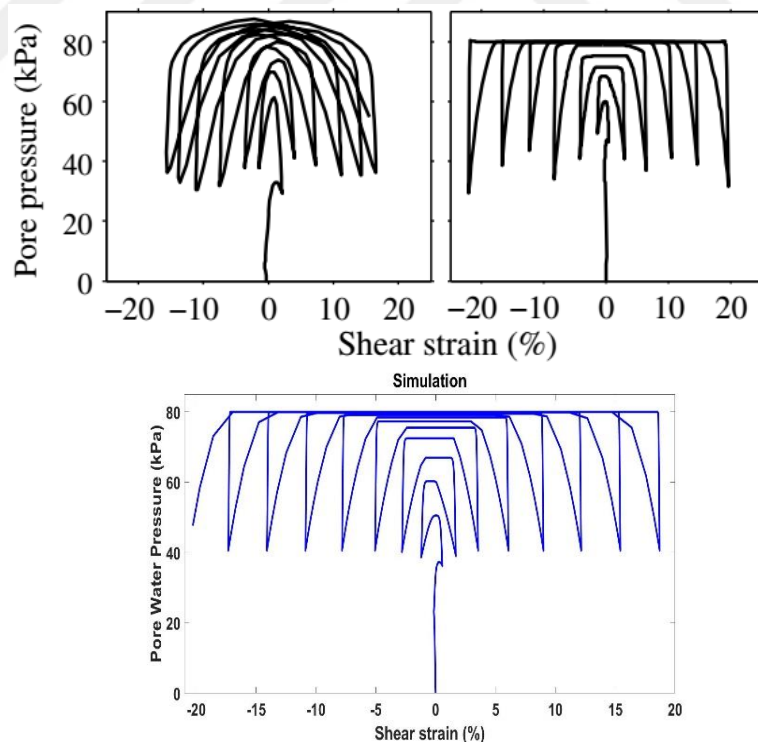


Figure 6.30 : Pore pressure versus shear strain comparison of the numerically simulated (bottom) and experimentally measured soil response for undrained cyclic simple shear (CSS) test performed on Nevada sand by Arulmoli et al, 1992 (top left) as cited by Karimi et al, 2015 (top right). Test conditions: $D_r = 63\%$, $\sigma_v' = 80$ kPa, and $CSR = 0.3$

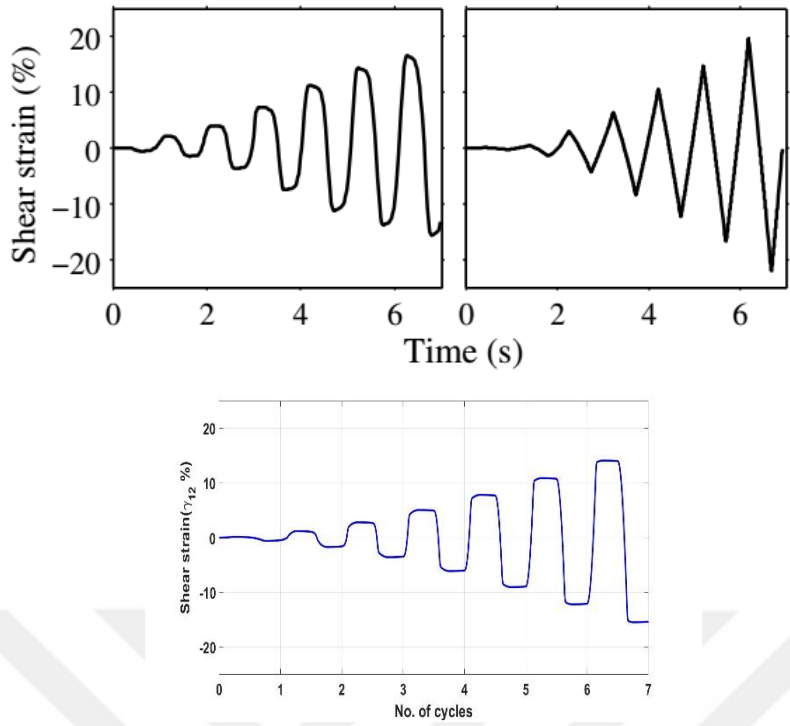


Figure 6.31 : Shear strain versus number of cycles comparison of the numerically simulated (bottom) and experimentally measured soil response for undrained cyclic simple shear (CSS) test performed on Nevada sand by Arulmoli et al, 1992 (top left) as cited by Karimi et al, 2015 (top right). Test conditions: $D_r = 63\%$, $\sigma_v0 = 80$ kPa, and $CSR = 0.3$

6.2 Finite Element Model Procedure for Nonlinear 2D Site Response

To evaluate the calibrated parameters for PDMY02 constitutive model a series of nonlinear 2D site response were conducted using nine-four nodes quadrilateral U-P plane strain element.

The nodes at the same level were tied together to constrain the deformation such as shear beam.

The downhole records for different depths were applied at the base of the model. In terms of using rock outcrop motion for nonlinear 2D site response , compliant boundary condition used at the base of the model which is implemented by using a dashpot with uniaxial viscous material at left lower corner of the model. As mentioned before, the coefficient of damper is defined as proposed by (Lysmer and Kuhlemeyer,1969) as follow:

$$c = AV_s\rho \quad (6.41)$$

Where, A is area of base, V_s is shear wave velocity of rock and ρ is density of elastic half-space at the base of the model.

The absorbent boundary condition absorbs the reflected wave propagating from surface to the bottom of the model acting as a viscous dashpot.

The input motion applied as a velocity history which is converted to force by dashpot coefficient. The force was equally applied to the base nodes by dividing it the number of base nodes.

$$F(t) = \tau_{xy} \cdot A \quad (6.42)$$

$$\tau_{xy} = V(t) \cdot V_s \cdot \rho \quad (6.43)$$

where $v(t)$ is velocity of the outcropped earthquake record.

Using viscous absorbent boundary condition together with velocity component of ground motion reduces the effect of high frequency noise within the soil profile.

Figure 6.32 represents Diagram of the finite element model with different boundary condition. Figure 6.32 (a) demonstrates compliant base boundary condition while Figure 6.32 (b) demonstrates rigid base boundary condition.

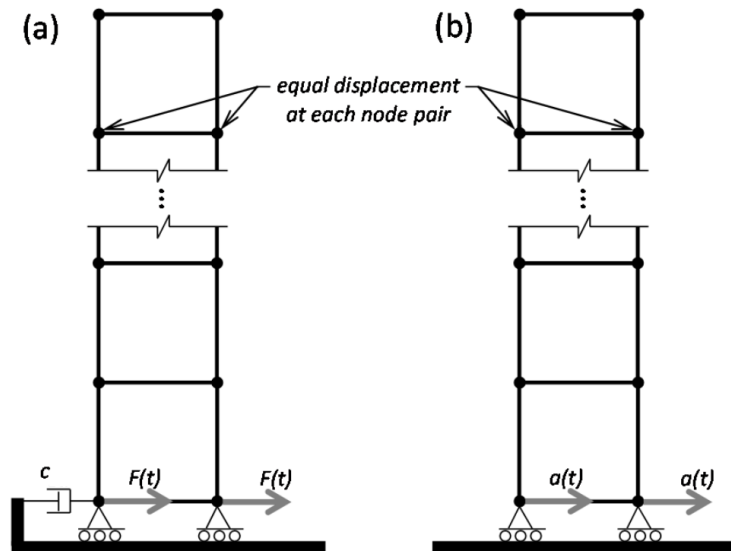


Figure 6.32 : Diagram of finite element model and boundary condition for (a) compliant base boundary condition ; (b) rigid base boundary condition.

PressureDependMultiYield and PressureIndependMultiYield constitutive models represent elastic behavior at very small strain without hysteretic behavior and corresponding damping.

6.3 Wildlife Array (WLA) Site Response Evaluation During 1987 Superstition Hills Earthquake

In 1982, United States Geological Survey (USGS) provided instruments in Wildlife array site near Salton sea 6 km away from Brawly,california. Superstition Hills earthquakes with magnitude 6.5M occurred on 24 November 1987 at Wildlife array site. During 2003 to 2004 extra instruments provided at site. Total of 24 CPT and 24 boring were provided. Extra 6 downhole array acelerometer, 3 ground level accelerometer, 8 piezometer also installed at site.

The profile of Wildlife array site involves 2.75m depth clay overlaying sand layer approximately 6.7m and then clay layer upto 12m depth. Below 12m depth the site profile consists silt, clay and sand extended to 32m depth.

The geotechnical data such as CPT resistance, number of blow counts for SPT test, shear wave velocity for the Wildlife array site are given in Figure 6.35.

For the clay from ground surface level to 2.75m depth and from 6.75 to 7.5m depth, the PressureIndependentMultiYield (PIMY) model was used with default G/Gmax vs. γ curve. For the sand layer from 2.75 to 6.75 m, the parameters for $D_r=57\%$ were used.it should be noted that a value of $y_1 = 0.5$ (instead of $y_1 = 1.0$) was selected since it created ground level response spectra and time histories that provided a somewhat better match to the recorded time histories.

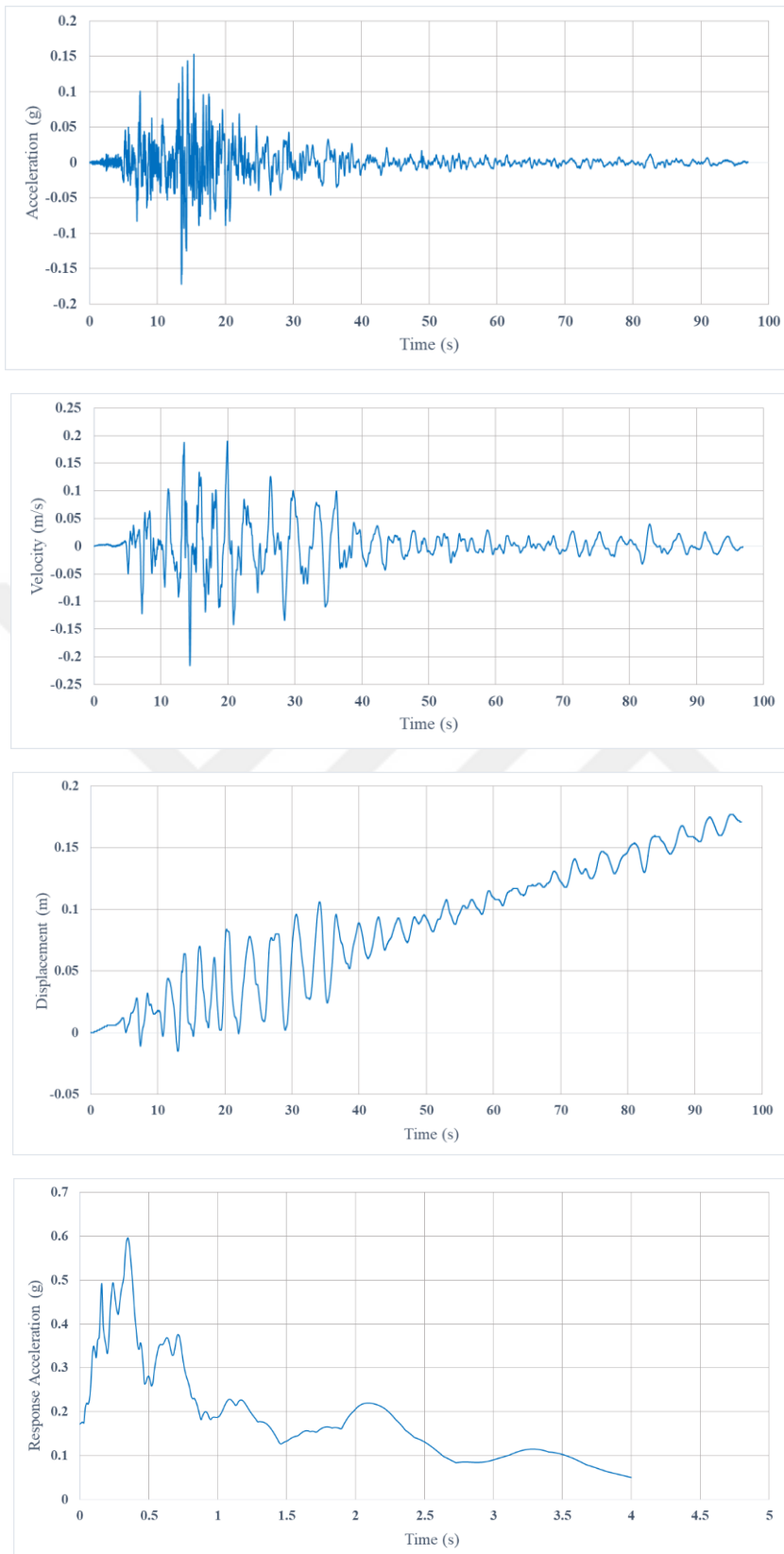


Figure 6.33 : WLA 360 component Superstition Hills earthquake recorded at 7.5m depth.

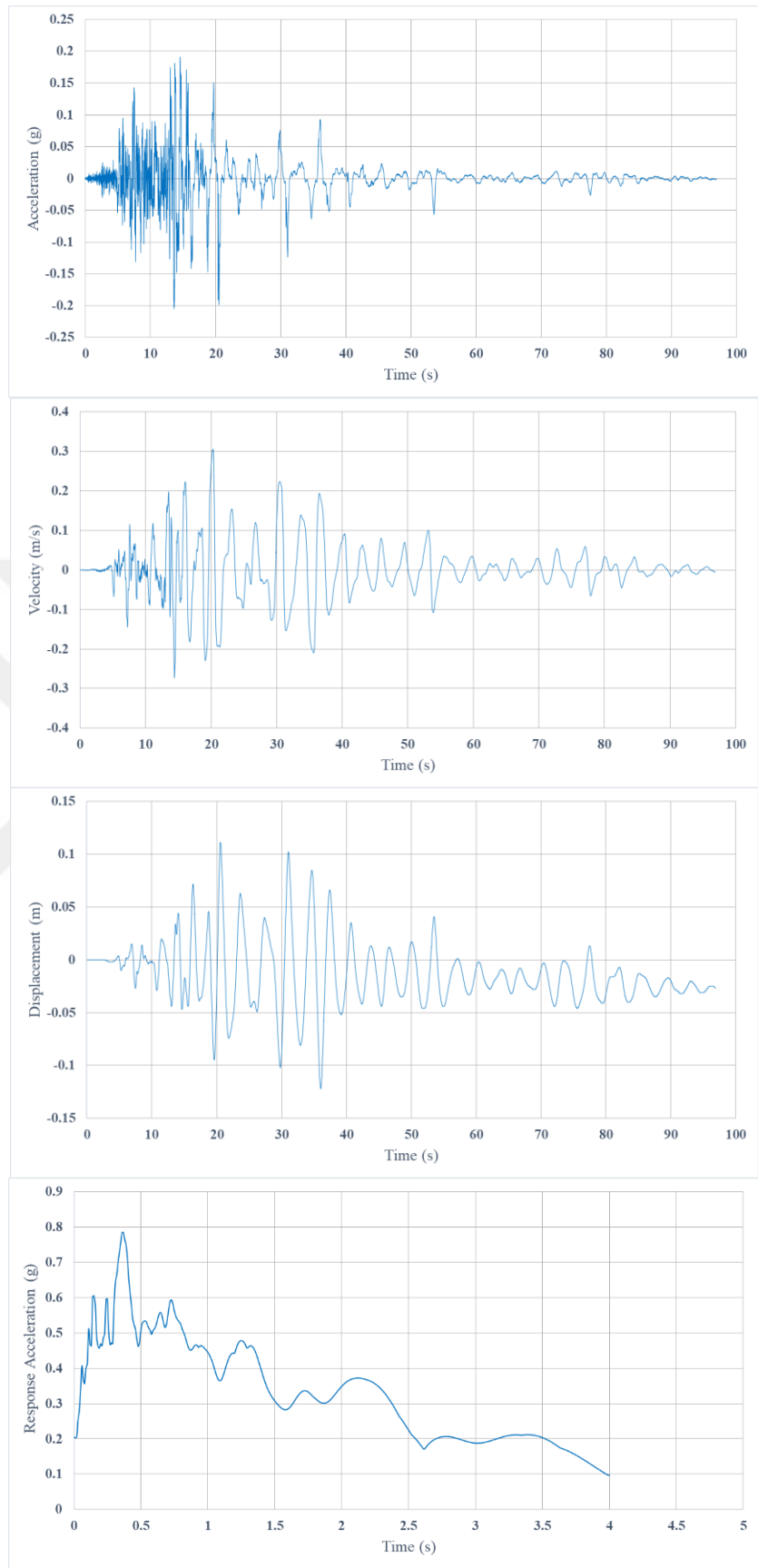


Figure 6.34 : WLA 360 component Superstition Hills earthquake recorded at ground surface level.

permeability of 1e-6 and 1e-8 m/s were used for the sand and clay layers, respectively. The analyses employed the 9-4-node quadrilateral u-p element. 2D Site response analysis was conducted using the 7.5 m deep velocity time history from the Superstition Hills earthquakes as input at the base of the model. Figure 6.33 and Figure 6.34 show the acceleration, velocity and displacement time history and response acceleration for the recorded ground surface motion at depth 7.5m and ground level respectively.

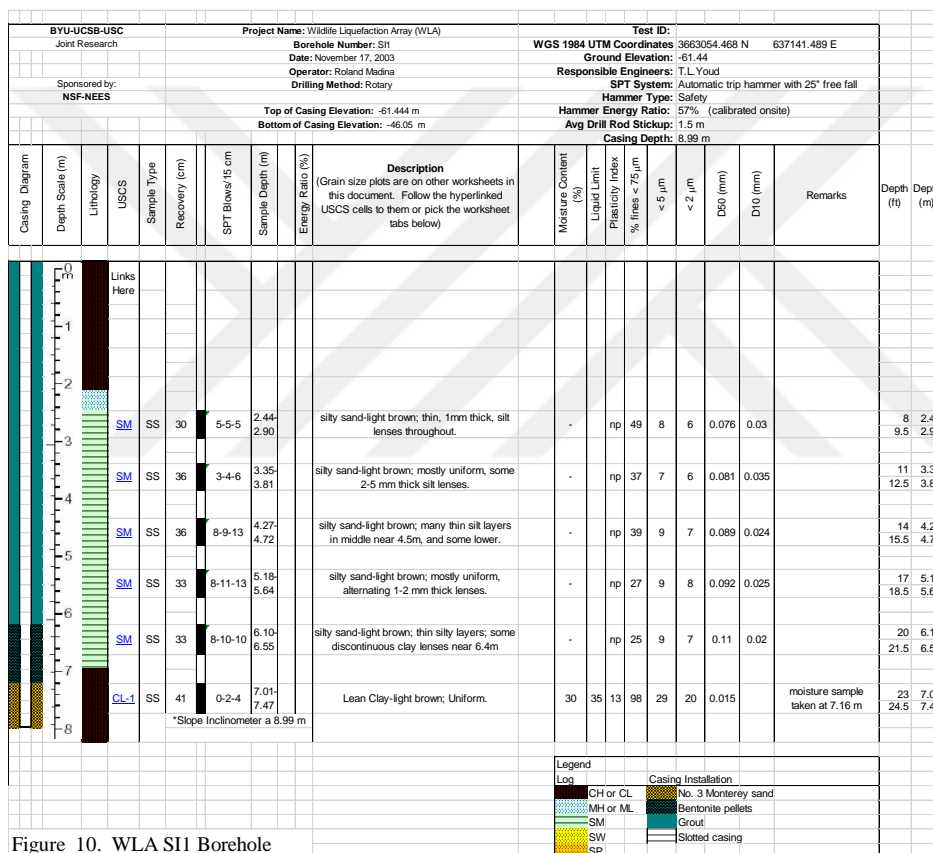


Figure 10. WLA S11 Borehole

Figure 6.35 : Wildlife Array geotechnical data for site response simulations (retrieved from NEES,2014).

Acceleration, velocity and displacement histories and response spectra of recorded ground motion of Superstition Hills earthquake at ground level are compared with time histories at ground surface of simulation in Figure 6.36.

The results from simulation are in good agreement with recorded data.

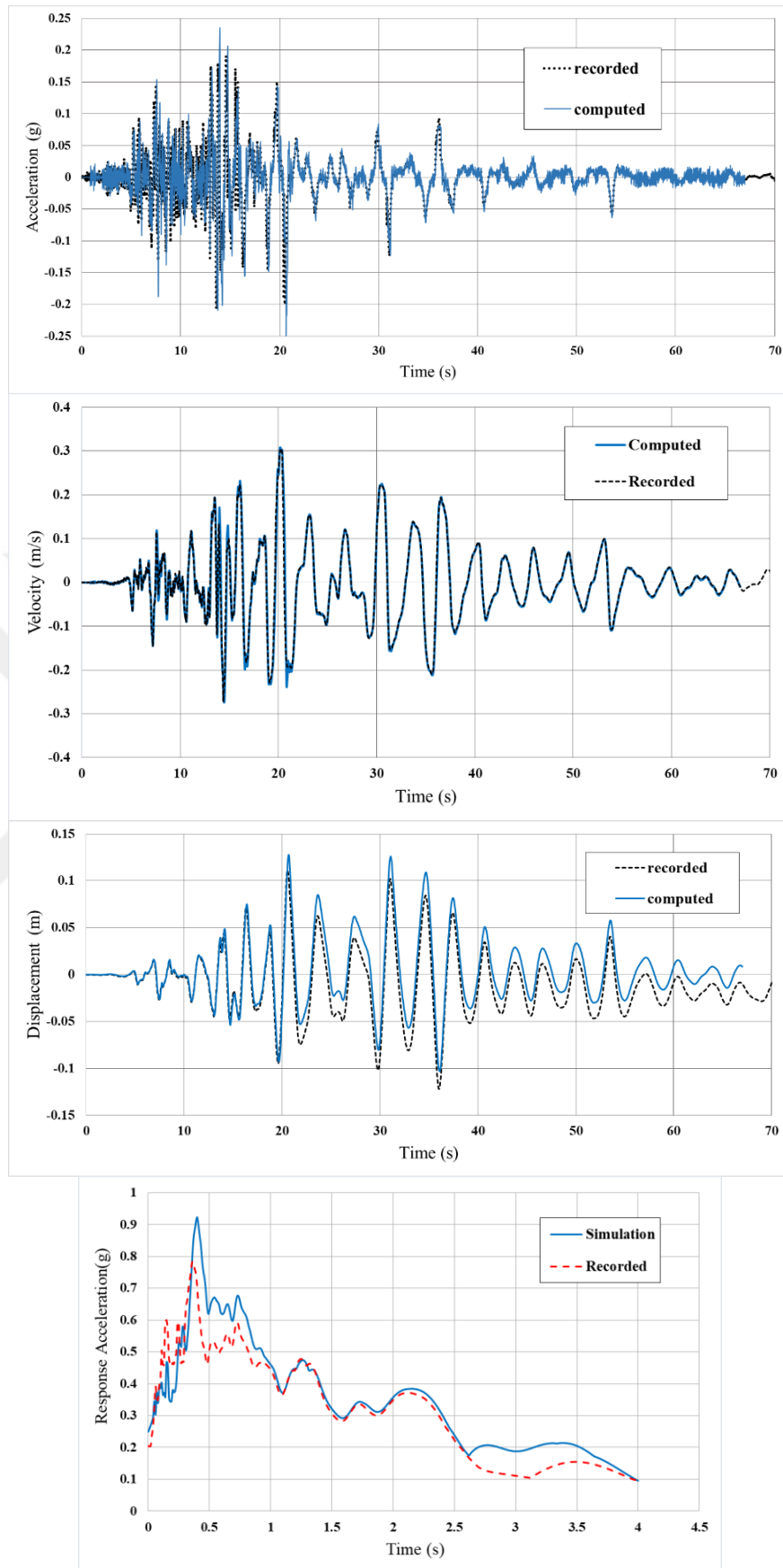


Figure 6.36 : Acceleration, velocity, displacement and response spectra at ground surface recorded vs computed by opensees for wildlife array site.

6.4 Port Island Station Site Response Evaluation During 1995 Kobe Hyogoken-Nanbu Earthquake

Port Island station is located at Kobe, Japan which is built on reclaimed land. The profile of the Port Island station subsurface soil layers illustrated in Figure 6.38. During 1995 Hyogoken-Nanbu, Kobe earthquake with magnitude 6.9 Mw, the ground motion recorded at 0, 16, 32 and 83m depths using a series of vertical arrays. Figures 6.37 shows the time histories of recorded ground motion at Port Island station during 1995 Kobe earthquake. In this study the soil profile modeled only for above 32m depth. The velocity history of recorded ground motion at 32m was applied to the base of the model as an input motion.

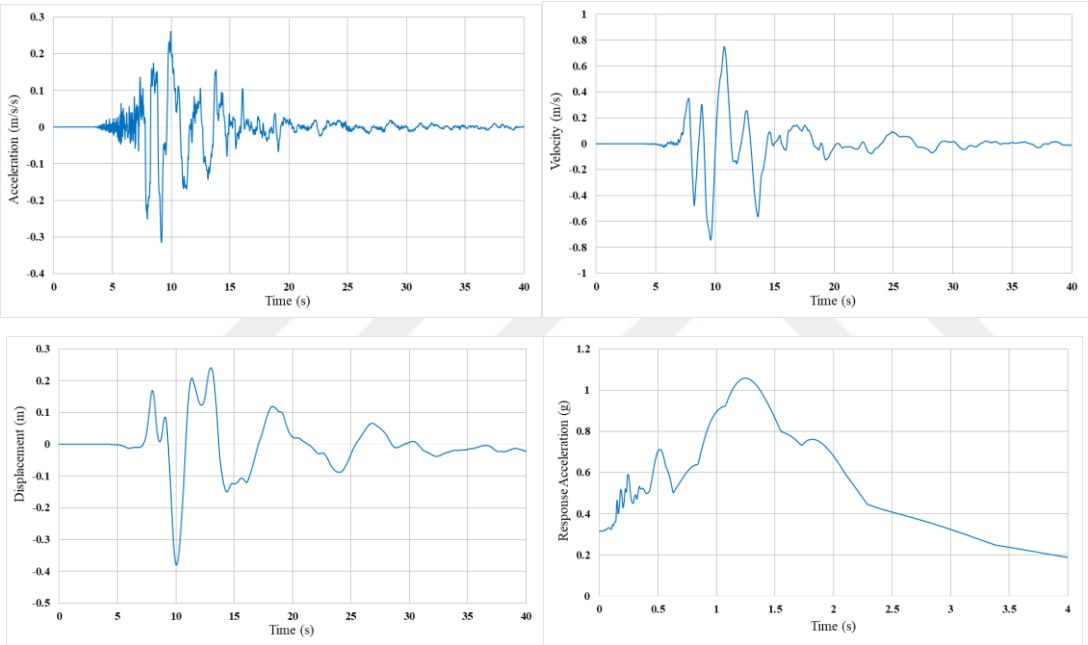


Figure 6.37 : Port Island component 1995 Kobe earthquake recorded at ground surface level.

For the Masado fill sand, the parameters for $D_r=57\%$ were used, except that the site-specific V_s values shown in Figure 6.36 were used, and the c_1 contraction parameter was set to 0.038 instead of 0.07 to make up from the deviation of V_s . The clay layers under the Masado sand upto 32m depth were modeled using the PressureIndependentMultiYield (PIMY) model with default G/G_{max} vs. γ curve. Permeability of $1e-6$ and $1e-8$ m/s were used for the silty sand and clay layer, respectively. The modeling protocols for mesh generation, boundary conditions and Rayleigh damping (set to 1%) described in previous chapter were followed.

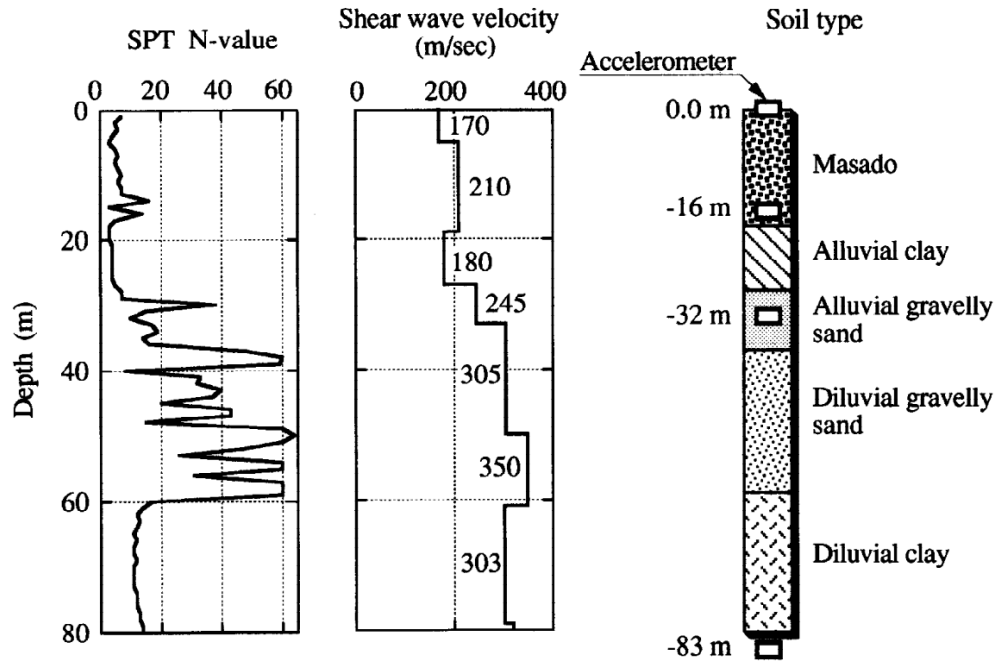


Figure 6.38 : Kobe Port Island geotechnical data for site response simulations (Cubrinovski et al.1996).

Recorded and computed time histories and spectra are presented in Figure 6.39. The results of computed times histories show a good agreement with the recorded ground motion time histories. It can be noted that the result of computed time histories at ground level also shows that the soil parameters were calibrated properly.

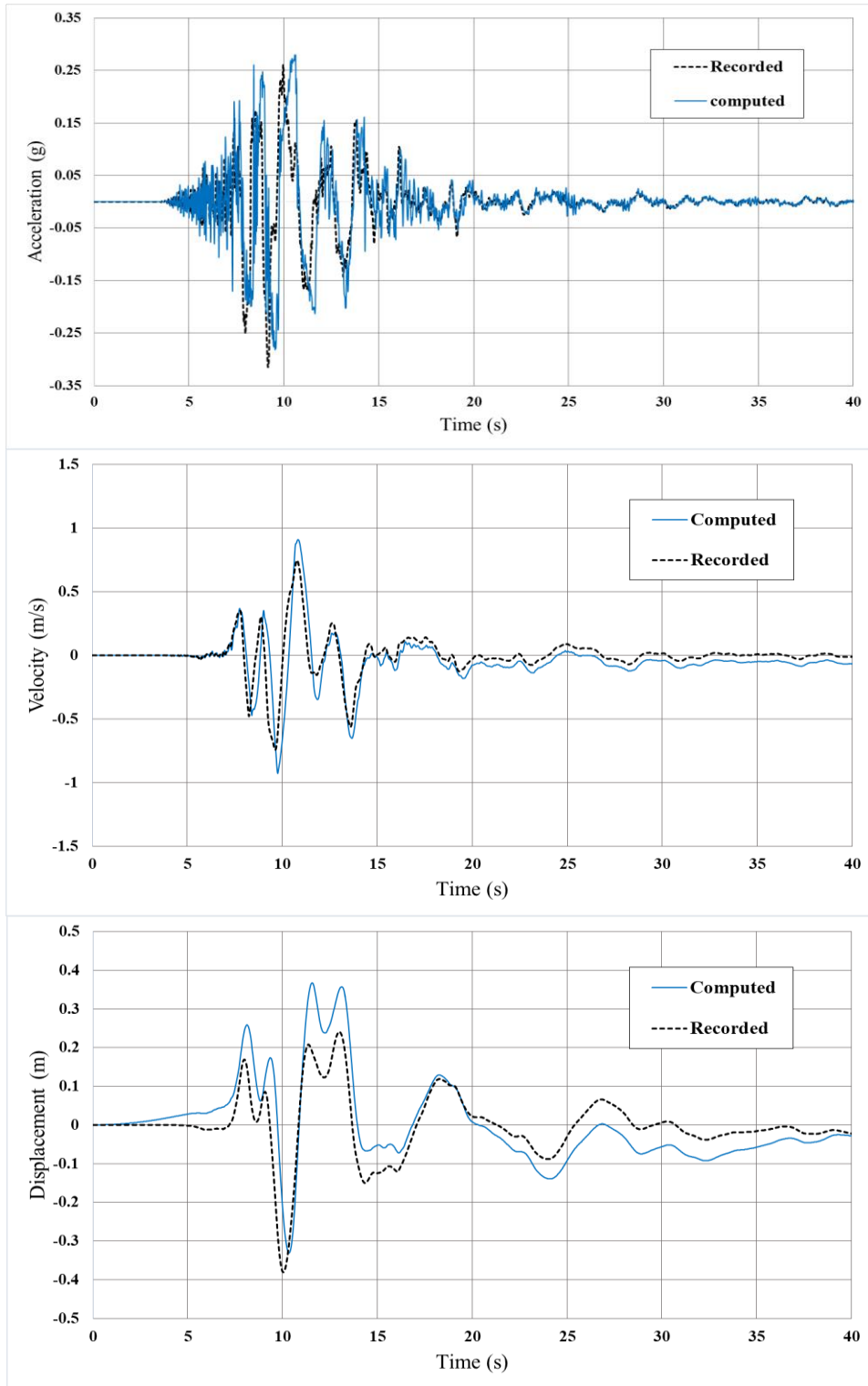


Figure 6.39 : Acceleration, velocity and displacement at ground surface recorded vs computed by opensees for wildlife array site.

6.5 Summary and Conclusion

An extensive soil constitutive model calibration was carried out for PressureDependentMultiYield model (PDMY02) in Opensees. The aim was to capture more accurate response of the soil to be implemented in nonlinear 2D site response analyses for real liquefiable profile case studies. Calibration was only conducted for loose to dense sand with different blow counts of SPT test reported by researchers.

Numerical evaluation was conducted with Single element simulation for monotonic and cyclic simple shear test. Different initial confining vertical pressures was considered to simulate soil behavior at different depths. The simulation results was compared with EPRI1993 recommended modulus reduction for sand. The result of calibrated parameters were in agreement with EPRI1993 recommended modulus reduction. Furthermore, the calibrated constitutive model parameters were used to validate the 2D site response of Wildlife Array site and Kobe port island site as real case studies. For Wildlife Array site, downhole array record of Superstition Hills earthquake was used as an input motion at the base of the model. For Kobe Port Island station site, the downhole array record at depth 32m of 1995 Kobe earthquake was used as an input motion. The acceleration, velocity and displacement time histories at ground surface level from simulations were in good agreement with recorded data at each site.



7. NUMERICAL EVALUATION OF TUNNEL BEHAVIOR IN LIQUEFIABLE SOIL

In this chapter, the results of analyses in terms of combination of vertical and horizontal excitation, post-liquefaction behavior of soil-tunnel system and effect of different relative densities is demonstrated. Before presenting the specific found outs in this research, the general observations that are common in literature and this research, are as follow:

- 1- During dynamic analysis pore water pressure increased suddenly at early stage of loading
- 2- Generation of pore water pressure beneath the tunnel has an important role in uplifting the structure.
- 3- The uplift displacement continue for some time even when earthquake stopped.

In the following sections additional finding will be presented which have not or less been investigated by previous works.

7.1 Effect of Frequency Content of Ground Motion on Uplift Behavior of Tunnel

To evaluate the effect of frequency content of input motion, horizontal component of Kobe ground motion with 0.1-10Hz and 0.1-25Hz band-pass filtered were applied at the base of the model. As illustrated in Figure 7.1, the result for first 16s of ground motion shows no effect due to higher frequency contents of motion.

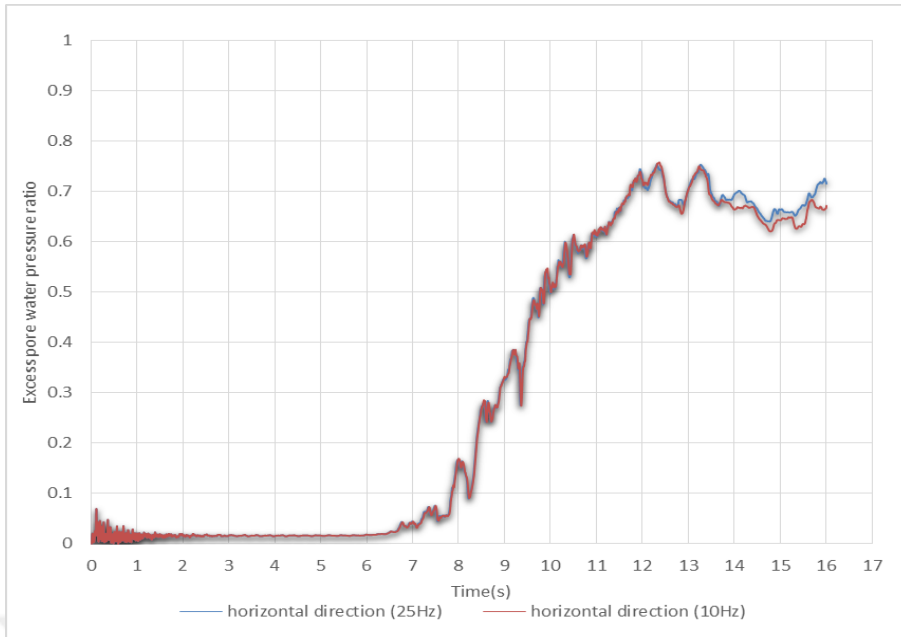


Figure 7.1 : Excess pore water pressure generation due to different frequency contents of horizontal component of 1995 Kobe earthquake.

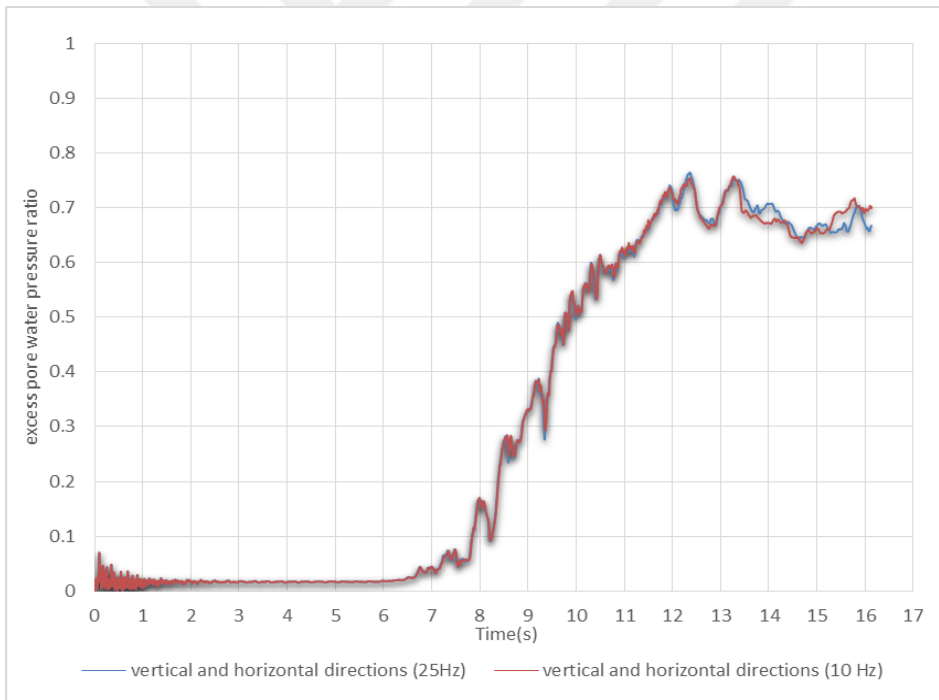


Figure 7.2 : Excess pore water pressure generation due to different frequency contents of horizontal component of Kobe earthquake.

7.2 Effect of Vertical Input Motion on Uplift Behavior of Tunnel

Whereas ground motion waves propagate in all directions through the ground, the motions created by ground motion waves can be described in translational and rotational directions according to the 3 dimensional coordinates. between 6 components of ground motions, 3 translation and 3 rotation, only 3 translation motions consist of 2 horizontal and a vertical excitation are evaluated through recording and signal processing procedure of ground motions. Horizontal components of ground motions are important components of earthquakes. However, although the vertical component of ground motion has less importance than horizontal components in seismic analysis and design, present investigations indicate that the vertical component has also a significant role in some earthquakes particularly in near fault areas. The vertical component effect is generally measured by vertical motion amplitude to horizontal one ratio (V/H). For evaluating effect of vertical excitation on tunnel behavior, horizontal and vertical components of 1995 Kobe earthquake were selected as an input motion. The original horizontal components of the Kobe record with 0.834g maximum acceleration amplitude was scaled to 0.334g without changing the frequency contents of the record. The length of the both horizontal and vertical excitations were truncated as 40s.

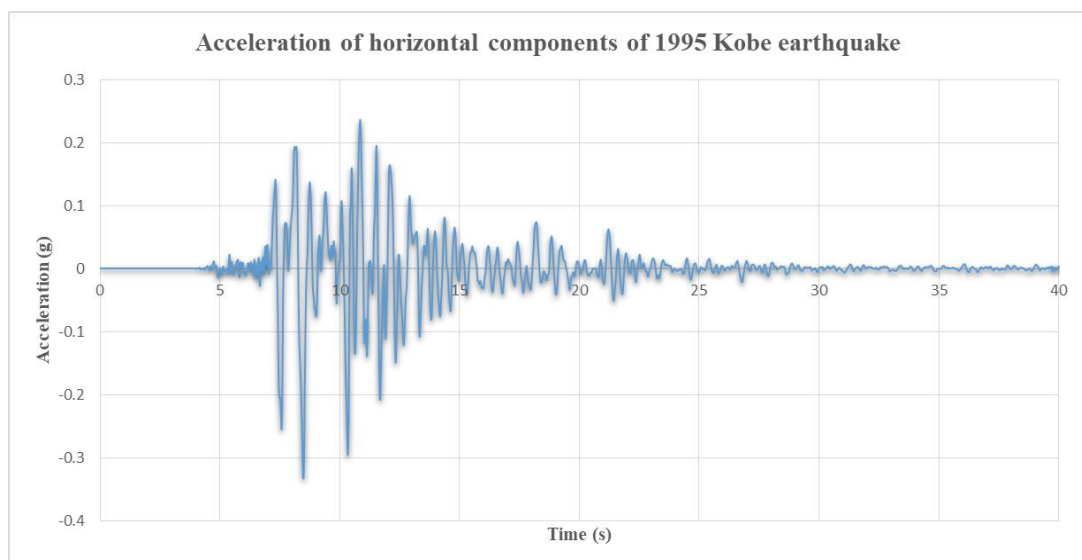


Figure 7.3 : Horizontal components of 1995 Kobe earthquake scaled to 0.3g amplitude.

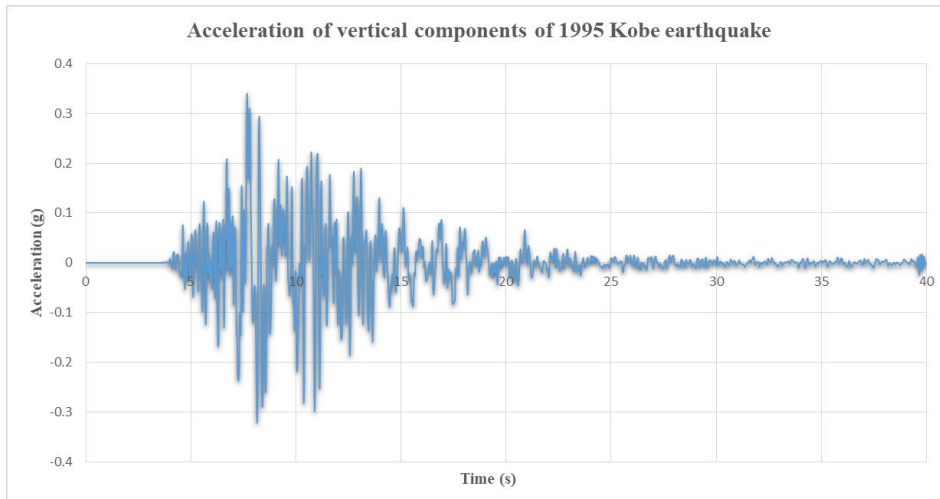


Figure 7.4 : Vertical components of 1995 Kobe earthquake 0.3g (not scaled).

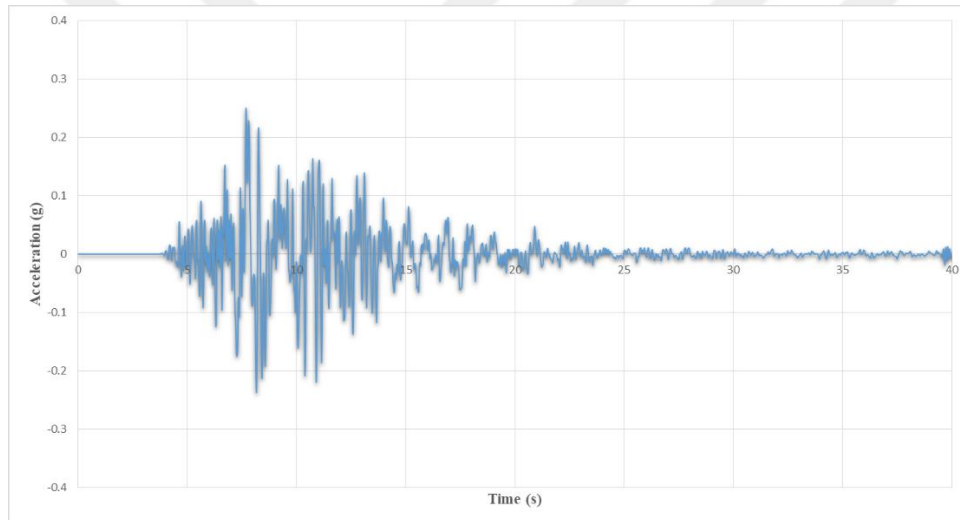


Figure 7.5 : Vertical components of 1995 Kobe earthquake 0.25g.

The vertical components of the record with 0.339g maximum acceleration amplitude was scaled to different amplitudes 0.25g, 0.35g and 0.4g. The simulation conducted by applying horizontal and vertical components concurrently with different vertical excitations while the horizontal component applied with same amplitude. The result of combined horizontal and vertical motions compared with horizontally only excitation to evaluate the effect of vertical motion on tunnel uplift. The scaled horizontal component and original vertical component of Kobe earthquake shown in Figure 7.4 and 7.5 respectively.

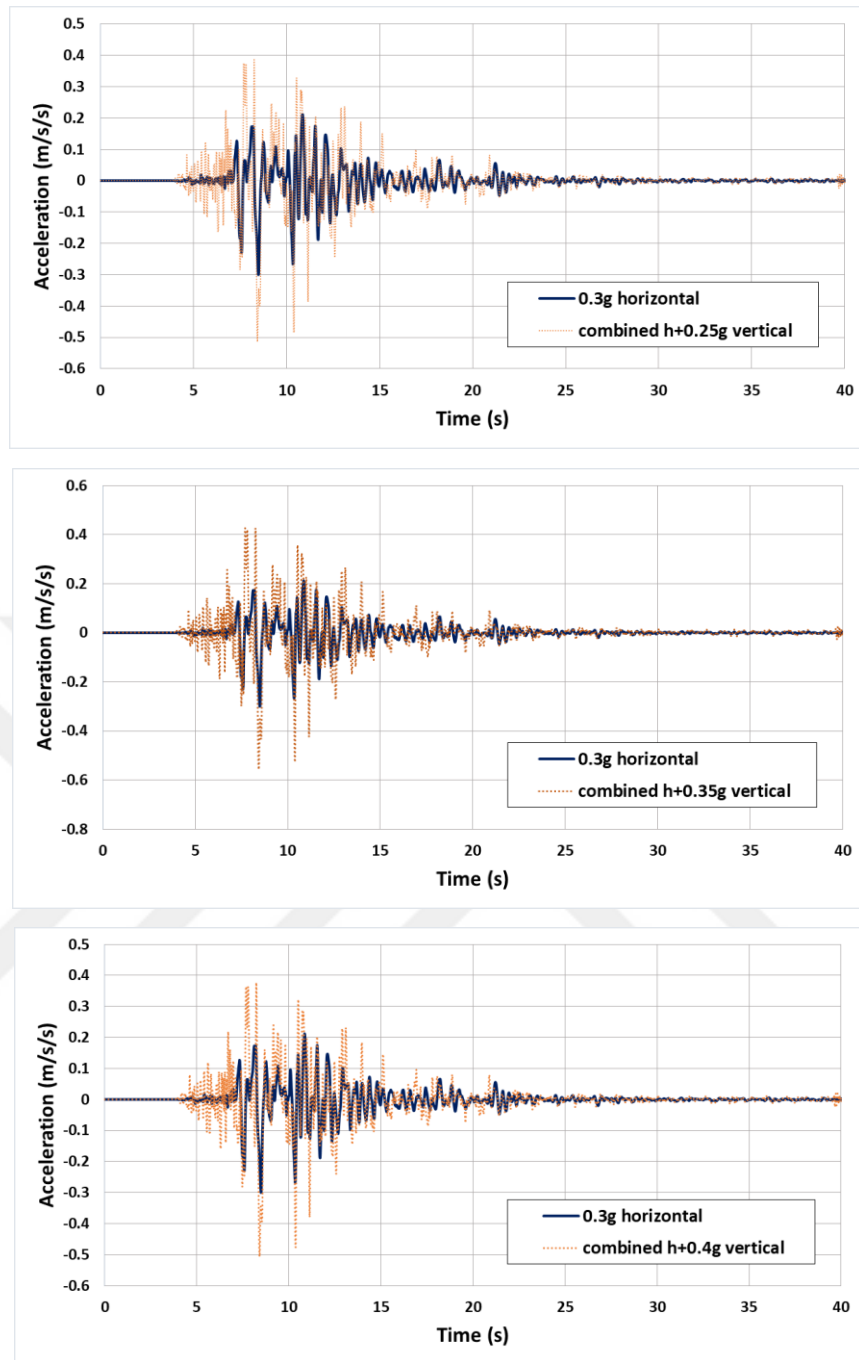


Figure 7.6 : Combined vertical and horizontal components of 1995 Kobe earthquake for vertical motion with 0.25g, 0.35g and 0.4g and horizontal motion 0.3g amplitudes.

As demonstrated in Figure 7.7, the result of combined horizontal and vertical excitations show uplift displacement at near-field around tunnel. The distribution of ground surface uplift displacement for combined horizontal and different vertical excitation amplitudes are given in Figure 7.8.

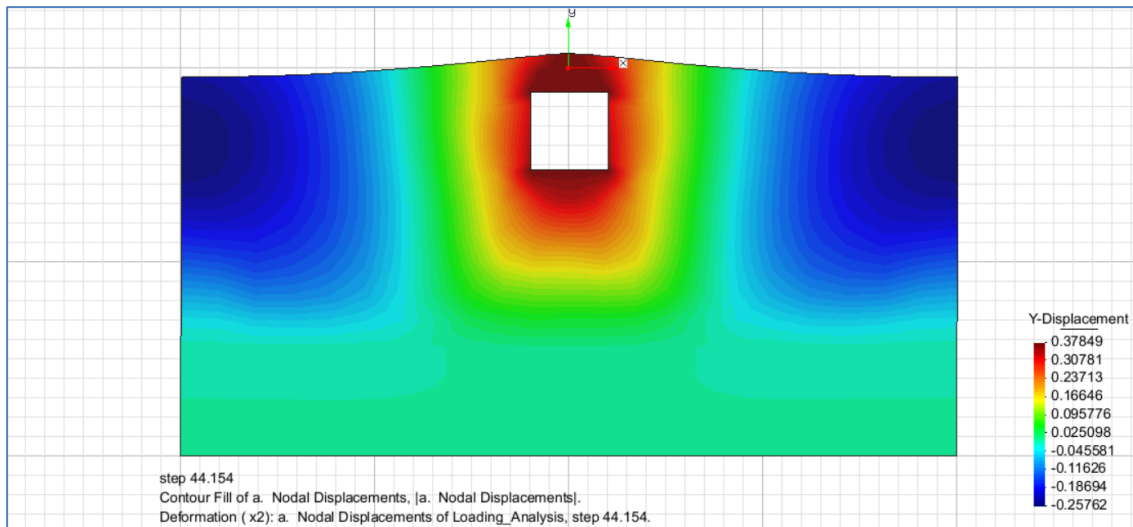


Figure 7.7 : Distribution of uplift displacement of ground surface.

The result of vertical displacement at ground surface level shows that by increasing the amplitude of vertical excitation the uplift of soil at the center of domain increases while at distance far away from the tunnel the soil settles more.

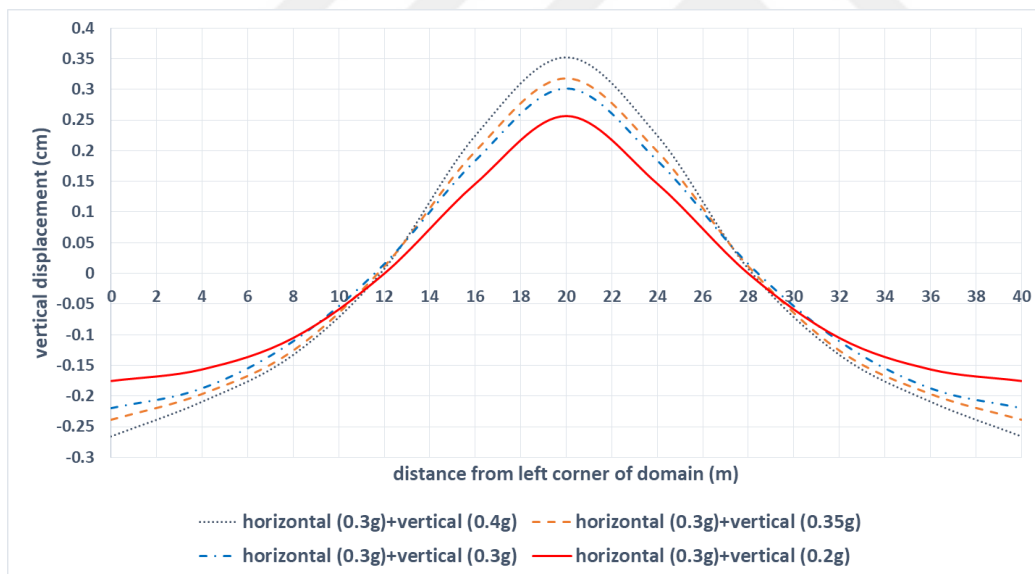


Figure 7.8 : Distribution of uplift displacement of ground surface due to horizontal component combined with various amplitude of vertical excitation.

Figure 7.9 illustrated the amount of tunnel uplift due to combined vertical and horizontal excitations. It is clear that by increasing the vertical motion amplitude the tunnel suffer more uplift. It should be noted that the ratio of vertical motion amplitude to the horizontal excitation amplitude (V/H) plays a key role for response of tunnel-soil system. For $V/H > 1$ the amount of uplift is more that case where only horizontal

excitation applied while the amount of uplift due to combined vertical and horizontal motions reduces if the ratio $V/H < 1$.

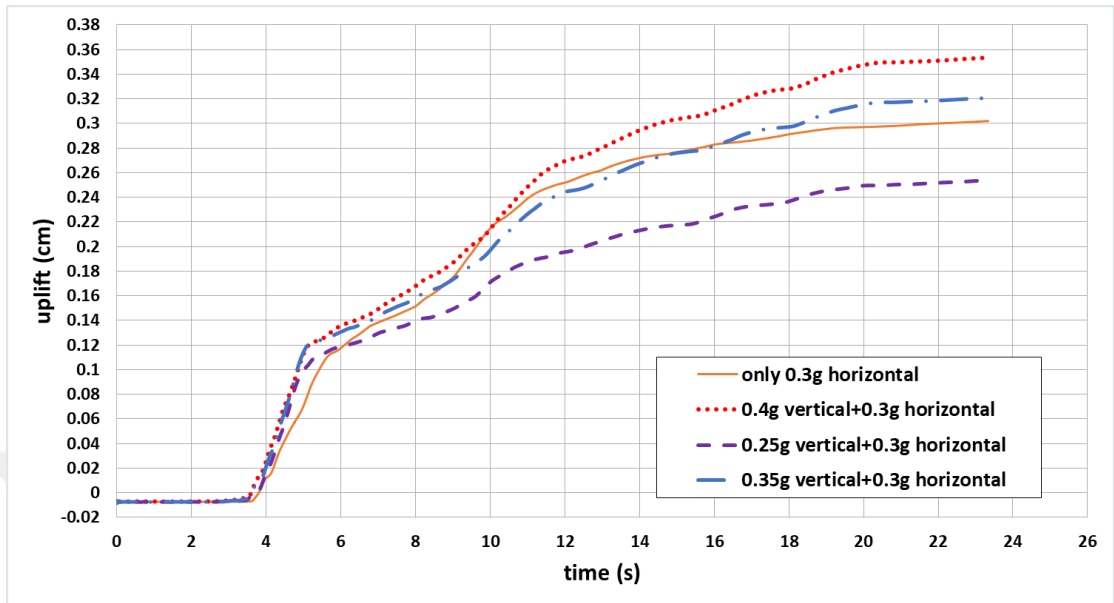


Figure 7.9 : Uplift displacement at lower middle node of tunnel due to horizontal and vertical components of 1995 Kobe earthquake.

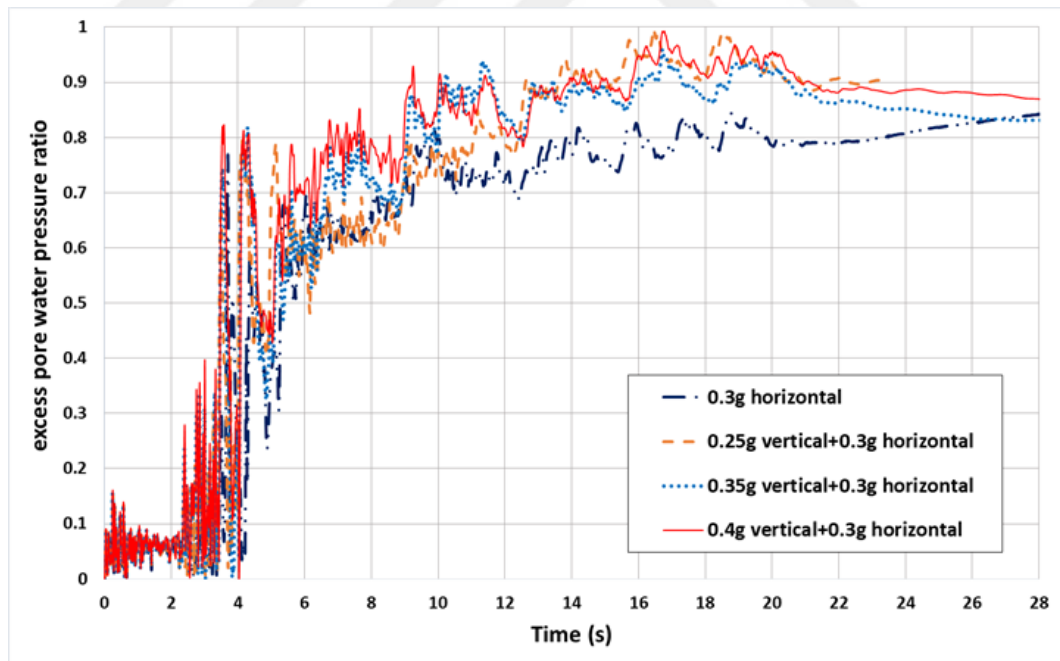


Figure 7.10 : Excess pore water pressure at lower middle node of tunnel due to horizontal and vertical components of 1995 Kobe earthquake.

The ratio of vertical motion amplitude to horizontal amplitude can be a key aspect for evaluating the behavior of underground structures in practice.

Results of excess pore water pressure ratio at the bottom of the tunnel reveals that the increasing the vertical excitation amplitude causes more oscillation during generation of excess pore water pressure at the very beginning of the excitation. However, as time pass there is no significant change in amount of excess pore water pressure ratio.

7.3 Post-liquefaction Consolidation Settlement Behavior of Tunnel-Soil System

For evaluation of post-liquefaction consolidation settlement of tunnel, horizontal components of 1995 Kobe earthquake records similar as previous section was selected and first 40s of records only considered in analyses without any change in frequency contents of motion. The soil assumed as medium dense Nevada sand with relative density $Dr=57\%$ overlaying dense sand with relative density $Dr=74\%$. The analyses performed by gravity analysis (elastic and plastic) followed by dynamic analysis. For analysis during post-liquefaction when the earthquake stopped, zero load added to the records with same time steps due to difficulty of interpret the result when different time steps are applied during analysis.

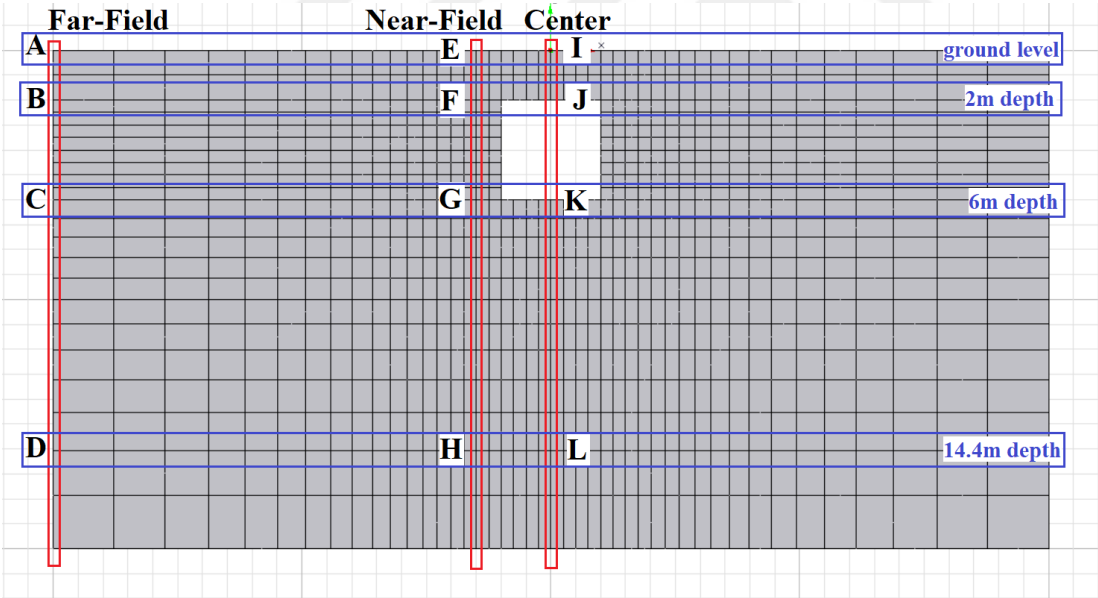


Figure 7.11 : Schematic of extracted results for Far-field, near-field and center nodes of domain.

As illustrated in Figure 7.11, to evaluate the tunnel behavior with the liquefiable soil, critical points within the soil domain are considered horizontally and vertically. The results are compared in vertical direction as follow:

- At far-field from point A to point D.
- At near-field from point E and point H.

- At center from point I to point L.

The results are also compared in horizontal direction as follow:

- At ground surface level from far-field point A to near-field point E and center point I.
- At 2m depth from far-field point B to near-field point F and point J.
- At 6m depth from far-field point C to near-field point G and point K.
- At 14.4m depth from far-field point D to near-field point H and center point L.

7.3.1 Comparison of Tunnel-Soil Response in Vertical Direction

7.3.1.1 Excess Pore Water Pressure Generation and Vertical Displacement of Soil in Far-Field

In this section, the results of numerical simulation in terms of excess pore water pressure and vertical displacement, uplift or settlement, at far-field from point A at ground surface level to point D at the bottom of liquefiable sand at 14.4m depth is compared.

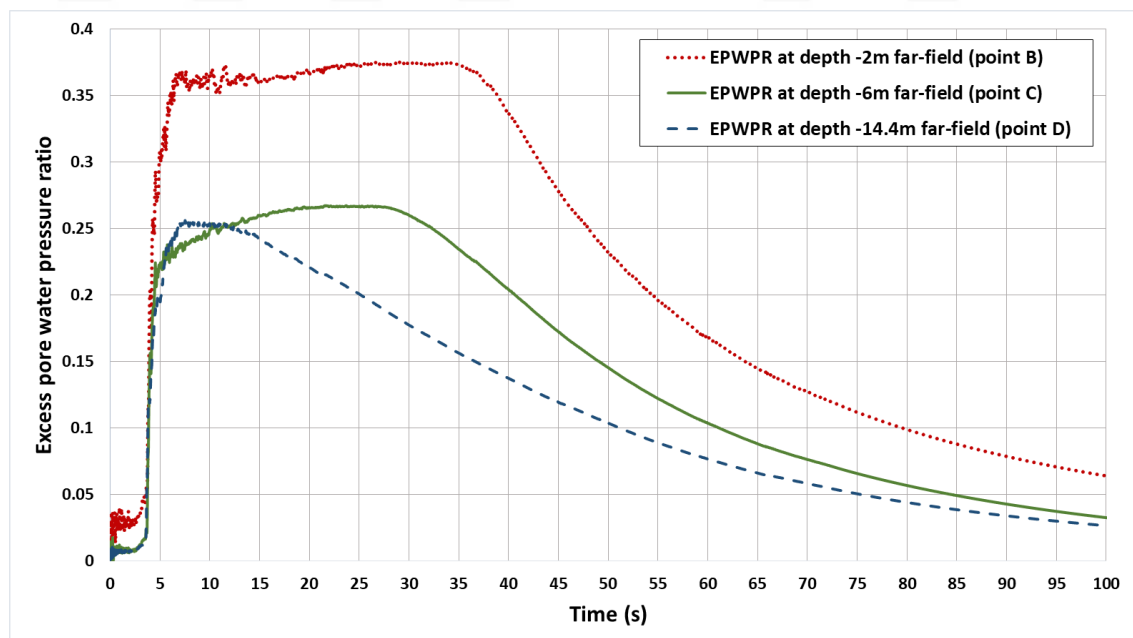


Figure 7.12 : Excess pore water pressure ratio variation in different depth at far-field.

Figure 7.12 shows the excess pore water pressure variation at the far-field. The result of excess pore water pressure generation at far-field show that by increasing the depth of liquefiable sand the excess pore water pressure decreases, however, liquefaction has not occurred during dynamic analyses. Despite the fact that sand did not liquefied, the saturated sand at far-field start to settle at the very beginning of the analysis as it is shown in Figures 7.13, 7.14 and 7.15.

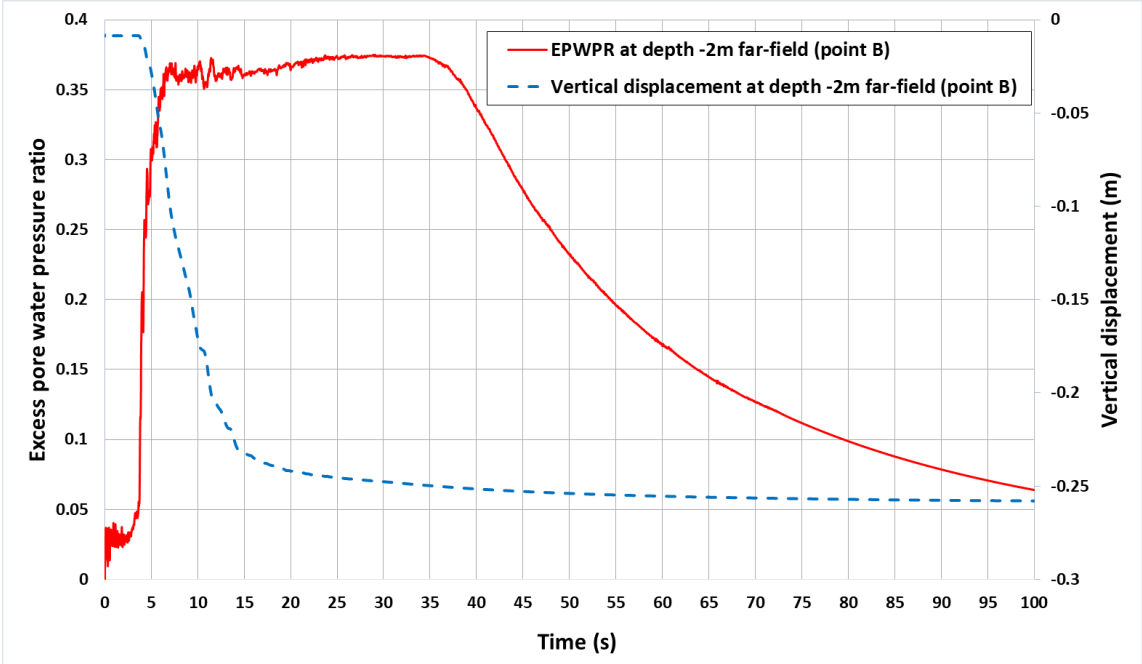


Figure 7.13 : Excess pore water pressure ratio and vertical displacement of saturated sand at depth 2m in far-field.

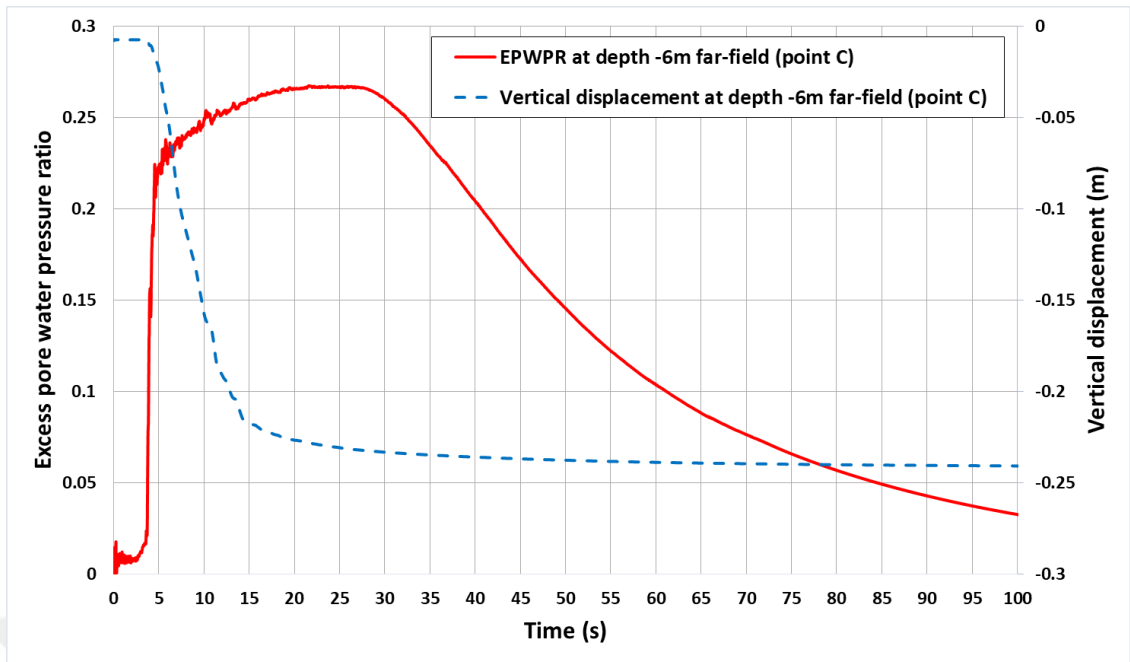


Figure 7.14 : Excess pore water pressure ratio and vertical displacement of saturated sand at depth 6m in far-field.

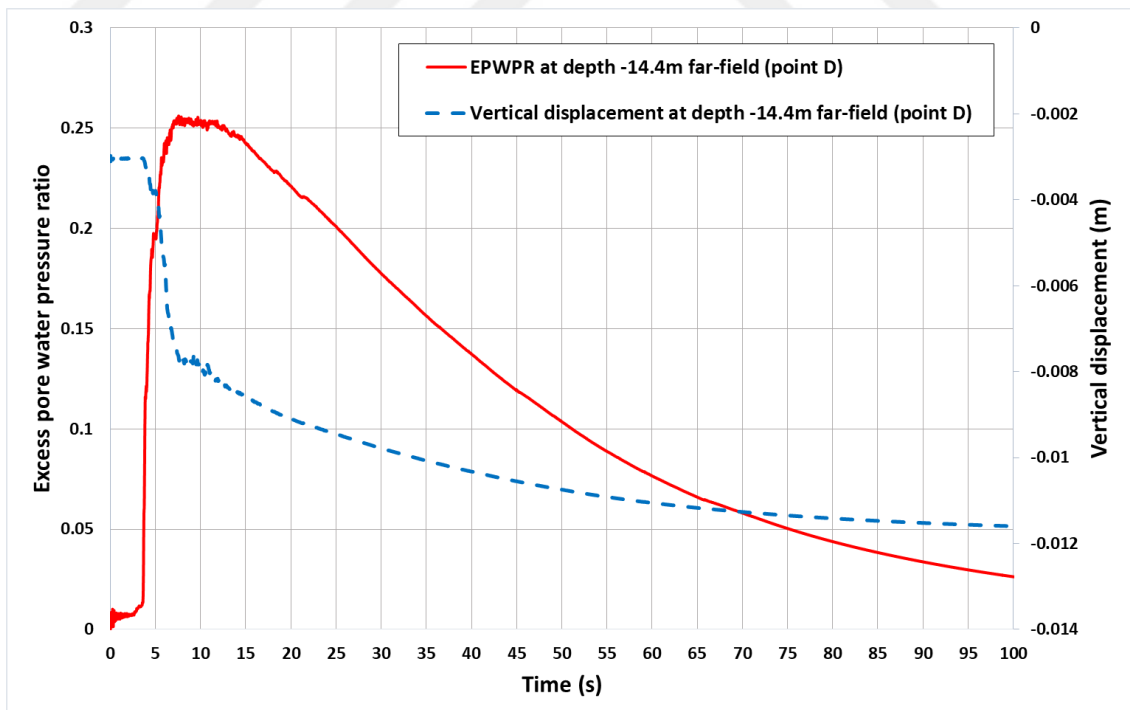


Figure 7.15 : Excess pore water pressure ratio and vertical displacement of saturated sand at 14.4m depth (bottom of liquefiable) sand in far-field.

It is also reasonable to compare the amount of settlement at far-field as illustrated in Figure 7.16 and 7.17.

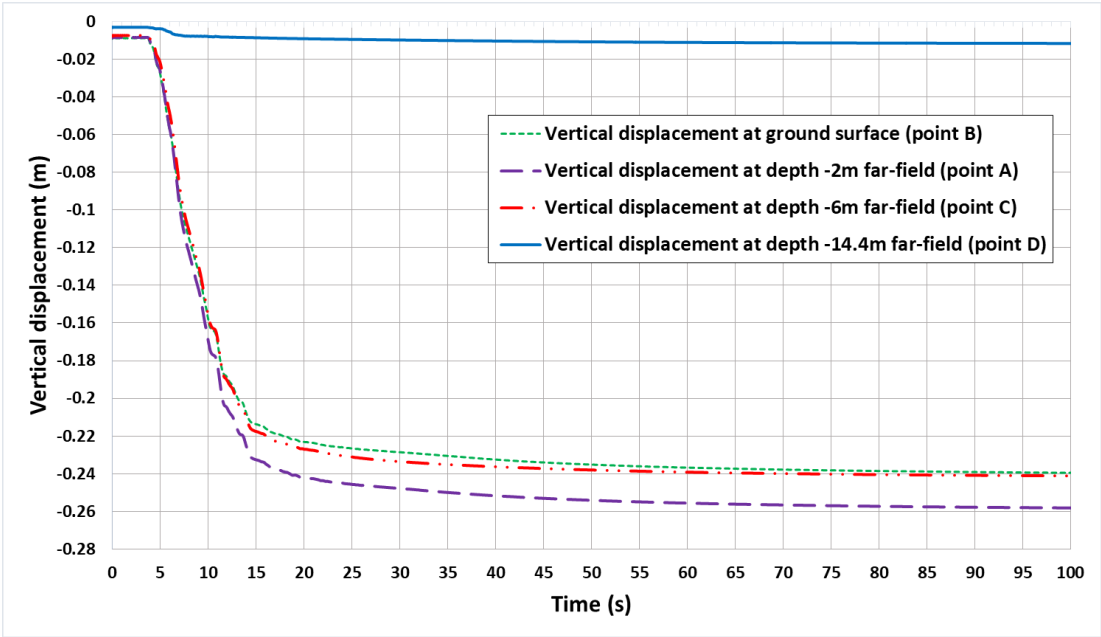


Figure 7.16 : Vertical displacement at different depth at far-field.

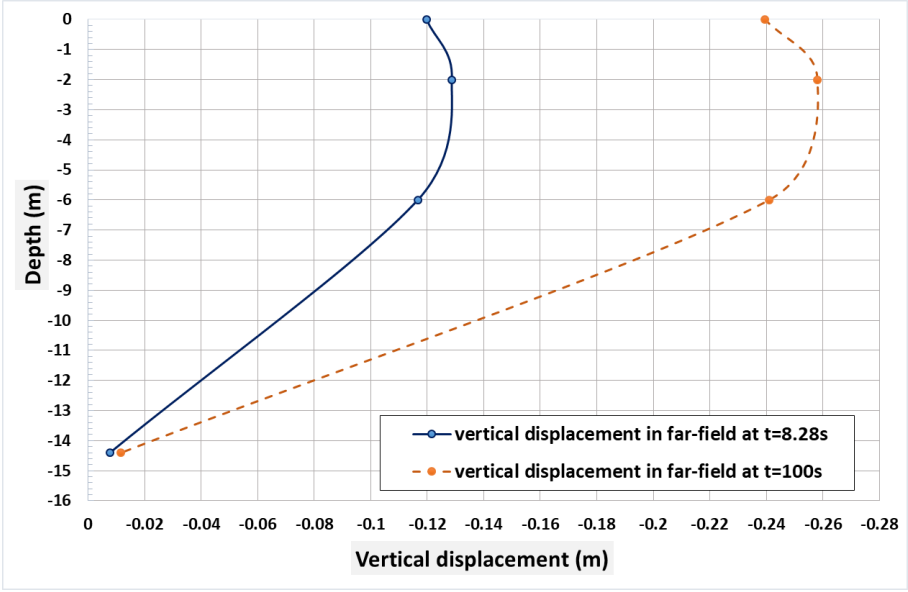


Figure 7.17 : Vertical displacement at different depth at far-field.

As demonstrated in Figure 7.16 and 7.17, the results of settlement at far-field shows that settlement reduces at higher depth where at the bottom of liquefiable layer settlement approaches to zero. The fact that ground surface level is the only way for pore fluid to dissipate is the reason that soil settles more at depth near ground surface level.

7.3.1.2 Excess Pore Water Pressure Generation and Vertical Displacement of Soil in Near-Field

Near field is defined as a subdomain where it is equal underground structure wide away from left and right side walls. Due to interaction between tunnel and soil it is vital to consider the behavior of soil at near-field. It is more reasonable to show the vertical displacement, uplift or settlement, and excess pore water pressure generated within the sand to evaluate the effect of excess pore water pressure on vertical displacement. Figures 7.18, 7.19 and 7.20 demonstrate the vertical displacement and excess pore water pressure ratio in vertical direction from point F at depth 2m then point G at depth 6m and finally point H at depth 14.4m respectively.

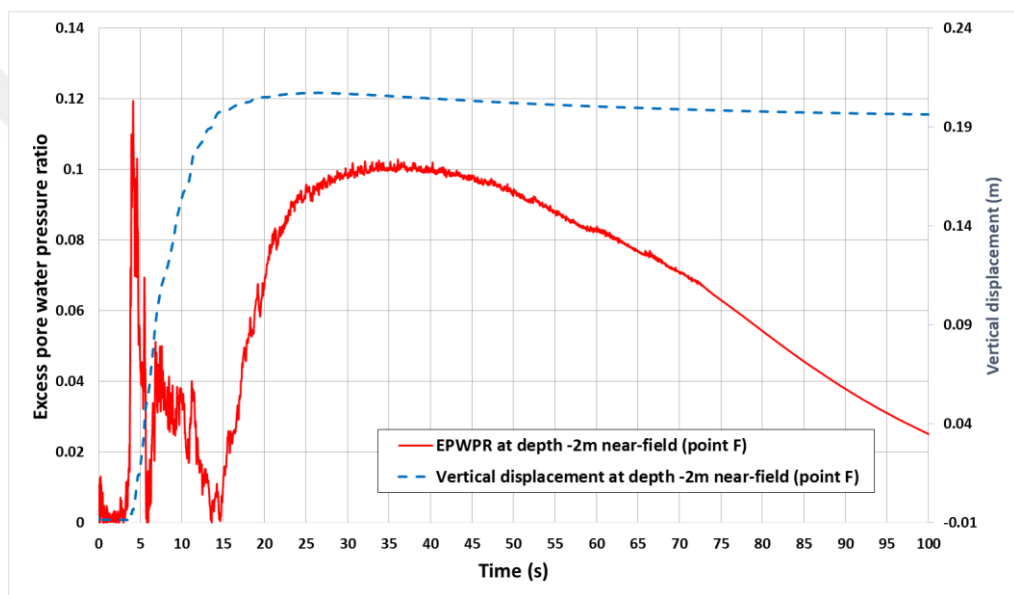


Figure 7.18 : Excess pore water pressure ratio vs. vertical displacement of saturated sand at depth 2m in near-field 3m away from tunnel.

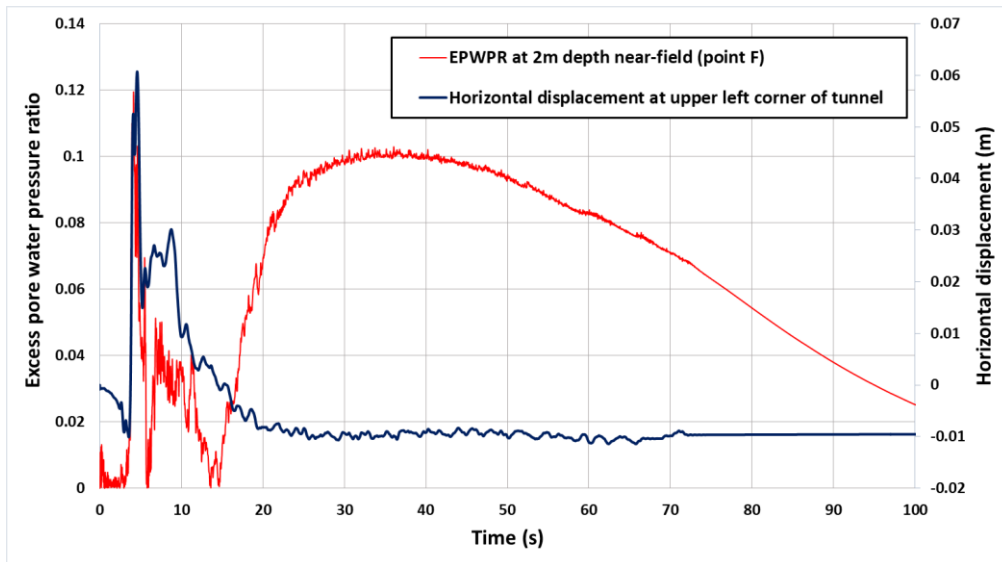


Figure 7.19 : Excess pore water pressure ratio vs. horizontal displacement of saturated sand at depth 2m in near-field 3m away from tunnel.

It clear from Figure 7.18, 7.19 and 7.20 that as soon as excess pore water pressure ratio increased the soil at near-field start moving upward. The excess pore water pressure tries to dissipate through ground surface and causes the soil to uplift.

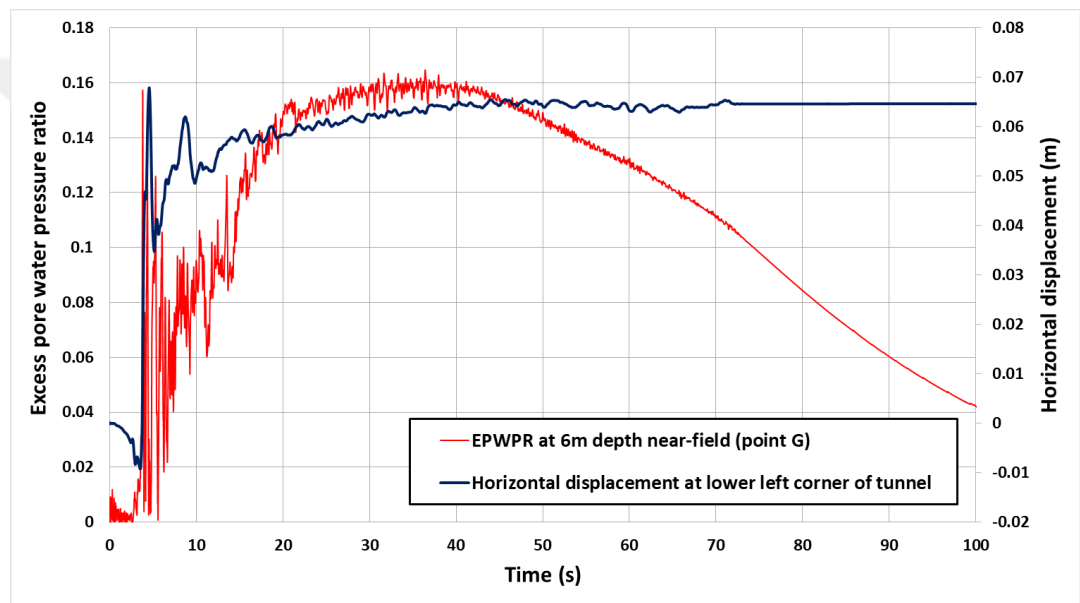
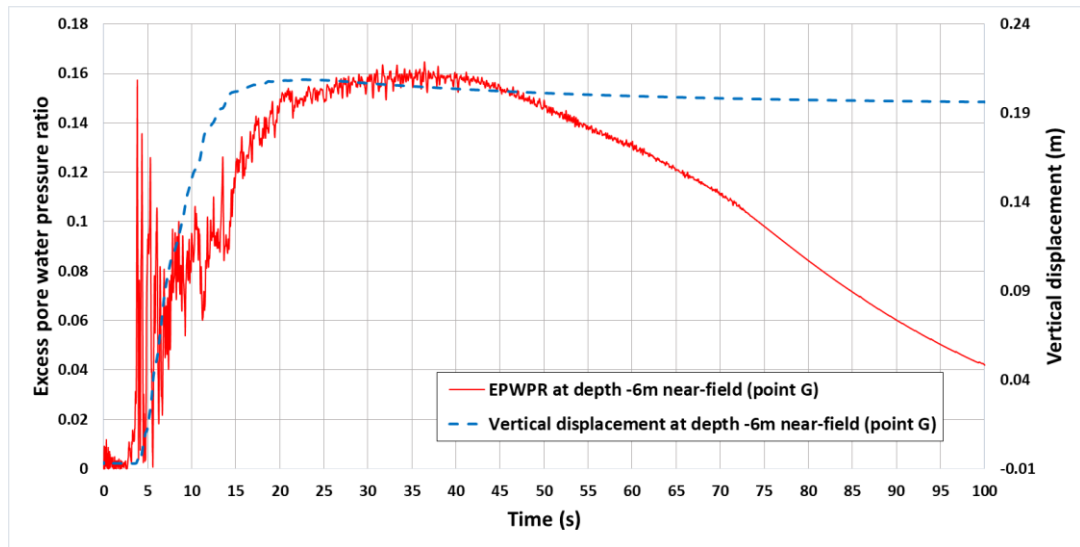


Figure 7.20 : Excess pore water pressure ratio and vertical displacement of saturated sand at depth 6m in near-field 3m away from tunnel.

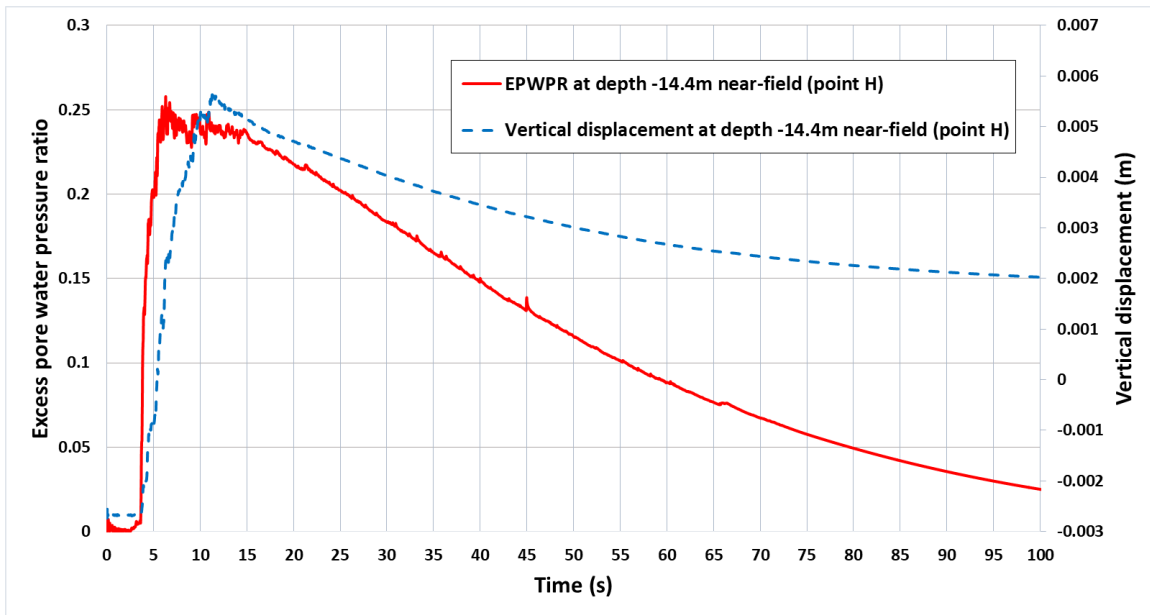


Figure 7.21 : Excess pore water pressure ratio and vertical displacement of saturated sand at bottom of liquefiable sand beneath the tunnel.

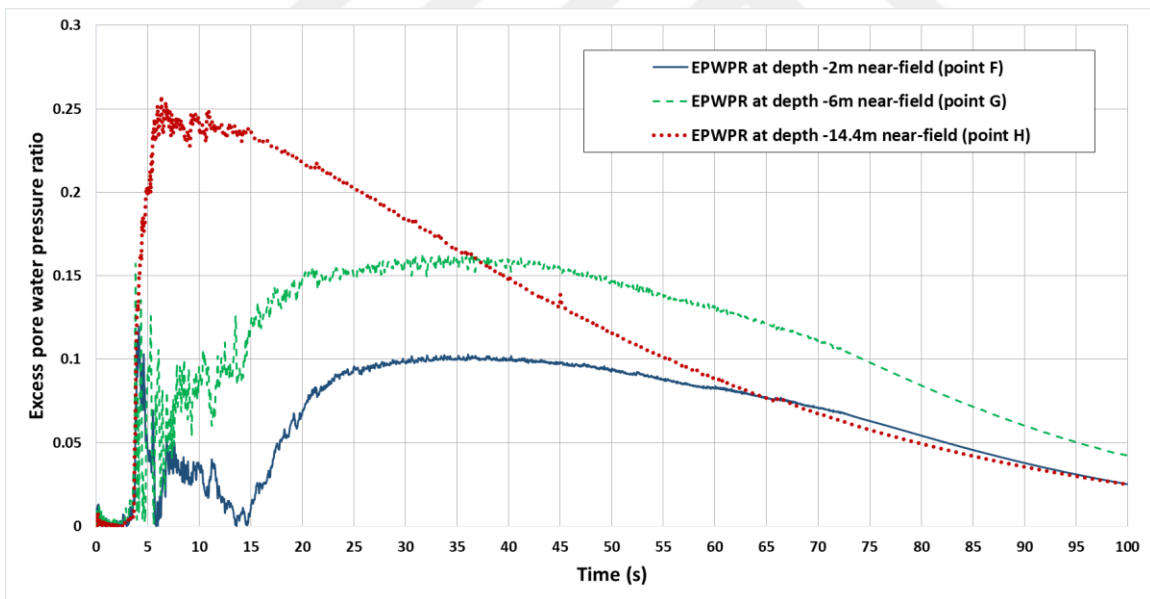


Figure 7.22 : Excess pore water pressure ratio of saturated sand at 2m, 6m and 14.4m depth within the liquefiable sand in near-field 3m away from tunnel.

The results of excess pore water pressure ratio at near-field shows that excess pore water pressure ratio increased suddenly at the early stage of the shaking as it is shown in Figure 7.21. However, the sand at near-field was not liquefied. The excess pore water pressure ratio increases as depth increases. The not smooth portion of excess

pore water pressure at depth near tunnel, at 2m and 6m depths, is due to existence of tunnel and therefore interaction between tunnel and soil.

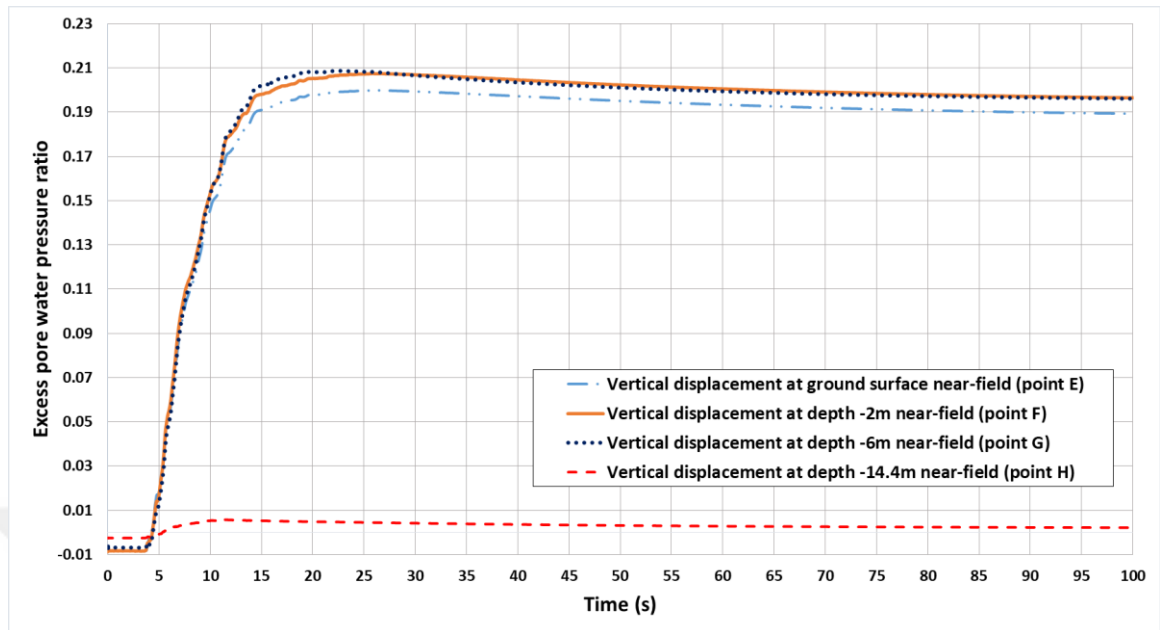


Figure 7.23 : Vertical displacement at different depth within the liquefiable sand in near-field 3m away from tunnel.

Figure 7.22 shows the amount of vertical displacement at the near-field. As it is shown in Figure 7.22, the rate of uplift decreases as depth increases where at the bottom of liquefiable layer loose sand the vertical displacement is approximately near zero same as far-field. However, the amount of uplift at depths within the domain is slightly higher than ground surface level due to dissipation process of excess pore water pressure.

7.3.1.3 Excess Pore Water Pressure Generation and Vertical Displacement of Soil at Center of Tunnel

At the center line of tunnel, the amount of uplift at points above and under the tunnel are almost similar and it decreases as depth increases. Figures 7.24, 7.25 and 7.26 shows the amount of uplift versus excess pore water pressure ratio at each depth. Figure 7.25 shows that the uplift started as excess pore water pressure ratio increased at early stage of analysis. However, after the soil under tunnel liquefied the amount of uplift shows small change while the excess pore water pressure start to dissipate.

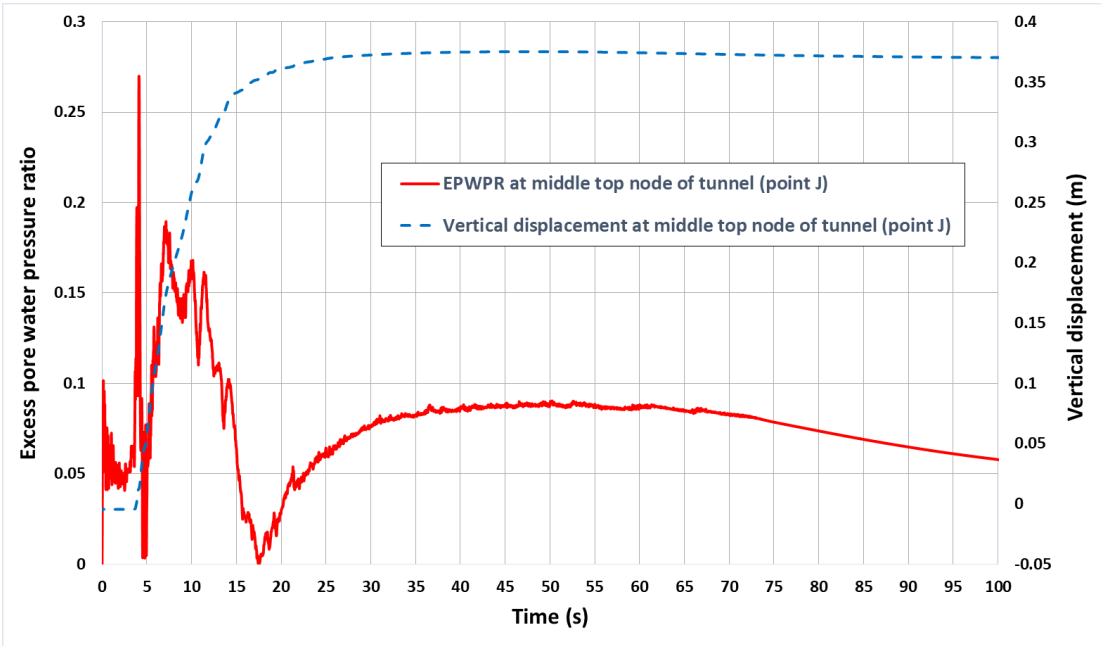


Figure 7.24 : Schematic of extracted results for Far-field, near-field and center nodes of domain.

As pore water pressure dissipate, the tunnel tends to settle but the amount of settlement at point far away from the tunnel is much higher than the points near tunnel because the water can dissipate faster due to existence of the tunnel at the middle of domain. Therefore, the liquefied sand at far-field and near-field start to flow toward beneath the tunnel and excess pore water pressure at the bottom of tunnel is increased for a while and then start to dissipate again.

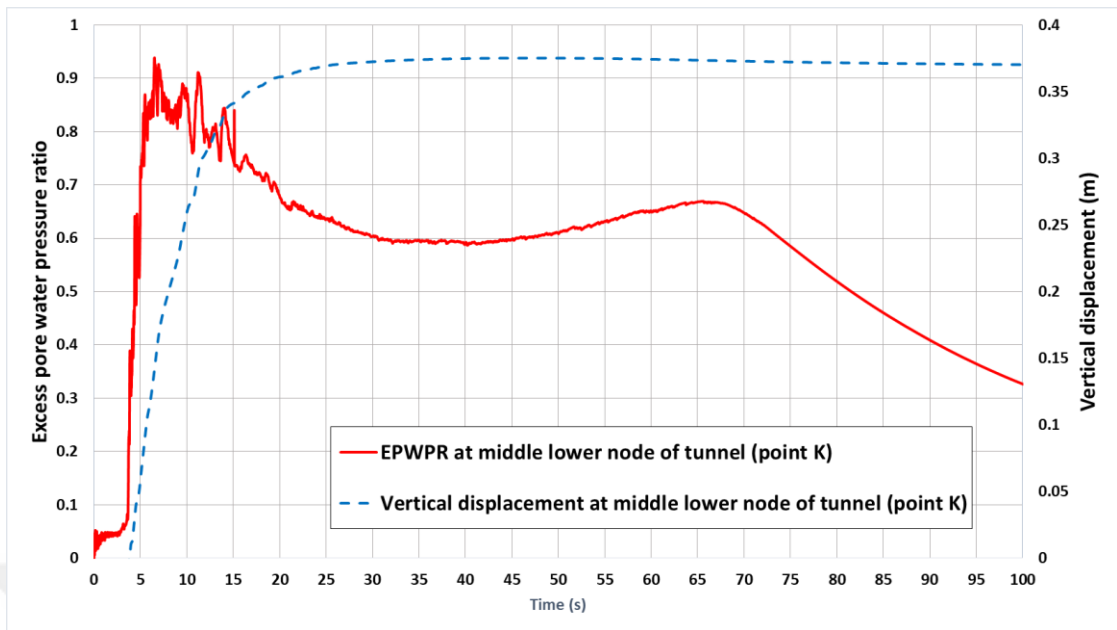


Figure 7.25 : Schematic of extracted results for Far-field, near-field and center nodes of domain.

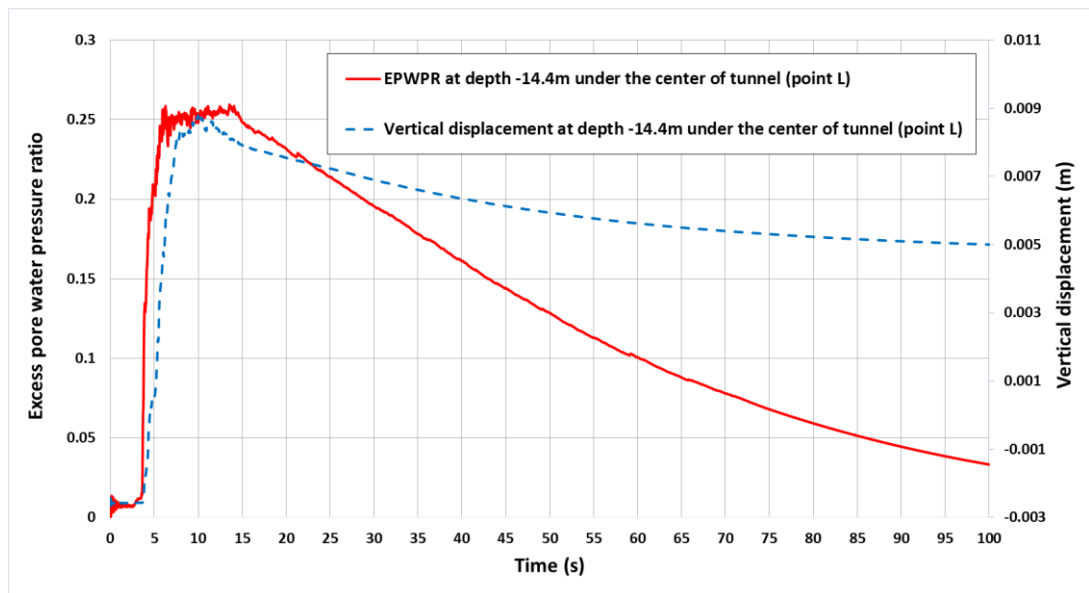


Figure 7.26 : Schematic of extracted results for Far-field, near-field and center nodes of domain.

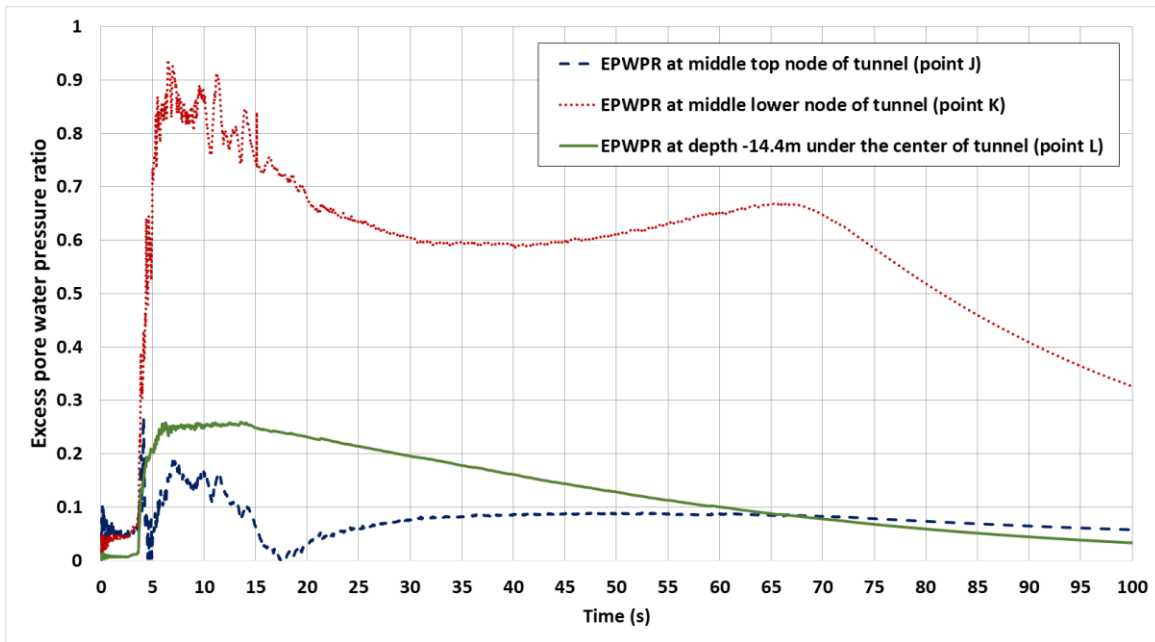


Figure 7.27 : Excess pore water pressure ratios at top and bottom middle point of tunnel and beneath the tunnel.

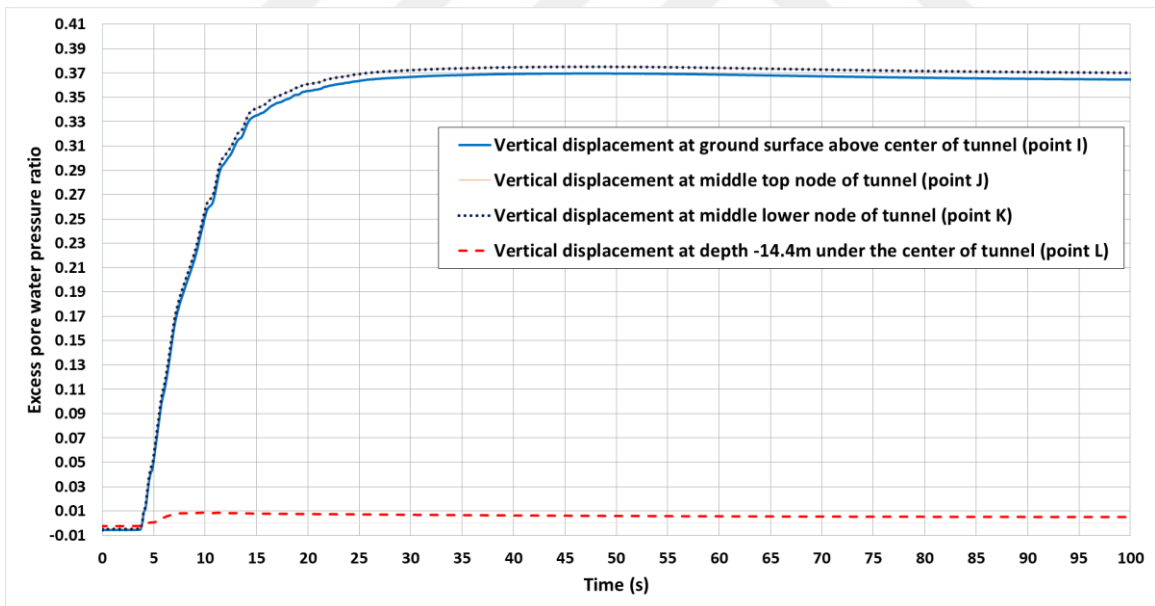


Figure 7.28 : Vertical displacement at different depth within the liquefiable sand in at vertical center line of tunnel.

7.3.2 Comparison of Tunnel-Soil Response in Horizontal Direction

Although, the soil has similar properties at each layer depth but it is essential to measure the behavior of soil in horizontal direction at different depth. Due to existence of underground structure, the behavior of the soil at each layer depth can be different. Figure 7.29 illustrated the distribution of vertical displacement at different depth within the liquefiable sand. The result shows that uplift displacement of tunnel and the overlaying soil mass are similar, however, the vertical displacement reduced as depth increases. The settlement at far-field is significant up to certain depth then it is decreased as depth increases.

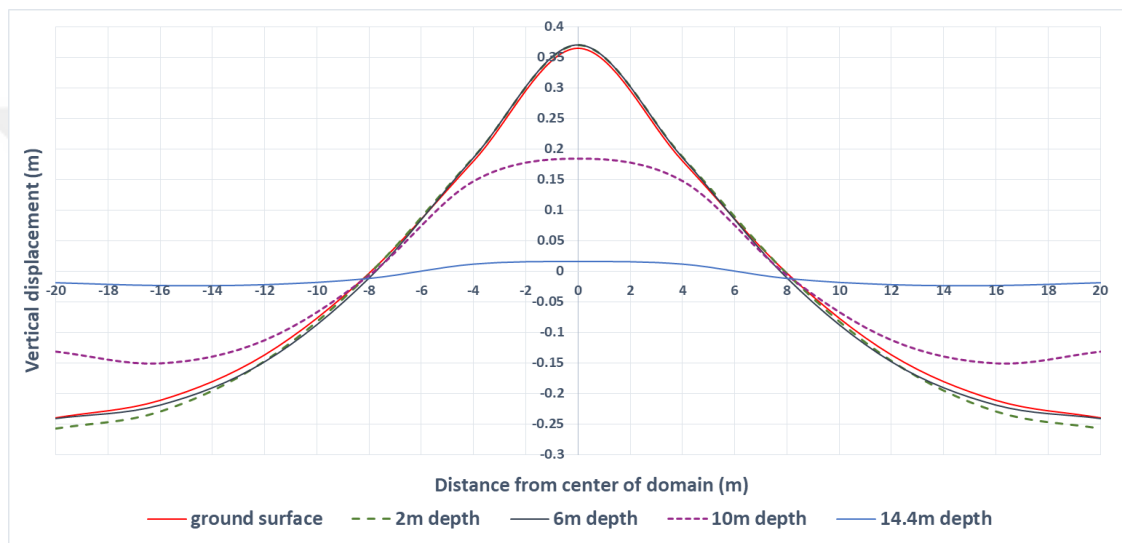


Figure 7.29 : Distribution of vertical displacement at different depth.

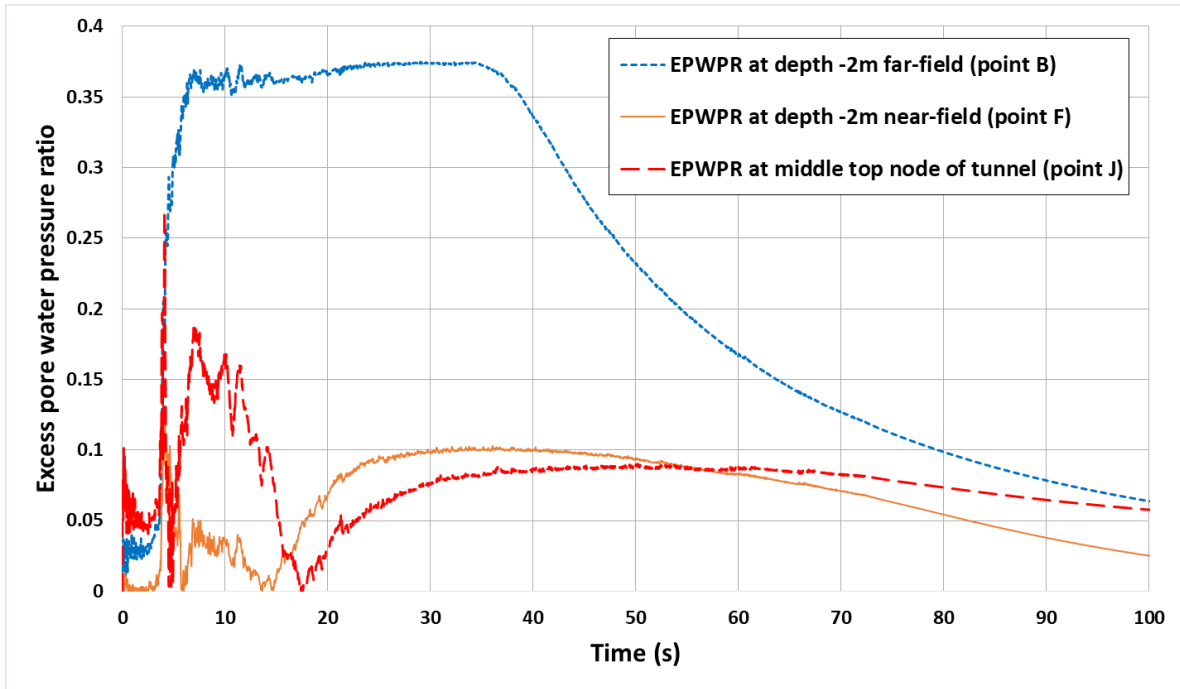


Figure 7.30 : Excess pore water pressure ratio comparison for far-field, near-field and at center of domain at 2m depth.

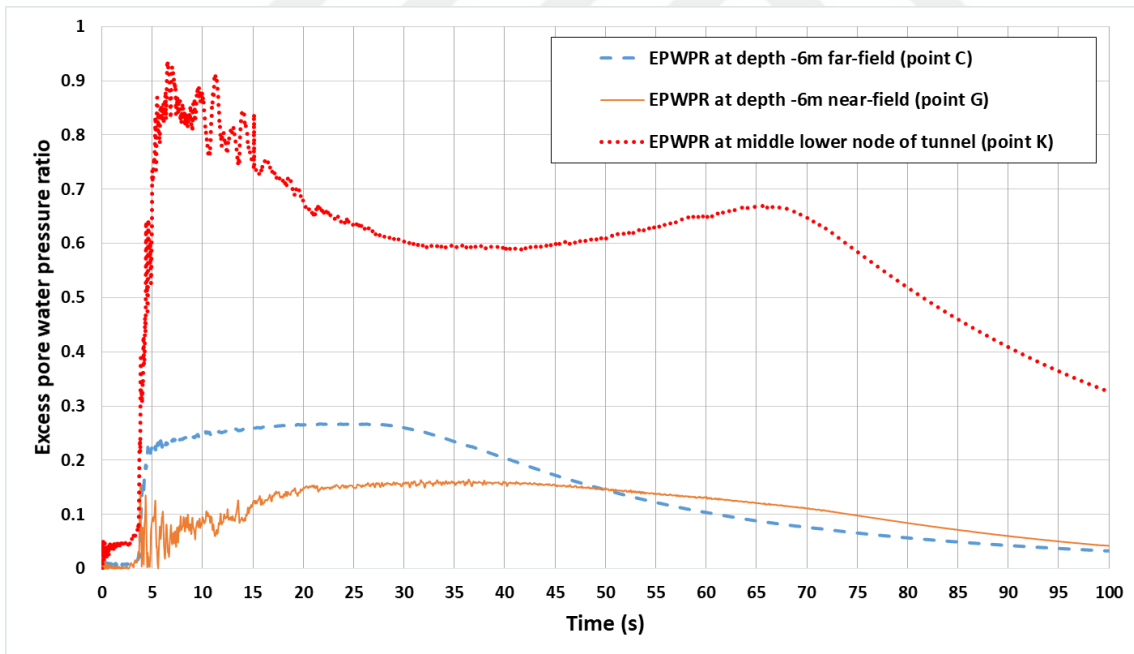


Figure 7.31 : Excess pore water pressure ratio comparison for far-field, near-field and at center of domain at 6m depth.

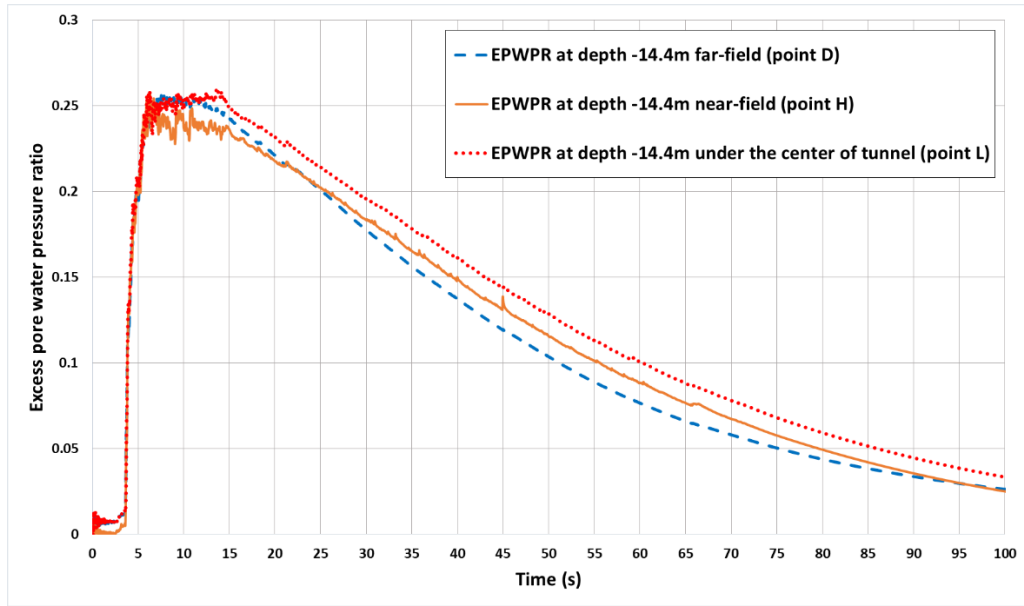


Figure 7.32 : Excess pore water pressure ratio comparison for far-field, near-field and at center of domain at 14.4m depth.

7.3.3 Ground Surface Vertical Displacement

During site response analysis, obtaining acceleration from simulation at ground surface should be in good match with recorded ground motion data. Therefore, it is also necessary to evaluate the accelerations at ground surface level when there is an interaction between underground structure and soil domain. The result of vertical displacement at ground level shown in Figures 7.33, 7.34 and 7.35.

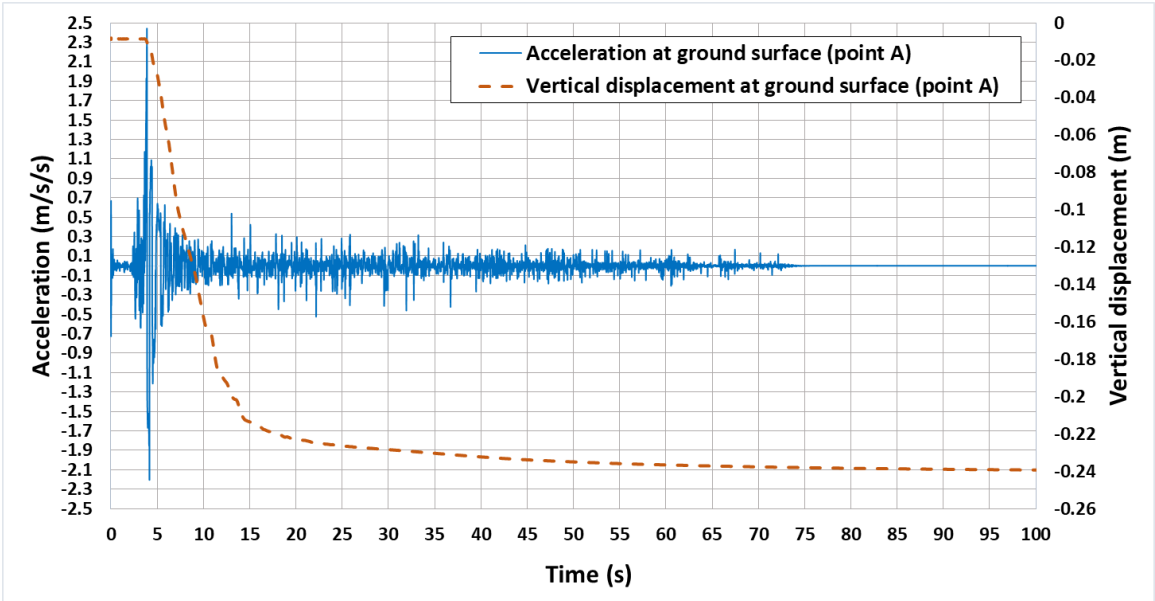


Figure 7.33 : Acceleration vs. vertical displacement at ground surface level in far-field

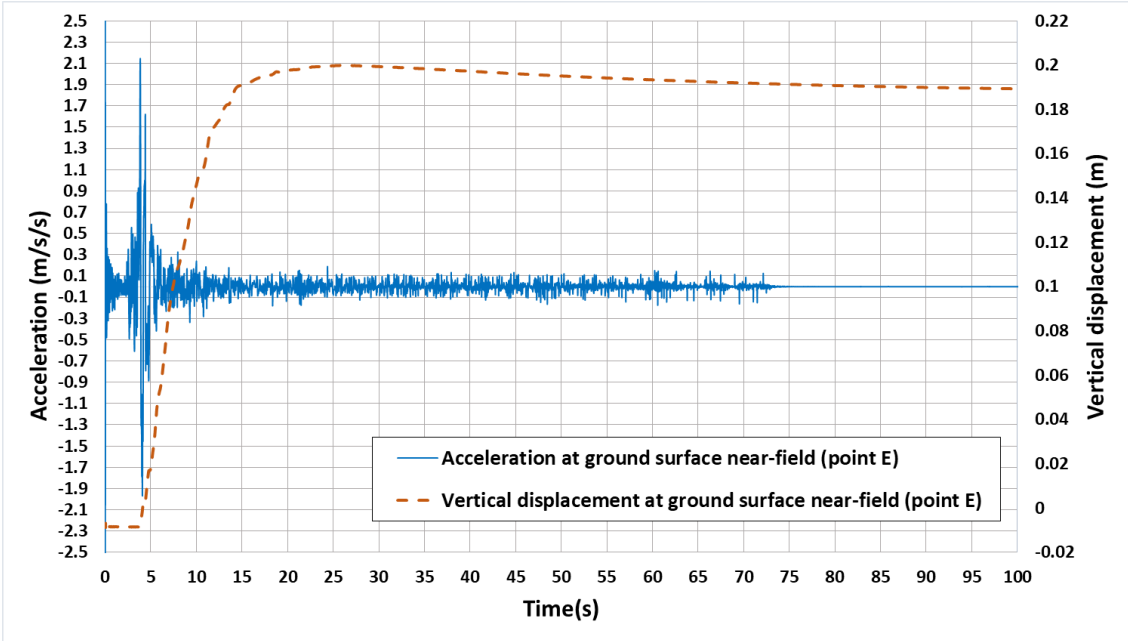


Figure 7.34 : Acceleration versus vertical displacement at ground surface level in near-field 3m away from tunnel.

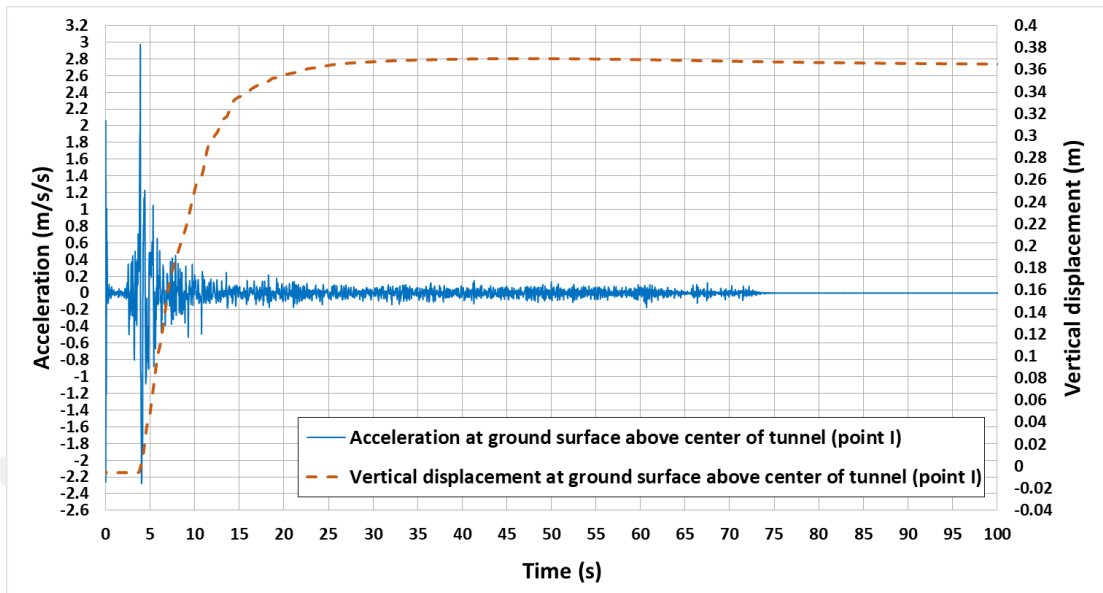


Figure 7.35 : Acceleration versus vertical displacement at ground surface level above the tunnel.

7.4 Effect of Relative Density and Permeability

To investigate the effect of relative density and permeability, Nevada sand with three different relative densities ($D_r=40\%$, 50% and 63%) considered as liquefiable sand overlaying medium dense sand with relative density 68% . The soil constitutive model calibrated parameters for Nevada loose to medium sand with relative densities $D_r=40\%$, 50% and 63% , medium dense sand with relative density $D_r=68\%$ and corresponding hydraulic conductivities are retrieved from (Karimi & Dashti,2016) as demonstrated in table 7.1 and table 7.2.

Table 7.1: Calibrated Parameters of PDMY02 soil constitutive model for various Relative Density. (Karimi & Dashti,2016)

Parameter	Nevada sand						Silica silt	Monterey sand	Description
	30	40	50	63	68	90	85	85	
D_r (%)	30	40	50	63	68	90	85	85	Relative density
e	0.76	0.73	0.70	0.66	0.65	0.58	0.88	0.56	Void ratio
ton/m ³	1.95	1.96	1.97	2.00	2.01	2.06	1.86	2.01	Saturated unit weight
P'_r (kPa)	101	101	101	101	101	101	101	101	Reference effective confining pressure
$G_{\max,1,\text{oct}}$ (MPa)	34.5	46.2	57.1	72.5	77.1	101.9	87.6	133.3	Octahedral low-strain shear modulus
$\gamma_{\max,r}$	0.1	0.1	0.1	0.1	0.1	0.1	0.1	0.1	Maximum octahedral shear strain
B_r (MPa)	92.0	123.3	152.4	193.6	205.9	272.1	233.8	264.0	Bulk modulus
d	0.5	0.5	0.5	0.5	0.5	0.5	0.5	0.5	Pressure dependency coefficient
$\varphi_{\text{TXC}}(\text{PDMY})$	31°	32°	33.5°	34.5°	36°	40.0°	41.0°	42°	Triaxial friction angle used by model
φ_{PT}	31°	30°	25.5°	26.5°	26°	26.5°	36.0°	32°	Phase transformation angle
c_1	0.087	0.067	0.05	0.04	0.02	0.016	0.3	0.014	Control the shear-induced volumetric change,
c_2	5.0	4.5	4.0	2.5	1.5	1.45	5.0	2.0	contraction tendency based on the dilation
c_3	0.3	0.27	0.25	0.2	0.15	0.14	1.5	0.15	history, and overburden stress effect, respectively
d_1	0.01	0.02	0.06	0.07	0.15	0.25	0.02	0.36	Reflect dilation tendency, stress history, and
d_2	3.0	3.0	3.0	3.0	3.0	3.0	3.0	3.0	overburden stress, respectively
d_3	0.0	0.0	0.0	0.0	0.0	0.0	0.0	0.005	
NYS	20	20	20	20	20	20	20	20	Number of yield surfaces generated by model
liq ₁	1.0	1.0	1.0	1.0	1.0	1.0	1.0	1.0	Account for permanent shear strain (slip strain
liq ₂	0.0	0.0	0.0	0.0	0.0	0.0	0.0	0.0	or cyclic mobility) in sloping ground

Table 7.2: Permeability coefficients for different relative densities. (Karimi & Dashti,2016)

Soil type	D_r (%)	Hydraulic conductivity k (m/s)		
		k at 1 g with water	Source	k at 55 g with fluid 22 times more viscous than water
Nevada sand	30–35	7.50×10^{-5}	Arulmoli et al. (1992)	1.88×10^{-4}
	40–45	6.50×10^{-5}		1.63×10^{-4}
	50–55	6.00×10^{-5}		1.50×10^{-4}
	60–65	5.00×10^{-5}		1.25×10^{-4}
	85–90	2.25×10^{-5}		5.63×10^{-5}
Monterey sand	85	5.29×10^{-4}	McCartney et al. (2005)	1.32×10^{-3}
Silica silt	—	3.00×10^{-8}	Malvick et al. (2006)	7.50×10^{-8}

The analyses procedure were similar to previous section as gravity analysis followed by dynamic analysis.

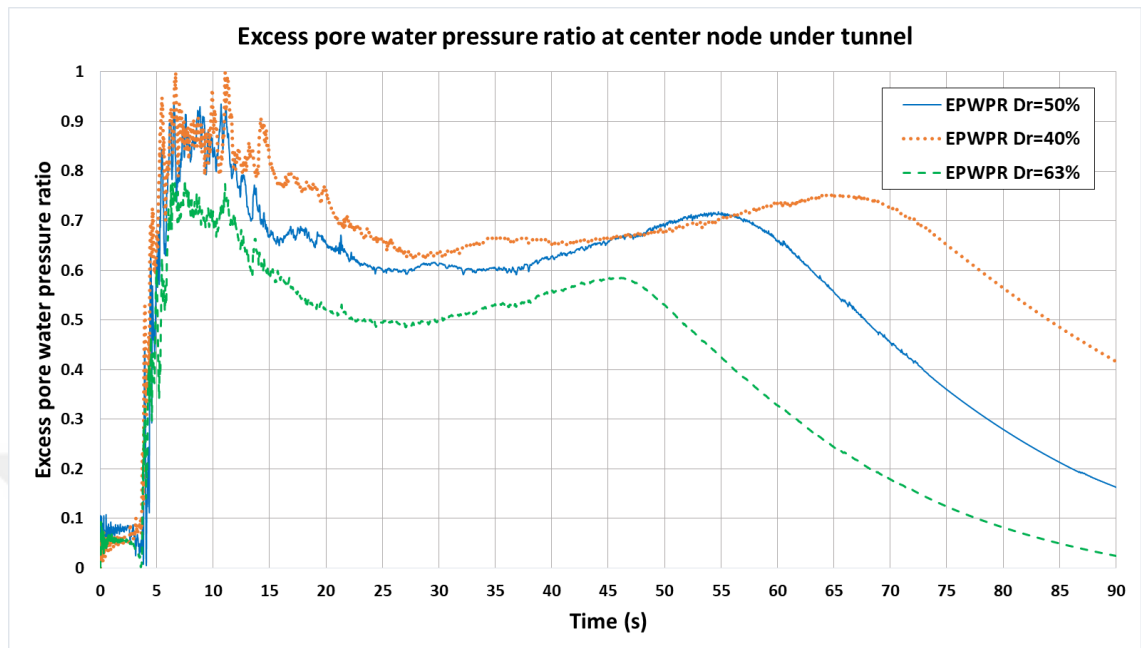


Figure 7.36 : Excess pore water pressure ratio generation and dissipation history at middle point under the tunnel.

The pore water pressure ratio histories in Figure 7.36 show that liquefaction onset is similar for different relative densities. However, it is observed that saturated sand with 63% not liquefied completely.

In terms of effect of permeability, pore water pressure dissipation occur in the similar manner as it decreases with approximately same slope. However, pore water pressure dissipation in sand with higher relative density happens earlier due to smaller permeability coefficient and consequently less pore water pressure generation.

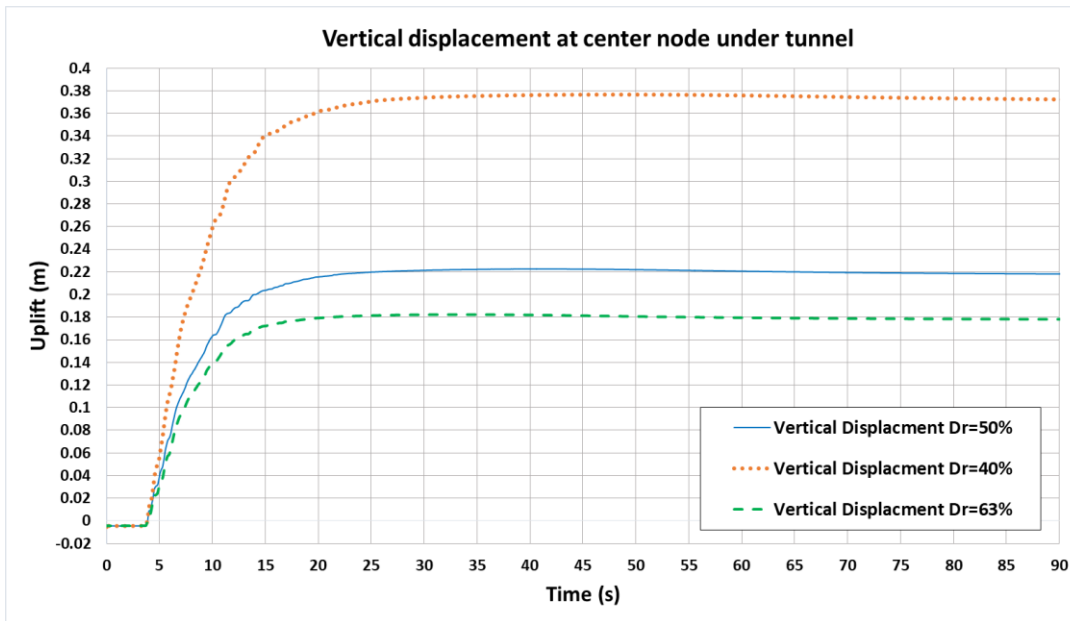


Figure 7.37 : Uplift of Tunnel due to different relative densities at middle point beneath the tunnel.

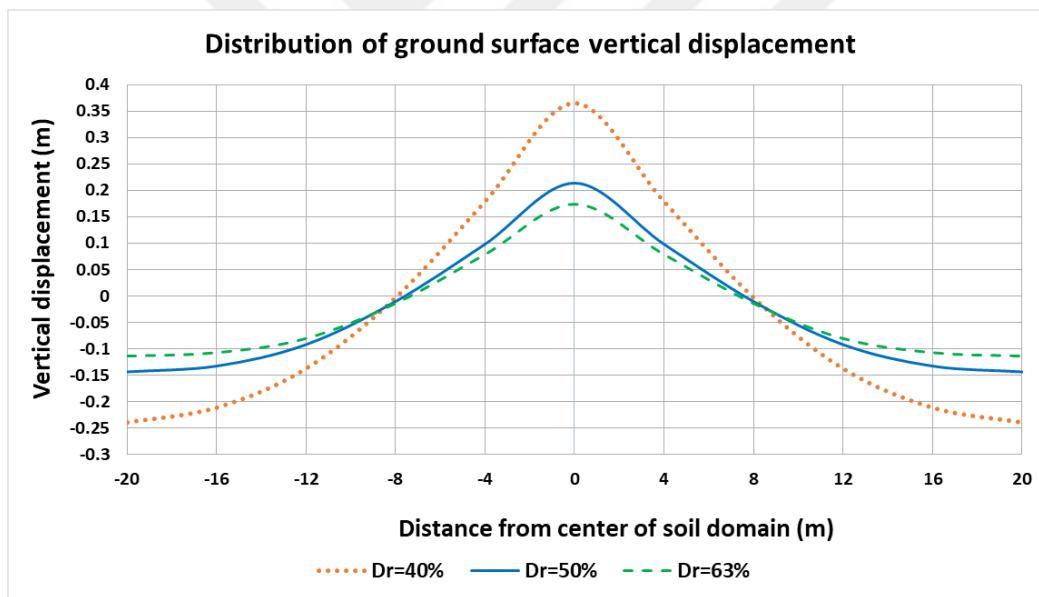


Figure 7.38 : Distribution of ground surface displacement for different relative densities.

Figure 7.38 shows the distribution of vertical displacement of ground surface for tunnel buried in liquefiable sand with different relative densities. The tunnel suffer less uplift and settlement in sand with higher relative density. However, the rate of uplift and settlement displacement decreases as relative density increases. The results of simulations are in agreement with the works done by (Sharafi & Parsafar,2016 ;Saeedzadeh & Hataf,2011).

8. CONCLUSION AND FUTURE WORK RECOMMENDATION

This thesis presents evaluation of tunnel behavior in liquefiable ground during strong ground motion shaking. To investigate the behavior of tunnel in liquefiable soil, numerical simulations using solid-fluid fully coupled effective stress were conducted in OpenSees open source code platform.

The parameters effecting behavior of tunnel can be categorized in three main group:

- Effect of different soil constitutive model parameters on uplift and settlement of soil-structure system.
- Effect of geometric of tunnel and soil domain on uplift and settlement of tunnel-soil system such as buried depth of tunnel and effect of height to wide ratio of tunnel.
- Effect of ground motion characteristic's parameters such as frequency contents of motion, amplitude of ground motion and duration.

In terms of investigation the effect of soil constitutive parameters on tunnel-soil behavior, it is not logical to compare the effect of material parameter by changing only one parameter as long as, changing one soil constitutive model parameter will effect on other correlated parameters. Therefore, changing a parameter will led to different soil behavior due to monotonic and cyclic loading under drained or undrained conditions and more advance procedure needed for soil constitutive model calibration for implementation in finite element modeling.

An extensive soil constitutive model calibration was carried out for PressureDependentMultiYield model (PDMY02) in Opensees. The aim was to capture more accurate response of the soil to be implemented in nonlinear 2D site response analyses for real liquefiable profile case studies. Calibration was only conducted for loose to dense sand with different blow counts of SPT test reported by researchers.

Numerical evaluation was conducted with Single element simulation for monotonic and cyclic simple shear test. Different initial confining vertical pressures was considered to simulate soil behavior at different depths. The simulation results was compared with EPRI1993 recomanded modulus reduction for sand. The result of calibrated parameters were in agreement with EPRI1993 recomanded modulus reduction. Furthermore, the calibrated constitutive model parameters were used to validate the 2D site response of Wildlife Array site and Kobe port island site as real case studies. For Wildlife Array site, downhole array record of Superstition Hills

earthquake was used as an input motion at the base of the model. For Kobe Port Island station site, the downhole array record at depth 32m of 1995 Kobe earthquake was used as an input motion. The acceleration, velocity and displacement time histories at ground surface level from simulations were in good agreement with recorded data at each site.

On the other hand, investigation the effect of geometry and ground motion characteristics, only frequency content and acceleration amplitude, on tunnel-soil system in liquefiable soil have been widely evaluated in literature due to simpler procedure for implementation.

In this research, emphasize was on evaluating effect of combined horizontal and vertical excitation, post-liquefaction phase on uplift and settlement of tunnel-soil system and effect of different relative density on tunnel uplift.

According to the results of tunnel-soil system in this research, the conclusions can be drawn as follow:

- The pore water pressure generated suddenly as amplitude of acceleration increased. The loose sand remain liquefied for some time
- In terms of evaluating the effect of horizontal and vertical excitation combination, for vertical to horizontal maximum amplitude ratio higher than unity ($V/H > 1$) an increase in uplift displacement of tunnel was observed. On the other hand, combination of horizontal and vertical excitation with V/H less than 1 will reduces the uplift displacement as it damps out the effect of horizontal excitation.
- In spite of different relative densities, liquefaction onset occur at the same time. However, it is observed that saturated sand with 63% not liquefied completely.
- Pore water pressure dissipated with similar rate for different relative densities.
- Sand with higher relative density did not liquefied due to generation of less pore water pressure. Therefore, dissipation begin earlier compare to sand with smaller relative density.
- Both uplift of tunnel near-field and settlement in far-field in sand with higher relative density are smaller as relative density increases.
- The rate of uplift and settlement displacement of tunnel increases as relative density decreases.

REFERENCES

- Baird, A., Palermo, A., and Pampanin, S.** (2013). Controlling Seismic Response using Passive Energy Dissipating Cladding Connections. New Zealand Society for Earthquake Engineering Conference. 2013, Christchurch, New Zealand.
- Adamidis, O., & Madabhushi, G. S. P.** (2016, February). Post-liquefaction reconsolidation of sand. In Proc. R. Soc. A (Vol. 472, No. 2186, p. 20150745). The Royal Society.
- Azadi, M., & Hosseini, S. M. M.** (2010). The uplifting behavior of shallow tunnels within the liquefiable soils under cyclic loadings. *Tunnelling and Underground Space Technology*, 25(2), 158-167.
- Azadi, M., & Hosseini, S. M. M.** (2010). Analyses of the effect of seismic behavior of shallow tunnels in liquefiable grounds. *Tunnelling and underground space technology*, 25(5), 543-552.
- Bao, X., Xia, Z., Ye, G., Fu, Y., & Su, D.** (2017). Numerical analysis on the seismic behavior of a large metro subway tunnel in liquefiable ground. *Tunnelling and Underground Space Technology*, 66, 91-106.
- Boore, D. M., & Bommer, J. J.** (2005). Processing of strong-motion accelerograms: needs, options and consequences. *Soil Dynamics and Earthquake Engineering*, 25(2), 93-115.
- Chen, R., Yao, Y., Wang, R., & Zhang, J. M.** (2014). Three-Dimensional Finite Element Analysis of Underground Structures' Dynamic Response in Liquefiable Soil. In *Advances in Soil Dynamics and Foundation Engineering* (pp. 572-578).
- Chen, G., Chen, S., Qi, C., Du, X., Wang, Z., & Chen, W.** (2015). Shaking table tests on a three-arch type subway station structure in a liquefiable soil. *Bulletin of Earthquake Engineering*, 13(6), 1675-1701.
- Chian, S. C., Tokimatsu, K., & Madabhushi, S. P. G.** (2014). Soil Liquefaction–Induced Uplift of Underground Structures: Physical and Numerical Modeling. *Journal of Geotechnical and Geoenvironmental Engineering*, 140(10), 04014057.
- Chian, S. C., Tokimatsu, K., & Gopal Madabhushi, S. P.** (2015). Closure to “Soil Liquefaction–Induced Uplift of Underground Structures: Physical and Numerical Modeling” by Siau Chen Chian, Kohji Tokimatsu, and Santana Phani Gopal Madabhushi. *Journal of Geotechnical and Geoenvironmental Engineering*, 141(9), 07015020.
- Chian, S. C., & Madabhushi, S. P. G.** (2012). Effect of soil conditions on uplift of underground structures in liquefied soil. *Journal of Earthquake and Tsunami*, 6(04), 1250020.
- Chian, S. C., & Madabhushi, S. P. G.** (2012). Effect of buried depth and diameter on uplift of underground structures in liquefied soils. *Soil Dynamics and Earthquake Engineering*, 41, 181-190.

- Choobbasti, A. J., Vahdatirad, M. J., Torabi, M., Firouzian, S., & Barari, A.** (2012). Assessment of soil liquefaction potential based on numerical method-a case study of an urban railway project. *Arabian Journal of Geosciences*, 5(4), 545-554.
- Cilingir, U., & Madabhushi, S. G.** (2011). A model study on the effects of input motion on the seismic behaviour of tunnels. *Soil Dynamics and Earthquake Engineering*, 31(3), 452-462.
- Cubrinovski, M., Ishihara, K., & Tanizawa, F.** (1996). Numerical simulation of the Kobe Port Island liquefaction. In Proc. 11th World Conf. on Earthquake Eng.
- Cuthill, E., & McKee, J.** (1969, August). Reducing the bandwidth of sparse symmetric matrices. In Proceedings of the 1969 24th national conference (pp. 157-172). ACM.
- Dikmen, S. U., & Ghaboussi, J.** (1984). Effective stress analysis of seismic response and liquefaction: theory. *Journal of Geotechnical Engineering*, 110(5), 628-644.
- Electric Power Research Institute (EPRI).** (1993). "Guidelines for determining design basis ground motions." Final Rep. EPRI TR-102293, Electric Power Research Institute, Palo Alto, CA.
- Elgamal, A., Yang, Z., & Parra, E.** (2002). Computational modeling of cyclic mobility and post-liquefaction site response. *Soil Dynamics and Earthquake Engineering*, 22(4), 259-271.
- Elgamal, A., Yang, Z., Parra, E., & Ragheb, A.** (2003). Modeling of cyclic mobility in saturated cohesionless soils. *International Journal of Plasticity*, 19(6), 883-905.
- Gingery, J. R.** (2014). Effects of Liquefaction on Earthquake Ground Motions. PhD dissertation draft, University of California, San Diego.
- Greenfield, M. W.** (2017). Effects of long-duration ground motions on liquefaction hazards (Doctoral dissertation).
- Hashash, Y. M., Dashti, S., Romero, M. I., Ghayoomi, M., & Musgrove, M.** (2015). Evaluation of 1-D seismic site response modeling of sand using centrifuge experiments. *Soil Dynamics and Earthquake Engineering*, 78, 19-31.
- Hu, J. L., & Liu, H. B.** (2017). The Uplift Behavior of a Subway Station during Different Degree of Soil Liquefaction. *Procedia Engineering*, 189, 18-24.
- Idriss, I. M., and Boulanger, R. W.** (2008). Soil liquefaction during earthquakes. Monograph MNO-12, Earthquake Engineering Research Institute, Oakland, CA, 261 pp.
- Ishihara, K.** (1996). Soil behaviour in earthquake geotechnics. Clarendon Press.
- Jefferies, M., & Been, K.** (2015). Soil liquefaction: a critical state approach. CRC press.)
- Jeremic, B.** (2001). Development of geotechnical capabilities in OpenSees. EERI.

- Jeremić, B., & Yang, Z.** (2002). Template elastic-plastic computations in geomechanics. *International Journal for Numerical and Analytical Methods in Geomechanics*, 26(14), 1407-1427.
- Joyner, W. B., & Chen, A. T.** (1975). Calculation of nonlinear ground response in earthquakes. *Bulletin of the Seismological Society of America*, 65(5), 1315-1336.
- Kang, G. C., Tobita, T., & Iai, S.** (2014). Seismic simulation of liquefaction-induced uplift behavior of a hollow cylinder structure buried in shallow ground. *Soil Dynamics and Earthquake Engineering*, 64, 85-94.
- Karimi, Z., & Dashti, S.** (2016). Seismic performance of shallow founded structures on liquefiable ground: validation of numerical simulations using centrifuge experiments. *Journal of Geotechnical and Geoenvironmental Engineering*, 142(6), 04016011.
- Karimi, Z., & Dashti, S.** (2015). Numerical and centrifuge modeling of seismic soil–foundation–structure interaction on liquefiable ground. *Journal of Geotechnical and Geoenvironmental Engineering*, 142(1), 04015061.
- Koseki, J., Matsuo, O., & Koga, Y.** (1997). Uplift behavior of underground structures caused by liquefaction of surrounding soil during earthquake. *Soils and Foundations*, 37(1), 97-108.
- Kramer, S. L.** (1996). *Geotechnical earthquake engineering*. Upper Saddle River, N.J: Prentice Hall.
- Lee, C. J., Wei, Y. C., Chuang, W. Y., Hung, W. Y., Wu, W. L., & Ho, T. Y.** (2017). Uplift mechanism of rectangular tunnel in liquefied soils. In *Geotechnical Hazards from Large Earthquakes and Heavy Rainfalls* (pp. 61-74). Springer Japan.
- Li, L., Wu, L., Wang, X., & Cui, Z.** (2015). Seismic Response of Underground Structures in Saturated Soil Based on the Fluid-Solid Coupling Dynamic Formulation. *Journal of Coastal Research*, 73(sp1), 432-435.
- Ling, H. I., Mohri, Y., Kawabata, T., Liu, H., Burke, C., & Sun, L.** (2003). Centrifugal modeling of seismic behavior of large-diameter pipe in liquefiable soil. *Journal of geotechnical and geoenvironmental engineering*, 129(12), 1092-1101.
- Liu, H., & Song, E.** (2005). Seismic response of large underground structures in liquefiable soils subjected to horizontal and vertical earthquake excitations. *Computers and Geotechnics*, 32(4), 223-244.
- Liu, H., & Song, E.** (2006). Working mechanism of cutoff walls in reducing uplift of large underground structures induced by soil liquefaction. *Computers and Geotechnics*, 33(4), 209-221.
- Lu, Y.** (2016). *Seismic soil-structure interaction in performance-based design* (Doctoral dissertation, University of Nottingham).
- Madabhushi, S. S. C., & Madabhushi, S. P. G.** (2015). Finite element analysis of floatation of rectangular tunnels following earthquake induced liquefaction. *Indian Geotechnical Journal*, 45(3), 233-242.

- Matyka, M., Khalili, A., & Koza, Z.** (2008). Tortuosity-porosity relation in porous media flow. *Physical Review E*, 78(2), 026306.
- Maugeri, M., & Soccodato, C. (Eds.)**. (2014). *Earthquake geotechnical engineering design* (Vol. 28). Springer Science & Business Media.
- Mazzoni, S., McKenna, F., Scott, M. H., & Fenves, G. L.** (2006). *The Open System for Earthquake Engineering Simulation (OpenSEES) User Command-Language Manual*.
- McGann, C., & Arduino, P.** (2011, March 24). Dynamic 2D Effective Stress Analysis of Slope. Retrieved January 6, 2018,
- McGann, C.** (2013). Numerical evaluation of forces on piled bridge foundations in laterally spreading soil (Doctoral dissertation).
- Orense, R. P., Morimoto, I., Yamamoto, Y. A., Yumiyama, T., Yamamoto, H., & Sugawara, K.** (2003). Study on wall-type gravel drains as liquefaction countermeasure for underground structures. *Soil Dynamics and Earthquake Engineering*, 23(1), 19-39.
- Rauch, A. F.** (1997). EPOLLS: An empirical method for predicting surface displacements due to liquefaction-induced lateral spreading in earthquakes. Virginia Polytechnic Institute and State University, USA.
- Saeedzadeh, R., & Hataf, N.** (2011). Uplift response of buried pipelines in saturated sand deposit under earthquake loading. *Soil Dynamics and Earthquake Engineering*, 31(10), 1378-1384.
- Sharafi, H., & Parsafar, P.** (2016). Seismic simulation of liquefaction-induced uplift behavior of buried pipelines in shallow ground. *Arabian Journal of Geosciences*, 9(3), 215.
- Sharp, M. K., Dobry, R., & Abdoun, T.** (2003). Liquefaction centrifuge modeling of sands of different permeability. *Journal of geotechnical and geoenvironmental engineering*, 129(12), 1083-1091.
- Su, D.** (2005). Centrifuge investigation on responses of sand deposit and sand-pile system under multi-directional earthquake loading (Doctoral dissertation).
- Ti, K.S., Huat, B.B.K., Noorzaei, J., Jaafar, M.S., Sew, G.S.,** 2009. A review of basic soil constitutive models for geotechnical application. *Electronic Journal of Geotechnical Engineering* 14, 1–18.
- Tobita, T., Kang, G. C., & Iai, S.** (2011). Estimation of liquefaction-induced manhole uplift displacements and trench-backfill settlements. *Journal of Geotechnical and Geoenvironmental Engineering*, 138(4), 491-499.
- Tokimatsu, K., Tamura, S., Suzuki, H., & Katsumata, K.** (2012). Building damage associated with geotechnical problems in the 2011 Tohoku Pacific Earthquake. *Soils and Foundations*, 52(5), 956-974.
- Unjoh, S., Kaneko, M., Kataoka, S., Nagaya, K., & Matsuoka, K.** (2012). Effect of earthquake ground motions on soil liquefaction. *Soils and Foundations*, 52(5), 830-841.

- Vaid, Y. P., Fisher, J. M., Kuerbis, R. H., & Negussey, D.** (1990). Particle gradation and liquefaction. *Journal of Geotechnical Engineering*, 116(4), 698-703.
- Veritas, D. N.** (2007). Global buckling of submarine pipelines—structural design due to high temperature/high pressure. *Prática Recomenda*, DNV RP-F110.
- Vytiniotis, A.** (2011). Contributions to the analysis and mitigation of liquefaction in loose sand slopes (Doctoral dissertation, Massachusetts Institute of Technology).
- Yang, J., & Wang, H.** (2013). Seismic Response Analysis of Shallow Utility Tunnel in Liquefiable Soils. In *ICPTT 2012: Better Pipeline Infrastructure for a Better Life* (pp. 1606-1618).
- Yang, Z., & Elgamal, A.** (2002). Influence of permeability on liquefaction-induced shear deformation. *Journal of Engineering Mechanics*, 128(7), 720-729.
- Yang, Z., Elgamal, A., & Parra, E.** (2003). Computational model for cyclic mobility and associated shear deformation. *Journal of Geotechnical and Geoenvironmental Engineering*, 129(12), 1119-1127.
- Ye, B., Ye, G., Zhang, F., & Yashima, A.** (2007). Experiment and numerical simulation of repeated liquefaction-consolidation of sand. *Soils and Foundations*, 47(3), 547-558.
- Zhang, F., Ye, B., & Ye, G.** (2011). Unified description of sand behavior. *Frontiers of Architecture and Civil Engineering in China*, 5(2), 121-150.
- Zhang, Y., Yang, Z., Bielak, J., Conte, J. P., & Elgamal, A.** (2003, July). Treatment of seismic input and boundary conditions in nonlinear seismic analysis of a bridge ground system. In *16th ASCE Engineering Mechanics Conference* (pp. 16-18). University of Washington, Seattle, USA.
- Zhou, J., Wang, Z., Chen, X., & Zhang, J.** (2014). Uplift mechanism for a shallow-buried structure in liquefiable sand subjected to seismic load: centrifuge model test and DEM modeling. *Earthquake Engineering and Engineering Vibration*, 13(2), 203-214.
- Zhuang, H., Hu, Z., Wang, X., & Chen, G.** (2015). Seismic responses of a large underground structure in liquefied soils by FEM numerical modelling. *Bulletin of Earthquake Engineering*, 13(12), 3645-3668.
- Zhuang, H., Chen, G., Hu, Z., & Qi, C.** (2016). Influence of soil liquefaction on the seismic response of a subway station in model tests. *Bulletin of Engineering Geology and the Environment*, 75(3), 1169-1182.
- Zienkiewicz, O. C., & Shiomi, T.** (1984). Dynamic behaviour of saturated porous media; the generalized Biot formulation and its numerical solution. *International journal for numerical and analytical methods in geomechanics*, 8(1), 71-96.



APPENDICES

APPENDIX A: Opensees and post-processing matlab codes

wipe

```
#-----  
# 1. CREATE PORE PRESSURE NODES AND FIXITIES  
#-----  
  
model BasicBuilder -ndm 2 -ndf 3  
  
# define pore pressure nodes:  
  
node 1 -20.000 -20.000  
node 5 -20.000 -18.600  
....  
node 2112 20.000 0.000  
  
set mNodeInfo [open nodeInfo.dat w]  
...  
  
close $mNodeInfo  
  
puts "Finished creating all -ndf 3 nodes..."  
  
# define fixities for pore pressure nodes:  
  
fix 1 0 1 0  
  
fix 1029 0 0 1  
  
....  
  
fix 2112 0 0 1  
  
puts "Finished creating all -ndf 3 boundary conditions..."  
  
# define equal degrees of freedom for pore pressure nodes  
  
equalDOF 1 1987 1 2  
  
....  
  
equalDOF 721 2112 1 2  
  
puts "Finished creating equalDOF for pore pressure nodes..."  
  
#-----  
# 2. CREATE INTERIOR NODES AND FIXITIES  
#-----
```

```

model BasicBuilder -ndm 2 -ndf 2

# define interior nodes

node 2 -20.000 -19.300
node 3 -19.100 -20.000
....
node 2109 20.000 -1.500
node 2111 20.000 -0.500

puts "Finished creating all -ndf 2 nodes..."

# define fixities for interior nodes:

fix 3 0 1
...
fix 1943 0 1

puts "Finished creating all -ndf 2 boundary conditions..."

# define equal degrees of freedom which have not yet been defined

equalDOF 2 1988 1 2
equalDOF 665 2111 1 2

puts "Finished creating equalDOF constraints..."

equalDOF 1 3 1
equalDOF 1 1943 1

puts "Finished creating equalDOF for base..."

#-----
# 3. CREATE SOIL MATERIALS
#-----

nDMaterial PressureDependMultiYield02 2 2 1.96 4.62e4 1.23e5 32\
                                0.1 101 0.5 30 0.067 0.27 0.02\
                                0.0 20 4.5 3.0 1.0 0.0 0.73

set thick2 1.0

```

```

set xWgt2 0.00
set yWgt2 -9.81
set uBulk2 5213698.63
set hPerm2 6.5e-5
set vPerm2 6.5e-5
nDMaterial PressureDependMultiYield02 1 2 2.1 77.1e3 205.9e3 36 0.1\
                                     101 0.5 26 0.02 0.15 0.15 0.0\
                                     20 1.5 3.0 1.0 0.0 0.65

```

```

set thick1 1.0
set xWgt1 0.00
set yWgt1 -9.81
set uBulk1 5584615.385
set hPerm1 3.5e-5
set vPerm1 3.5e-5
puts "Finished creating all soil materials..."

```

```

#-----
# 4. CREATE SOIL ELEMENTS
#-----
# permeabilities are initial set at 1.0 m/s for gravity analysis, values are updated after gravity
element 9_4_QuadUP 1 1036 882 785 952 967 833 865 996 915 $thick2 2 $uBulk2 1.0 1.0 1.0
                $xWgt2 $yWgt2
....
element 9_4_QuadUP 496 2085 2110 2112 2096 2102 2111 2108 2090 2105 $thick2 2 $uBulk2 1.0
                1.0 1.0 $xWgt2 $yWgt2
puts "Finished creating all soil elements..."
#-----
# 6. CREATE BEAM NODES AND FIXITIES

```

```

#-----
model BasicBuilder -ndm 2 -ndf 3

# define beam nodes

node          5222  -2.00  -2.00

....

node          5216  -2.00  -2.25

puts "Finished creating all -ndf 3 beam nodes..."

#-----

# 7. CREATE BEAM MATERIALS AND ELEMENTS

#-----

# beam properties

# geometric transformation

geomTransf Linear $stransTag

# beam section

puts "Finished creating all beam materials..."

element forceBeamColumn      5000  5222  5230  $numIntPts $secTag $stransTag

....

element forceBeamColumn      5063  5216  5222  $numIntPts $secTag $stransTag

puts "Finished creating all beam elements..."

model BasicBuilder -ndm 2 -ndf 2

node          6222  -2.00  -2.00

....

node          7333  0.75  -2.00

puts "Finished creating all zerolengthelement nodes..."

equalDOF      7222  1222  1      2

....

equalDOF      6216  5216  1      2

puts "Finished creating all equal degree of freedom nodes for soil,springs and beamcolumns..."

#-----

# 2. CREATE zerolength SPRING MATERIAL

```



```

#-----
puts "Finished creating all zerolength SPRING materials..."
#-----

# 3. CREATE zerolength SPRING ELEMENTS
#-----

element zeroLength      6000   6222   7222   -mat  4   -dir  1  2
....
element zeroLength      6067   8036   9036   -mat  4   -dir  1  2
puts "Finished creating all zerolength elements..."

```

```

#-----
# 5. LYSMER DASHPOT
#-----

# define dashpot nodes
node  2212  -20.000  -20.000
node  2213  -20.000  -20.000

# define fixities for dashpot nodes
fix 2212  1  1
fix 2213  0  1

# define equal DOF for dashpot and base soil node
equalDOF 1 2213  1

puts "Finished creating dashpot nodes and boundary conditions..."

# define dashpot material
set baseArea  40.0
set dashpotCoeff  1750.00
uniaxialMaterial Viscous 3 [expr $dashpotCoeff*$baseArea] 1

# define dashpot element
element zeroLength 497 2212 2213 -mat 3 -dir 1

puts "Finished creating dashpot material and element..."

```

```

#-----
# 6. DEFINE NODAL MASSES FOR MODELING WATER
#-----

# define nodal masses for 3 dof nodes
model BasicBuilder -ndm 2 -ndf 3

puts "Finished creating -ndf 3 nodal masses..."

# define nodal masses for 2 dof nodes
model BasicBuilder -ndm 2 -ndf 2

puts "Finished creating -ndf 2 nodal masses..."

#-----
# 7. CREATE GRAVITY RECORDERS
#-----

# create list for pore pressure nodes
set nodeList3 {}

set channel [open "nodeInfo.dat" r]

set count 0;

foreach line [split [read -nonewline $channel] \n] {

set count [expr $count+1];

set lineData($count) $line

set nodeNumber [lindex $lineData($count) 0]

lappend nodeList3 $nodeNumber

}

close $channel

# record nodal displacement, acceleration, and porepressure
eval "recorder Node -file Gdisplacement.out -time -node $nodeList3 -dof 1 2 disp"
eval "recorder Node -file Gacceleration.out -time -node $nodeList3 -dof 1 2 accel"
eval "recorder Node -file GporePressure.out -time -node $nodeList3 -dof 3 vel"

# record elemental stress and strain

recorder Element -file Gstress1.out -time -eleRange 1 496 material 1 stress
recorder Element -file Gstress2.out -time -eleRange 1 496 material 2 stress

```

```

recorder Element -file Gstress3.out -time -eleRange 1 496 material 3 stress
recorder Element -file Gstress4.out -time -eleRange 1 496 material 4 stress
recorder Element -file Gstress5.out -time -eleRange 1 496 material 5 stress
recorder Element -file Gstress6.out -time -eleRange 1 496 material 6 stress
recorder Element -file Gstress7.out -time -eleRange 1 496 material 7 stress
recorder Element -file Gstress8.out -time -eleRange 1 496 material 8 stress
recorder Element -file Gstress9.out -time -eleRange 1 496 material 9 stress
recorder Element -file Gstrain1.out -time -eleRange 1 496 material 1 strain
recorder Element -file Gstrain2.out -time -eleRange 1 496 material 2 strain
recorder Element -file Gstrain3.out -time -eleRange 1 496 material 3 strain
recorder Element -file Gstrain4.out -time -eleRange 1 496 material 4 strain
recorder Element -file Gstrain5.out -time -eleRange 1 496 material 5 strain
recorder Element -file Gstrain6.out -time -eleRange 1 496 material 6 strain
recorder Element -file Gstrain7.out -time -eleRange 1 496 material 7 strain
recorder Element -file Gstrain8.out -time -eleRange 1 496 material 8 strain
recorder Element -file Gstrain9.out -time -eleRange 1 496 material 9 strain
puts "Finished creating gravity recorders..."

```

```
#-----
```

```
# 8. CREATE FILES FOR POSTPROCESSING IN GiD
```

```
#-----
```

```
set meshFile [open renameMe.flavia.msh w]
```

```
puts $meshFile "MESH 94quad dimension 2 ElemType Quadrilateral Nnode 4"
```

```
close $meshFile
```

```
set eleFile [open elementInfo.dat w]
```

```
close $eleFile
```

```
#-----
```

```
# 9. DEFINE ANALYSIS PARAMETERS
```

```

#-----
#---GROUND MOTION PARAMETERS
# time step in ground motion record
set motionDT 0.01
# number of steps in ground motion record
set motionSteps 2164002
#---RAYLEIGH DAMPING PARAMETERS
set pi 3.141592654
# damping ratio
set damp 0.02
# lower frequency
set omega1 [expr 2*$pi*0.2]
# upper frequency
set omega2 [expr 2*$pi*20]
# damping coefficients
set a0 [expr 2*$damp*$omega1*$omega2/($omega1 + $omega2)]
set a1 [expr 2*$damp/($omega1 + $omega2)]
puts "damping coefficients: a_0 = $a0; a_1 = $a1"
#---DETERMINE STABLE ANALYSIS TIME STEP USING CFL CONDITION
# maximum shear wave velocity (m/s)
set vsMax 250.0
# element size (m)
set eleSize 1
# duration of ground motion (s)
set duration [expr $motionDT*$motionSteps]
# trial analysis time step
set kTrial [expr $eleSize/(pow($vsMax,0.5))]
# define time step and number of steps for analysis
if { $motionDT <= $kTrial } {
    set nSteps $motionSteps
}

```

```

    set dT    $motionDT
} else {
    set nSteps [expr int(floor($duration/$kTrial)+1)]
    set dT    [expr $duration/$nSteps]
}

puts "number of steps in analysis: $nSteps"
puts "analysis time step: $dT"

#---ANALYSIS PARAMETERS

# Newmark parameters
set gamma 0.5
set beta 0.25
#-----
# 10. GRAVITY ANALYSIS
#-----

# update materials to ensure elastic behavior
updateMaterialStage -material 1 -stage 0
updateMaterialStage -material 2 -stage 0

constraints Penalty 1.e18 1.e18

test    NormDispIncr 1e-3 35 1

algorithm Newton

numberer RCM

system ProfileSPD

integrator Newmark $gamma $beta

analysis Transient

set startT [clock seconds]

analyze 10 500
analyze 10 5000

puts "Finished with elastic gravity analysis..."

# update materials to consider plastic behavior

```

```
updateMaterialStage -material 1 -stage 1
```

```
updateMaterialStage -material 2 -stage 1
```

```
# plastic gravity loading
```

```
analyze 10 5.0e-3
```

```
puts "Finished with plastic gravity analysis..."
```

```
#-----
```

```
# 11. UPDATE ELEMENT PERMEABILITY VALUES FOR POST-GRAVITY ANALYSIS
```

```
#-----
```

```
# choose base number for parameter IDs which is higher than other tags used in analysis
```

```
set ctr 10000.0
```

```
# loop over elements to define parameter IDs
```

```
for {set i 1} {$i<=496} {incr i 1} {
```

```
    parameter [expr int($ctr+1.0)] element $i vPerm
```

```
    parameter [expr int($ctr+2.0)] element $i hPerm
```

```
    set ctr [expr $ctr+2.0]
```

```
}
```

```
# update permeability parameters for each element
```

```
updateParameter 10001 $vPerm1
```

```
updateParameter 10002 $hPerm1
```

```
....
```

```
updateParameter 10990 $vPerm1
```

```
updateParameter 10991 $vPerm2
```

```
updateParameter 10992 $hPerm2
```

```
#-----
```

```
# 12. CREATE POST-GRAVITY RECORDERS
```

```
#-----
```

```
# reset time and analysis
```

```
setTime 0.0
```

```
wipeAnalysis
```

```

remove recorders

# recorder time step

set recDT [expr 2*$motionDT]

# record nodal displacement, acceleration, and porepressure

eval "recorder Node -file displacement.out -time -dT $recDT -node $nodeList3 -dof 1 2 disp"
eval "recorder Node -file acceleration.out -time -dT $recDT -node $nodeList3 -dof 1 2 accel"
eval "recorder Node -file porePressure.out -time -dT $recDT -node $nodeList3 -dof 3 vel"

# record elemental stress and strain

recorder Element -file stress1.out -time -dT $recDT -eleRange 1 496 material 1 stress
recorder Element -file stress2.out -time -dT $recDT -eleRange 1 496 material 2 stress
recorder Element -file stress3.out -time -dT $recDT -eleRange 1 496 material 3 stress
recorder Element -file stress4.out -time -dT $recDT -eleRange 1 496 material 4 stress
recorder Element -file stress5.out -time -dT $recDT -eleRange 1 496 material 5 stress
recorder Element -file stress6.out -time -dT $recDT -eleRange 1 496 material 6 stress
recorder Element -file stress7.out -time -dT $recDT -eleRange 1 496 material 7 stress
recorder Element -file stress8.out -time -dT $recDT -eleRange 1 496 material 8 stress
recorder Element -file stress9.out -time -dT $recDT -eleRange 1 496 material 9 stress

recorder Element -file strain1.out -time -dT $recDT -eleRange 1 496 material 1 strain
recorder Element -file strain2.out -time -dT $recDT -eleRange 1 496 material 2 strain
recorder Element -file strain3.out -time -dT $recDT -eleRange 1 496 material 3 strain
recorder Element -file strain4.out -time -dT $recDT -eleRange 1 496 material 4 strain
recorder Element -file strain5.out -time -dT $recDT -eleRange 1 496 material 5 strain
recorder Element -file strain6.out -time -dT $recDT -eleRange 1 496 material 6 strain
recorder Element -file strain7.out -time -dT $recDT -eleRange 1 496 material 7 strain
recorder Element -file strain8.out -time -dT $recDT -eleRange 1 496 material 8 strain
recorder Element -file strain9.out -time -dT $recDT -eleRange 1 496 material 9 strain

puts "Finished creating all recorders..."

#-----
# 13. DYNAMIC ANALYSIS
#-----

```

```

model BasicBuilder -ndm 2 -ndf 3

# define constant scaling factor for applied velocity
set cFactor [expr $baseArea*$dashpotCoeff]

# define velocity time history file
set velocityFile velocityHistoryhorizontal.out

# timeseries object for force history
set mSeries "Path -dt $motionDT -filePath $velocityFile -factor $cFactor"

# loading object
pattern Plain 10 $mSeries {
    load 1 1.0 0.0 0.0
}
puts "Dynamic loading created..."
constraints Penalty 1.e20 1.e20
test    NormDispIncr 1.0e-3 35 1
algorithm Newton
numberer RCM
system ProfileSPD

integrator Newmark $gamma $beta
rayleigh $a0 $a1 0.0 0.0
analysis Transient

# perform analysis with timestep reduction loop
set ok [analyze $nSteps $dT]

# if analysis fails, reduce timestep and continue with analysis
if {$ok != 0} {
    puts "did not converge, reducing time step"
    set curTime [getTime]
    puts "curTime: $curTime"
    set curStep [expr $curTime/$dT]
    puts "curStep: $curStep"
    set remStep [expr int(($nSteps-$curStep)*2.0)]
}

```



```

puts "remStep: $remStep"

set dT    [expr $dT/2.0]

puts "dT: $dT"

set ok [analyze $remStep $dT]

# if analysis fails again, reduce timestep and continue with analysis
if {$ok != 0} {

    puts "did not converge, reducing time step"

    set curTime [getTime]

    puts "curTime: $curTime"

    set curStep [expr $curTime/$dT]

    puts "curStep: $curStep"

    set remStep [expr int(($remStep-$curStep)*2.0)]

    puts "remStep: $remStep"

    set dT    [expr $dT/2.0]

    puts "dT: $dT"

    set ok [analyze $remStep $dT]

}

# if analysis fails again, reduce timestep and continue with analysis
if {$ok != 0} {

    puts "did not converge, reducing time step"

    set curTime [getTime]

    puts "curTime: $curTime"

    set curStep [expr $curTime/$dT]

    puts "curStep: $curStep"

    set remStep [expr int(($remStep-$curStep)*2.0)]

    puts "remStep: $remStep"

    set dT    [expr $dT/2.0]

    puts "dT: $dT"

```

```

set ok [analyze $remStep $dT]
}
# if analysis fails again, reduce timestep and continue with analysis
if {$ok != 0} {
    puts "did not converge, reducing time step"
    set curTime [getTime]
    puts "curTime: $curTime"
    set curStep [expr $curTime/$dT]
    puts "curStep: $curStep"
    set remStep [expr int(($remStep-$curStep)*2.0)]
    puts "remStep: $remStep"
    set dT [expr $dT/2.0]
    puts "dT: $dT"

    analyze $remStep $dT
}
}
set endT [clock seconds]
puts "Finished with dynamic analysis..."
puts "Analysis execution time: [expr $endT-$startT] seconds"
wipe

```

Matlab code for Post processing in GiD:

```
function flaviaWriter()

% creates GiD post-processing results file from OpenSees data
fid = fopen('freeFieldLiq.flavia.res','w');
fprintf(2,'%s\n','Creating flavia.res from FEA. THIS MAY TAKE A FEW MINUTES ...')
fprintf(fid,'GiD Post Results File 1.0 \n\n');
%-----DISPLACEMENT-----
% node pointer
nodePtr = load('ppNodesInfo.dat');
% displacement data files
gdisp = load('Gdisplacement.out');
pdisp = load('displacement.out');
% adjust times on gravity analysis
gdisp(:,1) = 1e-8*gdisp(:,1);
% combine into a single array
disp = [gdisp;pdisp];
% transformation to GiD format
time = disp(:,1);
disp(:,1) = [];
clear gdisp pdisp
[nStep,nDisp] = size(disp);
nNode = nDisp/2;
for k = 1:nStep
```

```

fprintf(fid,'Result "a. Nodal Displacements" "Loading_Analysis"\t%12.5g Vector OnNodes\n',
        time(k));

    fprintf(fid,'ComponentNames "X-Displacement" "Y-Displacement"\n');

    fprintf(fid,'Values\n');

    u = reshape(displacement(k,:), 2, nNode);

    for j = 1:nNode
        fprintf(fid, '%d \t %-12.8e %-12.8e\n', nodePtr(j), u(:,j));
    end

    fprintf(fid,'End Values \n');

    fprintf(fid,' \n');

end

clear disp

fprintf(2,'* %s\n','Done with displacements ...')

%-----PORE PRESSURE-----

% pore pressure data files

gpwp = load('GporePressure.out');
ppwp = load('porePressure.out');

% adjust time on gravity analysis

gpwp(:,1) = 1e-8*gpwp(:,1);

% combine into single array

pwp = [gpwp;ppwp];

clear gpwp ppwp

% transformation to GiD format

time = pwp(:,1);

pwp(:,1) = [];

for k = 1:nStep

    fprintf(fid,'Result "a. Nodal PorePressures" "Loading_Analysis"\t%12.5g Scalar OnNodes\n',
            time(k));

        fprintf(fid,'ComponentName "Pore Pressure"\n');

        fprintf(fid,'Values\n');

        for j = 1:nNode

```

```

        fprintf(fid, '%d \t %-12.8e\n', nodePtr(j), pwp(k,j));
    end

    fprintf(fid, 'End Values \n');

    fprintf(fid, ' \n');

end

fprintf(2, '* %s\n', 'Done with porePressures ...')

%-----PORE PRESSURE RATIO-----

% load elemental data from center gaussPt

stress = load('Gstress9.out');

stress(:,1) = [];

stress = stress(1,:);

[m,n] = size(stress);

nElem = m/5;

sig = reshape(stress, 5, nElem);

clear stress

% write stress as 6x1 tensor representation

sten = zeros(6,nElem);

for k = 1:nElem

    for j = 1:4

        sten(j,k) = sig(j,k);

    end

end

clear sig

% trace of stress

I1 = zeros(nElem,1);

for k = 1:nElem

    I1(k) = sum(sten(1:3,k),1);

end

% mean stress

mStress = -I1/3;

```

```

clear I1

% average stresses at nodal depths

P = zeros(nElem-1,1);

sigV = P;

for k = 1:(nElem-1)

    P(k) = (mStress(k)+mStress(k+1))/2;

    sigV(k) = (sten(2,k)+sten(2,k+1))/2;

end

% location of mean stress values

vInfo = sort(unique(nodePtr(:,3)), 'ascend');

% vertical element size

vsize = vInfo(1)-vInfo(2);

% extrapolate first and last points

f = mStress(1) - ((mStress(2)-mStress(1))/vsize)*(vsize/2);

l = mStress(end) + ((mStress(end)-mStress(end-1))/vsize)*(vsize/2);

P = [f;P;l];

f = sten(2,1) - ((sten(2,2)-sten(2,1))/vsize)*(vsize/2);

l = sten(2,end) - ((sten(2,end) - sten(2,end-1))/vsize)*(vsize/2);

sigV = [f;sigV;l];

clear mStress

% excess pore pressure

for k = 1:nStep

    exPwp(k,:) = abs(pwp(k,:) - pwp(1,:));

end

id1 = abs(exPwp)<1e-6;

exPwp(id1) = 0.0;

% compute pore pressure ratio

ru = zeros(nStep,nNode);

ru2 = ru;

```

```

for k = 1:nNode
    for j = 1:length(P)
        if (nodePtr(k,3)==vInfo(j))
            ru(:,k) = exPwp(:,k)/abs(P(j));
            ru2(:,k) = exPwp(:,k)/abs(sigV(j));
            break
        end
    end
end

clear P exPwp

% transformation to GiD format
for k = 1:nStep
    fprintf(fid,'Result "a. PorePressureRatio (mean stress)" "Loading_Analysis"\t%12.5g Scalar
            OnNodes\n', time(k));

    fprintf(fid,'ComponentNames "Pore Pressure Ratio (mean stress)"\n');
    fprintf(fid,'Values\n');

    for j = 1:nNode
        fprintf(fid, '%d \t %-12.8e\n', nodePtr(j), ru(k,j));
    end

    fprintf(fid,'End Values \n');
    fprintf(fid,' \n');
end

for k = 1:nStep
    fprintf(fid,'Result "a. PorePressureRatio (vertical stress)" "Loading_Analysis"\t%12.5g Scalar
            OnNodes\n', time(k));

    fprintf(fid,'ComponentNames "Pore Pressure Ratio (vertical stress)"\n');
    fprintf(fid,'Values\n');

    for j = 1:nNode
        fprintf(fid, '%d \t %-12.8e\n', nodePtr(j), ru2(k,j));
    end
end

```

```

fprintf(fid,'End Values \n');

fprintf(fid,' \n');

end

fprintf(2,'* %s\n','Done with porePressureRatio ...')

%-----STRESS-----

% load and combine data

for i = 1:4

    mLoad = sprintf('gstress{i} = load("Gstress%i.out");',i);

    eval(mLoad)

    gstress{i}(:,1) = [];

    mLoad = sprintf('pstress{i} = load("stress%i.out");',i);

    eval(mLoad)

    pstress{i}(:,1) = [];

    stress{i} = [gstress{i};pstress{i}];

end

clear gstress pstress

[nStep,nStress] = size(stress{1});

nElem = nStress/5;

for k = 1:nStep

    fprintf(fid,'GaussPoints "stress" ElemType Quadrilateral\n');

    fprintf(fid,'Number of Gauss Points: 4\n');

    fprintf(fid,'Natural Coordinate: Internal\n');

    fprintf(fid,'End Gausspoints\n\n');

    fprintf(fid,'Result "Gauss Point Stress" "Loading_Analysis"\t%12.5g', time(k));

    fprintf(fid,'\tPlainDeformationMatrix OnGaussPoints "stress"\n');

    fprintf(fid,'Values\n');

    for i = 1:4

        gp{i} = reshape(stress{i}(k,:), 5, nElem);

    end

    for j = 1:nElem

```



```
fprintf(fid,'%6.0f ', j);  
  
for i = 1:4  
    fprintf(fid,'%12.6g %12.6g %12.6g %12.6g\n', gp{i}(1,j), gp{i}(2,j), gp{i}(4,j), gp{i}(3,j));  
end  
  
end  
  
fprintf(fid,'End Values \n');  
  
fprintf(fid,'\n');  
  
end  
  
clear stress gp  
  
fprintf(2,'%s\n','Done with stress ...')  
  
fclose(fid);  
  
return
```



CURRICULUM VITAE

Name Surname: Mohsen Fathieh

Place and Date of Birth: IRAN 11.09.1979

E-Mail: mohsenf120@gmail.com

B.Sc.: EASTERN MEDITERRANEAN UNIVERSITY



